An Analytical Approach to Real-Time Linearization of a Gas Turbine Engine Model

A Dissertation
Presented to
The Academic Faculty

by

Gi Yun Chung

In Partial Fulfillment
Of the Requirements for the Degree of
Doctor of Philosophy in Aerospace Engineering

Georgia Institute of Technology

August 2013

An Analytical Approach to Real-Time Linearization of a Gas Turbine Engine Model

Approved by:

Dr. J.V.R Prasad, Advisor
School of Aerospace Engineering
Georgia Institute of Technology

Dr. Eric M. Feron
School of Aerospace Engineering
Georgia Institute of Technology

Dr. Brian German
School of Aerospace Engineering
Georgia Institute of Technology

Dr. Manuj Dhingra
Pratt & Whitney

Mr. Richard Meisner
Pratt & Whitney

Date Approved: June 18, 2013

ACKNOWLEDGEMENTS

First of all, I would like to thank Professor J.V.R Prasad for his guidance and support during my studies. His truly amazing insight of physical systems has always led my research in the right direction. Without his patient guidance, I would not have been able to finish this journey. I also would like to thank Dr. Manuj Dhingra for his continuous support. I learned greatly from his problem solving skills and ability to approach the problem from a fundamental perspective. He willingly provided valuable inputs during countless discussions. I would like to extend my gratitude to Mr. Richard Meisner for sharing his experience and expertise in jet engine control. I have learned immensely from his in-depth knowledge of engine control and his keen ability to analyze the problem at hand. I also would like to thank my thesis committee members, Professor Eric Feron and Professor Brian German for providing me with thoughtful feedback and suggestions to improve the quality of the thesis.

I am grateful to James Liu for our countless discussions on the research. His ability to explain complex problems in a simple manner has helped me to recover from overwhelming emotion when I first encountered my research topic.

I would not have been able to finish my studies without the support of my dear comrades, Soyoung Kim, Jenna Stahl, and Jean Francois Castet, whose friendships made it possible to go through this difficult endeavor.

My gratitude extends to my past and current labmates, including but not limited to Ahn Binh Vu, Fahri Ersel Olcer, Keeryun Kang, Mark Lopez, Min Zhou, and Reema Kundu, who not only shared an office with me, but countless ups and downs, joyful and despairing moments. Special thanks go to controls lab TA's, Neel, Raghu, Sam, and Chris, who welcomed me to the Georgia Tech community with open hearts and made my first couple of years at Tech the most enjoyable years. I also would like to thank Juhyun and Jihee for the enjoyable coffee breaks and fun times we shared.

I am grateful to my family for their never ending support and love and for always encouraging me to go one step further. I am ever so thankful to God for His unconditional love and for providing me and leading me to the best I can be in all these years.

TABLE OF CONTENTS

LIST OF TABLES

LIST OF FIGURES

LIST OF SYMBOLS

A	Area
c_p	Specific heat
C_v	Nozzle exit velocity coefficient
e	error
F	Thrust
FAR	Fuel to Air Ratio
h	Enthalpy
h	Convective heat transfer coefficient
inf	infimum
K	Loss factor
M	Mach number
N	Shaft speed
P ,p	Pressure
P^*	$P^T(-s)$
PR	Pressure Ratio

PWR	Power
Q	Low heating value
R	Specific gas constant
S	Entropy
sup	supremum
T	Temperature
t	Time
u	velocity
u	Input
w	Mass flow rate
$wno(g(s))$	Winding number of $g(s)$
x	Slow dynamic state
y	Output
z	Fast dynamic state
$Z(g)$	Number of RHP zeros of $g(s)$
η	Efficiency
$\eta(g)$	Number of open RHP poles of $g(s)$

$\eta_0(g)$	Number of open imaginary axis poles of *g(s)*
τ	Torque
γ	Heat capacity ratio (adiabatic index)
ρ	Density
$\overline{\sigma}(A)$	Largest singular value of A
$\underline{\sigma}(A)$	Smallest singular value of A

AL	Analytical Linear
HPC	High Pressure Compressor
HPT	High Pressure Turbine
LPC	Low Pressure Compressor
LPT	Low Pressure Turbine
LPV	Linear Parameter Varing
MIMO	Multiple in multiple out
NL	Numerical Linear(truth model) or Nonlinear (truth model)
NRMSE	Normalized Root Mean Squared Error

PID	Proportional Integral derivative
PL	Piecewise Linear
PLA	Power Lever Angle
RMSE	Root mean squared error
SISO	Single in single out

Subscripts

avg	average
b ,burner	burner
bleed,bld	bleed
c	corrected
c_bleed	customer bleed
e	Exit
f	fuel
HPC	High Pressure Compressor
HPT	High Pressure Turbine
i	ideal
i,in	inlet

LPC	Low Pressure Compressor
LPT	Low Pressure Turbine
$nozpri$	Core Nozzle
$nozsec$	Bypass Nozzle
o, out	outlet
std	Standard atmospheric condition
t	Stagnation
tca	Turbine cooling flow
$\_c$	core

SUMMARY

A recent development in the design of control system for a jet engine is to use a suitable, fast and accurate model running on board. Development of linear models is particularly important as most engine control designs are based on linear control theory. Engine control performance can be significantly improved by increasing the accuracy of the developed model. Current state-of-the-art is to use piecewise linear models at selected equilibrium conditions for the development of set point controllers, followed by scheduling of resulting controller gains as a function of one or more of the system states. However, arriving at an effective gain scheduler that can accommodate fast transients covering a wide range of operating points can become quite complex and involved, thus resulting in a sacrifice on controller performance for its simplicity.

This thesis presents a methodology for developing a control oriented analytical linear model of a jet engine at both equilibrium and off-equilibrium conditions. This scheme requires a nonlinear engine model to run onboard in real time. The off-equilibrium analytical linear model provides improved accuracy and flexibility over the commonly used piecewise linear models developed using numerical perturbations. Linear coefficients are obtained by evaluating, at current conditions, analytical expressions which result from differentiation of simplified nonlinear expressions. Residualization of the fast dynamics states are utilized since the fast dynamics are typically outside of the primary control bandwidth. Analytical expressions based on the physics of the aerothermodynamic processes of a gas turbine engine facilitate a systematic approach to the analysis and synthesis of model based controllers. In addition, the use of analytical expressions reduces the computational effort, enabling linearization in real time at both equilibrium and off-equilibrium conditions for a more accurate capture of system dynamics during aggressive transient maneuvers.

The methodology is formulated and applied to a separate flow twin-spool turbofan engine model in the Numerical Propulsion System Simulation (NPSS) platform. The fidelity of linear model is examined by validating against a detailed nonlinear engine model using time domain response, the normalized additive uncertainty and the ν-gap metric. The effects of each simplifying assumptions, which are crucial to the linear model development, on the fidelity of the linear model are analyzed in detail. A case study is performed to investigate the case when the current state (including both slow and fast states) of the system is not readily available from the nonlinear simulation model. Also, a simple model based control is used to illustrate benefits of using the proposed modeling approach.

CHAPTER 1

INTRODUCTION

The operation of a jet engine is complex as it involves a combination of aerodynamic, thermodynamic, chemical and mechanical processes [37]. A control system is essential to delivering the appropriate input for achieving the desired thrust level of a jet engine for proper operation. The control system of a jet engine serves two main functions: *power management* and *protection logic* [8,20,37]. First, a control system is required to maintain "consistent and stable thrust levels" during steady state engine operation and to provide "smooth and repeatable performance" during transient operation[8,20,37]. Second, a control system must ensure safe engine operation by keeping shaft speeds, temperatures, and pressures within allowable operating limits[8,20,37,51]. Because engine performance is highest near hardware operational limits such as those on turbine temperature, shaft speed and compressor pressure ratio [51] as shown in Figure 1.1, a trade-off exists between achieving desired performance and maintaining operability margins for safety and reliability. In addition, a wide operating envelope, shown in Figure 1.2, makes control system synthesis difficult.

The engine control system has evolved greatly from simple metering of fuel to the combustor at the proper fuel-to-air ratio to achieving more challenging objectives such as higher thrust-to-weight ratios and improving specific fuel consumption [39]. Potential benefit of using an advanced engine control system includes expanding engine operation envelope by reducing conservative built-in margins for operation limits using more accurate prediction of engine performance.

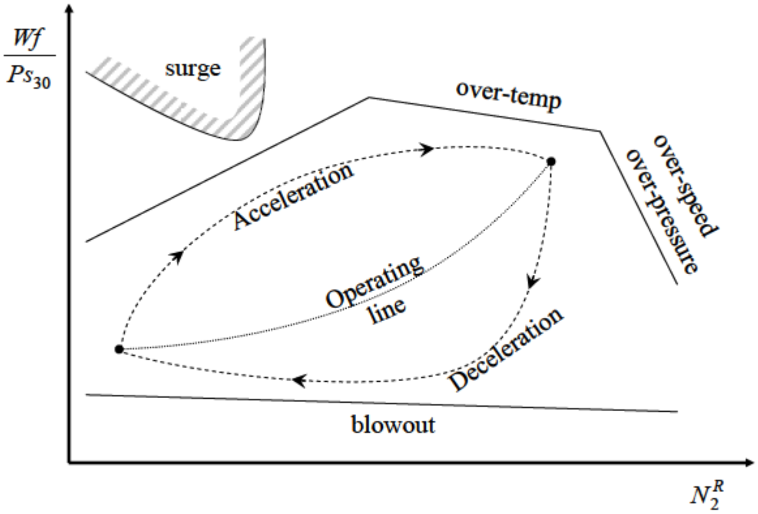

Figure 1.1 Engine operating limits [13]

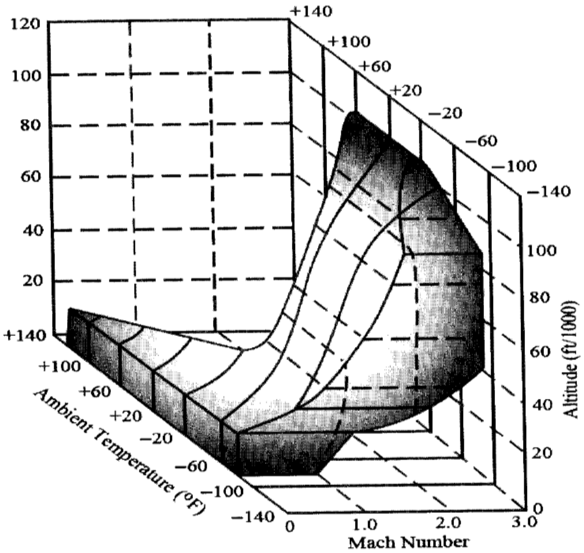

Figure 1.2 Jet engine operational range [20]

Jaw and Garg [21] present a comprehensive coverage of the advancement of control technology for aircraft gas turbine engines in the United States. Some of key milestone are described here. In the early days of the jet engine, before the 1950s, a simple controller that regulated fuel flow in proportion to the difference between the set speed and the actual speed was designed using classical frequency domain techniques and time-domain step response analysis method [21]. In this era, the modeling capability was limited as a slide rule or desk calculator was used to compute the conditions for an engine operating point[21]. The steady-state performance was calculated using performance maps, constant gas properties and an iterative process for balancing internal engine flow and energy transfers.[21].

The first computerized steady-state engine performance model was developed in 1953 and by the mid-60s, 90 percent of dynamic performance analysis was achieved using computers[21]. Frequency response methods using the gain and the phase margin as leading parameters for closed-loop system stability were used for control design in this era [21].

Engine control systems routinely incorporated engine models in the design process by the early 1970s [21]. Also, the research on multivariable control design for the gas turbine engine became active around the mid-1970s[21,39]. Multivariable control emphasizes the use of state space representation in control design [30]. This allows for a more systematic way of designing controllers in comparison to the classical single-input single-output (SISO) proportional-integral-derivative (PID) control approach when applied to complex systems [39]. A recent development in the design of control systems is to use a suitable, fast and accurate model running onboard as part of the control loop. Such a real-time model can provide estimates of the unmeasured outputs which may be used in control algorithms [9,43]. As an example, engine thrust is typically not a directly measurable parameter but may be estimated using an onboard model. In general, any control approach that utilizes a model as part of the control loop is known as model based control. Tagashira et al [54] discuss the development and the test of a model based control for a single spool turbojet engine. Mahmood et al [34] have applied the inverse model control to a three-spool gas turbine simulation model and have shown improved performance over results using classical gain scheduled control. Turevskiy et al [55] discuss the development of the model based control system for a large scale turbofan engine using a real-time engine model. A popular subclass of model based control is model predictive control, where an onboard, faster than real-time model is used for short horizon prediction. This enables prediction of limit boundary violation and hence can be used to obtain constrained locally optimal control update laws. Several research efforts have investigated the different aspects of model predictive control [4,12,46,57].

A robust engine model, capable of running at least in real-time, is a basic requirement of model based control. Since the accuracy and performance of model based control laws are dependent on the engine model, it follows that developing accurate models is the first step in any such effort. Further, as the model based control laws are continually updated, the requirement to capture global behavior of the system can be relaxed as long as locally accurate models can be efficiently obtained.

A detailed model of the engine is usually developed to simulate the engine behavior across the entire operating envelope [13,23,49]. This model can also serve as the basis of simpler, faster models targeted at control. Control oriented engine modeling methods can be broadly classified into two categories: physics based models and data-driven black box models. Typically, a physics based approach directly models the inter-component aero-thermal properties as well as shaft dynamics while employing a map/look-up table type representation of the components. A black-box approach may attempt to derive arbitrary mathematical functional relationships between input and output data, where the data is either obtained experimentally or via simulation. Examples of this approach include neural network based engine models and support vector machine (SVM) based engine models. In practice, a control and/or health monitoring engine model may mix the two approaches. Traditional on-board models have more emphasis on physics based part with a limited number of correlation parameters derived from test data to fill any missing information [11,24]. However, there is an increasing focus on hybrid approaches that incorporate neural networks to augment a state-space, physics based model [50,61]. The chief motivation is to improve the accuracy while minimizing computational costs.

Linear models have been used widely in the design and analysis of control algorithms for gas turbine engines [25]. Although, jet engines are significantly nonlinear in full operation range, the small signal response near a nominal operating point of an engine can be well represented by a linear model. The use of such linear models enables the use of well-established approaches for the synthesis and analysis of control laws and estimators, simplifying the control design process. Thus, derivation of an accurate linear engine model is crucial for successful engine control.

In the next section, different control oriented engine modeling approaches are surveyed. The first part focuses on nonlinear engine models developed for engine control. The second part focuses on the linearization methods of nonlinear engine models.

1.1 Literature Review

1.1.1 Real Time Nonlinear Engine Models

Performance-based detailed engine models often utilize pressure and temperature dynamics to simulate engine performance [49]. These models based on the intercomponent volume method require a small integration time step as a large integration time step causes inaccurate and/or unstable transient response for the stiff system [47]. High stiffness makes these models computationally expensive to run in real time. Control oriented detailed engine models are often based on the reduced order dynamic states as pressure and temperature dynamics are outside the interested frequency range [13]. In these reduced order models, the solver convergence is achieved by forcing continuity of the mass flow rate at each component level. Solver tolerance determines the convergence accuracy and the number of iterations. In addition to the number of dynamic states and solver tolerance, accuracy of the model depends on the level of simplifications related to the thermodynamic properties [9]

An engine model has become the integral part of the control architecture as the engine control has been moving from the classical PID control to the model based control as described in the previous section. Engine operation spans a considerable range and having a model that runs in real time enables model based control by providing an accurate model at the particular operating conditions. Some modifications to the detailed engine model are essential for achieving real-time capability. The requirement of real-time models has been relaxed and a more accurate model can run onboard as a result of rapid advancement of processor capability. The following research efforts have been made to add real-time run capability to existing detailed engine models.

Sanghi et al [47] developed a real-time engine model that is based on the explicit time-integrated, aerothermodynamic transient model of a twin-spool, mixed-flow turbofan engine based on state variables and control volume approaches. The original intercomponent based model is generally not suitable for real-time model because a small integration time step of 0.1 ms is required to produce stable system for stiff jet engine. Sanghi et al reduced the number of states from nine to six by enforcing the main mixer to be a static component. With this assumption, the frame time could be increased to 0.4 ms with actual control volumes and up to 1.2 ms with the time scaling of control volume methods. The model was validated against the baseline model. Although rapid development of the processor industry has relaxed computational cost constraints tremendously, there is still restriction on the frame rate. Expansion in the number of dynamic states in high frequency should be accompanied by reduction in frame rate to improve model accuracy without suffering instability.

Camporeale et al [5] developed a high fidelity modular code for real-time dynamic simulation of a gas turbine engine in the Simulink environment. Comporelae et al modeled each component using aerothermodynamics of the fluid properties. No iteration was required at the component level. Compressor and turbine were modeled as volumeless elements and a volume capacity was introduced between these elements in order to account for the unsteady mass balance. Shaft dynamics, actuators dynamics and transducer dynamics were implemented. Algebraic expressions were arranged to obtain the solution using forward substitution. A sequential solving technique was used where each parameter was calculated as an explicit function of known quantities, getting rid of iteration.

Martin et al [35] presented the development and validation of a civil aircraft engine simulation for advanced controller design. They developed a direct non-iterative model based on intercomponent volume approach similar to the model developed by Comporeale et al. Their model was characterized by modularity of each component and the adherence to underlying physics. Empirical approximation was minimized to increase flexibility of the model and to provide physical justifications. They represented gas properties with polynomial fits in order to increase the accuracy of the model. Detailed description of the model and the controller is provided in the paper. The model included 41 states incorporating shaft dynamics, heat soak dynamics and volume dynamics.

Rahman and Whidborne [44] presented a real-time engine model based on a hybrid approach of the iterative method and the intercomponent volume technique. They calculated compressor/turbine mass flows and efficiencies using static maps. An iterative approach was applied at each engine subsystem to solve algebraic thermodynamic equations for exit enthalpy, entropy, and temperature. This iteration method for solving thermodynamic properties improved the simulation accuracy over methods using the standard relationship shown in equation (1.1) which assumes calorically perfect gas with the constant specific heat parameter.

$$\Delta T_C = \frac{1}{\eta_c} T_1 \left(\left(\frac{P_2}{P_1} \right)^{\frac{\gamma - 1}{\gamma}} - 1 \right) \tag{1.1}$$

The intercomponent volume method was used to calculate pressure derivatives, and hence, pressure at corresponding engine stations. Simulation results exhibited significant improvement of the hybrid model over the pure intercomponent volume technique without iteration when compared to a more accurate non real-time engine model. This model has a potential to run in real time with careful selection of the component volumes and simulation step time.

All models described above belong to the category of physics based aerothermodynamic models. The data driven engine models which are trained using either actual engine measurements or a detailed engine model are described next.

Venturini [58] presented simulation of compressor transients using recurrent neural network models. He investigated a self-adapting model capable of reproducing time-dependent data with high computational speed. Recurrent neural networks utilize the memory process in order to take time dependent data characteristics. Venturini modeled a compressor using recurrent neural networks with one feedback loop in the recursive computational structure. He examined effects of the number of neurons, length of time delay, and number of outputs on the output accuracy using root mean square error. He validated the model output against the physics based model as well as actual experimental data. Unfortunately, the neural networks were trained using data from the physics based model; thus, results were always worse than that of the physics based model. Different results may be expected if the model is trained against actual measurements. In addition, this paper only presented the neural network model for a compressor. Although the approach can be extended to an entire engine, its complexity may grow exponentially with larger number of inputs and outputs. Also, selection of the correct inputs and outputs are vital in the neural network approach. Finally, whereas the self-adapting approach seems attractive, certifiability becomes an issue.

Rezvani et al [45] established the engine transient modeling methodology based on a neural network without use of a recurrent approach. Details of selecting a proper training data set were discussed. A training data set was selected based on a random ramp input within the feasible input range. Model output resulted in a good match with that of the truth model.

Neural network based models will exhibit notable accuracy within a trained operating range, but may diverge from actual engine responses outside the trained range. The data driven dynamic model that covers the entire operation range is still at the experimental stage because of shortcomings, including unknown behaviors in the case of extrapolation and lack of physical insights, makes it vulnerable for control application. In the control applications, the failure to predict the system dynamics within reasonable range may result in a catastrophic failure of an engine. The use of a data driven model is more versatile in health management where the failure to predict the system dynamics is less catastrophic.

Any of modeling approaches examined in this section can serve as a basis for the linear model development. Further approximations of thermodynamic properties may be required on some of the physics based models described above for achieving real-time linearization. The number of simplifying assumptions should be minimized to achieve linearization accuracy while satisfying computational requirement. Neural network based models can be directly linearized using simple differentiation of the basis function.

1.1.2 Linear Engine Models

Development of an accurate linear engine model is crucial to successful engine control as most multivariable control methods utilized for engine control systems are based on linear control theory. There are a few different approaches to linearization of an engine model. The most common/researched approach is derivation of linear coefficients using numerical schemes based on small input and state perturbations. Since the engine model is highly nonlinear in its nature, the common practice is to schedule multiple linear models developed at different operating conditions.

Seldner and Cwynar [48] presented a detailed procedure for generating linear models of a turbofan engine. Linearization based on classical Taylor's series expansion about the nominal operating condition was achieved using the numerical perturbation method. The proposed scheme was implemented on the F100 engine and linear responses were compared with nonlinear responses in simulations. Some steady-state error was observed in the simulation. In addition, a detailed procedure of reducing the full order state of 16 to reduced order of 7 was outlined. Simulation results demonstrated agreement between the reduced order model and the full order model. The developed linear model is only valid for small disturbances about a steady-state operating point. Seldner and Cwynar commented that several linear models are required at different operating conditions; however, no detailed procedure is outlined regarding interpolation of different linear models.

Sugiyama [53] derived linear matrices from a nonlinear dynamic simulation using numerical perturbation techniques similar to the method of Seldner and Cwynar. An optimal perturbation size and a numerical scheme were selected based on simulation results of experimenting with various numerical schemes and different perturbation sizes. The numerical scheme was applied at equilibrium condition. Simulation results inferred a five point Lagrange formula with 0.5% perturbation size to be optimal. A different engine may require a different perturbation size and a numerical scheme for optimality. Sugiyama expanded the linearization approach to cover different atmospheric conditions by redefining dynamics in the corrected space. Each linear coefficient was re-derived by correcting with temperature and pressure ratio. Whole corrected elements of system matrices became function of corrected control variables and flight Mach number.

Kim et al [24] presented a real-time engine model for a three-spool turbofan engine which combines two different models at different operating regimes for improving accuracy. Both models were based on aerothermodynamic engine models, one developed for idle to max power range and the other one developed at sub-idle regime. Again, the model was linearized using the small perturbation scheme. Variable perturbation sizes using fuzzy logic in sub-idle regime were introduced to prevent solver convergence issue. A partial derivative of each parameter from the nonlinear model was fine-tuned by comparison with a steady-state value of each parameter and integrated partial derivatives were compared with a steady-state value. When differences were observed, adjustment of each integrated partial derivative was made according to relative weight of each integrated partial derivative contribution to the whole. Two data sets from two different models were merged in smooth fashion. In order to cope with nonlinearity of engine dynamics over entire flight spectrum, a piecewise linear modeling approach, utilizing rotational speed of high pressure shaft, N_3, and Mach number for the interpolation, was adapted.

Linear models by Seldner and Cwynar, Sugiyama, and Kim et al adequately capture system dynamics near the operating condition where linear sensitivities are developed; however, deviation from the actual dynamics is unavoidable away from such operating conditions. Piecewise linear models, which are developed by interpolating linear models at selected steady-state conditions, are commonly used to cover different power levels. Scheduling of the liner models is key to achieving the desired accuracy. These piecewise linear models are often used in combination with a gain scheduling controller[42]. However, the linear responses deviate from the nonlinear responses when the system becomes highly nonlinear with respect to fuel flow, dynamics states, and different operating conditions during large transient operations even if an optimum scheduling is achieved. The following studies were conducted to improve accuracy during transient operations.

Lichtsinder and Levy [28] developed a real-time quasilinear model using a generalized describing function that can be used during aggressive transient operations. The main objective of Lichtsinder and Levy was to overcome disadvantages of the traditional linear and piecewise linear model during fast changes of fuel input command signal in a large transient. A linear model developed around an operating point does not provide adequate information in an aggressive transient operation. Engine dynamics were represented by a combination of some initial condition dynamics and the variance in the dynamic state from that arbitrary operating condition. They used generalized describing functions to determine linear sensitivity matrices. Inputs were generalized using quasi-polynomial expressions and outputs were approximated by quasi-polynomial expressions. Errors between the actual output and an assumed output were used to derive optimal time constant and gain for each dynamic equation. This model provided maximal accuracy for the largest variance of fuel flow input for different Mach number and altitude operating conditions. The key in the approach was to assume that the fuel flow input function of the open loop engine is known. Gains and time constants were computed for the maximal variance of a closed loop input (from idle to maximal power level) at each combination of Mach number and altitude operating condition. When an input signal differed from the maximal signal used for the fast model design, model accuracy deteriorated. The danger for stall is minimal when fuel flow input command is significantly less than the maximum; thus, reduced accuracy is tolerable. The main objective of the model of avoiding the most dangerous situation during a large transient was met. The model offered a simple linear real-time model that can be used for large transient operation; however, the authors noted that it may become complicated to develop precise real-time engine simulations with full-envelope coverage for all possible inputs.

Shankar and Yedavalli [50] presented a parameter estimation model utilizing a neural-network based observer that augments a linear Kalman filter to compensate for accounted nonlinearity. The neural network utilized a radial basis function and was trained offline using simulation data. The basis linear model was obtained using traditional small perturbation techniques at each operating condition. Results indicated accurate prediction of steady-state values but transient responses exhibited comparatively larger error. Shankar and Yedavalli claimed that transient response characteristics could be improved with the redesign of a gain matrix. Unfortunately, the modeling approach is highly dependent on a training data set and parameters used in the algorithm. Shankar and Yedavalli stated that the neural network has to be trained not only at different flight conditions, but also at different deterioration levels. Design of the sample space itself requires more in-depth research which was in part discussed by Rezvani et al [45]

Volponi [61] presented a hybrid engine model that integrates a physics based state variable linear model with an empirical neural network to improve model accuracy. The model was developed for tracking engine health performance. A piecewise linear model was augmented with both a Kalman filter for tuning engine model error and a neural network to capture any unmodeled engine dynamics. Training of the neural network was carried onboard in non-real time using different networks at different flight envelops. Volponi also discussed details of real-time code development. The hybrid modeling approach utilized the advantages of both physics based models and neural network models. The difficulty with scheduling of linear models at different operating condition was still an issue. Also, for a control application, training and validation of the neural network becomes more difficult since changes in engine dynamics need to be captured in real time. The hybrid modeling approach, while promising, remains problematic.

These efforts to achieve more accurate engine models have been made to answer the following continuously sought research question:

> *How can a linear model accurately capture the engine dynamics during transient operation?*

This thesis focuses on finding more dependable answers to the above question to progress one step forward in the advancement of an engine control system.

1.2 Objectives

The effort to capture dynamics far away from equilibrium points using sets of linear models have been made continuously by many control engineers in different areas [22,27,40]. Johansen et al [22] tried to capture transient operations by including a set of off-equilibrium linear models in addition to linear models developed at equilibrium to improve the accuracy. Murray et al [40] enhanced the work of Johansen et al by introducing nonparametric Gaussian process to provide better local models for blending. Leith and Leithead[27] have developed a family of velocity-based linearization which is valid in vicinity of any operating point. The gas turbine engine can also benefit from off-equilibrium linearization that accurately captures the dynamics of engine away from equilibrium conditions as discussed in the previous section. In addition, the improvement can be made to existing gas turbine model based control synthesis if an accurate linear model that is independent of selection of scheduling parameters and training set can be developed.

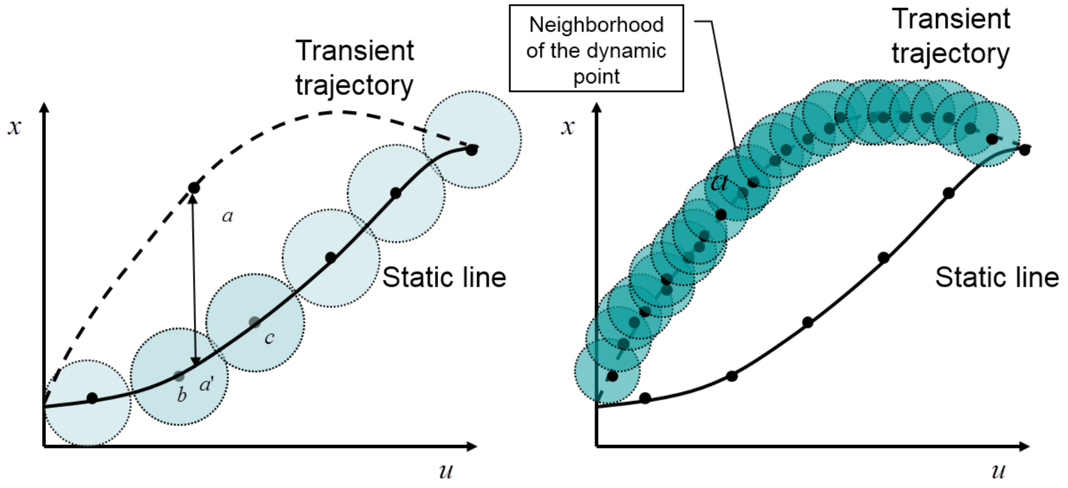

Figure 1.3 a) Steady-state operation[22] b) transient operation

The necessity to capture off-equilibrium dynamics is illustrated in Figure 1.3, which demonstrates the relationship between the state and input during steady-state and transient operations. The error caused by scheduling linear coefficients as functions of a state is negligible for the two-dimensional case in steady-state operation, represented by solid line in Figure 1.3a. However, as the trajectory moves away from the steady-state operating line as described by the dashed line, the error due to scheduling linear coefficients increases. For example, the weighted sum of slopes at equilibrium points *b* and *c* typically used in piecewise linear models as an estimate of the slope at point *a* of the actual trajectory would be quite different from the true value of the slope at point *a*.

The error can be even larger due to increased dimensionality. A linear model that is developed at each point along the trajectory (both on- and off- equilibrium), as shown in Figure 1.3b, offers an improvement over traditional piecewise linear models. The model is linearized at every time step along the transient trajectory, thus resulting in more accurate linear models along the transient trajectory. Moreover, the real time linearization eliminates the difficulty associated with scheduling a piecewise linear model.

An off-equilibrium linear model can be developed either analytically or numerically at every time step along the trajectory. In addition, a linear model based on a neural network can be utilized. The neural network based model offers the key benefit that engine dynamics can be represented by simple algebraic expressions; however, difficulties associated with the selection of training data and the validation of the model may exceed benefits with existing technology as stated before. The numerical real-time model offers accuracy but the computational cost would be too expensive for the real time implementation. The physics based analytical linear model shares the advantage of a neural network based linear model in that linearization is based on sets of algebraic expressions, keeping the computational cost low.

The analytical approach has been widely used during early years of aviation, mainly in flight dynamics and control applications[1]; however, this approach has not yet been applied to an aircraft jet engine dynamic model. Chung et al [6] developed an analytical linearization scheme for a static model of a generic back end (turbine – nozzle) of a turbofan engine as a proof of concept validation test. Development of an analytical linear model of a jet engine can benefit from well-known advantages of analytical linearization such as its strong ties to physical insights and reusability. It also offers excellent physical insight into engine dynamics. The analytical linear model may suffer from reduced accuracy due to required simplifications; however, it provides a much simpler solution computationally than numerical linearization[7]. Also, modifications of the model to incorporate health degradation or other external factors become easier as the algebraic expressions can be easily modified.

The analytical linearization of a jet engine model is achieved in a two-step process as shown in Figure 1.4. The first step is to make simplifying assumptions to put a nonlinear model in an analytically linearizable form. The second step is to linearize the engine model by taking derivatives of these analytical expressions. The analytical linearization can be applied as long as the engine model is in a suitable form, i.e., typically in a reduced order form, where analytical expressions approximate all input-to-output relationships. As analytical approximations are necessarily based on a physical understanding of the engine dynamics, they can also provide a convenient computational framework for detailed analysis of an engine model. In this thesis, various simplifying assumptions are used in arriving at an analytical linear model of a gas turbine engine valid over its transient operations.

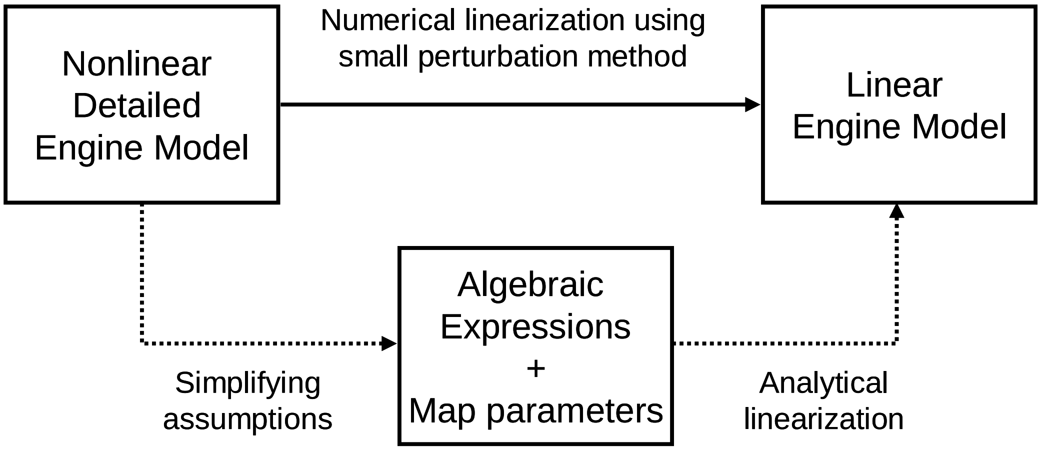

Figure 1.4 Different linearization approach

In summary, the linearization approach proposed in this thesis offers a twofold advancement in current jet engine control technology.

- First, the real time linearization based on both on- and off- equilibrium captures large transient dynamics more accurately, as discussed.
- Secondly, an analytical linearization approach using the sets of algebraic expressions derived from Taylor series expansion offers physical insights, computational efficiency and flexibility.

In addition, this thesis offers in-depth analysis of the analytical linear model to demonstrate the validity of the proposed model and its potential future use.

1.3 Thesis Organization

The thesis is organized as follows:

Chapter 2 through 4 describe the linearization and validation methodology. Chapter 2 describes a control oriented turbofan engine model in detail. Sets of expressions representing each component are presented. This control oriented nonlinear model is the basis for the linearization methods that follow. Chapter 3 discusses details of the novel linearization method. First, a general linearization scheme around arbitrary operating conditions (including on- and off- equilibrium conditions) is explained. Then, the simplifying assumptions necessary for achieving the analytical linearization are stated. Subsequently, the details of a component level linearization and integration of component linear models are presented. Chapter 4 presents the different validation methods to measure the linear model fidelity, including the normalized root mean squared error, normalized additive uncertainty and the ν-gap metric. The rationale behind using these validation measures is also discussed. The selected transient profile and the models for comparative study are described.

Chapter 5 and 6 present the simulation results and the in-depth analysis of the linear model. Chapter 5 presents the simulations results to show achievement of desired fidelity using the proposed linearization approach. The results are compared with those obtained using a traditional piecewise linear model to demonstrate the superiority of the proposed approach during the transient operation. Numerical aspects of the analytical linear model are also analyzed in this chapter. Chapter 6 presents the analysis of the simplifying assumptions and shows the effects of each assumption on the fidelity of model.

Chapter 7 presents simple control and estimation application examples. The case study of a situation where the nonlinear values are not available is conducted. Moreover, a simple model inversion controller to track fan speed is used to illustrate the benefits of using off-equilibrium analytical linear models.

Finally, chapter 8 summarizes the thesis and presents suggested future work based on this research.

CHAPTER 2

CONTROL ORIENTED NONLINEAR ENGINE MODEL

The proposed linearization approach requires a nonlinear engine model to run onboard in real time. Description of a control oriented nonlinear engine model is given in this chapter. The 0-D onboard model is based on the averaged fluid characteristics at discrete positions inside the engine, generally at the inlet and the outlet of each component [41]. It is common practice to represent the engine with a reduced number of dynamic states to achieve real time capability. A generic twin-spool turbofan engine diagram is presented in Figure 2.1.

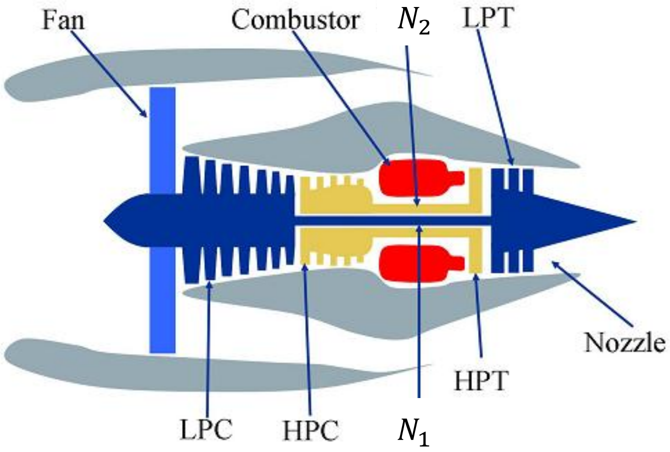

Figure 2.1 Generic two-spool turbofan engine diagram [17]

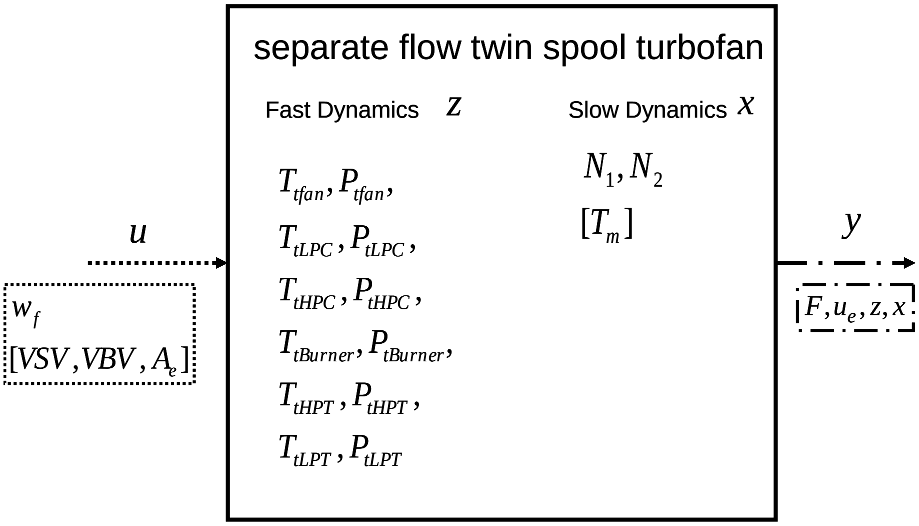

Figure 2.2 Nonlinear engine model description

Typical inputs, outputs and states of a generic twin-spool turbofan are shown in Figure 2.2. The primary control input of system is fuel flow rate. Common additional control variables include variable stator vanes, variable bleed valve and variable exit nozzle area. Dynamic states are divided into two groups based on their frequency response. Shaft dynamics and heat soak dynamics are in a low frequency range whereas flow dynamics including pressure and temperature dynamics occur at high frequency. Outputs of system include selected flow properties, shaft dynamics, thrust and exit velocity.

A more detailed block diagram for a generic separate flow twin spool turbofan model is shown in Figure 2.3. Solid lines represent the fluid connections, dotted lines represent mechanical connections and dashed lines represent solver parameters. In this model, the “LPC” model consists of both the inner annulus of the fan as well as the low pressure compressor stages. The typical convention for station numbering of twin-spool turbofan models is used.

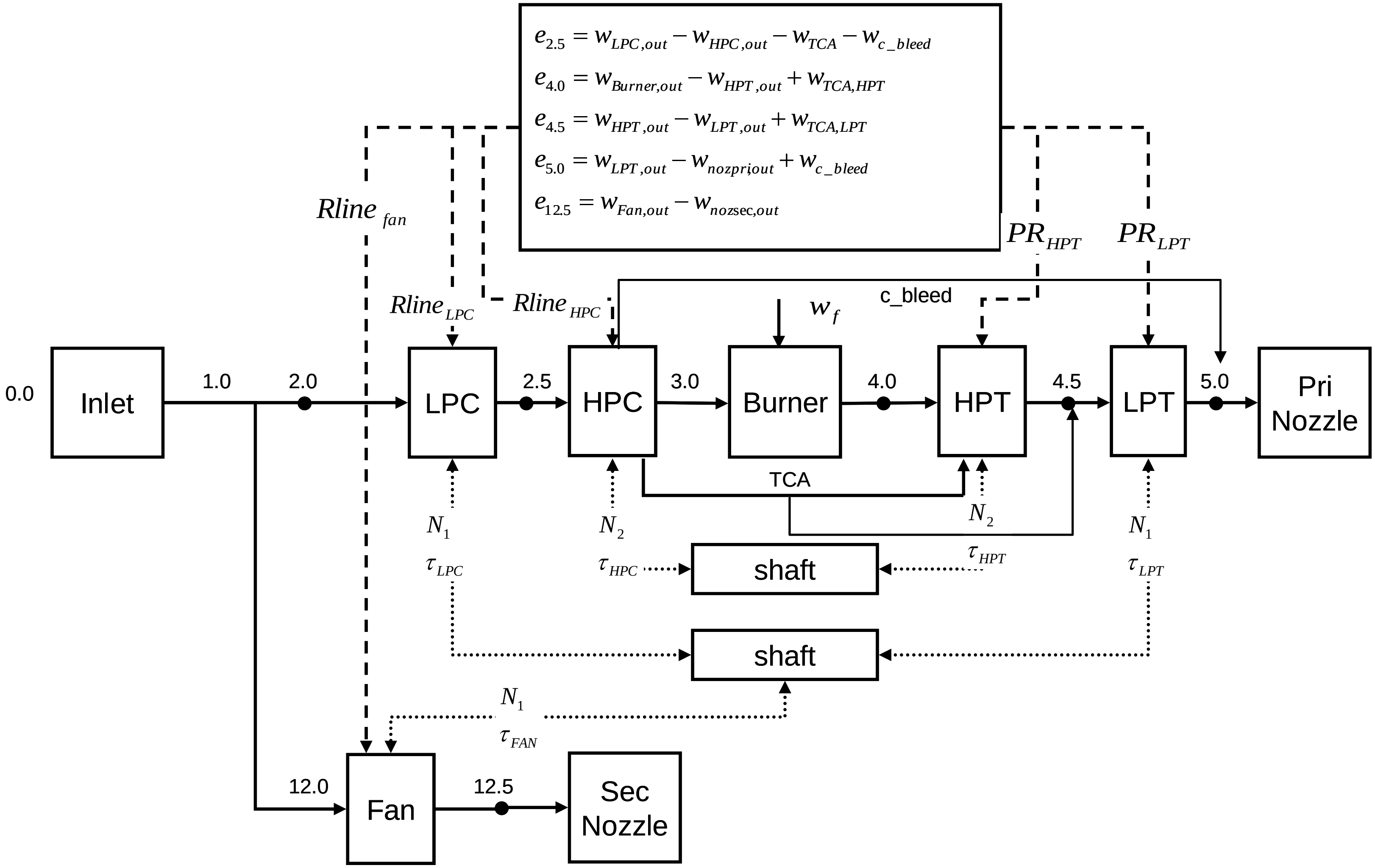

Figure 2.3 Separate flow twin-spool turbofan model

2.1 Simplifications in Nonlinear Model

The following simplifications are present in the detailed engine model.

1. Bleed flow is extracted as a constant ratio of the total core flow.

   The rate of change of bleed mass flow rate is assumed to be the same as the core flow.

   $$w_{bleed} = Kw_{total}$$

2. Bleed flow is assumed to be extracted from the exit air flow of the high pressure compressor.
3. Cooling flow is added to the high pressure turbine before expansion.
4. A constant fraction of the bleed flow is assigned as customer bleed.
5. Parasitic flows, except for turbine cooling air and customer bleed, are ignored.
6. Torque losses in shaft are neglected.
7. A converging nozzle type is used for both core and bypass flow.
8. Pressure losses in the nozzle and duct are neglected.
9. Rayleigh pressure drop is neglected inside the burner.

2.2 Engine Dynamics Decomposition

Turbofan engines have multiple dynamic states at different frequency ranges as shown in Figure 2.4. Shaft dynamics and heat soak dynamics are in a low frequency range of less than 2 Hz whereas pressure and temperature dynamics occur at much higher frequency.

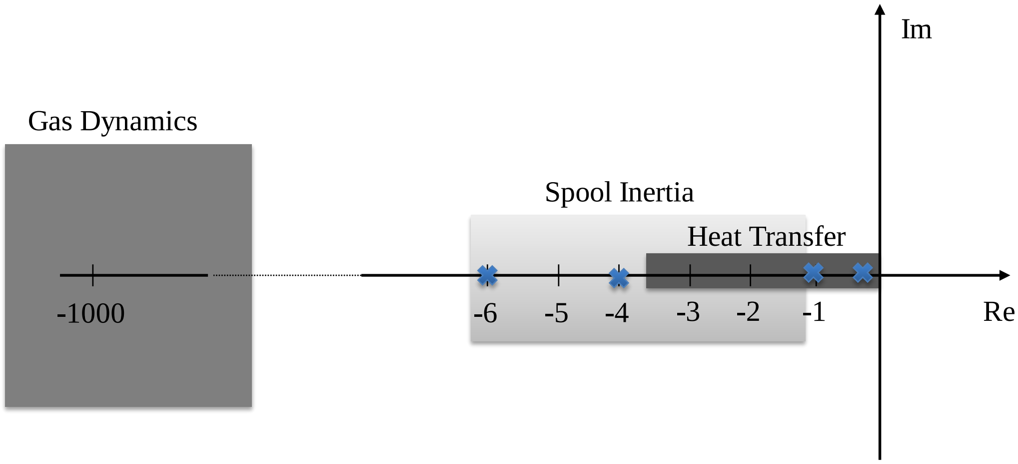

Figure 2.4 Typical locations of jet engine poles [29]

Such a nonlinear system with slow and fast dynamics is represented in terms of slow states *x* (shaft dynamics, heat soak dynamics, etc) and fast states *z* (flow dynamics in different components of an engine) as follows.

$$\begin{aligned} \dot{x} &= f(x, z_, u) \\ \dot{z} &= g(x, z, u) \end{aligned} \quad \textbf{(2.1)}$$

It is often desirable to reduce the system's order to facilitate the analysis and design of dynamic control systems[14]. Less dominant poles on the far left of the dominant poles are considered as the quasi steady-states in order to reduce the order of the system. When one considers the flow behavior of an engine, the flow dynamics may be considered to be relatively fast, which are outside the typical bandwidth of primary engine controller (0-2 Hz, [20]). Hence, the flow dynamics of such a system may be residualized, i.e. the dynamic equations associated with *z* are treated as algebraic equations. Hence, the residualized form of the fast dynamics are given by

$$g(x, z_{o,} u) = 0 \tag{2.2}$$

The resulting equation (2.2) is an algebraic expression and can be solved for the residualized fast dynamic state z_0. The residualization process is captured in the flow chart shown in Figure 2.5. In the present work, the engine model is reduced to include only the shaft dynamics.

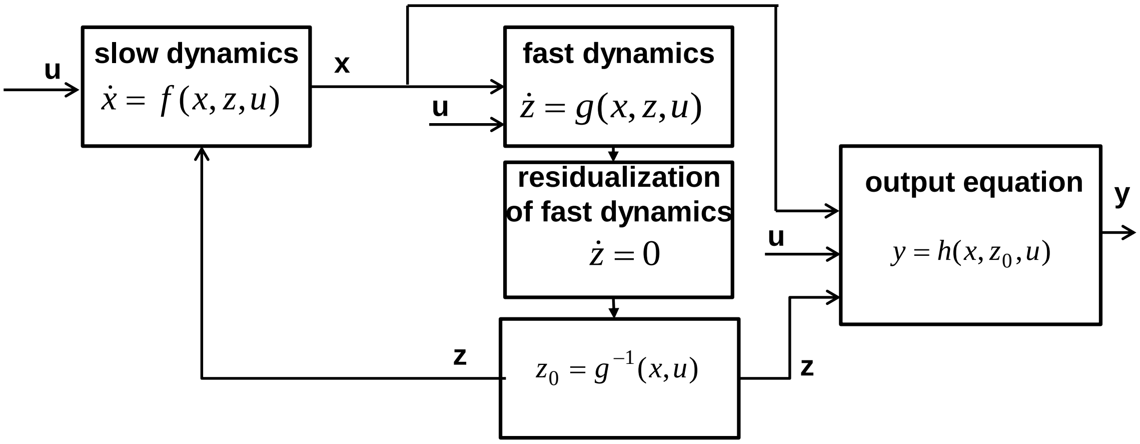

Figure 2.5 Engine dynamics residualization

2.3 Component Description

Details of the reduced order model at the component level for the generic turbofan are discussed in the following sub-sections. The details of generic component models of an engine required for linearization, such as compressor, combustor, turbine and nozzle, are adapted from NPSS component models and textbooks on gas turbine propulsion [3,16,23,36]. Any gas turbine engine model can be constructed using these generic components in conjunction with some auxiliary components such as ducts and splitters. Bypass flow and core flow are treated in a similar manner. The component level equations are applied to both high speed spool and low speed spool elements and repeated as necessary. Gas properties are obtained from the gas tables.

2.3.1 Compressor

Figure 2.6 shows representative inputs and outputs of a compressor type element. Fluid properties at the inlet of a compressor in addition to the shaft speed are necessary inputs for computing fluid properties at the outlet and the torque required for compression. Fluid properties of a compressor represented by stagnation temperature and stagnation pressure shown as a solid line in Figure 2.6 are fast dynamical states. Shaft speed represents a slow dynamical state. The *Rline* is used to uniquely identify pressure ratio, mass flow rate and shaft speed. It has no physical meaning and typically the first *Rline* coincides with the surge line. The remaining *Rlines* are roughly parallel to the surge line [23]. Other types of index system can also replace the *Rline*. Then equations (2.7)-(2.9) are adjusted accordingly.

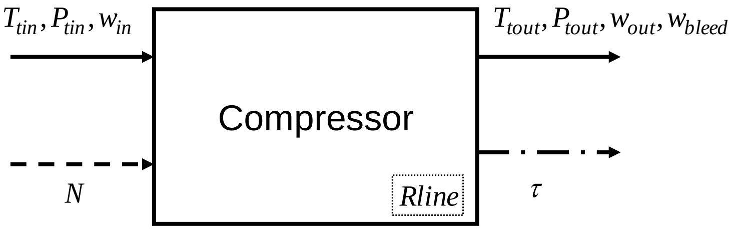

Figure 2.6 Compressor block diagram

A compressor is connected to the shaft and the torque supplied by the shaft is utilized to compress the flow. Processes inside a compressor can be represented by equations (2.3)-(2.19) where f_1, f_2, and f_3 are functions representing a typical compressor map as shown in Figure 2.7 [23]. Fluid properties at the outlet are calculated by using changes in the thermodynamic properties given by the pressure ratio obtained from the compressor map. Relationships between thermodynamic properties are generalized as the function F. Loss in a compressor component is represented by the efficiency values from the compressor maps. Equations (2.15)-(2.17) allow turbine cooling air to be extracted at any compression stage. Fluid properties of bleed flow are determined by applying partial compression, given by constant K_2 and K_3. As discussed in the simplifying assumption section, it is assumed that the turbine cooling air is extracted at the end of the final stage of the compression of the compressor and K_2 and K_3 are set to one.

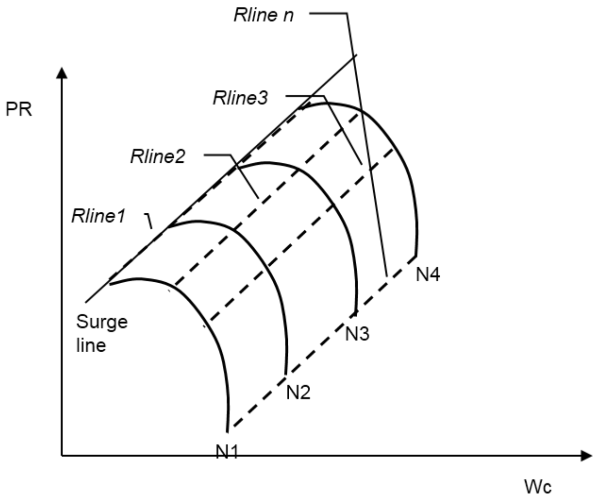

Figure 2.7 Compressor map [23]

In the control oriented 0-D model, a compressor is considered as a whole and the stage by stage characterization is not included. The generic compressor component model described above can be used to represent individually fan, low pressure compressor and high pressure compressor components.

$$\theta = \frac{T_{tin}}{T_{std}} \tag{2.3}$$

$$\delta = \frac{P_{tin}}{P_{std}} \tag{2.4}$$

$$N_c = \frac{N}{\sqrt{\theta}} \tag{2.5}$$

$$[S_{in}, h_{in}] = F(P_{tin,} T_{tin}) \tag{2.6}$$

$$w_{out} = f_1(N_c, Rline) \tag{2.7}$$

$$PR_{out} = f_2(N_c, Rline) \tag{2.8}$$

$$\eta = f_3(N_c, Rline) \tag{2.9}$$

$$P_{tout} = PR_{out} \cdot P_{tin} \tag{2.10}$$

$$[T_{ideal}, h_{ideal}] = F(P_{tout}, S_{in}) \tag{2.11}$$

$$h_{out} = \frac{h_{ideal} - h_{in}}{\eta} + h_{in} \tag{2.12}$$

$$[S_{out}, T_{tout}] = F(P_{tout,} h_{out}) \tag{2.13}$$

$$PWR_1 = w_{out}(h_{in} - h_{out}) \tag{2.14}$$

$$P_{t\_bleed} = P_{tin} + K_2(P_{tout} - P_{tin}) \tag{2.15}$$

$$h_{bleed\_out} = h_{in} + K_3(h_{out} - h_{in}) \tag{2.16}$$

$$PWR_{bleed} = w_{bleed}(h_{bleed\_out} - h_{out}) \tag{2.17}$$

$$PWR = PWR_1 + PWR_{bleed} \tag{2.18}$$

$$\tau = \left(\frac{60}{2\pi}\right)\frac{PWR}{N} \tag{2.19}$$

2.3.2 Combustor

Typical inputs and outputs of a combustor component are shown in Figure 2.8. In addition to inlet fluid properties, fuel flow is a direct input to the burner. The output of the combustor is the product of the combustion process.

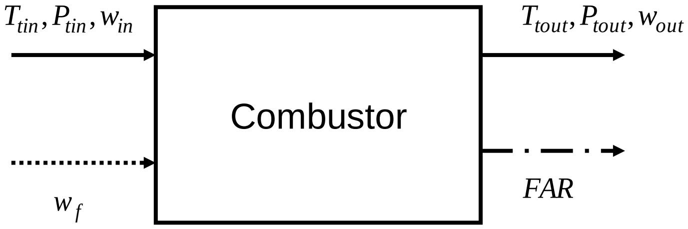

Figure 2.8 Combustor block diagram

Inside the combustor, the air and fuel are mixed and burned to produce high temperature gas which drives the turbine and produces thrust by passing through the nozzle. The pressure drop in the combustor due to friction is assumed to be constant. Heat is released in the combustion process and enthalpy at the exit of the combustor is given by energy balance. The lower heating value ,Q, depends on the specific type of fuel used and is constant.

$$P_{tout} = (1 - K) P_{tin} \tag{2.20}$$

$$FAR = \frac{w_f}{w_{in}} \tag{2.21}$$

$$\left(w_{in} + w_f\right) h_{tout} = w_{in} h_{tin} + w_f Q \eta_b \tag{2.22}$$

2.3.3 Turbine

Inputs and outputs of a turbine component are given in Figure 2.9.

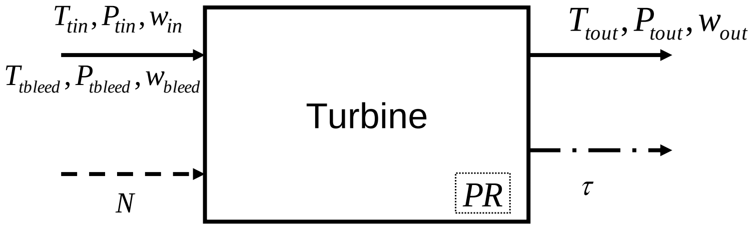

Figure 2.9 Turbine block diagram

Processes inside the turbine are characterized by equations (2.23)-(2.39). Energy of gas flow in the turbine produces work on the shaft and drives the compressor. Mass flow rate and efficiency are obtained from the turbine maps which are similar to the compressor maps as given by equations (2.27) and (2.28). Expansion of gas inside the turbine causes a decrease in enthalpy, which is the source of the work that drives the compressor. The bleed flow to cool down the turbine is added at the inlet, which also expands to produce work as shown in equations (2.35) and (2.36).

$$\theta = \frac{T_{tin}}{T_{std}} \tag{2.23}$$

$$\delta = \frac{P_{tin}}{P_{std}} \tag{2.24}$$

$$N_c = \frac{N}{\sqrt{\theta}} \tag{2.25}$$

$$[S_{in}, h_{tin}] = F(P_{tin,} T_{tin}, FAR) \tag{2.26}$$

$$w_{out} = g_1(N_c, PR) \tag{2.27}$$

$$\eta = g_2(N_c, PR) \tag{2.28}$$

$$[T_{ideal}, h_{outi}] = F(P_{tout}, S_{in}) \tag{2.29}$$

$$h_{tout\_c} = h_{tin} - (h_{tin} - h_{touti})\eta \tag{2.30}$$

$$[S_{out}, T_{tout\_c}] = F(P_{tout,} h_{tout\_c}) \tag{2.31}$$

$$PWR_1 = w_{out}(h_{tin} - h_{tout\_c}) \tag{2.32}$$

$$w_{out} = w_{core} + w_{bleed} \tag{2.33}$$

$$[T_{bleedi}, h_{bleedi}] = F(S_{bleed\_in}, P_{tout}) \tag{2.34}$$

$$PWR_{bleed} = \eta w_{bleed}(h_{bleed} - h_{bleedi}) \tag{2.35}$$

$$PWR = PWR_1 + PWR_{bleed} \tag{2.36}$$

$$\tau = \left(\frac{60}{2\pi}\right)\frac{PWR}{N} \tag{2.37}$$

$$h_{tout} = \frac{1}{w_{out}}\left[h_{tin}w_{in} + h_{bleed}w_{bleed} - \eta\{(h_{tin} - h_{touti})w_{in} + h_{bleedi}w_{bleed}\}\right] \tag{2.38}$$

$$[S_{out}, T_{tout}] = F(P_{tout,} h_{out}) \tag{2.39}$$

2.3.4 Nozzle

Figure 2.10 shows typical inputs and outputs of a converging nozzle. In addition to basic fluid properties of incoming flow at the inlet, the ambient static pressure at the outlet determines fluid properties at the exit of the nozzle. Outputs of the nozzle include the thrust and flow velocity.

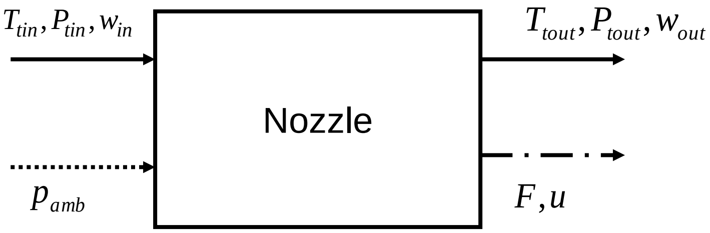

Figure 2.10 Nozzle block diagram

For subsonic flight, a converging nozzle is typically used. Distinctive flow characteristics based on choking and non-choking of the flow are determined by comparing the pressure ratio of the nozzle to the critical pressure as shown in equation (2.43). The nozzle is expected to choke at higher pressure ratios. When the nozzle is choked, the pressure at the exit does not fully expand to the ambient pressure and part of thrust is generated due to the pressure differential at the exit of the nozzle. When the flow is subsonic, the pressure at the exit fully expands to the ambient pressure and this becomes the condition for solving for the exit velocity.

$$P_{tout} = P_{tin}(1 - K_{loss}) \tag{2.40}$$

$$PR = \frac{P_{tin}}{P_{amb}} \tag{2.41}$$

$$P_s = F(h_{tin,} P_{tout,} M = 1) \tag{2.42}$$

$$PR_{critical} = \frac{P_{tin}}{P_s} \tag{2.43}$$

$$M_e = F(h_{tin}, P_{tout,} P_s = P_{amb}) \tag{2.44}$$

$$\begin{gathered} \text{if } \ (PR > PR_{critical}) \\ [P_s, u] = F(h_{tin}, P_{tout}, M = 1) \\ \text{else} \\ [P_s, u] = F(h_{tin}, P_{tout}, P_s = P_{amb}) \end{gathered} \tag{2.45}$$

$$F = w_{out} u C_v + (P_{out} - P_{amb}) A_e \text{, } C_v = 1 \tag{2.46}$$

2.3.5 Shaft

Shaft speed is determined from the conservation of angular momentum. Using the summation of the torque produced by turbine and torque required by compressor, the equation for shaft speed can be written as

$$N = \frac{60}{2\pi} \int \frac{\tau_{turbine} - \tau_{compressor}}{J} dt \tag{2.47}$$

2.3.6 Heat Soak Effect[3]

The heat transfer from the hot gas to the metal mass may become significant at the high pressure turbine due to large temperature gradient and metal mass. Transient energy caused by metal mass absorbing heat from hot gases can be represented by a simple first order transfer equation as shown in equation (2.48). The heat transfer effect of the metal temperature on the output gas can be represented by equation (2.49). The thermal lag due to the storage of heat in the engine metal may also be included in other elements (such as high pressure compressor) if the heat soak effect becomes significant. In this research effort, the heat soak effect is excluded due to limitation of a model used for validation process

$$\dot{T}_m = -\frac{hA_m}{c_{pm}M} T_m + \frac{hA_m}{c_{pm}M} T_{gi} \tag{2.48}$$

$$T_{go} = \frac{hA_m}{c_{pg} w_g} T_m + \left(1 - \frac{hA_m}{c_{pg} w_g} \right) T_{gi} \tag{2.49}$$

2.3.7 Continuity Equations/Flow Dynamics

Solver convergence is achieved by forcing mass flow rate at each component to match with one another. The solver is iterated until the following error terms achieve the desired tolerance.

$$e_1 = w_{LPC,out} - w_{HPC,out} - w_{TCA} - w_{c\_bleed} \tag{2.50}$$

$$e_2 = w_{Burner,out} - w_{HPT,out} + w_{TCA,HPT} \tag{2.51}$$

$$e_3 = w_{HPT,out} - w_{LPT,out} + w_{TCA.LPT} \tag{2.52}$$

$$e_4 = w_{LPT,out} - w_{nozpri,out} + w_{c\_bleed} \tag{2.53}$$

$$e_5 = w_{Fan,out} - w_{nozsec,out} \tag{2.54}$$

Solver iteration is not necessary if the volume dynamics for fluid properties are directly implemented. Volume dynamics are represented by a plenum between each of the major components in many existing engine models [5,35]. However, a model including volume dynamics must run at much higher frequency and is not feasible for real time implementation.

2.4 Summary

In this chapter, the details of the nonlinear engine model used for the control were described. The control oriented model is usually a 0-D component based model with reduced order dynamic states. A reduction in dynamic states is required to fulfill the computation requirement. It has been shown that residualization of the fast states can be utilized to reduce the order since the fast dynamics states are far outside the control bandwidth. The equations described in this chapter are the foundation for the development of linear models.

CHAPTER 3

LINEARIZATION

In this chapter the development of an analytical linear model is discussed in detail. First, general on- and off-equilibrium linearization for the gas turbine engine model is briefly introduced. Then, the component level linearization process is explained in detail, including reduction of the set of nonlinear equations into analytically differentiable forms. The details of integrating the component level linear models to develop system level linear models are discussed next. This chapter concludes with a simple example of integration of component linear models.

3.1 General Linearization Approach [4,22,26,32,56]

The nonlinear engine dynamics are written in generic form as

$$\begin{aligned} g(x, z_0, u) &= 0 \\ \dot{x} &= f(x, z_0, u) \end{aligned} \tag{3.1}$$

where *g* represents fast dynamics equations and *f* represents the slow dynamics equations. The nonlinear dynamics about some arbitrary position, $(\bar{x}, \bar{z}_0, \bar{u})$, can be written as follows.

$$\begin{aligned} g(\bar{x}, \bar{z}_0, \bar{u}) &= 0 \\ \dot{\bar{x}} &= f(\bar{x}, \bar{z}_0, \bar{u}) \end{aligned} \tag{3.2}$$

The plant is linearized using Taylor series expansion about the arbitrary position, $(\bar{x}, \bar{z}_0, \bar{u})$, as follows:

$$\begin{aligned}
& g(\bar{x}+\delta x, \bar{z}_0+\delta z, \bar{u}+\delta u)=0 \\
& \left.\frac{\partial g}{\partial x}\right|_{\bar{x},\bar{z}_0,\bar{u}} \delta x+\left.\frac{\partial g}{\partial z}\right|_{\bar{x},\bar{z}_0,\bar{u}} \delta z+\left.\frac{\partial g}{\partial u}\right|_{\bar{x},\bar{z}_0,\bar{u}} \delta u+H.O.T=0 \\
& \mathbf{M}\delta x+\mathbf{K}\delta z+\mathbf{L}\delta u=0
\end{aligned} \tag{3.3}$$

$$\begin{aligned}
& \frac{dx}{dt}=f(\bar{x}+\delta x, \bar{z}_0+\delta z, \bar{u}+\delta u) \\
& \approx f(\bar{x},\bar{z}_0,\bar{u})+\left.\frac{\partial f}{\partial x}\right|_{\bar{x},\bar{z}_0,\bar{u}} \delta x+\left.\frac{\partial f}{\partial z}\right|_{\bar{x},\bar{z}_0,\bar{u}} \delta z+\left.\frac{\partial f}{\partial u}\right|_{\bar{x},\bar{z}_0,\bar{u}} \delta u+H.O.T \\
& \approx f(\bar{x},\bar{z}_0,\bar{u})+\mathbf{A}'\delta x+\mathbf{F}\delta z+\mathbf{B}'\delta u \\
& = f(\bar{x},\bar{z}_0,\bar{u})+(\mathbf{A}'-\mathbf{F}\mathbf{K}^{-1}\mathbf{M})\delta x+(\mathbf{B}'-\mathbf{F}\mathbf{K}^{-1}\mathbf{L})\delta u \\
& = f(\bar{x},\bar{z}_0,\bar{u})+\mathbf{A}\delta x+\mathbf{B}\delta u
\end{aligned} \tag{3.4}$$

where δx, δz, δu are perturbations from the linearization point, $(\bar{x},\bar{z}_0,\bar{u})$, and

$$\begin{aligned}
x &= \bar{x}+\delta x \\
z &= \bar{z}_0+\delta z \\
u &= \bar{u}+\delta u
\end{aligned} \tag{3.5}$$

Higher order terms have been neglected. Linearization is often conducted about an equilibrium condition where $f(\bar{x},\bar{z}_0,\bar{u})=0$, in which case, equation (3.4) is simplified to

$$\begin{aligned}
& \frac{dx}{dt}\approx\left.\frac{\partial f}{\partial x}\right|_{\bar{x},\bar{z}_0,\bar{u}} \delta x+\left.\frac{\partial f}{\partial z}\right|_{\bar{x},\bar{z}_0,\bar{u}} \delta z+\left.\frac{\partial f}{\partial u}\right|_{\bar{x},\bar{z}_0,\bar{u}} \delta u \\
& \approx \mathbf{A}'\delta x+\mathbf{F}\delta z+\mathbf{B}'\delta u \\
& \delta\dot{x}=\mathbf{A}\delta x+\mathbf{B}\delta u
\end{aligned} \tag{3.6}$$

In this work, linearization is conducted about an arbitrary position along the trajectory so equation (3.3) and (3.4) are preserved. Equation (4) can be rewritten into a more conventional form as

$$\begin{aligned}
& \delta\dot{x}=\mathbf{A}\delta x+\mathbf{B}\delta u \\
& \delta\dot{x}:=\frac{dx}{dt}-f(\bar{x},\bar{z}_0,\bar{u})
\end{aligned} \tag{3.7}$$

Note that the use of $\delta\dot{x}$ is not conventional since it is now a perturbation of the time derivative, $\frac{dx}{dt}$, as it includes an extra term given by $f(\bar{x}, \bar{z}_0, \bar{u})$ [32]. Linear coefficients, **A** and **B,** are computed analytically in the present work. A pictorial description of linearization about an arbitrary point is shown in Figure 3.1 where the solid arrow describes $f(\bar{x}, \bar{z}_0, \bar{u})$ and the dashed arrow describes $\dot{x}$. The dashed arrow can be seen as the combination of solid arrow and perturbation from the solid arrow. The linear coefficients represent the change in slope of the trajectory.

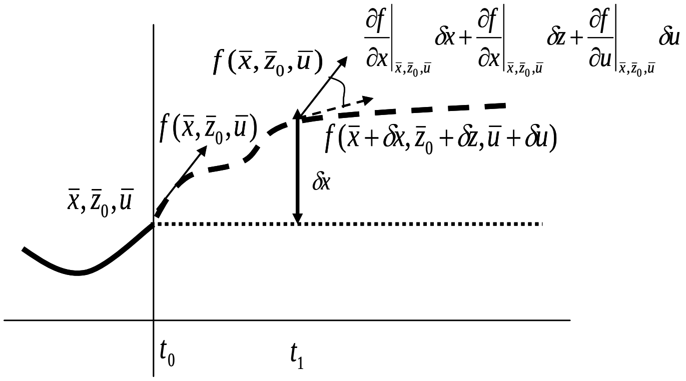

Figure 3.1 Linearization about arbitrary point

Similarly, the outputs of the engine can be linearized at $(\bar{x}, \bar{z}_0, \bar{u})$ as follows

$$
\begin{aligned}
&y = h(x, z_0, u) \\
&y \approx h\left(\bar{x}, \bar{z}_0, \bar{u}\right) + \left.\frac{\partial h}{\partial x}\right|_{\bar{x},\bar{z}_0,\bar{u}} \delta x + \left.\frac{\partial h}{\partial z}\right|_{\bar{x},\bar{z}_0,\bar{u}} \delta z + \left.\frac{\partial h}{\partial u}\right|_{\bar{x},\bar{z}_0,\bar{u}} \delta u + H.O.T \\
&\approx h(\bar{x}, \bar{z}_0, \bar{u}) + \mathbf{C}'\delta x + \mathbf{E}\delta z + \mathbf{D}'\delta u \\
&= h(\bar{x}, \bar{z}_0, \bar{u}) + (\mathbf{C}' - \mathbf{E}\mathbf{K}^{-1}\mathbf{M})\delta x + (\mathbf{D}' - \mathbf{E}\mathbf{K}^{-1}\mathbf{L})\delta u \\
&= h(\bar{x}, \bar{z}_0, \bar{u}) + \mathbf{C}\delta x + \mathbf{D}\delta u
\end{aligned}
\tag{3.8}
$$

3.2 Simplifying Assumptions for Linearization

The core of the development of an analytical linear model is to put a detailed nonlinear model into an analytically linearizable form by making simplifying assumptions. Simplification of the detailed model is first achieved at the component level and then at the system level. The following simplifying assumptions are applied to each component to reduce the detailed engine model into an analytically linearizable form. Details of how each assumption is applied at the component level are discussed in the subsequent subsections.

1. Assume gas is thermally perfect, where the following relationship holds.

$$P = \rho RT \tag{3.9}$$

Also, enthalpy of the thermally perfect gas is a function of temperature only (not of pressure) as shown below.

$$dh = c_p(T)dT \tag{3.10}$$

2. Gas path thermodynamic properties, c_p and γ are assumed to be independent of temperature and, thus, constant (calorically perfect) within one component during one time step; however, variation in the properties due temperature differences among different components is considered. Using this assumption, the specific heat becomes constant and enthalpy can be further simplified as follows:

$$h = c_p T \tag{3.11}$$

This also causes γ to be constant.

3.3 Component Level Linearization

A nonlinear engine model provides the parameters that are used for calculation of linear coefficients. Each component is independently linearized. Each component represents a simple static system as a result of the residualization of flow dynamics. Inputs and outputs of a single component are tied by nonlinear analytical expressions presented earlier. A linear model of each component is established by using Taylor series expansion about the current operating point. This is achieved by taking the partial derivative of each output with respect to an individual input as shown by the following equations.

$$\begin{aligned}
&h_b(\mathbf{z}_0, \mathbf{x}, \mathbf{u}, \mathbf{y}) = 0 \\
&h_b(\bar{\mathbf{z}}_0, \bar{\mathbf{u}}, \bar{\mathbf{x}}, \bar{y}) + \sum_{i=1}^{l} \left.\frac{\partial h_b}{\partial z_i}\right|_{\bar{\mathbf{z}}_0, \bar{\mathbf{u}}, \bar{\mathbf{x}}, \bar{y}} \delta z_i + \sum_{j=1}^{m} \left.\frac{\partial h_b}{\partial x_j}\right|_{\bar{\mathbf{z}}_0, \bar{\mathbf{u}}, \bar{\mathbf{x}}, \bar{y}} \delta x_j + \sum_{k=1}^{n} \left.\frac{\partial h_b}{\partial u_k}\right|_{\bar{\mathbf{z}}_0, \bar{\mathbf{u}}, \bar{\mathbf{x}}, \bar{y}} \delta u_k + \sum_{r=1}^{p} \left.\frac{\partial h_b}{\partial y_r}\right|_{\bar{\mathbf{z}}_0, \bar{\mathbf{u}}, \bar{\mathbf{x}}, \bar{y}} \delta y_r = 0 \\
&\Rightarrow \sum_{i=1}^{l} \left.\frac{\partial h_b}{\partial z_i}\right|_{\bar{\mathbf{z}}_0, \bar{\mathbf{u}}, \bar{\mathbf{x}}, \bar{y}} \delta z_i + \sum_{j=1}^{m} \left.\frac{\partial h_b}{\partial x_j}\right|_{\bar{\mathbf{z}}_0, \bar{\mathbf{u}}, \bar{\mathbf{x}}, \bar{y}} \delta x_j + \sum_{k=1}^{n} \left.\frac{\partial h_b}{\partial u_k}\right|_{\bar{\mathbf{z}}_0, \bar{\mathbf{u}}, \bar{\mathbf{x}}, \bar{y}} \delta u_k + \sum_{r=1}^{p} \left.\frac{\partial h_b}{\partial y_r}\right|_{\bar{\mathbf{z}}_0, \bar{\mathbf{u}}, \bar{\mathbf{x}}, \bar{y}} \delta y_r = 0
\end{aligned} \tag{3.12}$$

Here, y represents any intermediate output parameters, such as torque, required to represent processes inside a component. The intermediate output parameters are used to reduce the size of fast dynamic states matrix.

Each component linearization is based on the model described in chapter 2. Note that nonlinear equations described in chapter 2 may require minor modifications depending on the nonlinear model being used, but the basis should remain the same as they are founded on generic thermodynamic relationships. In the following subsections, the linearization approach is applied to generic components of a gas turbine engine.

3.3.1 Compressor

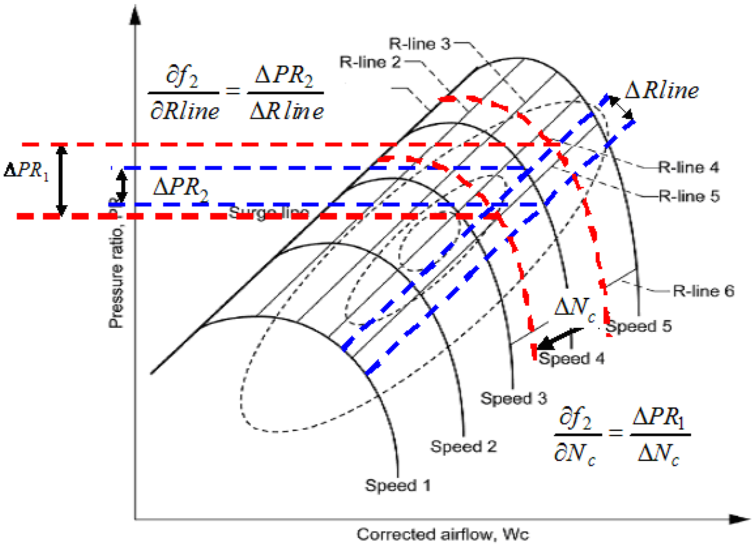

Figure 3.2 Obtaining compressor map sensitivities

First, simplifications are applied in order to put all expressions into an analytically linearizable form. An analytically linearizable function is defined as a function whose derivatives can be analytically calculated (i.e. without applying numerical schemes) into a closed form format. Using the assumption 2 in Section 3.2 that c_p and γ are constant and independent of temperature within one time step, equation (2.11) can be written as follows.

$$\eta_c = \frac{h_{tout\_isentropic} - h_{tin}}{h_{tout} - h_{tin}} \approx \frac{T_{tout\_isentropic} - T_{tin}}{T_{tout} - T_{tin}} = \frac{\left(\frac{P_{tout}}{P_{tin}}\right)^{\frac{\gamma-1}{\gamma}} - 1}{\frac{T_{tout}}{T_{tin}} - 1} \tag{3.13}$$

Also the stagnation temperature at the outlet of the compressor can be written as follows:

$$T_{tout} = T_{tin}\left[\frac{1}{\eta_c}\left(\left(\frac{P_{tout}}{P_{tin}}\right)^{\frac{\gamma-1}{\gamma}} - 1\right) + 1\right] \tag{3.14}$$

Equation (3.14) would have much smaller error due to simplification if the efficiency of the compressor map is defined using temperature instead of enthalpy.

Again, using the assumption 2, equation (2.19) is simplified to

$$\tau_{out} = \frac{60}{2\pi}\frac{wc_{pc}(T_{tin} - T_{tout})}{N} \tag{3.15}$$

The average gas properties c_p and γ of inlet and outlet are used in each equation. Applying these simplifications, the compressor is represented by following group of equations

$$w - \frac{\delta}{\sqrt{\theta}} f_1(N_c, Rline) = 0 \tag{3.16}$$

$$T_{tout} - T_{tin}\left[\frac{1}{\eta_c}\left(\left(\frac{P_{tout}}{P_{tin}}\right)^{\frac{\gamma-1}{\gamma}} - 1\right) + 1\right] = 0 \tag{3.17}$$

$$P_{tout} - P_{tin} f_2(N_c, Rline) = 0 \tag{3.18}$$

$$\tau_{out} - \frac{60}{2\pi}\frac{wc_p\left(T_{tin} - T_{tout}\right)}{N} = 0 \tag{3.19}$$

Since these are now in analytically linearizable form with exception of map parameters, linear coefficients are obtained by taking partial derivatives of each output with respect to each input. A compressor map is in tabular form and either spline or neural network type [18] representation can be utilized to convert it into an analytically linearizable functional representation. An alternative approach is to store pre-computed values of derivatives (slopes) of the maps as indicated by Figure 3.2, which can be directly used in the linearization. For the proof of concept of real time linearization considered in this study, the latter approach is used. The linearized equations for compressor in explicit form are shown in equation (3.20).

(3.20)

$$
\begin{bmatrix}\delta w_{out}\\ \delta T_{tout}\\ \delta p_{tout}\\ \delta\tau_{out}\end{bmatrix}=
\left[\begin{array}{c:c:c:c:c}
\frac{\delta}{\sqrt{\theta}}\frac{\partial f_1}{\partial Rline} &
\frac{\delta}{\theta}\frac{\partial f_1}{\partial N_c} &
-\frac{\delta}{\theta^2}\frac{\partial f_1}{\partial N_C}\frac{N}{2T_{std}}-\frac{1}{2}\frac{w_c}{\theta^{3/2}}\frac{\delta}{T_{std}} &
\frac{w_c}{\sqrt{\theta}}\frac{1}{P_{std}} &
0 \\ \hdashline
\begin{gathered}-\frac{T_{tin}}{{\eta_c}^2}\left[\left(\frac{p_{tout}}{p_{tin}}\right)^{\frac{\gamma-1}{\gamma}}-1\right]\frac{\partial f_3}{\partial Rline}\\ +\frac{T_{tin}}{\eta_c}\left(\frac{\gamma-1}{\gamma}\right)\left(\frac{p_{tout}}{p_{tin}}\right)^{\frac{-1}{\gamma}}\frac{\partial f_2}{\partial Rline}\end{gathered} &
\begin{gathered}-\frac{T_{tin}}{{\eta_c}^2}\left[\left(\frac{p_{tout}}{p_{tin}}\right)^{\frac{\gamma-1}{\gamma}}-1\right]\frac{\partial f_3}{\partial N_C}\frac{1}{\sqrt{\theta}}\\ +\frac{T_{tin}}{\eta_c}\left(\frac{\gamma-1}{\gamma}\right)\left(\frac{p_{tout}}{p_{tin}}\right)^{\frac{-1}{\gamma}}\frac{\partial f_2}{\partial N_c}\frac{1}{\sqrt{\theta}}\end{gathered} &
\begin{gathered}\left\{\frac{1}{\eta_c}\left[\left(\frac{p_{tout}}{p_{tin}}\right)^{\frac{\gamma-1}{\gamma}}-1\right]+1\right\}+\frac{T_{tin}}{{\eta_c}^2}\left[\left(\frac{p_{tout}}{p_{tin}}\right)^{\frac{\gamma-1}{\gamma}}-1\right]\frac{\partial f_3}{\partial N_C}\frac{N}{\sqrt{\theta}}\frac{1}{2\theta}\frac{1}{T_{std}}\\ +\frac{T_{tin}}{\eta_c}\left(\frac{\gamma-1}{\gamma}\right)\left(\frac{p_{tout}}{p_{tin}}\right)^{\frac{-1}{\gamma}}\frac{\partial f_2}{\partial N_C}\frac{N}{\sqrt{\theta}}\frac{1}{2\theta}\frac{1}{T_{std}}\end{gathered} &
0 &
0 \\ \hdashline
p_{tin}\frac{\partial f_2}{\partial Rline} &
p_{tin}\frac{\partial f_2}{\partial N_C}\frac{1}{\sqrt{\theta}} &
-p_{tin}\frac{\partial f_2}{\partial N_C}\frac{N}{\sqrt{\theta}}\frac{1}{2\theta}\frac{1}{T_{std}} &
\frac{p_{tout}}{p_{tin}} &
0 \\ \hdashline
\begin{gathered}-\left(\frac{60}{2\pi}\right)\frac{w_{in}c_p}{N}[-\frac{T_{tin}}{{\eta_c}^2}\left[\left(\frac{p_{tout}}{p_{tin}}\right)^{\frac{\gamma-1}{\gamma}}-1\right]\frac{\partial f_3}{\partial Rline}\\ +\frac{T_{tin}}{\eta_c}\left(\frac{\gamma-1}{\gamma}\right)\left(\frac{p_{tout}}{p_{tin}}\right)^{\frac{-1}{\gamma}}\frac{\partial f_2}{\partial Rline}]\end{gathered} &
\begin{gathered}-\left(\frac{60}{2\pi}\right)\frac{w_{in}c_p}{N}[-\frac{T_{tin}}{{\eta_c}^2}\left[\left(\frac{p_{tout}}{p_{tin}}\right)^{\frac{\gamma-1}{\gamma}}-1\right]\frac{\partial f_3}{\partial N_C}\frac{1}{\sqrt{\theta}}\\ +\frac{T_{tin}}{\eta_c}\left(\frac{\gamma-1}{\gamma}\right)\left(\frac{p_{tout}}{p_{tin}}\right)^{\frac{-1}{\gamma}}\frac{\partial f_2}{\partial N_c}\frac{p_{tin}}{\sqrt{\theta}}]\\ -\left(\frac{60}{2\pi}\right)\frac{w_{in}c_p}{N^2}\left(T_{tin}-T_{tout}\right)\end{gathered} &
\begin{gathered}\left(\frac{60}{2\pi}\right)\frac{w_{in}c_p}{N}-\left(\frac{60}{2\pi}\right)\frac{w_{in}c_p}{N}[\left\{\frac{1}{\eta_c}\left[\left(\frac{p_{tout}}{p_{tin}}\right)^{\frac{\gamma-1}{\gamma}}-1\right]+1\right\}\\ +\frac{T_{tin}}{{\eta_c}^2}\left[\left(\frac{p_{tout}}{p_{tin}}\right)^{\frac{\gamma-1}{\gamma}}-1\right]\frac{\partial f_3}{\partial N_C}\frac{N}{\sqrt{\theta}}\frac{1}{2\theta}\frac{1}{T_{std}}\\ +\frac{T_{tin}}{\eta_c}\left(\frac{\gamma-1}{\gamma}\right)\left(\frac{p_{tout}}{p_{tin}}\right)^{\frac{-1}{\gamma}}\frac{\partial f_2}{\partial N_C}\frac{N}{\sqrt{\theta}}\frac{1}{2\theta}\frac{1}{T_{std}}]\end{gathered} &
0 &
\left(\frac{60}{2\pi}\right)\frac{c_p\left(T_{tin}-T_{toutt}\right)}{N}
\end{array}\right]
\begin{bmatrix}\delta Rline\\ \delta N\\ \delta T_{tin}\\ \delta p_{tin}\\ \delta w_{in}\end{bmatrix}
$$

3.3.2 Combustor

The specific heat, c_p, is assumed to be constant during the linearization process with its value being different upstream and downstream of the burner by applying the assumption 2 in Section 3.2 [36]. Equation (2.22) is simplified as follows.

$$\begin{aligned}&(w_{in} + w_f)h_{tout} = w_f Q\eta_b - w_{in}h_{tin}\\ &\Rightarrow (w_{in} + w_f)c_{pout}T_{tout} = w_f Q\eta_b - w_{in}c_{pin}T_{tin}\end{aligned} \tag{3.21}$$

The combustor is represented by following analytic equations.

$$w_{out} - w_f - w_{in} = 0 \tag{3.22}$$

$$\eta_b w_f Q - [(w_{in} + w_f)c_{pout}T_{tout} - w_{in}c_{pin}T_{tin}] = 0 \tag{3.23}$$

$$P_{tout} - (1-K)P_{tin} = 0 \tag{3.24}$$

$$FAR - \frac{w_f}{w_{in}} = 0 \tag{3.25}$$

Using the above simplified set of equations, analytical linearization of the burner component model is obtained in explicit form as equation (3.26).

$$\begin{bmatrix}\delta p_{tout}\\ \delta FAR\\ \delta T_{tout}\end{bmatrix} = \left[\begin{array}{c:c:c:c} 0 & 1-K & 0 & 0\\ \hdashline 0 & 0 & -\dfrac{w_f}{w_{in}^2} & \dfrac{1}{w_{in}}\\ \hdashline \dfrac{1}{1+FAR}\dfrac{c_{pin}}{c_{pout}} & 0 & -\dfrac{\eta_b Q - c_{pout}T_{tout}}{(1+FAR)c_{pout}}\dfrac{w_f}{w_{in}^2} & \dfrac{\eta_b Q - c_{pout}T_{tout}}{(1+FAR)c_{pout}}\dfrac{1}{w_{in}}\end{array}\right]\begin{bmatrix}\delta T_{tin}\\ \delta p_{tin}\\ \delta w_{in}\\ \delta w_f\end{bmatrix} \tag{3.26}$$

3.3.3 Turbine

Similar simplifications (assumption 2) made for the compressor component model are also applied to the turbine component model for achieving the analytical linearization.

Using these assumptions, the following analytic equations represent the turbine element. The second part of equations (3.28) and (3.30) are zero for the low pressure turbine.

$$w - w_{bleed} - \frac{\delta}{\sqrt{\theta}} g_1(N_c, Rline) = 0 \tag{3.27}$$

$$\begin{gathered}
-T_{tout} + \frac{w_{in}}{w_{out}} T_{tin} \left[1 - \eta_t \left(1 - \left(\frac{P_{tout}}{P_{tin}} \right)^{\frac{\gamma-1}{\gamma}} \right) \right] + \frac{w_{bld}}{w_{out}} T_{tbld} \left[1 - \eta_t \left(1 - \left(\frac{P_{tout}}{P_{tbld}} \right)^{\frac{\gamma-1}{\gamma}} \right) \right] = 0 \\
\Rightarrow -T_{tout} + kT_{tin} \left[1 - \eta_t \left(1 - \left(\frac{P_{tout}}{P_{tin}} \right)^{\frac{\gamma-1}{\gamma}} \right) \right] + (1-k) T_{tbld} \left[1 - \eta_t \left(1 - \left(\frac{P_{tout}}{P_{tbld}} \right)^{\frac{\gamma-1}{\gamma}} \right) \right] = 0
\end{gathered} \tag{3.28}$$

$$P_{tout} + PR \cdot P_{tin} = 0 \tag{3.29}$$

$$-\tau_{out} + \frac{60}{2\pi} \left[\frac{c_p (T_{tin} - T_{tout}) w_{in}}{N} + \frac{c_p (T_{tbld} - T_{tout}) w_{bld}}{N} \right] = 0 \tag{3.30}$$

These expressions are linearized as follows:

(3.31)

$$
\begin{bmatrix}\delta w_{out}\\ \delta T_{tout}\\ \delta p_{tout}\\ \delta\tau_t\end{bmatrix}=
\left[\begin{array}{c:c:c:c:c}
\frac{1}{k}\frac{\delta}{\sqrt{\theta}}\frac{\partial f}{\partial PR} & \frac{1}{k}\frac{\delta}{\theta}\frac{\partial f}{\partial N_c} & -\frac{1}{k}\frac{\delta}{\theta^2}\frac{\partial f}{\partial N_c}\frac{N}{2}\frac{1}{T_{std}}-\frac{1}{2}w_c\frac{\delta}{\theta^{3/2}}\frac{1}{T_{std}} & \frac{1}{k}\frac{w_c}{\sqrt{\theta}}\frac{1}{p_{std}} & 0 \\ \hdashline
-k\left\{\begin{array}{l} T_{tin}\left[1-\left(\frac{p_{tout}}{p_{tin}}\right)^{\frac{\gamma-1}{\gamma}}\right]\frac{\partial g}{\partial PR} \\ +\left(\frac{\gamma-1}{\gamma}\right)\left(\frac{p_{tout}}{p_{tin}}\right)^{-\frac{1}{\gamma}}\frac{\eta_t T_{tin}}{p_{tin}}\frac{p_{tin}}{PR^2}\end{array}\right\} & -kT_{tin}\left[1-\left(\frac{p_{tout}}{p_{tin}}\right)^{\frac{\gamma-1}{\gamma}}\right]\frac{\partial g}{\partial N_c}\frac{1}{\sqrt{\theta}} & \begin{array}{l} k\left\{1-\eta_t\left[1-\left(\frac{p_{tout}}{p_{tin}}\right)^{\frac{\gamma-1}{\gamma}}\right]\big]\right\}+kT_{tin}\left[1-\left(\frac{p_{tout}}{p_{tin}}\right)^{\frac{\gamma-1}{\gamma}}\right]\frac{\partial g}{\partial N_c}\frac{N}{2}\frac{1}{\theta^{3/2}}\frac{1}{T_{std}} \\ +(1-k)T_{tbleed}\left[1-\left(\frac{p_{tout}}{p_{tbleed}}\right)^{\frac{\gamma-1}{\gamma}}\right]\frac{\partial g}{\partial N_c}\frac{N}{2}\frac{1}{\theta^{3/2}}\frac{1}{T_{std}}\end{array} & (1-k)\left\{\left(\frac{\gamma-1}{\gamma}\right)\left(\frac{p_{tout}}{P_{tbleed}}\right)^{-\frac{1}{\gamma}}\eta_t\frac{T_{tbleed}}{p_{tbleed}}\frac{p_{tout}}{p_{tin}}\right\} & 0 \\ \hdashline
-\frac{{p_{45t}}^{2}}{p_{4t}} & 0 & 0 & \frac{p_{tout}}{p_{tin}} & 0 \\ \hdashline
k\frac{60}{2\pi}\frac{c_pw_{in}}{N}\left\{\begin{array}{l} T_{tin}\left[1-\left(\frac{p_{tout}}{p_{tin}}\right)^{\frac{\gamma-1}{\gamma}}\right]\frac{\partial g}{\partial PR} \\ +\left(\frac{\gamma-1}{\gamma}\right)\left(\frac{p_{tout}}{p_{tin}}\right)^{-\frac{1}{\gamma}}\frac{\eta_t T_{tin}}{p_{tin}}\frac{p_{tin}}{PR^2}\end{array}\right\} & \frac{60}{2\pi}\left\{\begin{array}{l} k\frac{c_pw_{in}}{N}T_{tin}\left[1-\left(\frac{p_{tout}}{p_{tin}}\right)^{\frac{\gamma-1}{\gamma}}\right]\frac{\partial g}{\partial N_c}\frac{1}{\sqrt{\theta}} \\ -\frac{c_p(T_{tin}-T_{tout})w_{in}}{N^2}\end{array}\right\} & \frac{60}{2\pi}\left\{\begin{array}{l} \frac{c_pw_{in}}{N}-k\frac{c_pw_{in}}{N}[\left\{1-\eta_t\left[1-\left(\frac{p_{tout}}{p_{tin}}\right)^{\frac{\gamma-1}{\gamma}}\right]\big]\right\}+T_{tin}\left[1-\left(\frac{p_{tout}}{p_{tin}}\right)^{\frac{\gamma-1}{\gamma}}\right]\frac{\partial g}{\partial N_c}\frac{N}{2}\frac{1}{\theta^{3/2}}\frac{1}{T_{std}}] \\ +(1-k)\frac{c_pw_{bleed}}{N}T_{tbleed}\left[1-\left(\frac{p_{tout}}{p_{tbleed}}\right)^{\frac{\gamma-1}{\gamma}}\right]\frac{\partial g}{\partial N_c}\frac{N}{2}\frac{1}{\theta^{3/2}}\frac{1}{T_{std}}\end{array}\right\} & \frac{60}{2\pi}\frac{c_pw_{bleed}}{N}(1-k)\left\{\left(\frac{\gamma-1}{\gamma}\right)\left(\frac{p_{tout}}{P_{tbleed}}\right)^{-\frac{1}{\gamma}}\eta_t\frac{T_{tbleed}}{p_{tbleed}}\frac{p_{tout}}{p_{tin}}\right\} & \frac{60}{2\pi}\frac{c_p(T_{tin}-T_{tout})}{N}
\end{array}\right]k\begin{bmatrix}\delta PR\\ \delta N\\ \delta T_{tin}\\ \delta p_{tin}\\ \delta w_{in}\end{bmatrix}
$$

$$
+\left[\begin{array}{c:c:c:c:c}
0 & 0 & 0 & 0 & 0 \\ \hdashline
-(1-k)\left\{\begin{array}{l} T_{tbleed}\left[1-\left(\frac{p_{tout}}{p_{tbleed}}\right)^{\frac{\gamma-1}{\gamma}}\right]\frac{\partial g}{\partial PR} \\ +\left(\frac{\gamma-1}{\gamma}\right)\left(\frac{p_{tout}}{p_{tbleed}}\right)^{-\frac{1}{\gamma}}\frac{\eta_t T_{tbleed}}{p_{tbleed}}\frac{p_{tin}}{PR^2}\end{array}\right\} & -(1-k)T_{tbleed}\left[1-\left(\frac{p_{tout}}{p_{tbleed}}\right)^{\frac{\gamma-1}{\gamma}}\right]\frac{\partial g}{\partial N_c}\frac{1}{\sqrt{\theta}} & (1-k)\left\{1-\eta_t\left[1-\left(\frac{p_{tout}}{p_{tbleed}}\right)^{\frac{\gamma-1}{\gamma}}\right]\big]\right\} & -(1-k)\left\{\left(\frac{\gamma-1}{\gamma}\right)\left(\frac{p_{tout}}{P_{tbleed}}\right)^{-\frac{\gamma-1}{\gamma}}\eta_t\frac{T_{tbleed}}{p_{tbleed}}\right\} & 0 \\ \hdashline
0 & 0 & 0 & 0 & 0 \\ \hdashline
(1-k)\frac{60}{2\pi}\frac{c_pw_{bleed}}{N}\left\{\begin{array}{l} T_{tbleed}\left[1-\left(\frac{p_{tout}}{p_{tbleed}}\right)^{\frac{\gamma-1}{\gamma}}\right]\frac{\partial g}{\partial PR} \\ +\left(\frac{\gamma-1}{\gamma}\right)\left(\frac{p_{tout}}{p_{tbleed}}\right)^{-\frac{1}{\gamma}}\frac{\eta_t T_{tbleed}}{p_{tbleed}}\frac{p_{tin}}{PR^2}\end{array}\right\} & \frac{60}{2\pi}\left\{\begin{array}{l} (1-k)\frac{c_pw_{bleed}}{N}T_{tbleed}\left[1-\left(\frac{p_{tout}}{p_{tbleed}}\right)^{\frac{\gamma-1}{\gamma}}\right]\frac{\partial g}{\partial N_c}\frac{1}{\sqrt{\theta}} \\ -\frac{c_p(T_{tbleed}-T_{tout})w_{bleed}}{N^2}\end{array}\right\} & \frac{60}{2\pi}\left\{\frac{c_pw_{tbleed}}{N}-(1-k)\frac{c_pw_{bleed}}{N}[\left\{1-\eta_t\left[1-\left(\frac{p_{tout}}{p_{tbleed}}\right)^{\frac{\gamma-1}{\gamma}}\right]\big]\right\}\right\} & 0 & \frac{60}{2\pi}\frac{c_p(T_{tbleed}-T_{tout})}{N}
\end{array}\right]\begin{bmatrix}\delta PR\\ \delta N\\ \delta T_{tbleed}\\ \delta p_{tbleed}\\ \delta w_{bleed}\end{bmatrix}
$$

3.3.4 Nozzle

Using the assumption that gas properties are constant for one time step at each component level, the expression for critical pressure is simplified as follows,

$$PR_{critical} = \left(\frac{\gamma+1}{2}\right)^{\frac{\gamma}{\gamma-1}} \tag{3.32}$$

Using the perfect gas assumption and the constant specific heat, the nozzle component model equations are simplified as the following two groups of equations depending on flow condition at the throat of nozzle. The pressure at the exit fully expands to the ambient pressure when the flow is subsonic while it only partially expands when the flow is choked. These expressions are linearized as follows:

Choked

$$u = \sqrt{\frac{2\gamma RT_{tin}}{\gamma+1}} \tag{3.33}$$

$$\rho = \frac{P_{tin}}{RT_{tin}}\left(\frac{2}{1+\gamma}\right)^{\frac{1}{\gamma-1}} \tag{3.34}$$

$$w_{out} = \rho A_e u \tag{3.35}$$

$$P_{out} = \frac{P_{tin}}{\left(\frac{1+\gamma}{2}\right)^{\frac{\gamma}{\gamma-1}}} \tag{3.36}$$

$$F = w_{out}u + (P_{out} - P_{amb})A_e \tag{3.37}$$

Unchoked

$$\rho = \frac{P_{tin}}{RT_{tin}} \left(\frac{P_{tin}}{P_{out}} \right)^{\frac{-1}{\gamma}} \tag{3.38}$$

$$u = \sqrt{\frac{2\gamma RT_{tin}}{\gamma - 1} \left[1 - \left(\frac{P_{out}}{P_{tin}} \right)^{\frac{\gamma - 1}{\gamma}} \right]} \tag{3.39}$$

$$w_{out} = \rho A_e u \tag{3.40}$$

$$F = w_{out} u \tag{3.41}$$

Choked

$$\begin{bmatrix}\delta u_{out}\\ \delta w_{out}\\ \delta F\end{bmatrix}=\left[\begin{array}{c:c:c}\sqrt{\dfrac{\gamma R}{2(\gamma+1)T_{tout}}} & 0 & 0\\ \hdashline 0.5\rho_{out}A_e\sqrt{\dfrac{2\gamma R}{(\gamma+1)T_{tout}}}-\dfrac{A_e u_{out}\rho_{out}}{T_{tout}}\dfrac{2}{\gamma+1} & \dfrac{A_e u_{out}\rho_{out}}{P_{out}}\left(\dfrac{2}{\gamma+1}\right)^{\frac{\gamma}{\gamma-1}} & \rho_{out}u_{out}\\ \hdashline u_{out}\left\{0.5\rho_{out}A_e\sqrt{\dfrac{2\gamma R}{(\gamma+1)T_{tout}}}-\dfrac{A_e u_{out}\rho_{out}}{T_{tout}}\dfrac{2}{\gamma+1}\right\}+w_{out}\sqrt{\dfrac{\gamma R}{2(\gamma+1)T_{tout}}} & u_{out}\dfrac{A_e u_{out}\rho_{out}}{P_{out}}\left(\dfrac{2}{\gamma+1}\right)^{\frac{\gamma}{\gamma-1}}+A_e\left(\dfrac{2}{\gamma+1}\right)^{\frac{\gamma}{\gamma-1}} & \rho_{out}u_{out}+P_{out}-P_{amb}\end{array}\right]\begin{bmatrix}\delta T_{tin}\\ \delta P_{tin}\\ \delta A_e\end{bmatrix}\tag{3.42}$$

Unchoked

$$\begin{bmatrix}\delta u_{out}\\ \delta w_{out}\\ \delta F\end{bmatrix}=\left[\begin{array}{c:c:c}0.5\sqrt{\dfrac{\gamma R}{(\gamma-1)}\left(1-\left(\dfrac{P_{out}}{P_{tin}}\right)^{\frac{\gamma-1}{\gamma}}\right)\dfrac{1}{T_{tin}}} & \left(1-\left(\dfrac{P_{out}}{P_{tin}}\right)^{\frac{\gamma-1}{\gamma}}\right)^{-0.5}\sqrt{\dfrac{\gamma RT_{tin}}{2(\gamma-1)}}\left(\dfrac{\gamma-1}{\gamma}\right)\left(\dfrac{P_{out}}{P_{tin}}\right)^{\frac{\gamma-1}{\gamma}}\dfrac{1}{P_{tin}} & 0\\ \hdashline A_e u_{out}\left(-\dfrac{P_{tin}}{RT_{tin}{}^2}\left(\dfrac{P_{out}}{P_{tin}}\right)^{\frac{1}{\gamma}}\right)+\rho_{out}A_e\dfrac{\partial u_{out}}{\partial T_{tin}} & A_e u_{out}\left(\left(\dfrac{P_{out}}{P_{tin}}\right)^{\frac{1}{\gamma}}\dfrac{1}{RT_{tin}}\left(1-\dfrac{1}{\gamma}\right)\right)+\rho_{out}A_e\dfrac{\partial u_{out}}{\partial P_{tin}} & \rho_{out}u_{out}\\ \hdashline u_{out}\dfrac{\partial w_{out}}{\partial T_{tin}}+w_{out}\dfrac{\partial u_{out}}{\partial T_{tin}} & u_{out}\dfrac{\partial w_{out}}{\partial P_{tin}}+w_{out}\dfrac{\partial u_{out}}{\partial P_{tin}} & \rho_{out}u_{out}{}^2\end{array}\right]\begin{bmatrix}\delta T_{tin}\\ \delta P_{tin}\\ \delta A_e\end{bmatrix}\tag{3.43}$$

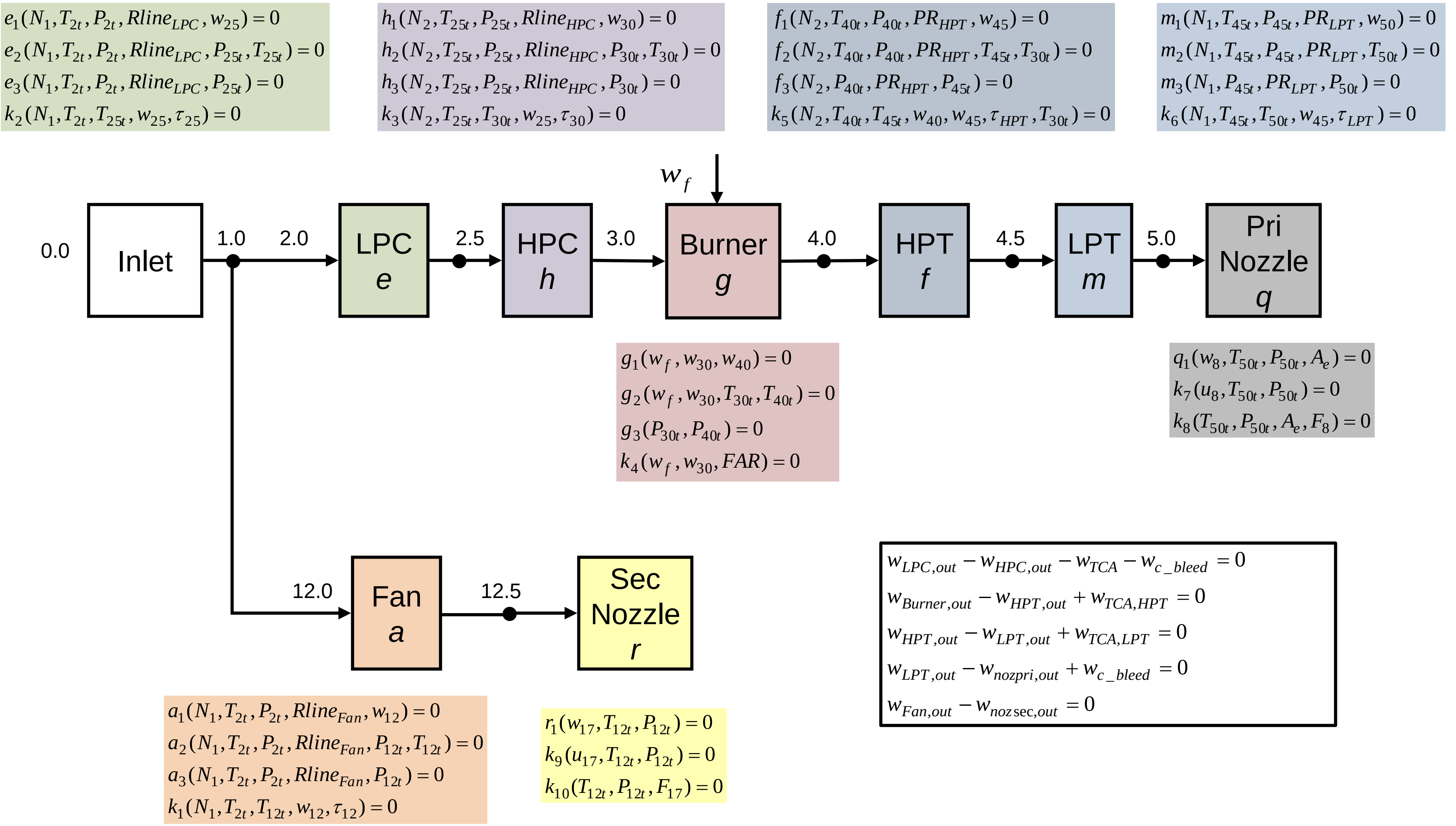

$$e_1(N_1, T_{2t}, P_{2t}, Rline_{LPC}, w_{25}) = 0$$
$$e_2(N_1, T_{2t}, P_{2t}, Rline_{LPC}, P_{25t}, T_{25t}) = 0$$
$$e_3(N_1, T_{2t}, P_{2t}, Rline_{LPC}, P_{25t}) = 0$$
$$k_2(N_1, T_{2t}, T_{25t}, w_{25}, \tau_{25}) = 0$$

$$h_1(N_2, T_{25t}, P_{25t}, Rline_{HPC}, w_{30}) = 0$$
$$h_2(N_2, T_{25t}, P_{25t}, Rline_{HPC}, P_{30t}, T_{30t}) = 0$$
$$h_3(N_2, T_{25t}, P_{25t}, Rline_{HPC}, P_{30t}) = 0$$
$$k_3(N_2, T_{25t}, T_{30t}, w_{25}, \tau_{30}) = 0$$

$$f_1(N_2, T_{40t}, P_{40t}, PR_{HPT}, w_{45}) = 0$$
$$f_2(N_2, T_{40t}, P_{40t}, PR_{HPT}, T_{45t}, T_{30t}) = 0$$
$$f_3(N_2, P_{40t}, PR_{HPT}, P_{45t}) = 0$$
$$k_5(N_2, T_{40t}, T_{45t}, w_{40}, w_{45}, \tau_{HPT}, T_{30t}) = 0$$

$$m_1(N_1, T_{45t}, P_{45t}, PR_{LPT}, w_{50}) = 0$$
$$m_2(N_1, T_{45t}, P_{45t}, PR_{LPT}, T_{50t}) = 0$$
$$m_3(N_1, P_{45t}, PR_{LPT}, P_{50t}) = 0$$
$$k_6(N_1, T_{45t}, T_{50t}, w_{45}, \tau_{LPT}) = 0$$

$$g_1(w_f, w_{30}, w_{40}) = 0$$
$$g_2(w_f, w_{30}, T_{30t}, T_{40t}) = 0$$
$$g_3(P_{30t}, P_{40t}) = 0$$
$$k_4(w_f, w_{30}, FAR) = 0$$

$$q_1(w_8, T_{50t}, P_{50t}, A_e) = 0$$
$$k_7(u_8, T_{50t}, P_{50t}) = 0$$
$$k_8(T_{50t}, P_{50t}, A_e, F_8) = 0$$

$$w_{LPC,out} - w_{HPC,out} - w_{TCA} - w_{c\_bleed} = 0$$
$$w_{Burner,out} - w_{HPT,out} + w_{TCA,HPT} = 0$$
$$w_{HPT,out} - w_{LPT,out} + w_{TCA,LPT} = 0$$
$$w_{LPT,out} - w_{nozpri,out} + w_{c\_bleed} = 0$$
$$w_{Fan,out} - w_{nozsec,out} = 0$$

$$a_1(N_1, T_{2t}, P_{2t}, Rline_{Fan}, w_{12}) = 0$$
$$a_2(N_1, T_{2t}, P_{2t}, Rline_{Fan}, P_{12t}, T_{12t}) = 0$$
$$a_3(N_1, T_{2t}, P_{2t}, Rline_{Fan}, P_{12t}) = 0$$
$$k_1(N_1, T_{2t}, T_{12t}, w_{12}, \tau_{12}) = 0$$

$$r_1(w_{17}, T_{12t}, P_{12t}) = 0$$
$$k_9(u_{17}, T_{12t}, P_{12t}) = 0$$
$$k_{10}(T_{12t}, P_{12t}, F_{17}) = 0$$

Figure 3.3 Generalized equations of turbofan

3.4 Component Level Linear Models in Generic Form

Algebraic expressions in section 3.3 are rewritten in more generic functional representations as shown in Figure 3.3. Each component is represented by functions with lower case alphabet. These equations are in implicit forms using the output of each element directly for simplification because all inputs and outputs of each component are combined to form vector *z*. For example, the fan is represented by functions a_1 *to* a_3 and k_1 . Functions k_1 to k_{10} represent the expressions for intermediate variables such as torque for different component. Nonlinear equations for each component are implicitly linearized as follows.

Fan

$$\begin{bmatrix} \frac{\partial a_1}{\partial w_{12t}} & 0 & 0 & \frac{\partial a_1}{\partial Rline_{Fan}} \\ 0 & \frac{\partial a_2}{\partial T_{12t}} & \frac{\partial a_2}{\partial P_{12t}} & \frac{\partial a_2}{\partial Rline_{Fan}} \\ 0 & 0 & \frac{\partial a_3}{\partial P_{12t}} & \frac{\partial a_3}{\partial Rline_{Fan}} \end{bmatrix} \begin{bmatrix} \delta w_{12} \\ \delta T_{12t} \\ \delta P_{12t} \\ \delta Rline_{Fan} \end{bmatrix} + \begin{bmatrix} \frac{\partial a_1}{\partial N_1} & 0 \\ \frac{\partial a_2}{\partial N_1} & 0 \\ \frac{\partial a_3}{\partial N_1\text{`}} & 0 \end{bmatrix} \begin{bmatrix} \delta N_1 \\ \delta N_2 \end{bmatrix} + \begin{bmatrix} 0 \\ 0 \\ 0 \end{bmatrix} \delta w_f + \begin{bmatrix} \frac{\partial a_1}{\partial T_{2t}} & \frac{\partial a_1}{\partial P_{2t}} \\ \frac{\partial a_2}{\partial T_{2t}} & \frac{\partial a_2}{\partial P_{2t}} \\ \frac{\partial a_3}{\partial T_{2t}} & \frac{\partial a_3}{\partial P_{2t}} \end{bmatrix} \begin{bmatrix} \delta T_{2t} \\ \delta P_{2t} \end{bmatrix} = \begin{bmatrix} 0 \\ 0 \\ 0 \end{bmatrix} \tag{3.44}$$

$$\frac{\partial k_1}{\partial N_1}\delta N_1 + \frac{\partial k_1}{\partial T_{2t}}\delta T_{2t} + \frac{\partial k_1}{\partial w_{12}}\delta w_{12} + \frac{\partial k_1}{\partial T_{12t}}\delta T_{12t} + \frac{\partial k_1}{\partial \tau_{12t}}\delta \tau_{12t} = 0$$

LPC

$$\begin{bmatrix} \frac{\partial e_1}{\partial w_{25t}} & 0 & 0 & \frac{\partial e_1}{\partial Rline_{LPC}} \\ 0 & \frac{\partial e_2}{\partial T_{25t}} & \frac{\partial e_2}{\partial P_{25t}} & \frac{\partial e_2}{\partial Rline_{LPC}} \\ 0 & 0 & \frac{\partial e_3}{\partial P_{25t}} & \frac{\partial e_3}{\partial Rline_{LPC}} \end{bmatrix} \begin{bmatrix} \delta w_{25} \\ \delta T_{25t} \\ \delta P_{25t} \\ \delta Rline_{LPC} \end{bmatrix} + \begin{bmatrix} \frac{\partial e_1}{\partial N_1} & 0 \\ \frac{\partial e_2}{\partial N_1} & 0 \\ \frac{\partial e_3}{\partial N_1\text{`}} & 0 \end{bmatrix} \begin{bmatrix} \delta N_1 \\ \delta N_2 \end{bmatrix} + \begin{bmatrix} 0 \\ 0 \\ 0 \end{bmatrix} \delta w_f + \begin{bmatrix} \frac{\partial e_1}{\partial T_{2t}} & \frac{\partial e_1}{\partial P_{2t}} \\ \frac{\partial e_2}{\partial T_{2t}} & \frac{\partial e_2}{\partial P_{2t}} \\ \frac{\partial e_3}{\partial T_{2t}} & \frac{\partial e_3}{\partial P_{2t}} \end{bmatrix} \begin{bmatrix} \delta T_{2t} \\ \delta P_{2t} \end{bmatrix} = \begin{bmatrix} 0 \\ 0 \\ 0 \end{bmatrix} \tag{3.45}$$

$$\frac{\partial k_2}{\partial N_1}\delta N_1 + \frac{\partial k_2}{\partial T_{2t}}\delta T_{2t} + \frac{\partial k_2}{\partial w_{25}}\delta w_{25} + \frac{\partial k_2}{\partial T_{25t}}\delta T_{25t} + \frac{\partial k_2}{\partial \tau_{25t}}\delta \tau_{25t} = 0$$

HPC

$$\begin{bmatrix} 0 & \frac{\partial h_1}{\partial T_{25t}} & \frac{\partial h_1}{\partial P_{25t}} & 0 & \frac{\partial h_1}{\partial w_{30}} & 0 & 0 & \frac{\partial h_1}{Rline_{HPC}} \\ 0 & \frac{\partial h_2}{\partial T_{25t}} & \frac{\partial h_2}{\partial P_{25t}} & 0 & 0 & \frac{\partial h_2}{\partial T_{30t}} & \frac{\partial h_2}{\partial P_{30t}} & \frac{\partial h_2}{Rline_{HPC}} \\ 0 & \frac{\partial h_3}{\partial T_{25t}} & \frac{\partial h_3}{\partial P_{25t}} & 0 & 0 & 0 & \frac{\partial h_3}{\partial P_{30t}} & \frac{\partial h_3}{Rline_{HPC}} \end{bmatrix} \begin{bmatrix} \delta w_{25} \\ \delta T_{25t} \\ \delta P_{25t} \\ \delta Rline_{LPC} \\ \delta w_{30} \\ \delta T_{30t} \\ \delta P_{30t} \\ \delta Rline_{HPC} \end{bmatrix} + \begin{bmatrix} 0 & \frac{\partial h_1}{\partial N_2} \\ 0 & \frac{\partial h_2}{\partial N_2} \\ 0 & \frac{\partial h_3}{\partial N_2} \end{bmatrix} \begin{bmatrix} \delta N_1 \\ \delta N_2 \end{bmatrix} + \begin{bmatrix} 0 \\ 0 \\ 0 \end{bmatrix} \delta w_f = \begin{bmatrix} 0 \\ 0 \\ 0 \end{bmatrix} \qquad (3.46)$$

$$\frac{\partial k_3}{\partial N_2}\delta N_2 + \frac{\partial k_3}{\partial T_{25t}}\delta T_{25t} + \frac{\partial k_3}{\partial w_{25}}\delta w_{25} + \frac{\partial k_3}{\partial T_{30t}}\delta T_{30t} + \frac{\partial k_3}{\partial \tau_{30t}}\delta \tau_{30t} = 0$$

Burner

$$\begin{bmatrix} \frac{\partial g_1}{\partial w_{30}} & 0 & 0 & 0 & \frac{\partial g_1}{\partial w_{40}} & 0 & 0 \\ \frac{\partial g_2}{\partial w_{30}} & \frac{\partial g_2}{\partial T_{30t}} & 0 & 0 & 0 & \frac{\partial g_2}{\partial T_{40t}} & 0 \\ 0 & 0 & \frac{\partial g_3}{\partial P_{30t}} & 0 & 0 & 0 & \frac{\partial g_3}{\partial P_{40t}} \end{bmatrix} \begin{bmatrix} \delta w_{30} \\ \delta T_{30t} \\ \delta P_{30t} \\ \delta Rline_{HPC} \\ \delta w_{40} \\ \delta T_{40t} \\ \delta P_{40t} \end{bmatrix} + \begin{bmatrix} 0 & 0 \\ 0 & 0 \\ 0 & 0 \end{bmatrix} \begin{bmatrix} \delta N_1 \\ \delta N_2 \end{bmatrix} + \begin{bmatrix} \frac{\partial g_1}{\partial w_f} \\ \frac{\partial g_2}{\partial w_f} \\ 0 \end{bmatrix} \delta w_f = \begin{bmatrix} 0 \\ 0 \\ 0 \end{bmatrix} \qquad (3.47)$$

$$\frac{\partial k_4}{\partial w_f}\delta w_f + \frac{\partial k_4}{\partial w_{30}}\delta w_{30} + \frac{\partial k_4}{\partial FAR}\delta FAR = 0$$

HPT

$$\begin{bmatrix} 0 & 0 & 0 & 0 & 0 & \frac{\partial f_1}{\partial T_{40t}} & \frac{\partial f_1}{\partial P_{40t}} & \frac{\partial f_1}{\partial w_{45}} & 0 & 0 & \frac{\partial f_1}{\partial PR_{HPT}} \\ 0 & \frac{\partial f_2}{\partial T_{30t}} & 0 & 0 & 0 & \frac{\partial f_2}{\partial T_{40t}} & \frac{\partial f_2}{\partial P_{40t}} & 0 & \frac{\partial f_2}{\partial T_{45t}} & 0 & \frac{\partial f_2}{\partial PR_{HPT}} \\ 0 & 0 & 0 & 0 & 0 & 0 & \frac{\partial f_3}{\partial P_{40t}} & 0 & 0 & \frac{\partial f_3}{\partial P_{45t}} & \frac{\partial f_3}{\partial PR_{HPT}} \end{bmatrix} \begin{bmatrix} \delta w_{30} \\ \delta T_{30t} \\ \delta P_{30t} \\ \delta Rline_{HPC} \\ \delta w_{40} \\ \delta T_{40t} \\ \delta P_{40t} \\ \delta w_{45} \\ \delta T_{45t} \\ \delta P_{45t} \\ \delta PR_{HPT} \end{bmatrix} + \begin{bmatrix} 0 & \frac{\partial f_1}{\partial N_2} \\ 0 & \frac{\partial f_2}{\partial N_2} \\ 0 & \frac{\partial f_3}{\partial N_2} \end{bmatrix} \begin{bmatrix} \delta N_1 \\ \delta N_2 \end{bmatrix} + \begin{bmatrix} 0 \\ 0 \\ 0 \end{bmatrix} \delta w_f = \begin{bmatrix} 0 \\ 0 \\ 0 \end{bmatrix} \qquad (3.48)$$

$$\frac{\partial k_5}{\partial N_2}\delta N_2 + \frac{\partial k_5}{\partial T_{40t}}\delta T_{40t} + \frac{\partial k_5}{\partial T_{45t}}\delta T_{45t} + \frac{\partial k_5}{\partial w_{40}}\delta w_{40} + \frac{\partial k_5}{\partial w_{45}}\delta w_{45} + \frac{\partial k_5}{\partial \tau_{45}}\delta \tau_{45} + \frac{\partial k_5}{\partial T_{30t}}\delta T_{30t} = 0$$

LPT

$$\begin{bmatrix} 0 & \frac{\partial m_1}{\partial T_{45t}} & \frac{\partial m_1}{\partial P_{45t}} & 0 & \frac{\partial m_1}{\partial w_{50t}} & 0 & 0 & \frac{\partial m_1}{\partial PR_{LPT}} \\ 0 & \frac{\partial m_2}{\partial T_{45t}} & \frac{\partial m_2}{\partial P_{45t}} & 0 & 0 & \frac{\partial m_2}{\partial T_{50t}} & 0 & \frac{\partial m_2}{\partial PR_{LPT}} \\ 0 & 0 & \frac{\partial m_3}{\partial P_{45t}} & 0 & 0 & 0 & \frac{\partial m_3}{\partial P_{50t}} & \frac{\partial m_3}{\partial PR_{LPT}} \end{bmatrix} \begin{bmatrix} \delta w_{45} \\ \delta T_{45t} \\ \delta P_{45t} \\ \delta PR_{HPT} \\ \delta w_{50} \\ \delta T_{50t} \\ \delta P_{50t} \\ \delta PR_{LPT} \end{bmatrix} + \begin{bmatrix} \frac{\partial m_1}{\partial N_1} & 0 \\ \frac{\partial m_2}{\partial N_1} & 0 \\ \frac{\partial m_3}{\partial N_1} & 0 \end{bmatrix} \begin{bmatrix} \delta N_1 \\ \delta N_2 \end{bmatrix} + \begin{bmatrix} 0 \\ 0 \\ 0 \end{bmatrix} \delta w_f = \begin{bmatrix} 0 \\ 0 \\ 0 \end{bmatrix} \tag{3.49}$$

$$\frac{\partial k_6}{\partial N_1}\delta N_1 + \frac{\partial k_6}{\partial T_{45t}}\delta T_{45t} + \frac{\partial k_6}{\partial T_{50t}}\delta T_{50t} + \frac{\partial k_6}{\partial w_{50}}\delta w_{50} + \frac{\partial k_6}{\partial \tau_{50}}\delta \tau_{50} = 0$$

Primary Nozzle

$$\begin{gathered} \frac{\partial q_1}{\partial w_8}\delta w_8 + \frac{\partial q_1}{\partial T_{50t}}\delta T_{50t} + \frac{\partial q_1}{\partial P_{50t}}\delta P_{50t} + \frac{\partial q_1}{\partial A_e}\delta A_e = 0 \\ \frac{\partial k_7}{\partial u_8}\delta u_8 + \frac{\partial k_7}{\partial T_{50t}}\delta T_{50t} + \frac{\partial k_7}{\partial P_{50t}}\delta P_{50t} = 0 \\ \frac{\partial k_8}{\partial T_{50t}}\delta T_{50t} + \frac{\partial k_8}{\partial P_{50t}}\delta P_{50t} + \frac{\partial k_8}{\partial A_e}\delta A_e + \frac{\partial k_8}{\partial F_8}\delta F_8 = 0 \end{gathered} \tag{3.50}$$

Secondary Nozzle

$$\begin{gathered} \frac{\partial r_1}{\partial w_{17}}\delta w_{17} + \frac{\partial r_1}{\partial T_{12t}}\delta T_{12t} + \frac{\partial r_1}{\partial P_{12t}}\delta P_{12t} = 0 \\ \frac{\partial k_9}{\partial u_{17}}\delta u_{17} + \frac{\partial k_9}{\partial T_{12t}}\delta T_{12t} + \frac{\partial k_9}{\partial P_{12t}}\delta P_{12t} = 0 \\ \frac{\partial k_{10}}{\partial T_{12t}}\delta T_{12t} + \frac{\partial k_{10}}{\partial P_{12t}}\delta P_{12t} + \frac{\partial k_{10}}{\partial F_{17}}\delta F_{17} = 0 \end{gathered} \tag{3.51}$$

Continuity in Mass Flow Rate

$$\begin{bmatrix} 0 & 0 & \frac{\partial l_1}{\partial w_{25}} & \frac{\partial l_1}{\partial w_{30}} & 0 & 0 & 0 \\ 0 & 0 & 0 & \frac{\partial l_2}{\partial w_{30}} & \frac{\partial l_2}{\partial w_{45}} & 0 & 0 \\ 0 & 0 & \frac{\partial l_3}{\partial w_{25}} & 0 & \frac{\partial l_3}{\partial w_{45}} & \frac{\partial l_3}{\partial w_{50}} & 0 \\ 0 & 0 & \frac{\partial l_4}{\partial w_{25}} & 0 & 0 & \frac{\partial l_4}{\partial w_{50}} & \frac{\partial l_4}{\partial w_8} \\ \frac{\partial l_5}{\partial w_{12}} & \frac{\partial l_5}{\partial w_{17}} & 0 & 0 & 0 & 0 & 0 \end{bmatrix} \begin{bmatrix} \delta w_{12} \\ \delta w_{17} \\ \delta w_{25} \\ \delta w_{30} \\ \delta w_{45} \\ \delta w_{50} \\ \delta w_8 \end{bmatrix} = \begin{bmatrix} 0 \\ 0 \\ 0 \\ 0 \\ 0 \\ 0 \\ 0 \end{bmatrix} \tag{3.52}$$

Shaft Dynamics

$$\delta\dot{N} = \frac{60}{2\pi}\left[\frac{\delta\tau_{turbine} - \delta\tau_{compressor}}{J}\right] \tag{3.53}$$

Heat Soak Dynamics (if it is included)

$$\delta\dot{T}_m = -\frac{hA_m}{c_{pm}M}\delta T_m + \frac{hA_m}{c_{pm}M}\delta T_{gi} \tag{3.54}$$

$$\delta T_{go} = \frac{hA_m}{c_{pg}w_g}\delta T_m + \left(1 - \frac{hA_m}{c_{pg}w_g}\right)\delta T_{gi} \tag{3.55}$$

3.5 Integrated Linearization Approach

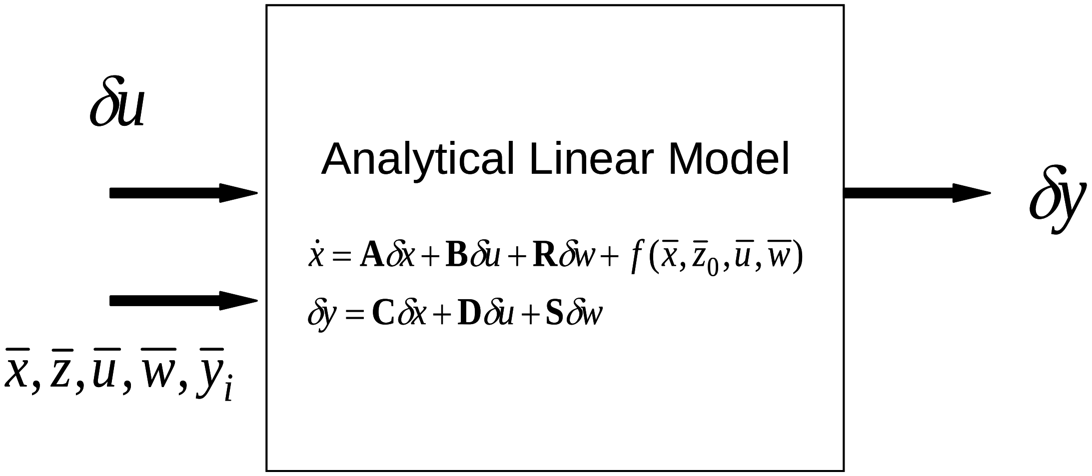

Figure 3.4 System-level linearization

Linearized component models are stacked to obtain the system level model as shown in Figure 3.4. Linearization requires current nonlinear values in addition to input variations. The inlet pressure and temperature which vary with ambient condition are considered to be a disturbance *w* from a control perspective. Bounds on these disturbance parameters may be used for designing robust controllers. For simplicity, disturbance is assumed to be negligible. A residualized engine dynamic model with two dynamic states, N_1 and N_2, are considered in this study. A complete description of the system level inputs and outputs is given in the following:

$$u = \begin{bmatrix} w_f \end{bmatrix} \quad x = \begin{bmatrix} N_1 \\ N_2 \end{bmatrix} \quad w = \begin{bmatrix} P_{tin} \\ T_{tin} \end{bmatrix} \quad y = \begin{bmatrix} x \\ \text{---} \\ z \\ \text{---} \\ y_i \end{bmatrix} \tag{3.56}$$

where

$$y_i^T = [\tau_{25} \quad \tau_{30} \quad FAR \quad \tau_{45} \quad \tau_{50} \quad u_8 \quad F_8 \quad \tau_{12.5} \quad u_{17} \quad F_{17}]$$

$$\begin{aligned} z^T = [&w_{25} \quad T_{25} \quad P_{25} \quad Rline_{LPC} \, w_{30} \quad T_{30} \quad P_{30} \quad Rline_{HPC} \\ &w_4 \quad T_4 \quad P_4 \quad w_{45} T_{45} \quad P_{45} \quad PR_{HPT} \quad w_5 \\ &T_5 \quad P_5 \quad PR_{LPC} \, w_8 \quad w_{12.5} \quad T_{12.5} \quad P_{12.5} \quad Rline_{fan} \quad w_{17} \quad] \end{aligned}$$

First, algebraic equations for fast dynamics are solved simultaneously by using matrix algebra. These equations are combination of equations (3.44)-(3.52) for each component. The internal solver variables in addition to the fast dynamics states such as the *Rline* and *PR* are included in the vector *z* for convenience. The resulting vector equation can be written as follows:

$$\mathbf{K}\Delta z + \mathbf{L}\Delta u + \mathbf{M}\Delta x = 0 \tag{3.57}$$

The extended form of the above equation is shown in the appendix at the end of the thesis. Each row block represents equations for individual component. Each row of the matrix **K** is independent of one another so the matrix **K** should be invertible. Numerical conditioning of the matrix **K** may improve the inversion accuracy. It may be possible to exploit the sparsity of **K** and develop computationally efficient algorithms to solve the set of linear equations. Equation (3.57) can be rewritten as follows to solve for Δz.

$$\Delta z = -\mathbf{K}^{-1}(\mathbf{L}\Delta u + \mathbf{M}\Delta x) \tag{3.58}$$

Intermediate outputs including torque, thrust and exit velocity can be solved using the following:

$$\begin{aligned} \Delta y_i &= \mathbf{E}\Delta z + \mathbf{F}\Delta u + \mathbf{G}\Delta x \\ &= (-\mathbf{EK}^{-1}\mathbf{M} + \mathbf{G})\Delta x + (-\mathbf{EK}^{-1}\mathbf{L} + \mathbf{F})\Delta u \end{aligned} \tag{3.59}$$

Intermediate outputs can be directly absorbed into the fast dynamics vector *z*, thus allowing one to combine matrices **K, L**, and **M** in equation (3.57) and **E, F**, and **G** in equation (3.60) to form an augmented matrix. However, the intermediate outputs are represented separately in this study to reduce the size of matrix **K**, thus reducing the computational cost for the matrix inversion of K. Finally, the linearized shaft dynamics can be written as follows:

$$
\begin{aligned}
&\Delta\dot{x} = \mathbf{P}\Delta y_i \\
&= (-\mathbf{PEK}^{-1}\mathbf{M} + \mathbf{PG})\Delta x + (-\mathbf{PEK}^{-1}\mathbf{L} + \mathbf{PF})\Delta u \qquad (3.60) \\
&= \mathbf{A}\mathit{\Delta} x + \mathbf{B}\Delta u
\end{aligned}
$$

Inputs and outputs of each component as well as the number of equations for each component are summarized in Table 3.1. The size of system level inputs, outputs and states are summarized in Table 3.2. Dimensions of each matrix are given in Table 3.3. The form of each matrix for the twin-spool turbofan is given in Appendix at the end of the thesis.

This linearization methodology can extend to any standard gas turbine engine that utilizes compressor, combustor, turbine and nozzle elements. The frequency range for residualization of fast dynamic states is determined based on the desired controller bandwidth. The numbers of slow and fast dynamic states is set accordingly. The addition of control input should be easily incorporated using the proposed linearization approach as long as the input appears in one or more of the algebraic expressions describing the components. For example, variable stator vane inputs may appear in the form of an additional parameter in the component map description. Then, component map sensitivities with respect to the variable stator vanes will be computed. The addition of a variable nozzle area is already present in the component level linear model description. The input sensitivity matrix will have an additional number of columns that corresponds to the additional inputs as the system model will include sensitivity terms with respect to the nozzle area in addition to the fuel flow.

Table 3.1 Summary of inputs, outputs, and number of equations of each component

Component	**Inputs**	**Outputs**	**Number of fast state dynamics equations**	**Number of output equations**
LPC	$T_{20t}, P_{20t}, Rline_{LPC}$	$T_{25t}, P_{25t}, w_{25}, \tau_{25}$	3	1
HPC	$T_{25t}, P_{25t}, w_{25}, Rline_{HPC}$	$T_{30t}, P_{30t}, w_{30}, \tau_{30}$	3	1
Burner	$T_{30t}, P_{30t}, w_{30}, w_f$	$T_{40t}, P_{40t}, w_{40}, FAR$	3	1
HPT	$T_{40t}, P_{40t}, w_{40}, PR_{HPT}, T_{30t}$	$T_{45t}, P_{45t}, w_{45}, \tau_{45}$	3	1
LPT	$T_{50t}, P_{50t}, w_{50}, PR_{LPT}$	$T_{50t}, P_{50t}, w_{50}, \tau_{50}$	3	1
Primary Nozzle	T_{50t}, P_{50t}, w_{50}	w_{80}, F_8, u_8	1	2
Fan	$T_{20t}, P_{20t}, Rline_{Fan}$	$T_{12t}, P_{12t}, w_{12}, \tau_{12}$	3	1
Secondary Nozzle	T_{12t}, P_{12t}, w_{12}	w_{17}, F_{17}, u_{17}	1	2
Continuity	N/A	N/A	5	0
Total			25	10

Table 3.2 Size of integrated system

n	Number of fast dynamic states	25
m	Number of slow dynamic states	2
l	Number of inputs	1
k	Number of intermediate outputs	10

Table 3.3 Matrix dimension

Matrix	**Size of matrix**
K	n x n
L	n x l
M	n x m
E	k x n
F	k x l
G	k x m
P	m x k

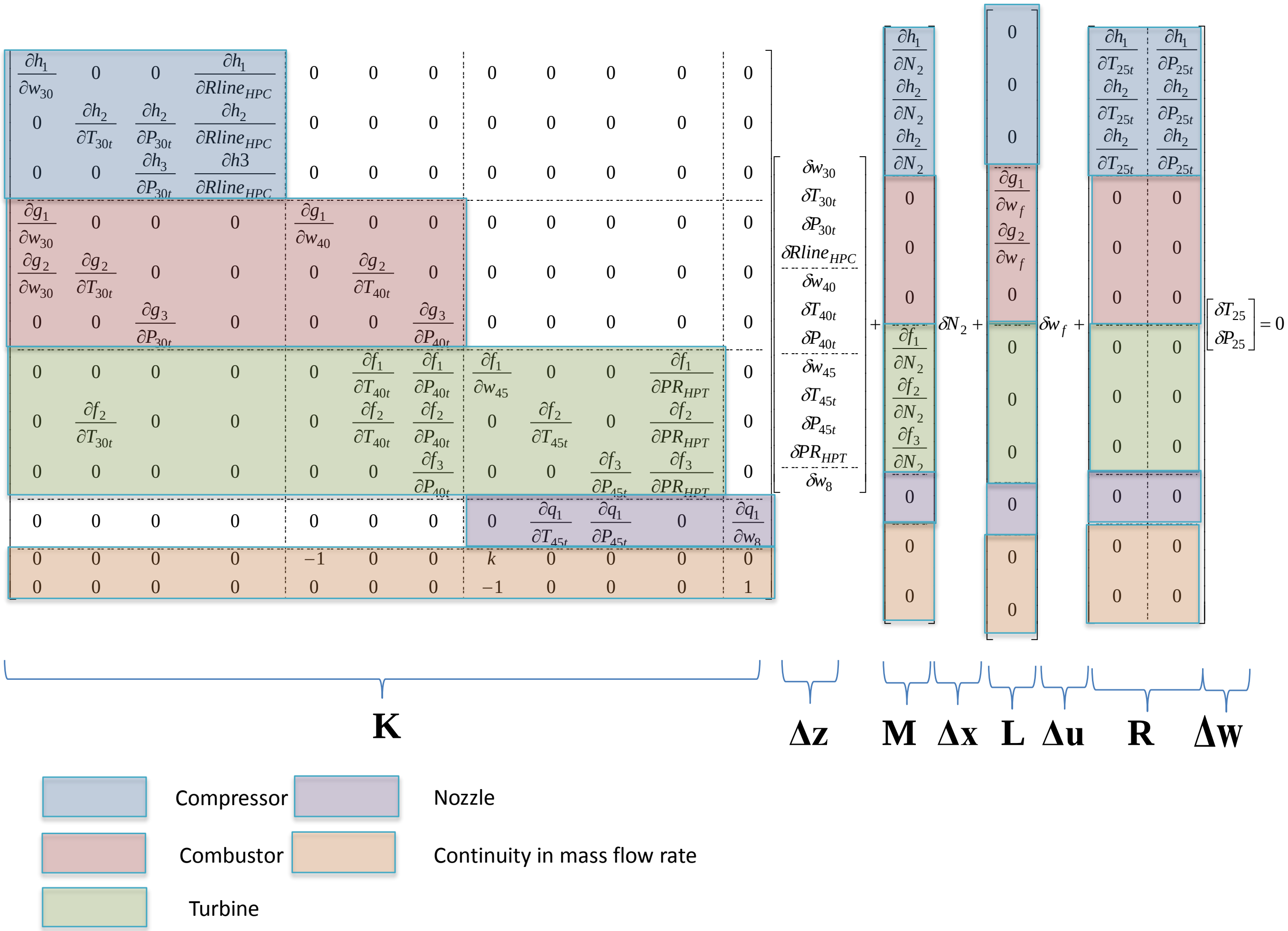

$$\underbrace{\begin{bmatrix}
\frac{\partial h_1}{\partial w_{30}} & 0 & 0 & \frac{\partial h_1}{\partial Rline_{HPC}} & 0 & 0 & 0 & 0 & 0 & 0 & 0 & 0 \\
0 & \frac{\partial h_2}{\partial T_{30t}} & \frac{\partial h_2}{\partial P_{30t}} & \frac{\partial h_2}{\partial Rline_{HPC}} & 0 & 0 & 0 & 0 & 0 & 0 & 0 & 0 \\
0 & 0 & \frac{\partial h_3}{\partial P_{30t}} & \frac{\partial h3}{\partial Rline_{HPC}} & 0 & 0 & 0 & 0 & 0 & 0 & 0 & 0 \\
\frac{\partial g_1}{\partial w_{30}} & 0 & 0 & 0 & \frac{\partial g_1}{\partial w_{40}} & 0 & 0 & 0 & 0 & 0 & 0 & 0 \\
\frac{\partial g_2}{\partial w_{30}} & \frac{\partial g_2}{\partial T_{30t}} & 0 & 0 & 0 & \frac{\partial g_2}{\partial T_{40t}} & 0 & 0 & 0 & 0 & 0 & 0 \\
0 & 0 & \frac{\partial g_3}{\partial P_{30t}} & 0 & 0 & 0 & \frac{\partial g_3}{\partial P_{40t}} & 0 & 0 & 0 & 0 & 0 \\
0 & 0 & 0 & 0 & 0 & \frac{\partial f_1}{\partial T_{40t}} & \frac{\partial f_1}{\partial P_{40t}} & \frac{\partial f_1}{\partial w_{45}} & 0 & 0 & \frac{\partial f_1}{\partial PR_{HPT}} & 0 \\
0 & \frac{\partial f_2}{\partial T_{30t}} & 0 & 0 & 0 & \frac{\partial f_2}{\partial T_{40t}} & \frac{\partial f_2}{\partial P_{40t}} & 0 & \frac{\partial f_2}{\partial T_{45t}} & 0 & \frac{\partial f_2}{\partial PR_{HPT}} & 0 \\
0 & 0 & 0 & 0 & 0 & 0 & \frac{\partial f_3}{\partial P_{40t}} & 0 & 0 & \frac{\partial f_3}{\partial P_{45t}} & \frac{\partial f_3}{\partial PR_{HPT}} & 0 \\
0 & 0 & 0 & 0 & 0 & 0 & 0 & 0 & \frac{\partial q_1}{\partial T_{45t}} & \frac{\partial q_1}{\partial P_{45t}} & 0 & \frac{\partial q_1}{\partial w_8} \\
0 & 0 & 0 & 0 & -1 & 0 & 0 & k & 0 & 0 & 0 & 0 \\
0 & 0 & 0 & 0 & 0 & 0 & 0 & -1 & 0 & 0 & 0 & 1
\end{bmatrix}}_{\mathbf{K}}
\underbrace{\begin{bmatrix}
\delta w_{30} \\ \delta T_{30t} \\ \delta P_{30t} \\ \delta Rline_{HPC} \\ \delta w_{40} \\ \delta T_{40t} \\ \delta P_{40t} \\ \delta w_{45} \\ \delta T_{45t} \\ \delta P_{45t} \\ \delta PR_{HPT} \\ \delta w_8
\end{bmatrix}}_{\mathbf{\Delta z}}
+
\underbrace{\begin{bmatrix}
\frac{\partial h_1}{\partial N_2} \\ \frac{\partial h_2}{\partial N_2} \\ \frac{\partial h_2}{\partial N_2} \\ 0 \\ 0 \\ 0 \\ \frac{\partial f_1}{\partial N_2} \\ \frac{\partial f_2}{\partial N_2} \\ \frac{\partial f_3}{\partial N_2} \\ 0 \\ 0 \\ 0
\end{bmatrix}}_{\mathbf{M}}
\underbrace{\delta N_2}_{\mathbf{\Delta x}}
+
\underbrace{\begin{bmatrix}
0 \\ 0 \\ 0 \\ \frac{\partial g_1}{\partial w_f} \\ \frac{\partial g_2}{\partial w_f} \\ 0 \\ 0 \\ 0 \\ 0 \\ 0 \\ 0 \\ 0
\end{bmatrix}}_{\mathbf{L}}
\underbrace{\delta w_f}_{\mathbf{\Delta u}}
+
\underbrace{\begin{bmatrix}
\frac{\partial h_1}{\partial T_{25t}} & \frac{\partial h_1}{\partial P_{25t}} \\
\frac{\partial h_2}{\partial T_{25t}} & \frac{\partial h_2}{\partial P_{25t}} \\
\frac{\partial h_2}{\partial T_{25t}} & \frac{\partial h_2}{\partial P_{25t}} \\
0 & 0 \\ 0 & 0 \\ 0 & 0 \\ 0 & 0 \\ 0 & 0 \\ 0 & 0 \\ 0 & 0 \\ 0 & 0 \\ 0 & 0
\end{bmatrix}}_{\mathbf{R}}
\underbrace{\begin{bmatrix}
\delta T_{25} \\ \delta P_{25}
\end{bmatrix}}_{\mathbf{\Delta W}}
= 0$$

Figure 3.5 Example of HPC-Burner-HPT-Nozzle

3.5.1 Example of matrix construction of HPC-Burner-HPT-Nozzle series in configuration

An example of a matrix to solve for the fast dynamics is shown in this section. Figure 3.5 only includes HPC-Burner-HPT-Nozzle components for readability. Equations of each component are stacked to form a larger matrix **K**. It is natural to follow the order of physical connections although it is not required. In an example, each colored block represents a single component. The matrix is not in a special form, but it is sparse, which should simplify the matrix inversion process. Other components are stacked similarly. The last block is reserved for the continuity of mass flow rate.

3.6 Summary

The off-equilibrium analytical linearization process was developed in this chapter. First, simplifying assumptions necessary for achieving analytical linearization were identified. Then, the nonlinear model described in the previous chapter was adjusted by applying these identified simplifying assumptions, and linear coefficients for each component were derived using the partial differentiation. Finally, the integration of component level linear model for developing a system level linear model utilizing the fast dynamics states were described in detail.

CHAPTER 4

MODEL VALIDATION METHOD

Any new modeling methodology needs to be validated before it can be applied to real-world applications. The validation of a model is not an easy task as careful selection of data sets, tools and method for the validation are necessary. Thus, the validation of a model itself constitutes a topic for in-depth research. In this chapter, validation metrics for a linear dynamic engine model are established. First, the selection of tools for the model validation is discussed. Then, different validation methods are discussed in detail. The rationale behind the selection of a particular validation method is discussed followed by a description of the actual method.

4.1 Validation tool

4.1.1 Numerical Propulsion System Simulation (NPSS)

An example engine given in the Numerical Propulsion System Simulation (NPSS) is selected for the proposed linearization method. NPSS is a cooperative effort among NASA, other government agencies and industry to provide a common tool for aerothermomechanical simulation of an aircraft engine [31]. Physical interactions inside an engine are captured in the NPSS. It provides a simulation environment of a generic zero-dimensional view of an engine[31]. The NPSS architecture is based on the component based object oriented concept and wide capability exists within the software for adding more features and fidelity. The NPSS library includes collection of components modules such as compressor, turbine and nozzle. These components are part of elements which are the main building blocks of an engine model [66]. The input file and gas table are selected by the user. For the purpose of this study, the default gas table is used.

4.1.2 Engine Characteristic

The NPSS distribution includes several gas turbine engine examples. The twin-spool, high bypass engine has been selected for evaluation of the proposed methodology. The example is complex enough to afford a realistic assessment of analytical linearization relative to legacy methods. It represents a 9000 lb commercial engine with a bypass ratio of 5.

The model has been adapted to retain two dynamic states, N_1 and $N_{2,}$ and one input, fuel flow rate. The analytical linearization method is equally applicable to a system with additional states and inputs, e.g., metal temperature states and variable geometry inputs. It is in fact anticipated that the advantage of the proposed method over the legacy piecewise linear approach will be more pronounced for increasingly complex, non-linear dynamical systems.

Minor modifications were applied to an example engine to achieve the more realistic transient profile of existing turbofan engines. High speed spool inertia was adjusted to bring out more separation between the acceleration curve and deceleration curve as shown in Figure 4.1. High pressure spool speed that is corrected with high pressure compressor inlet condition is plotted against the corrected low pressure spool speed. The solid line represents the steady-state operating points. The profiles using the original inertia, given by the dashed line, shows a very small separation between the acceleration and deceleration segments. The engine with modified inertia, given in the dash dot line, exhibits more separation between the acceleration and deceleration profiles. The LPC may surge during the deceleration maneuver due to spool mismatch[20]. Benefits of using off-equilibrium linearization are expected to be larger for the larger separation profile as the transient is further away from the steady-state line. Also the map parameter for the fan stall line is adjusted to further from a steady-state operation line to enable more aggressive acceleration profile.

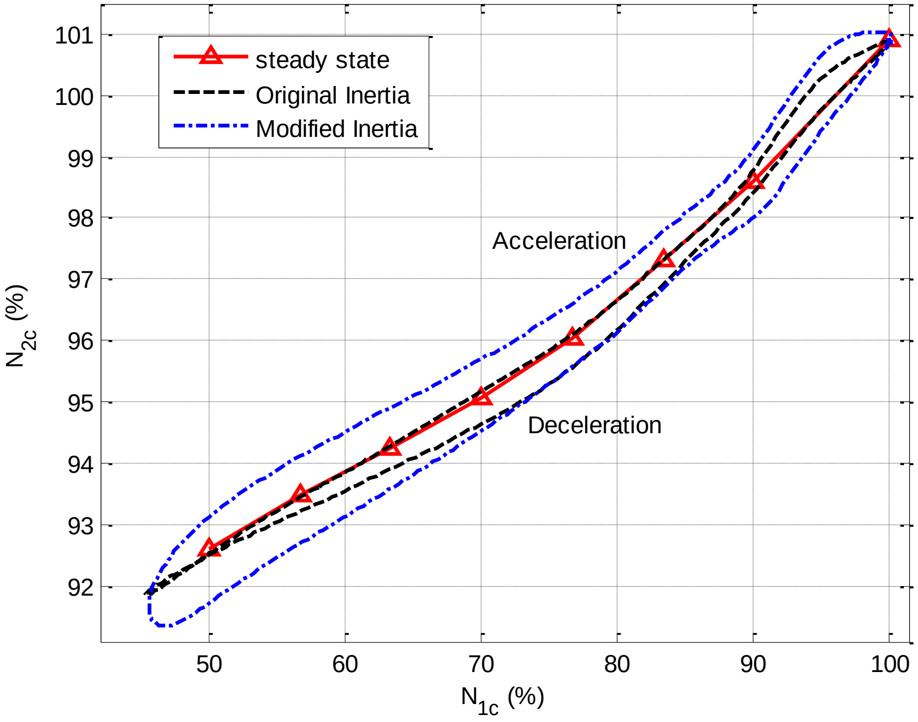

Figure 4.1 N_{2c} vs. N_{1c} (at sea-level static condition)

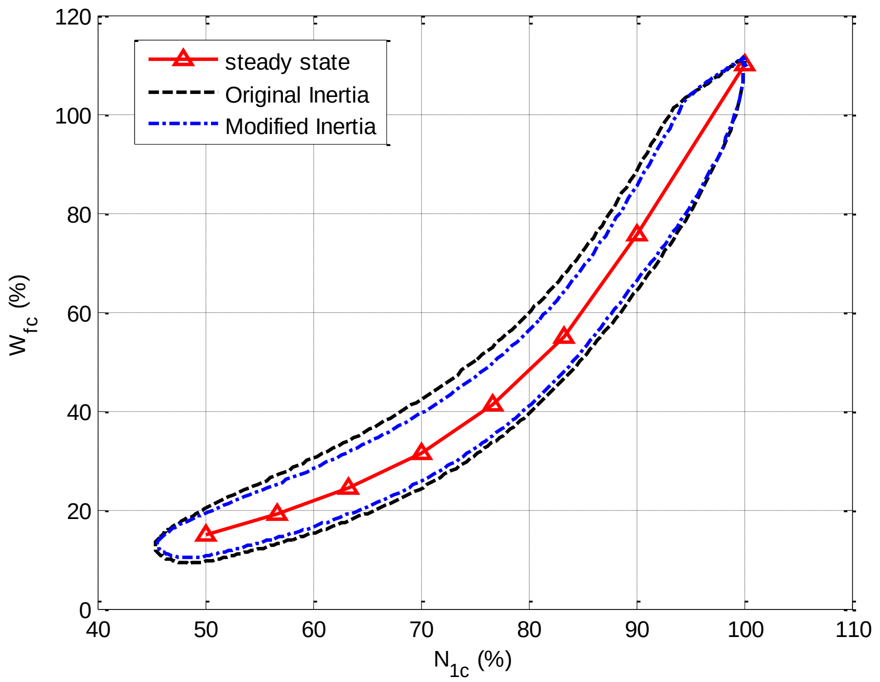

Figure 4.2 w_{fc} vs. N_{1c} (at sea-level static condition)

The equilibrium of the example gas turbine engine for different flight conditions is given in Table 4.1 to Table 4.4 for different operating conditions. Table 4.1 shows the variation of engine equilibrium values for different power levels. Table 4.2 shows the effect of Mach number on the engine equilibrium values. Table 4.3 shows the variation in engine equilibrium values for different temperature variations from the standard day. Table 4.4 shows the engine equilibrium values at different altitude.

Table 4.1 The equilibrium values for engine states and inputs as a function of power lever angle (PLA)

PLA (°)	Alt (ft)	Mach number	dTs (°R)	w_f (lbm/s)	N_1 (rpm)	N_2 (rpm)	Net thrust (lbf)	Gross thrust (lbf)
50	0	0	0	1.1604	3779.1	9790.3	9470.9	9470.9
40	0	0	0	0.7985	3401.2	9373.3	7382.3	7382.3
30	0	0	0	0.5805	3149.3	9116.2	5805.5	5805.5
20	0	0	0	0.4344	2897.3	8865.6	4579.2	4579.2
10	0	0	0	0.3318	2645.4	8631.2	3606.4	3606.4
0	0	0	0	0.2574	2393.4	8421.4	2846.4	2846.4
-10	0	0	0	0.2019	2141.5	8223	2223.1	2223.1
-20	0	0	0	0.1579	1889.6	8020.1	1691.3	1691.3

Table 4.2 Engine equilibrium values for a fixed PLA as a function of Mach number

Mach number	Alt (ft)	dTs (°R)	PLACS (°)	w_f (lbm/s)	N_1 (rpm)	N_2 (rpm)	Net thrust (lbf)	Gross thrust (lbf)
0	0	0	50	1.1604	3779.1	9790.3	9470.9	9470.9
0.2	0	0	50	1.1845	3794.2	9811.6	8063.8	9897.6
0.4	0	0	50	1.2610	3832.5	9876.2	7290.2	11226
0.6	0	0	50	1.3438	3834.6	9944.3	6812.0	13335
0.8	0	0	50	1.4418	3791.9	10041	6520.8	16338

Table 4.3 Engine equilibrium values for a fixed PLA as a function of dTs

dTs (°R)	Alt (ft)	Mach number	PLACS (°)	w_f (lbm/s)	N_1 (rpm)	N_2 (rpm)	Net thrust (lbf)	Gross thrust (lbf)
-60	0	0	50	1.07528	3553.80	9231.16	9469.29	9469.29
-40	0	0	50	1.10687	3630.46	9423.89	9471.38	9471.38
-20	0	0	50	1.12582	3705.54	9598.18	9447.57	9447.57
0	0	0	50	1.16038	3779.09	9790.28	9470.88	9470.88
20	0	0	50	1.09003	3742.89	9867.54	8952.77	8952.77
40	0	0	50	1.01435	3706.56	9927.91	8402.72	8402.72
60	0	0	50	0.95371	3681.86	9996.63	7926.07	7926.07

Table 4.4 Engine equilibrium values for a fixed PLA as a function of altitude

Alt (ft)	Mach number	dTs (°R)	PLACS (°)	w_f (lbm/s)	N_1 (rpm)	N_2 (rpm)	Net thrust (lbf)	Gross thrust (lbf)
0	0	0	50	1.1604	3779.1	9790.3	9470.9	9470.9
5000	0	0	50	0.9383	3713.6	9616.7	7858.9	7858.9
10000	0	0	50	0.76537	3646.87	9464.71	6512.25	6512.25
15000	0	0	50	0.61291	3578.93	9295.25	5345.19	5345.19
20000	0	0	50	0.48537	3509.66	9118.72	4348.99	4348.99
25000	0	0	50	0.37558	3439.01	8919.78	3493.11	3493.11
30000	0	0	50	0.29011	3366.87	8720.57	2783.40	2783.40
35000	0	0	50	0.22800	3293.15	8559.34	2214.32	2214.32

4.1.3 The Truth Model

In order to assess the proposed methodology, it is first necessary to establish the definition of a truth model. For time-domain analysis, the output of the nonlinear model provides a direct measure of the truth. In addition, the numerically derived linear model using the small perturbation method along a transient trajectory is considered as the truth plant for validation purpose. The central differencing scheme shown in equations (4.1) and (4.2) are used to minimize the effect of asymmetry. The plant is perturbed with 1% change in both positive and negative directions for each state and input independently to compute desired linear coefficients. The perturbation size is reduced until the desired tolerance is met to reduce the error caused by severe nonlinearity.

$$a_{ji} = \frac{f_j(\bar{x}_i + \delta x_i, \bar{x}_j, \bar{u}) - f_j(\bar{x}_i - \delta x_i, \bar{x}_j, \bar{u})}{2\delta x_i} \tag{4.1}$$

$$b_i = \frac{f_i(\bar{x}, \bar{u} + \delta u) - f_i(\bar{x}, \bar{u} - \delta u)}{2\delta u} \tag{4.2}$$

4.1.4 Piecewise Linear Model

An analytical linear model developed at every time step along the transient trajectory is compared with conventional piecewise linear models scheduled with fan speed. Multiple linear models are developed numerically at steady-state conditions and are scheduled with scheduling parameter, η , as shown in equation (4.3) [25]. Steady-state values are also scheduled using parameter, η. The piecewise linear mode matches the truth model exactly at steady-state conditions where they are derived. The continuously scheduled linear model developed at each steady-state condition corresponding to N_1 represents the asymptotic limit of conventional piecewise linear models.

$$\begin{aligned}\dot{\mathbf{X}} &= \mathbf{A}(\eta)(\mathbf{X}-\mathbf{X_{st}}(\eta)) + \mathbf{B}(\eta)(\mathbf{U}-\mathbf{U_{st}}(\eta)) \\ \mathbf{Y} &= \mathbf{C}(\eta)(\mathbf{X}-\mathbf{X_{st}}(\eta)) + \mathbf{D}(\eta)(\mathbf{U}(t)-\mathbf{U_{st}}(\eta)) + \mathbf{Y_{st}}(\eta)\end{aligned} \tag{4.3}$$

4.1.5 Steady-state Condition Validation

The analytical linear model developed at selected steady-state conditions is compared with the truth model developed using numerical perturbations. The validation of the linear model at the steady-state conditions are achieved via the normalized additive uncertainty and the ν-gap metric (which will be described in latter sections) between the analytical linear model and the truth model computed at selected steady-state conditions.

4.1.6 The Bodie Maneuver

The validation of the linear model can be achieved using different transient trajectories. It is important to select an aggressive yet critical maneuver to ensure that the methodology works in all situations. In addition, the benefits of using off-equilibrium real-time linearization are well illustrated by using an aggressive transient maneuver that covers a large operating region. Hence, the linear model is validated using the *Bodie* maneuver, named after the pilot who first used the maneuver during engine flight trials as shown in Figure 4.3 (a) [63]. The *Bodie* maneuver in which snap acceleration immediately follows snap deceleration represents the most aggressive transient operation that an engine would possibly need to go through during its operation. The transient trajectory of the *Bodie* profile on scaled compressor and turbine component maps are shown in Figure 4.4 through 4.8. Since the *Bodie* maneuver does not allow time for the carcass to thermally soak at the low speed which results in transient operation closer to the stall line than normal acceleration[63], the separation between the acceleration and deceleration is expected to be larger than if the heat soak dynamics were included. The simulation is done using the NPSS model at selected operating conditions.

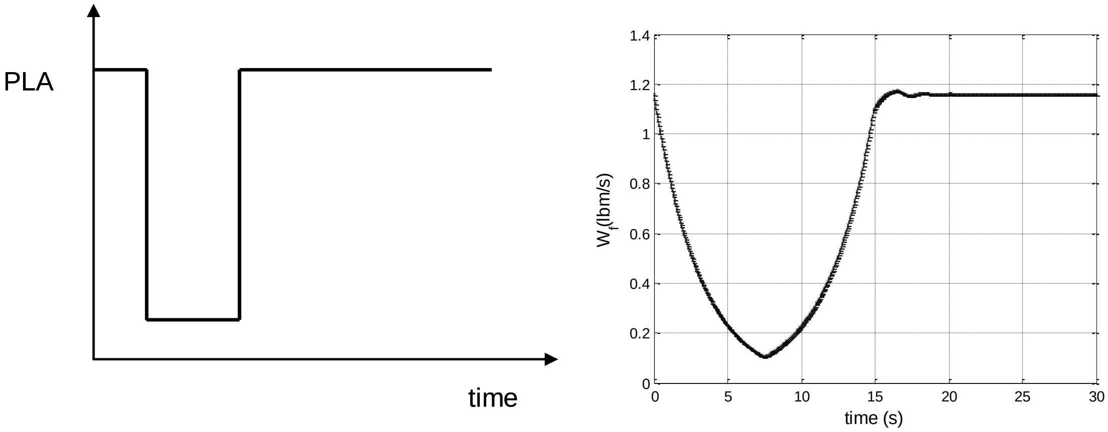

Figure 4.3 (a)Power lever angle as function of time during *Bodie* maneuver (b) fuel input during *Bodie* maneuver

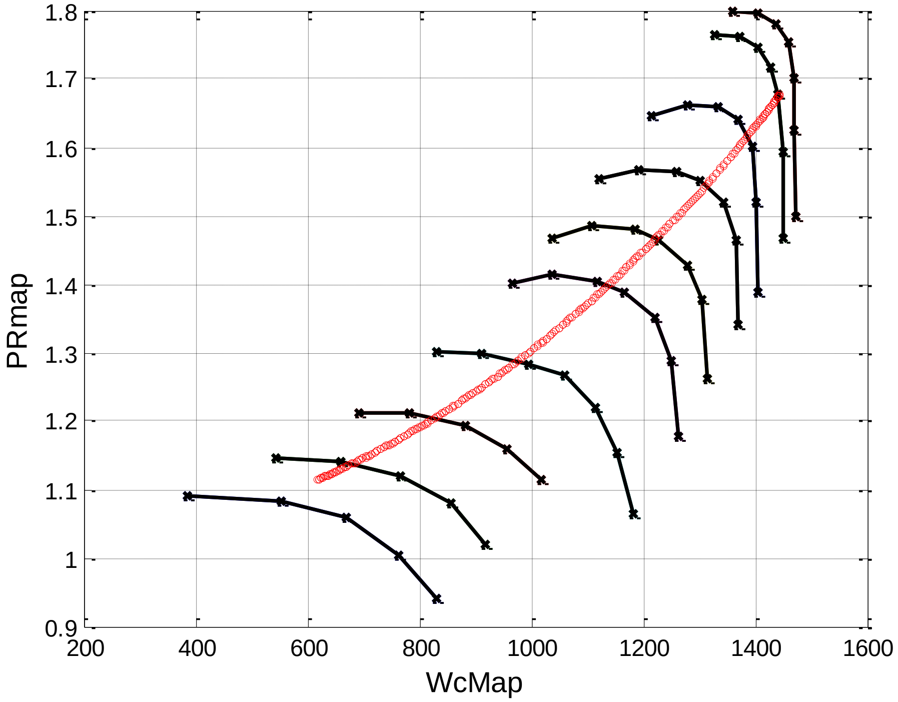

Figure 4.4 *Bodie* trajectory on Fan map (scaled)

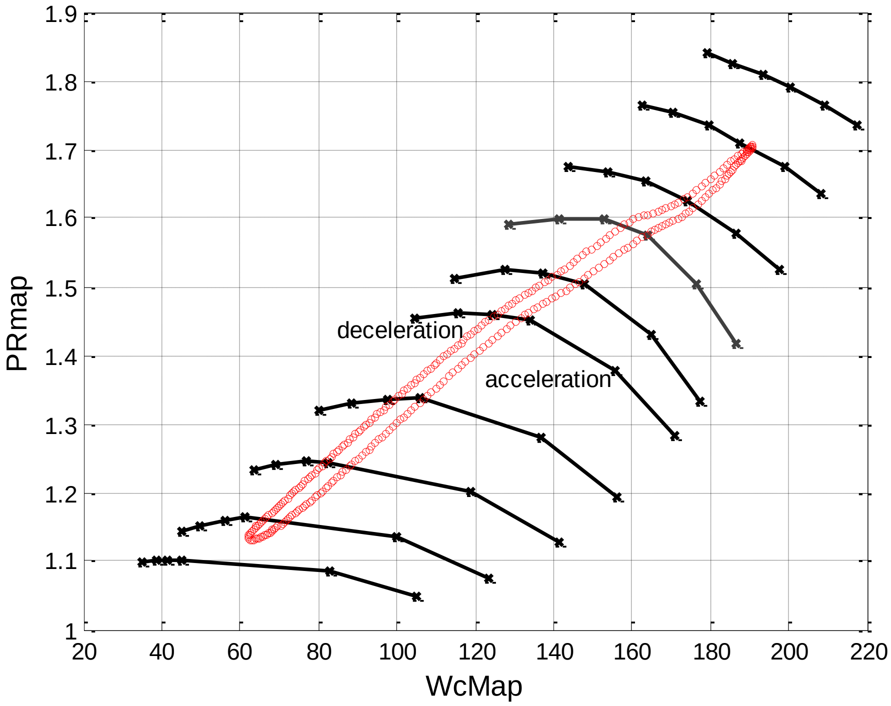

Figure 4.5 *Bodie* trajectory on LPC map (scaled)

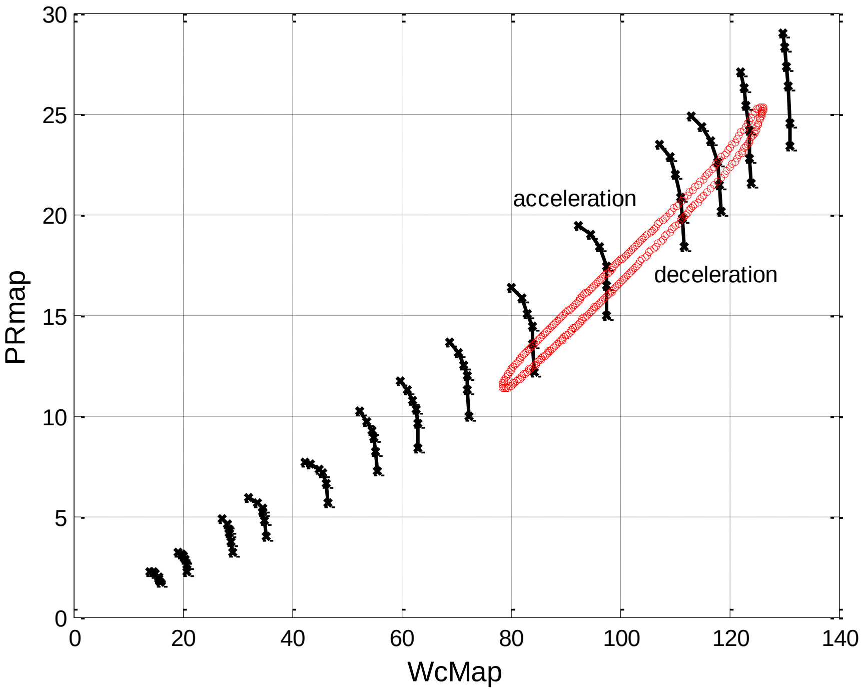

Figure 4.6 *Bodie* trajectory on HPC map (scaled)

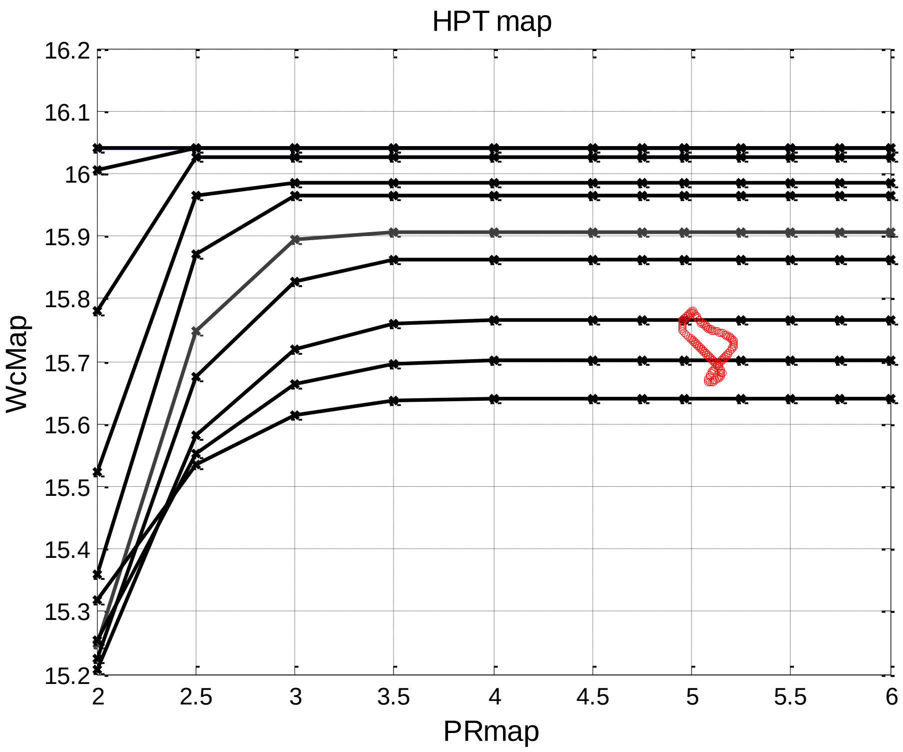

Figure 4.7 *Bodie* trajectory on HPT map (scaled)

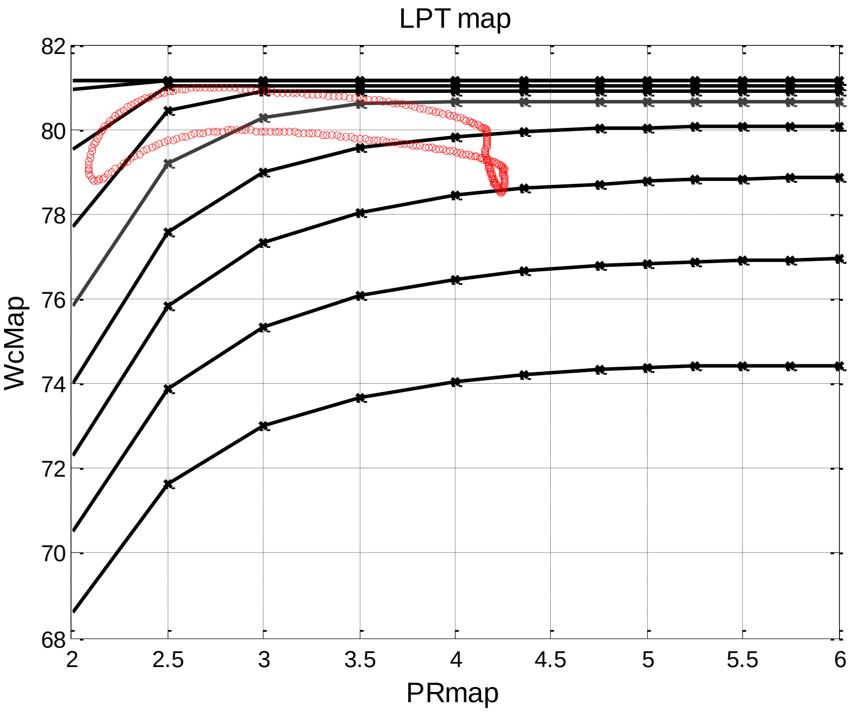

Figure 4.8 *Bodie* trajectory on LPT map (scaled)

4.1.7 Controller Description

The turbofan simulation includes a simple controller that converts the Power Lever Angle (PLA) command to fuel input while providing limit regulations. The controller architecture is shown in Figure 4.9. The PLA command is translated into the corresponding fan speed using the table look up. The error between desired fan speed and the actual fan speed is used to compute the incremental change in fuel flow rate to meet the demanded fan speed. This is integrated with a limit regulator to prevent the HPT inlet temperature and the fan speed from going over the design limits. The control logic selects the minimum of fuel increments calculated independently by each one of limit regulators. In addition, control logic is implemented to limit acceleration and deceleration rate of the fuel to avoid compressor stall. The controller is used only to provide reasonable fuel input to the engine in simulation and is not optimized in this study.

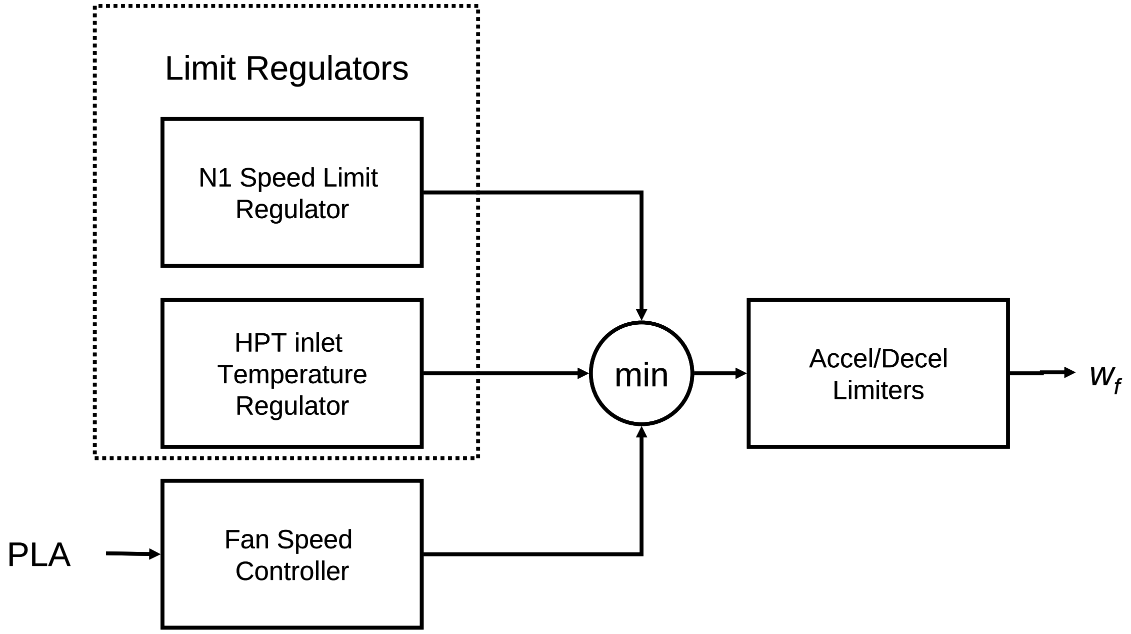

Figure 4.9 Diagram of an engine control system

4.2 Validation Method

Different model applications require different validation metrics. Three different metrics are selected to validate the model and to measure fidelity of the model from different perspectives. While time domain validation gives good qualitative measure, the interpretation of results in terms of control synthesis is difficult. The normalized additive uncertainty and the ν−gap metric compensate for this shortcoming by providing the modeling error in terms of the robust control synthesis problem. The normalized additive uncertainty captures the maximum error that occurs in the whole frequency spectrum in an open loop while the ν−gap metric measures the maximum error in a closed loop response.

4.2.1 Time Domain Validation

4.2.1.1 Component Level Validation

Each component is represented by sets of algebraic expressions and no dynamic equations are involved since all fast dynamics states are residualized. Thus, only time domain validation is processed for the component level validation. The difference between the nonlinear responses and the linear estimations are computed and normalized using the maximum change in nonlinear response per time step to calculate the error as shown in equation (4.4).

$$error = \frac{\delta y_{NL} - \delta y_{AL}}{\delta y_{NL_{\max}}} \tag{4.4}$$

4.2.1.2 Integrated System Fidelity Measure

The time domain response comparison immediately reveals the qualitative similarity/dissimilarity of the trend between two different models. To represent the error in single quantity, the model error is quantified using the standard root mean squared error (RMSE) over a specific trajectory.

$$RMSE = \sqrt{\frac{1}{n}\sum_{i=1}^{n}(y_{0i} - y_{1i})^2} \tag{4.5}$$

Here, y_0 represents the results from the truth model and y_1 represents the model to be validated. The RMSE can be normalized using the maximum change over a single time step as shown in equation (4.6) where NRMSE represents normalized root mean squared error.

$$NRMSE = \frac{1}{(y_{\max} - y_{\min})}\sqrt{\frac{1}{n}\sum_{i=1}^{n}(y_{0i} - y_{1i})^2} \tag{4.6}$$

There are multiple outputs in the model. The weighted sum of RMSE of useful outputs can be used to determine the model uncertainty as follows if desired weights are known.

$$NRMSE_{weighted} = \sum_{j=1}^{p} w_j \frac{1}{(y_{j\max} - y_{j\min})}\left[\frac{1}{n}\sqrt{\sum_{i=1}^{n}(y_{0i} - y_{1i})^2}\right] \tag{4.7}$$

$$\text{where } \sum_{j=1}^{p} w_j = 1$$

In this thesis, un-weighted NRMSE is used since the desired weight is unknown. The weight selection is part of the controller synthesis and depends greatly on the controller requirement. The actual value from the nonlinear simulation is used for the truth model; therefore, the NRMSE captures error due to nonlinearity as well as the modeling error.

4.2.2 Robust Control Essentials

4.2.2.1 Performance Specifications [38,64,65]

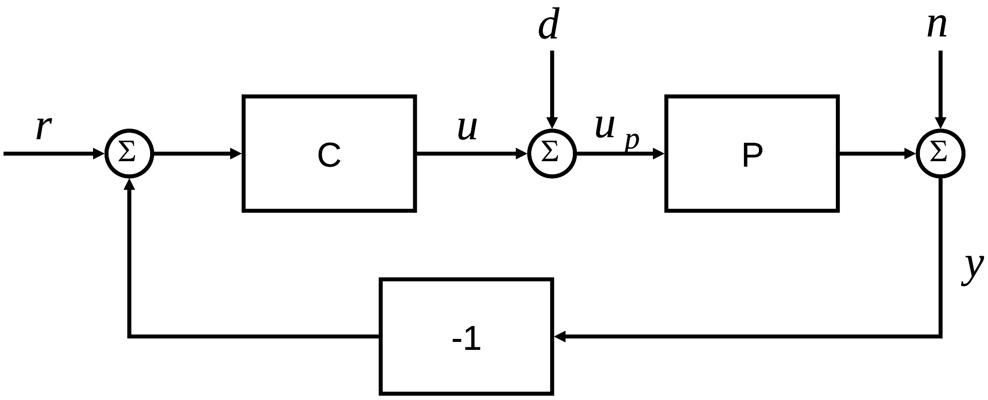

Figure 4.10 Feedback configuration

The standard configuration for the feedback system is shown in Figure 4.10. The relations between output, reference signal, disturbances and noises are given by equation (4.8).

$$\begin{bmatrix} \mathbf{y} \\ \mathbf{e} \\ \mathbf{u} \\ \mathbf{u_p} \end{bmatrix} = \begin{bmatrix} \mathbf{PC(I+PC)^{-1}} & \mathbf{(I+PC)^{-1}P} & \mathbf{(I+PC)^{-1}} \\ \mathbf{(I+PC)^{-1}} & -\mathbf{(I+PC)^{-1}P} & -\mathbf{(I+PC)^{-1}} \\ \mathbf{C(I+PC)^{-1}} & -\mathbf{CP(I+CP)^{-1}} & -\mathbf{C(I+PC)^{-1}} \\ \mathbf{C(I+PC)^{-1}} & \mathbf{(I+CP)^{-1}} & -\mathbf{C(I+PC)^{-1}} \end{bmatrix} \begin{bmatrix} \mathbf{r} \\ \mathbf{d} \\ \mathbf{n} \end{bmatrix} \tag{4.8}$$

Of all transfer matrices described above, the following transfer matrix describes how the system reacts to load disturbances and the measurement noise [2].

$$\bar{\sigma}\left((\mathbf{I}+\mathbf{PC})^{-1}\right)\ \bar{\sigma}\left((\mathbf{I}+\mathbf{CP})^{-1}\right) \quad \text{(output) sensitivity matrix, (input) sensitivity matrix} \tag{4.9}$$

$$\bar{\sigma}\left((\mathbf{I}+\mathbf{PC})^{-1}\mathbf{P}\right) \quad \text{load sensitivity matrix} \tag{4.10}$$

$$\bar{\sigma}\left(\mathbf{C}(\mathbf{I}+\mathbf{CP})^{-1}\right) \qquad \text{noise sensitivity matrix} \tag{4.11}$$

$$\bar{\sigma}\left(\mathbf{PC}(\mathbf{I}+\mathbf{PC})^{-1}\right) \qquad \text{complementary sensitivity matrix} \tag{4.12}$$

Good performance requires that following values to be small particularly in a low frequency range

$$\bar{\sigma}\left((\mathbf{I}+\mathbf{PC})^{-1}\right),\ \bar{\sigma}\left((\mathbf{I}+\mathbf{PC})^{-1}\mathbf{P}\right),\ \bar{\sigma}\left((\mathbf{I}+\mathbf{CP})^{-1}\right),\ \bar{\sigma}\left(\mathbf{C}(\mathbf{I}+\mathbf{CP})^{-1}\right) \tag{4.13}$$

Good robustness requires that following to be small particularly in a high frequency range.

$$\bar{\sigma}\left(\mathbf{PC}(\mathbf{I}+\mathbf{PC})^{-1}\right),\ \bar{\sigma}\left(\mathbf{CP}(\mathbf{I}+\mathbf{CP})^{-1}\right) \tag{4.14}$$

At frequencies such that $\underline{\sigma}(\mathbf{PC}) >> 1$ or $\underline{\sigma}(\mathbf{CP}) >> 1$, the following are true.

$$\bar{\sigma}((\mathbf{I}+\mathbf{PC})^{-1}\mathbf{P}) \approx \bar{\sigma}(\mathbf{C}^{-1}) = \frac{1}{\underline{\sigma}(\mathbf{C})} \tag{4.15}$$

$$\bar{\sigma}((\mathbf{I}+\mathbf{PC})^{-1}) \approx \bar{\sigma}((\mathbf{PC})^{-1}) = \frac{1}{\underline{\sigma}(\mathbf{PC})} \tag{4.16}$$

$$\bar{\sigma}(\mathbf{C}(\mathbf{I}+\mathbf{PC})^{-1}) \approx \bar{\sigma}(\mathbf{P}^{-1}) = \frac{1}{\underline{\sigma}(\mathbf{P})} \tag{4.17}$$

If $\bar{\sigma}(\mathbf{PC}) << 1$, then

$$\bar{\sigma}(\mathbf{C}(\mathbf{I}+\mathbf{PC})^{-1}) \approx \bar{\sigma}(\mathbf{C}) \tag{4.18}$$

$$\bar{\sigma}(\mathbf{PC}(\mathbf{I}+\mathbf{PC})^{-1}) \approx \bar{\sigma}(\mathbf{PC}) \tag{4.19}$$

Equations (4.15)-(4.19) suggest that the desired closed loop behavior can be achieved by manipulation of the open loop gains $\bar{\sigma}(\mathbf{PC}), \underline{\sigma}(\mathbf{PC})$ [38]. Hence, the requirement for achieving good robust stability and performance translates to the open loop requirement of achieving

$$\underline{\sigma}(\mathbf{PC}) \gg 1, \underline{\sigma}(\mathbf{CP}) \gg 1,\ \underline{\sigma}(\mathbf{C}) \gg 1$$

in some high frequency range for achieving good performance and

$$\overline{\sigma}(\mathbf{PC}) \ll 1,\ \overline{\sigma}(\mathbf{CP}) \ll 1,\ \overline{\sigma}(\mathbf{C}) \ll M$$

in some low frequency range where M is not too large for achieving good robustness.

Robust stability and performance is defined by Zhou et al as following:

Definition 4.1 **[65]**

Suppose the nominal plant, $P_1 \in \Pi$*, where* Π *is an uncertainty model set and K is the resulting controller which stabilizes the nominal plant* P_1 *for a set of performance objective. Then the closed-loop feedback system is said to have robust stability if K internally stabilizes every plant belong to* Π*. The closed loop feedback system is said to have robust performance if the performance objectives are satisfied for every plant belong to* Π*.*

Definition 4.1 is valid under different assumptions on the uncertainty set Π. For example, it is defined as $\prod = \{P + W_1 \Delta W_2 : \Delta \in \Re \mathrm{H}_\infty\}$ for the additive uncertainty.

4.2.2.2 H_∞ Loop Shaping

The H_∞ loop shaping design procedure introduced by McFarlane and Glover [38] is described in this section. This design procedure guarantees closed-loop stability and a level of robust stability at all frequencies while obtaining performance/robust stability tradeoffs described in previous section. The loop shaping is achieved in three main steps as shown in Figure 4.11.

1. First, the precompensator, W_1 and/or postcompensator, W_2 are applied so the nominal plant is in a desired shape. The shaped plant P_s is shown in the dashed line in Figure 4.11.
2. Calculate b_{max} where

$$\begin{aligned} b_{\max} &= \left(\inf_{C stabilizing} \left\| \begin{bmatrix} I \\ C \end{bmatrix} (I + P_s C)^{-1} \tilde{M}_s^{-1} \right\|_\infty \right)^{-1} \\ &= \sqrt{1 - \left\| \begin{bmatrix} \tilde{N}_s & \tilde{M}_s \end{bmatrix} \right\|_H^2} < 1 \end{aligned} \tag{4.20}$$

Here $\tilde{N}_s, \tilde{M}_s$ are the normalized coprime factors of P_s. If $b_{max} << 1$, then adjust W_1 and W_2 in step 1. Select $b \leq b_{max,}$ and synthesize C_∞ which satisfies the following

$$\left\| \begin{bmatrix} I \\ C_\infty \end{bmatrix} (I + P_s C_\infty)^{-1} \tilde{M}_s^{-1} \right\|_\infty \leq b^{-1} \tag{4.21}$$

3. The feedback controller is given by following.

$$C = W_1 C_\infty W_2 \tag{4.22}$$

Note that the generalized stability margin b can also be written as

$$b_{P,C} := \begin{cases} \left\| \begin{bmatrix} I \\ P \end{bmatrix} (I + PC)^{-1} [P] \right\|_\infty^{-1}, & \text{if } [P,C] \text{ is stable} \\ 0, & \text{otherwise} \end{cases}$$

Maximizing the generalized stability margin can be seen as the minimization of the H infinity norm of the closed loop sensitivity and complementary sensitivity functions. The following theorem relates the generalized stability margin to the well-known gain margin and phase margin parameters.

Theorem 4.1[60]

If [P,C] is stable, then $GM(P,C) \geq (1+b_{P,C})/(1-b_{P,C})$ *and* $PM(P,C) \geq 2arcsin(b_{P,C})$

The ν gap metric which will be introduced later in this chapter quantifies the model uncertainty in terms of reduction in the generalized stability margin *b*.

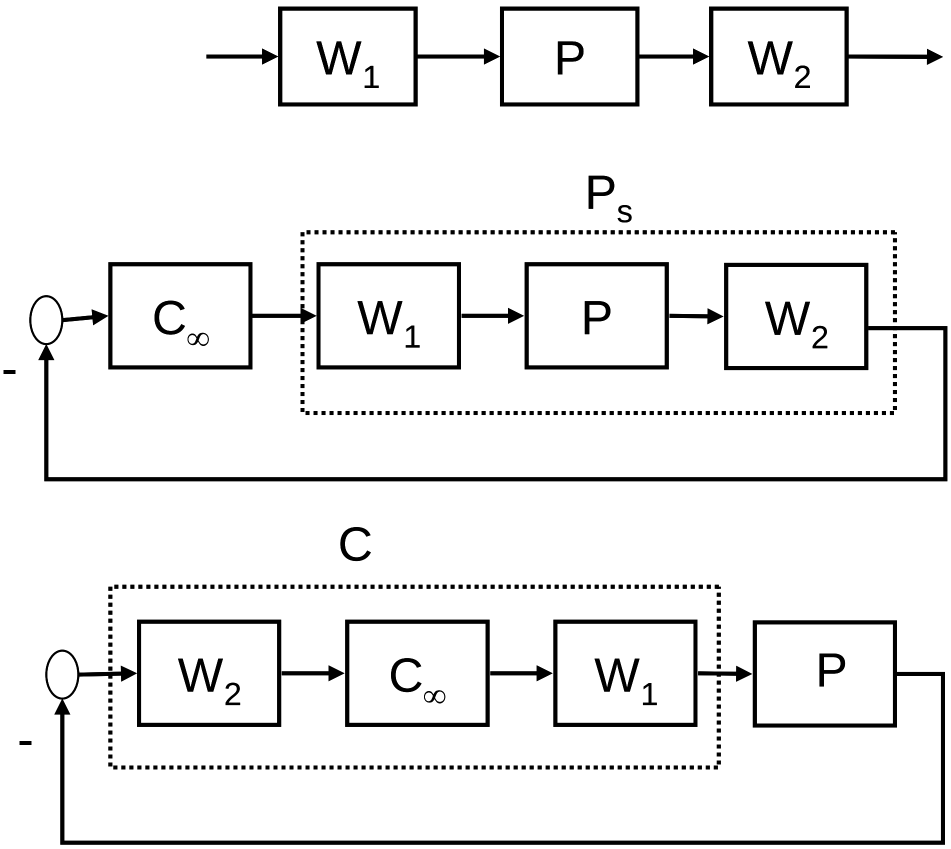

Figure 4.11 H_∞ **loop shaping [64]**

4.2.3 Normalized Additive Model Error [33,64,65]

Dynamic system modeling error can be captured in a form of plant uncertainty that includes unmodeled dynamics and poorly known system parameters as shown in Figure 4.12. This is common representation in robust control problem.

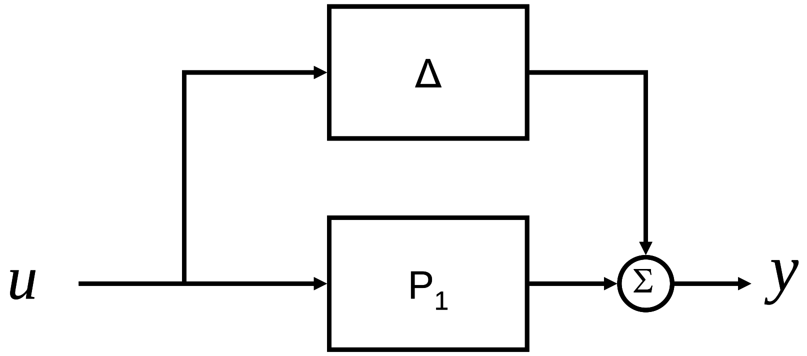

Figure 4.12 Additive uncertainty

The difference between the nominal plant P_1 and the truth model P_0 is treated as the additive model uncertainty described by equations (4.23) [33].

$$P_0(s) = P_1(s) + \Delta_a(s) \tag{4.23}$$

This additive uncertainty is measured using the H_∞ norm as shown in equation (4.24) whose measure is in the absolute value.

$$\|\Delta_a\|_\infty = \|P_0 - P_1\|_\infty \tag{4.24}$$

where the H_∞ norm of system *G(s)* is the distance in the complex plane from the origin to the farthest point on the Nyquist plot of *G(s)* [64]. H_∞ norm of the system is defined as follows.

$$\|G\|_\infty = \sup_{\omega \in R} \bar{\sigma}(G(j\omega)) \tag{4.25}$$

This term is finite only if *G* is proper and there are no poles on the right half plane. The H_∞ norm is interpreted as the peak of the frequency response.

The additive uncertainty representation is practical in a robust stabilization problem, and normalization of this measure provides better understanding of model fidelity between different models. The additive uncertainty is normalized with the H_∞ norm of the true plant as shown in (4.26) for comparing uncertainties of different approximated linearized models.

$$\frac{\|\Delta_a\|_\infty}{\|P_0\|_\infty} = \frac{\|P_0 - P_1\|_\infty}{\|P_0\|_\infty} \tag{4.26}$$

$$\|\Delta_m\|_\infty = \frac{\|P_0 - P_1\|_\infty}{\|P_1\|_\infty} \tag{4.27}$$

The normalized additive uncertainty is utilized instead of the conventional multiplicative uncertainty shown in equation (4.27). The difference is that the normalized additive uncertainty is normalized with the true system instead of the nominal model. This approach is taken for fair comparison of the different modeling approach (where nominal model changes but the truth model is the same. Both errors are normalized with the same value). The true system is known unlike conventional robust control problem where only nominal model is provided. Moreover, the quantification of the error is the objective here rather than designing robust controller for unknown truth plant; therefore, the definition is taken from a different context. The following theorem relates the additive uncertainty to the robust stability problem.

Theorem 4.2 [64]

Let $\prod = \{P + W_1 \Delta W_2 : \Delta \in \Re \mathrm{H}_\infty\}$ *and let K be a stabilizing controller for the nominal plant P. Then the closed-loop system is well-posed and internally stable for all* $\|\Delta\|_\infty < 1$ *if and only if* $\left\| W_2 K (I + PK)^{-1} W_1 \right\|_\infty \le 1$.

The proof utilizing the small gain theorem is given in [64].

4.2.4 The [nu]-Gap Metric [59,60,64]

4.2.4.1 Rationale

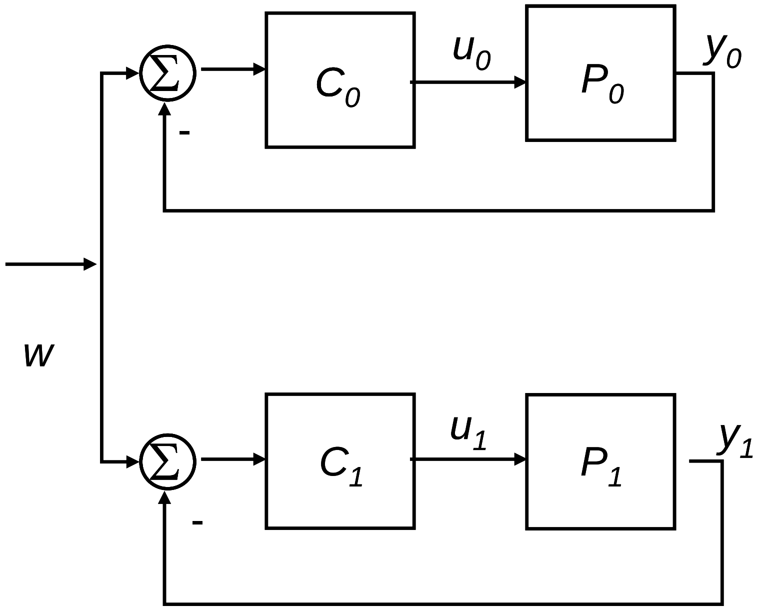

Figure 4.13 Closed loop model uncertainty [59]

The gap metric numerically assesses the model accuracy in terms of close loop controller performance. The gap metric quantifies a distance between two dynamical systems. The concept of the gap metric was first introduced by El-Sakkary to compute the gap between two closed operators [15]. Benefits of the gap metric include its ability to measure the distances between two unstable systems and a symmetry property under operator inversion[59]. The gap metric does not measure the difference between two open loop systems; rather it measures a distance between two closed loop systems. Time domain response analysis described in the previous section validates the open loop response of the linear model against the nonlinear model. A detailed analysis of the gap metric measure in the interest of the controller design will be carried out for the closed loop response comparison.

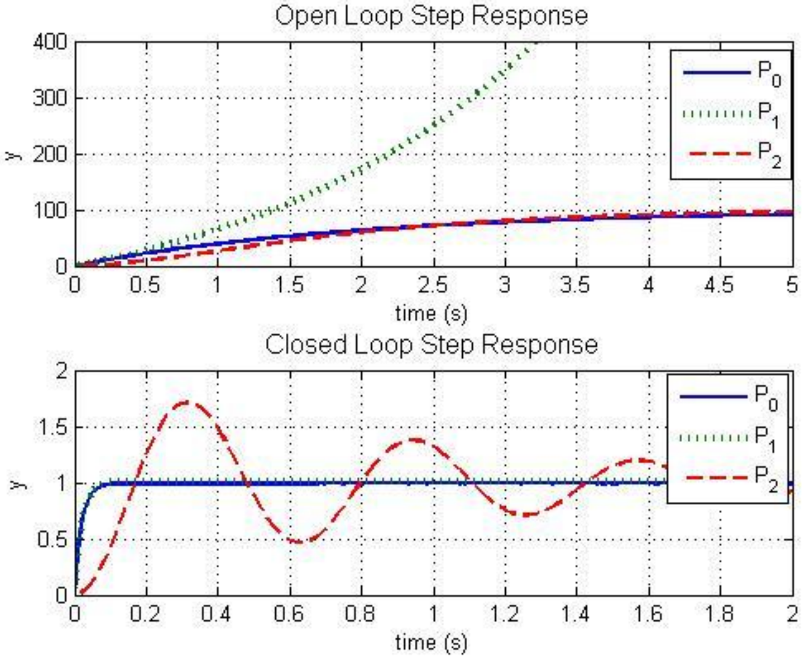

Figure 4.14 a) Open loop step responses b) closed loop step responses [59]

Vinnicombe has illustrated the importance of measuring distance between two closed loop systems using the following example [59]. Consider three systems as follows:

$$\begin{aligned} P_0 &= \frac{100}{2s+1} \\ P_1 &= \frac{100}{2s-1} \\ P_2 &= \frac{100}{(s+1)^2} \end{aligned} \tag{4.28}$$

Open loop system responses to the step command are shown in Figure 4.14 a). System P_0, and P_2 have similar responses while system P_1 exhibits very different open loop response to the step command. However, when each system is closed with the unity feedback controller, system P_1 behaves similar to P_0 and P_2 exhibits very different closed loop step response. The ν-gap metric between system P_0 and P_1 is a small value of 0.02 and ν-gap metric between P_0 and P_2 is a large value of 0.898. This illustrates the importance of measuring system distance under the closed loop performance from the controller design perspective.

4.2.4.2 The [nu]– gap metric definition [59,60]

A metric on a space $\mathcal{S}$ satisfies following properties.

1. $\delta(x,y) = \delta(y,x)$
2. $\delta(x,y) = 0$ *if and only if x=y.*
3. $\delta(x,y) \geq 0$ *for all x,y in* $\mathcal{S}$.
4. $\delta(x,y) \leq \delta(x.,z) + \delta(z,y)$ *for all x,y in* $\mathcal{S}$.

The gap metric and ν-gap metric is a metric and therefore satisfies the above axioms.

Definition 4.2 [15,59]:

The gap between two closed operators K_1 and K_2 in a Hilbert space H is defined as the gap between their graphs viewed as closed subspaces of the Hilbert space H x H, i.e.,,

$$\delta(P_1, P_2) = \max\left\{\vec{\delta}(P_1, P_2), \vec{\delta}(P_2, P_1)\right\}$$

where

$$\vec{\delta}(P_1, P_2) := \sup_{\begin{bmatrix} u_1 \\ y_1 \end{bmatrix} \in G_1} \inf_{\begin{bmatrix} u_2 \\ y_2 \end{bmatrix} \in G_2} \frac{\left\| \begin{bmatrix} y_1 \\ u_1 \end{bmatrix} - \begin{bmatrix} y_2 \\ u_2 \end{bmatrix} \right\|_2}{\left\| \begin{bmatrix} y_1 \\ u_1 \end{bmatrix} \right\|_2}$$

Note that the gap metric by El-Sakkary is defined as the gap between H_2 graph spaces. Later Vinnicombe proposed a new definition of gap metric using L_2 space with the winding number condition shown in definition 2 [19,52,59]. The winding number is defined as follows:

Definition 4.3 [64]

Let g(s) be a scalar transfer function and let Γ denote a Nyquist contour indented around the right of any imaginary axis poles of g(s). Then the winding number of g(s) with respect to this contour, denoted by wno(g) is the number of counterclockwise encirclement around the origin by g(s) evaluated on the Nyquist contour Γ.

Cauchy's argument principle

Let f(s) be an analytic function along the contour Γ in the complex plane. Then

N=Z-P

where N= number of positive encirclements of the origin

Z= number of zeros of f(s) inside Γ

P=number of poles of f(s) inside Γ.

Using the Cauchy's argument principle stated above, the winding number can be computed as follows:

$$wno\,(g(s)) = \mathrm{Z}(g) - \eta(g)$$
$$\mathrm{Z}(g) = \text{number of open RHP zeros of } g(s)$$
$$\eta(g) = \text{number of open RHP poles of } g(s)$$

It is also true that, for a square, non-singular, real rational transfer function matrix *G(s)* the following is true.

$$wno\,(\det \mathrm{G}(s)) = \mathrm{Z}(G) - \eta(G)$$

Graph symbols *G* and $\tilde{G}$ denote normalized right and left graph symbols for P_i and are defined as follows:

$$G_i := \begin{bmatrix} N_i \\ M_i \end{bmatrix}, \tilde{G}_i := \begin{bmatrix} -\tilde{M}_i & \tilde{N}_i \end{bmatrix}$$

where M_i, and N_i are normalized right co-prime factorization. The Vinnicombe metric also known as *v*-gap metric is defined as follows:

Definition 4.4[59]*:*

$$\delta_\nu(P_1,P_2) := \begin{cases} \left\| \tilde{G}_2 G_1 \right\|_\infty & \text{if } \det(\tilde{G}_2 G_1)(j\omega) \neq 0 \forall \omega \in (-\infty,\infty) \\ & \text{and } wno\det(G_2^* G_1) = 0 \\ 1 & \text{otherwise} \end{cases}$$

$$= \inf_{\substack{Q,Q^{-1}\in L_\infty \\ wno\det(Q)=0}} \left\| G_1 - G_2 Q \right\|_\infty$$

$$= \inf_{\substack{Q,Q^{-1}\in L_\infty \\ wno\det(Q)=0}} \left\| \begin{matrix} G_2^* G_1 - Q \\ \tilde{G}_2 G_1 \end{matrix} \right\|_\infty$$

It can also be written as follows:

Definition 4.5[59]*:*

$$\delta_\nu(P_0,P_1) := \begin{cases} \left\| (I + P_1 P_1^*)^{-1/2} (P_1 - P_0)(I + P_0^* P_0)^{-1/2} \right\|_\infty \\ \quad \text{if } \det(I + P_1^* P_0)(j\omega) \neq 0 \forall \omega \in (-\infty,\infty) \\ \quad \text{and } wno\det(I + P_1^* P_0) + \eta(P_0) - \eta(P_1) - \eta_0(P_1) = 0 \\ 1 \quad \text{otherwise} \end{cases}$$

The ν-gap metric is the smallest metric that holds the following two statements:

> ***RS1***[59]***:*** *Given a nominal plant* $P_1 \in \mathscr{R}^{pxq}$ *, a compensator* $C \in \mathscr{R}^{pxq}$ *and a number* β*, then:*
>
> *[P$_2$,C] is stable for all plants, P$_2$, satisfying* $\delta_\nu(P_1,P_2) \le \beta$ *if, and only if,* $b_{P_1,C} > \beta$.
>
> ***RS2***[59]***:*** *Given a nominal plant P$_1$, a perturbed plant P$_2$,* $\in \mathscr{R}^{pxq}$ *and a number* $\beta < b_{opt}(P_1)$ *then:*

[P₂,C] is stable for all compensators, C, satisfying $b_{P_1,C} > \beta$ *if, and only if,* $\delta_\nu(P_1,P_2) \le \beta$,

where $b_{opt}(P_1) := \sup_C b_{P,C}$

The first statement states that any plant distanced less than β from the nominal plant P_1, is stabilized by any compensator stabilizing the nominal plant P_1, with the stability margin that is at least β. The second statement states that if a plant P_2, is distanced from the nominal plant by δ_ν that is greater than β, then there exist some compensator C stabilizing a nominal plant with stability margin β, which destabilizes P_2. The general stability margin, b, defined in the previous section, is directly related to the H_∞ loop shaping procedure.

The following theorem gives useful bound to the reduction in the stability margin caused by the distance from the nominal plant.

Theorem 4.3[59]

For any P_0, P_1, C,

$$\arcsin b_{P_1,C} \ge \arcsin b_{P_0,C} - \arcsin \delta_\nu(P_0,P_1)$$

The proof is given in reference[59]. The above theorem implies that a smaller gap metric results in a smaller reduction in the general stability margin.

4.2.4.3 Scaling

Each output measure can be scaled so all outputs are in the similar magnitude range of the ν-gap metric for easy comparison between different output measures. The individual outputs can either be scaled with the maximum value of possible perturbation or with the DC gain of the system with a single output. Using the DC gain of the system shown in equation (4.29), all transfer functions for individual output are scaled to magnitude of 1 and the comparison becomes more meaningful.

$$S = D - CA^{-1}B \tag{4.29}$$

$$y = \lfloor C(sI - A)^{-1}B + D \rfloor u \tag{4.30}$$

$$S^{-1}y = S^{-1}\lfloor C(sI - A)^{-1}B + D \rfloor \tag{4.31}$$

The scaled ν-gap metric is used to determine the appropriate output for the controller design. If a certain output has much larger ν-gap metric than other outputs, it is recommended to avoid that particular output for designing the controller. The scaled ν-gap metric should only be considered in terms of comparing different outputs, and should not be treated as the absolute value of controller specification as weight selection determines the loop shape and improves the ν-gap metric in the interested frequency range. Weight selection is important, but out of the scope of this thesis as the objective is not to design a controller.

4.3 Summary

In this chapter, methods for validating a linear model were discussed. An example engine model in NPSS was modified to give more realistic transient behavior to be used for the validation. The *Bodie* profile was selected for generating the largest separation between the acceleration and deceleration curve. The response in time domain was selected for validation of the component level models. Three different methods chosen for the validation of an integrated model are NRMSE, normalized additive uncertainty, and the ν-gap metric. The time domain response gives good qualitative measure and quantifies the modeling error including the nonlinearity. The normalized additive uncertainty captures the modeling error in terms of robust control problem in the open loop. Finally, the ν-gap metric captures the modeling error in the closed loop control context and provides the modeling error in terms of the well known stability measure. Three methods described above cover the model validation from different contexts and should provide basis for a comprehensive model validation.

CHAPTER 5

ASSESSMENT OF MODEL FIDELITY

In this chapter, the fidelity of the analytical linear model is assessed using the validation methods described in chapter 4. The analytical linearization method was applied to the NPSS example model for the in-depth analysis of the fidelity of the model. Furthermore, simulation results are compared to the results of a conventional piecewise linear model. The model is first validated at the component level; the validation of the integrated model follows.

5.1 Component Level Validation

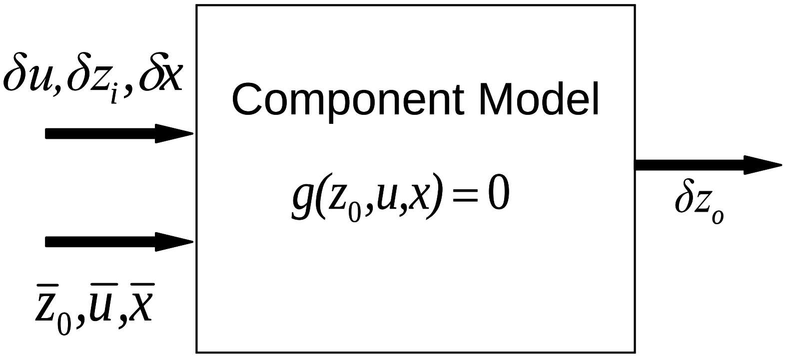

Figure 5.1 Component level linearization

Figure 5.1 represents the inputs and outputs of each component. Each component is validated using responses to a simple doublet fuel input and the *B*odie profile before the integration of component level linear models. Explicit forms of input to output relationships were described in Chapter 2. Changes in each of the component outputs are computed by evaluating inputs to the linearized functions at the current operating condition. Figure 5.1 – Figure 5.9 present simulation results of each component. Linear responses of the analytical off-equilibrium linear model are compared with nonlinear simulation results. Change in each of output parameter is plotted against time. Error is normalized with the maximum change per time step as described in chapter 4. These figures show that each component is bounded by 5% error for the doublet fuel input and 10% error for the *Bodie* maneuver. Error close to the boundary occurs only when the nonlinear simulation values themselves have discrete jumps, and stays much less than the bounds most of time. Most of discrete jumps should vanish if component maps are smoothed out. A large error of approximately 60% is observed once around 12 seconds to the primary nozzle velocity, as shown in Figure 5.8. This is due to the primary nozzle moving from subsonic flow to choked flow. The effect of this large error on the thrust and mass flow rate is minimal and can be neglected for the purpose of this study.

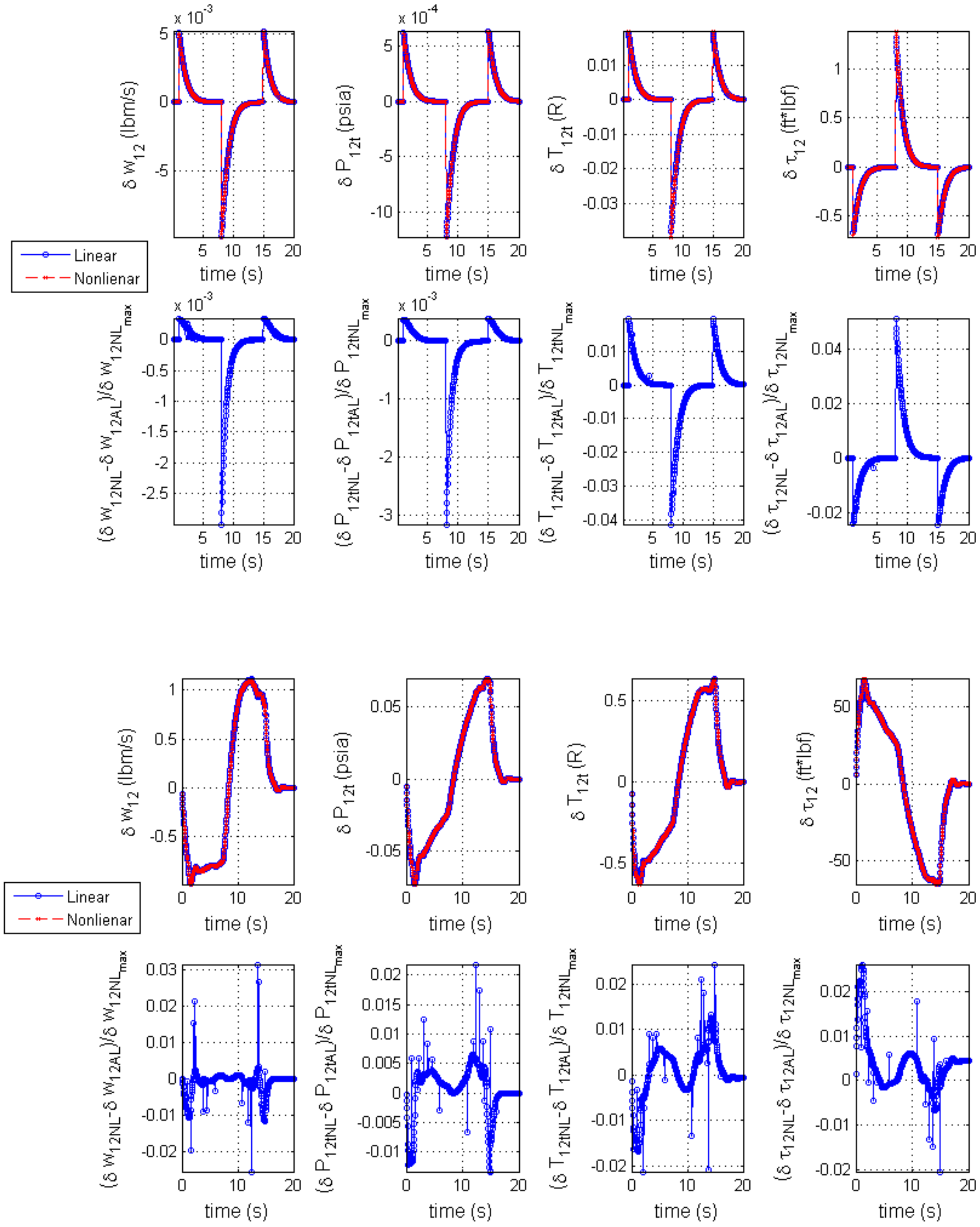

Figure 5.2 Fan validation: response to a) double fuel profile b) *Bodie* maneuver (bottom)

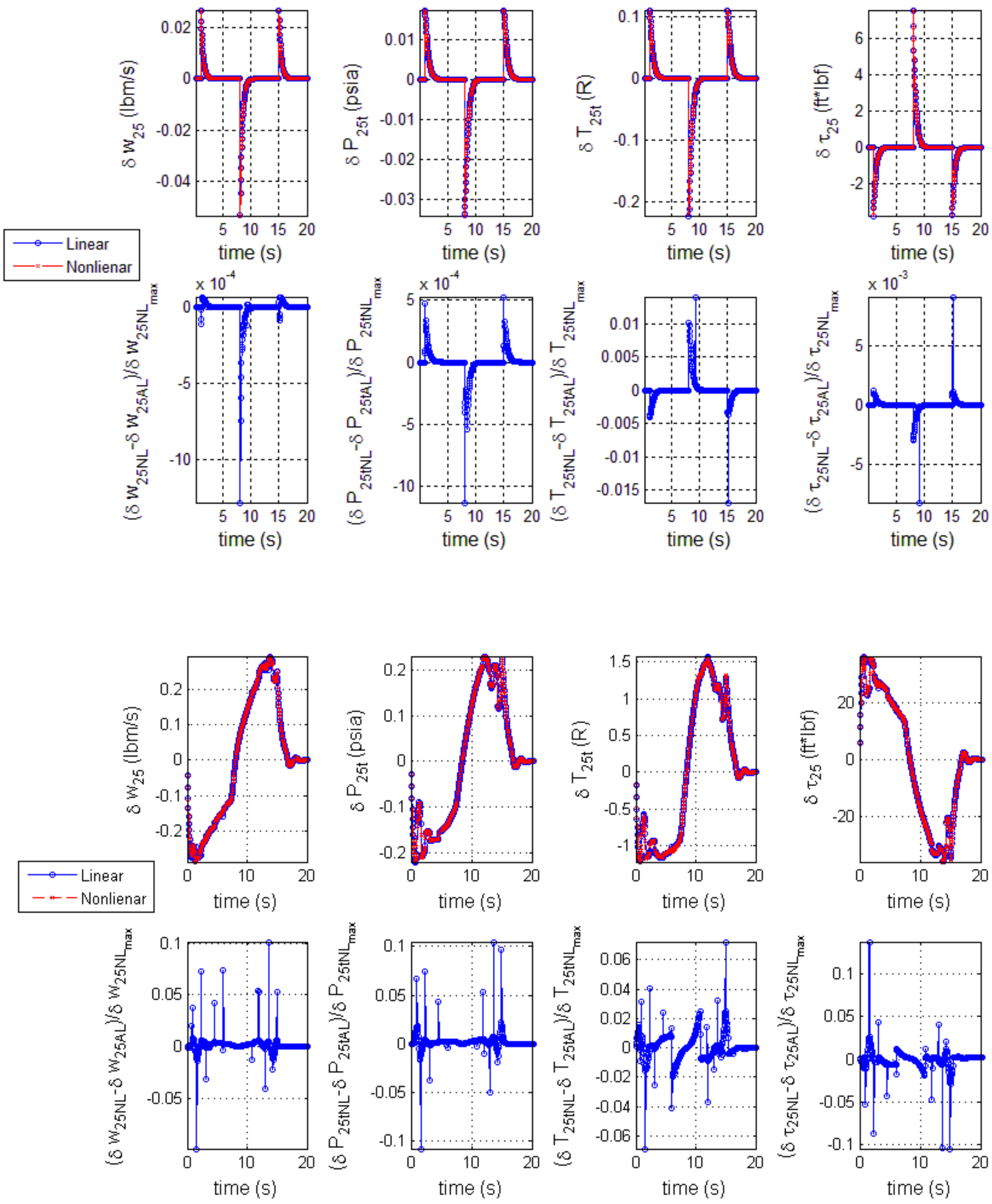

Figure 5.3 LPC validation: response to a) doublet fuel profile b) *Bodie* maneuver (bottom)

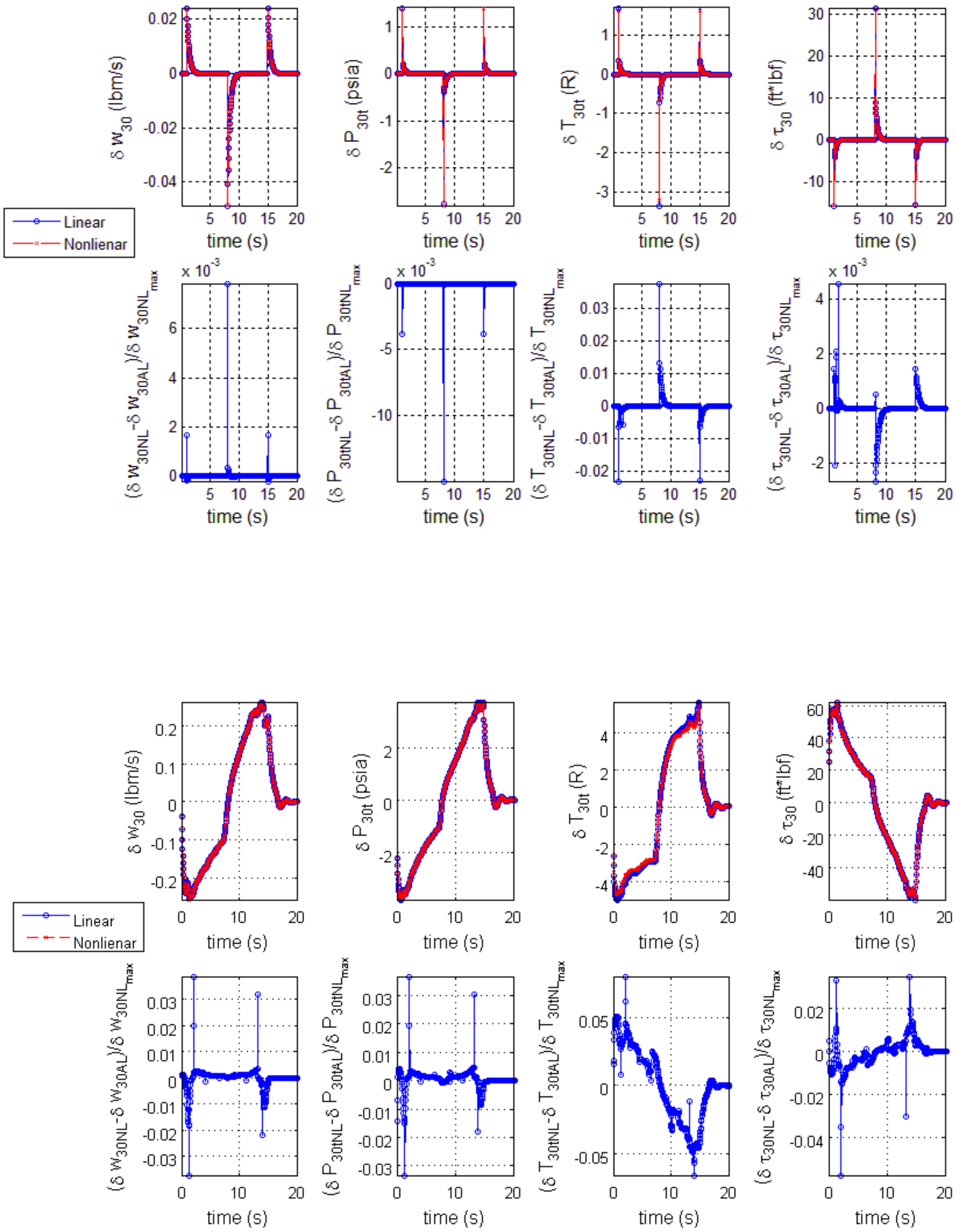

Figure 5.4 HPC Validation: response to a) doublet fuel profile b) *Bodie* maneuver (bottom)

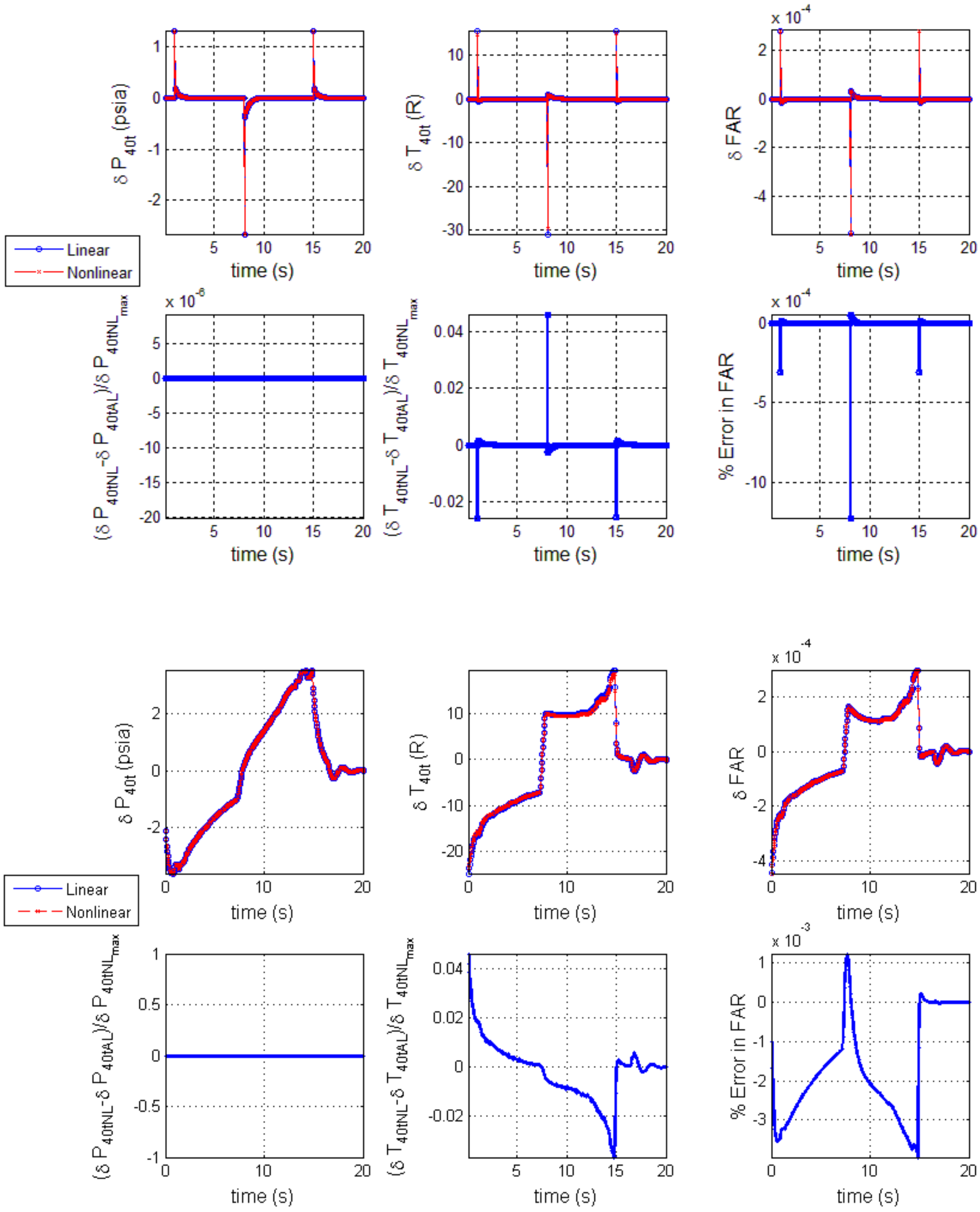

Figure 5.5 Combustor validation: response to a) doublet fuel profile b) *Bodie* maneuver (bottom)

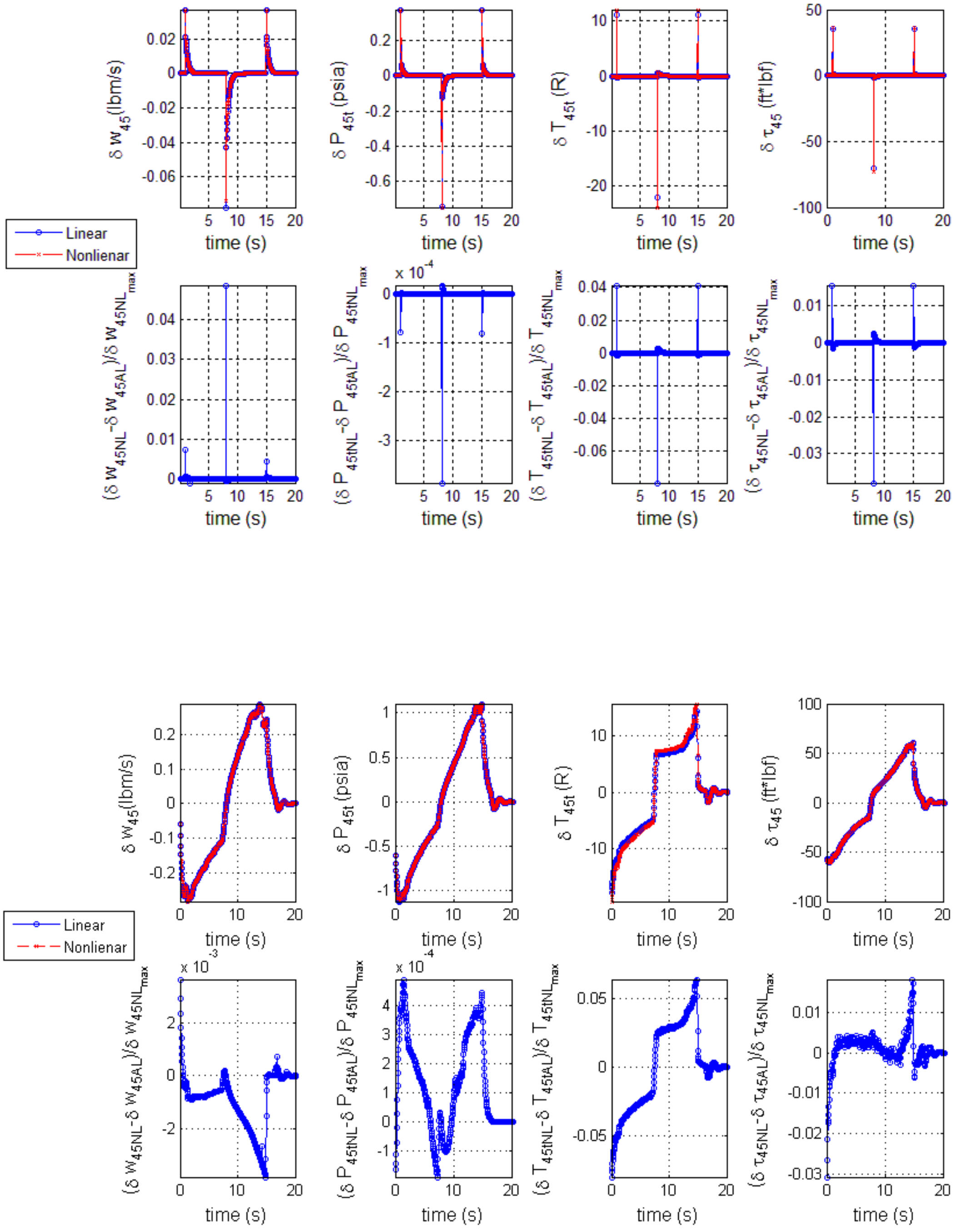

Figure 5.6 HPT validation: response to a) doublet fuel profile b) *Bodie* maneuver (bottom)

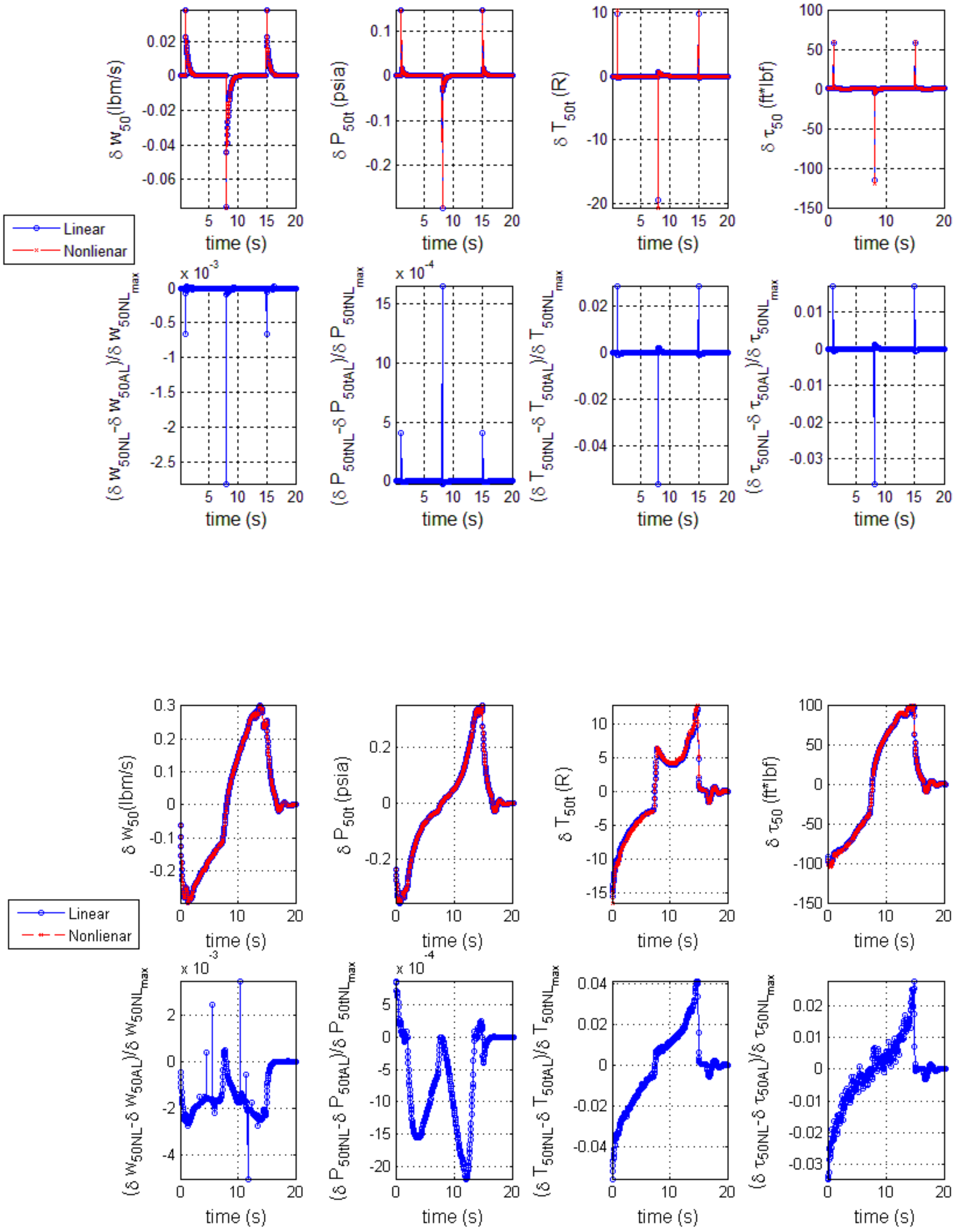

Figure 5.7 LPT validation: response to a) doublet fuel profile b) *Bodie* maneuver (bottom)

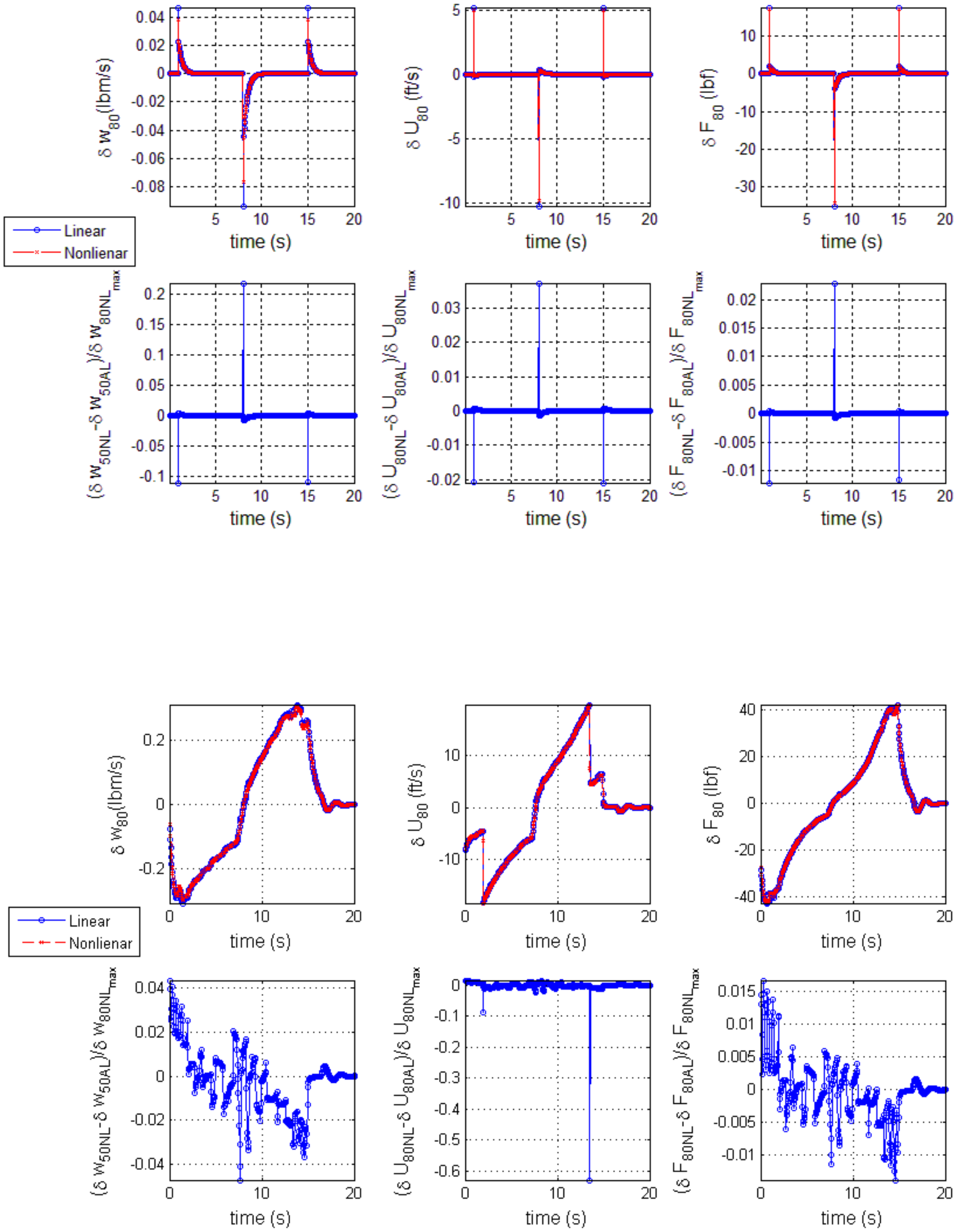

Figure 5.8 Primary nozzle validation: response to a) doublet fuel profile b) *Bodie* maneuver (bottom)

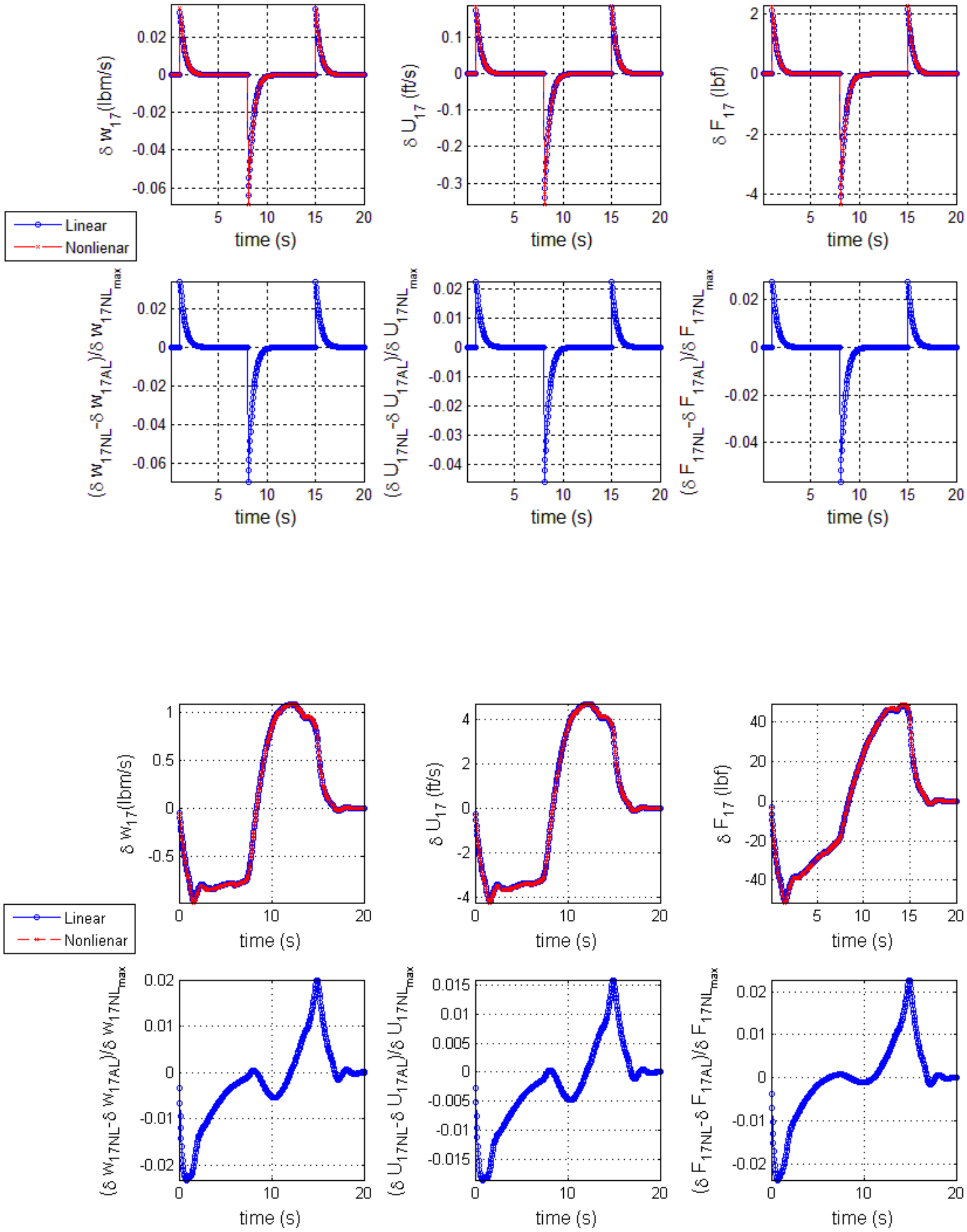

Figure 5.9 Secondary nozzle validation: response to a) doublet fuel profile b) *Bodie* maneuver (bottom)

5.2 Integrated Model

5.2.1 Steady-state Operation

After each component level linear model is validated, all component level linear models are integrated to form a full analytical linear model. In this section, the fidelity of an analytical linear model is evaluated during steady-state operation. Normalized additive uncertainty and the ν-gap metric for different outputs at the selected power levels at sea-level static condition is given in Table 5.1. The normalized additive uncertainty is bounded by 0.063 and the ν-gap metric is bounded by 0.026. Although strong correlations between the normalized additive uncertainty and the ν-gap metric are not necessary as the former measures the error in open loop system response while the latter measures the error in closed loop system response, they exhibit qualitatively similar trends in this particular flight condition.

Table 5.1 Validation of linear model at steady-state operation at sea-level static

PLA	N_1	N_2	W_f	**Normalized additive uncertainty (N_1)**	**Normalized additive uncertainty (N_2)**	**ν-gap metric (N_1)**	**ν-gap metric (N_2)**
50	3779.1	9790.3	1.1604	0.0079	**0.0525**	0.0086	0.0210
40	3401.2	9373.3	0.7985	0.0112	0.0370	0.00121	0.0132
30	3149.3	9116.2	0.5805	0.0203	0.0135	0.0152	0.0060
20	2897.3	8865.6	0.4344	0.0082	0.0375	0.0134	0.0150
10	2645.4	8631.2	0.3318	0.0164	0.0626	0.0188	0.0099
0	2393.4	8421.4	0.2574	0.0076	0.0449	0.012	0.0138
-10	2141.5	8223	0.2019	0.0139	0.0215	**0.0254**	0.0085
-20	1889.6	8020.1	0.1579	0.0039	0.0231	0.0063	0.0101

Table 5.2 Validation of linear model at steady-state operation at alt=25000ft, dTs=20°R, M=0.5

PLA	N_1	N_2	W_f	**Normalized additive uncertainty (N_1)**	**Normalized additive uncertainty (N_2)**	**ν-gap metric (N_1)**	**ν-gap metric (N_2)**
50	3605.1	9264.3	0.4466	0.0136	**0.0484**	0.00063	0.0209
40	3244.6	8943.0	0.3253	0.0168	0.0281	0.0123	0.0173
30	3004.2	8699.8	0.2362	0.0094	0.0360	0.0032	0.0145
20	2763.9	8431.9	0.1683	0.0023	0.0290	0.0032	0.0120
10	2523.5	8190.9	0.1251	0.0376	0.0249	0.0082	0.0081
0	2283.2	7961.0	0.0921	0.0165	0.0349	0.0208	0.0097
-10	2042.9	7730.1	0.0660	0.0199	0.0321	**0.0264**	0.000759
-20	1802.5	7501.9	0.0466	0.0213	0.0419	0.0130	0.0024

Table 5.2 gives normalized additive uncertainty and ν-gap metric for different outputs at the selected power levels at an altitude of 25000ft, Mach number of 0.5, and +20°R from the standard day temperature. This flight condition is selected to give a similar *Bodie* profile while away from standard day sea-level static condition. The normalized additive uncertainty is bounded by 0.05 and the ν-gap metric is bounded by 0.027. These modeling errors are within reasonable range for robust controller design. In these flight conditions, the normalized additive uncertainty for the system with output of N_2 and both ν-gap metrics show similar trends. The normalized additive uncertainty for the system with output of N_1 has a different trend, which is the lowest of all four measures and bounded by less than 0.02 in all cases, showing the least amount of variation.

The evaluation of the model fidelity during steady-state operation is significant since it measures the fidelity of the analytical linearization method. The analytical linearization method can either be used in combination with the off-equilibrium linearization or with the conventional piecewise linearization approach. The analytical linearization method can replace the conventional small perturbation method for developing a piecewise linear model. This results in only a minor reduction in fidelity while gaining flexibility and physical insights.

5.2.2 Response in Time Domain

The integrated model is validated using methods described in chapter 4. The fidelity of the analytical linear model during large transient operation is assessed using the *Bodie* maneuver in the time domain. Firstly, a qualitative assessment is made by comparing outputs of the off-equilibrium analytical linear model with the results from the nonlinear simulations. Figure 5.10 shows the change in shaft dynamics during the *Bodie* maneuver. Figure 5.11 and Figure 5.12 present the comparison between the linear estimates and the actual nonlinear change in temperature and pressure at selected stations, respectively. The linear model captures the trend in rapidly changing engine parameters.

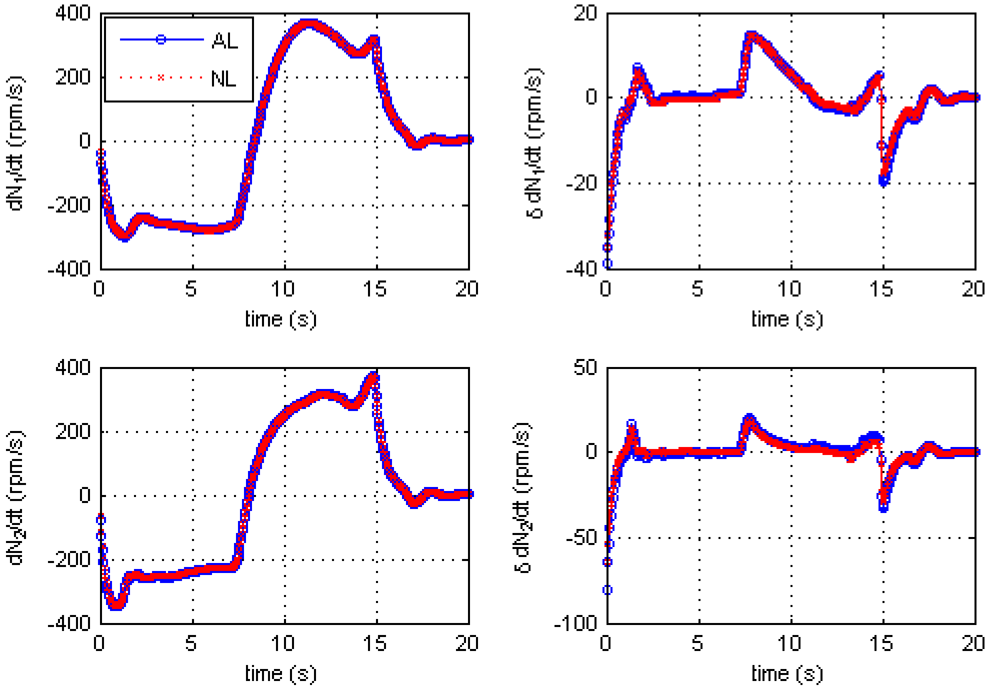

Figure 5.10 Shaft dynamics during *Bodie* manuever at sea-level static

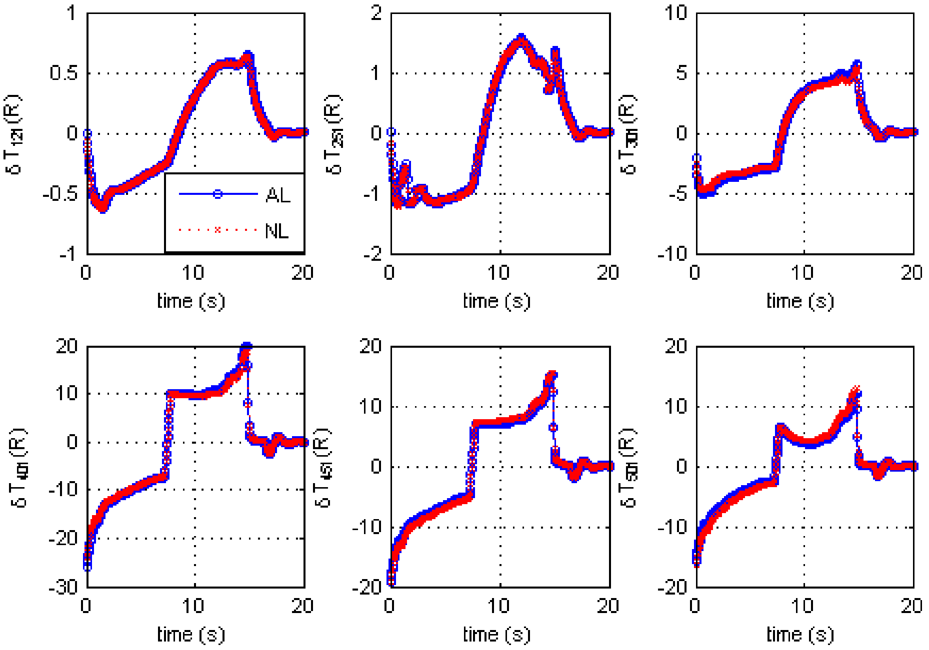

Figure 5.11 Change in temperature at different stations during *Bodie* manuever at sea-level static

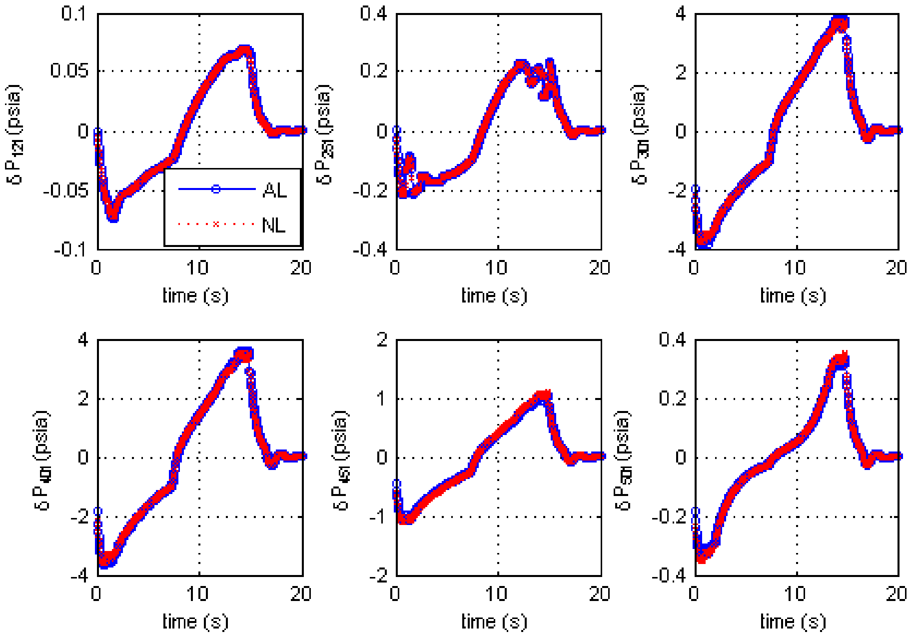

Figure 5.12 Change in pressure at different stations during *Bodie* manuever at sea-level static

Figure 5.13 and Figure 5.14 show the evolving linear coefficients during the *Bodie* maneuver. These are elements of linear matrix **A** and **B** which represent the system dynamics in state space representation as introduced in Chapter 3. Each coefficient is plotted against time and compared with linear coefficients of the truth model which are obtained using numerical perturbation along the trajectory as explained in chapter 4. Linear sensitivities are also compared to the traditional piecewise linear models generated using a different number of interpolation points. The plots of linear coefficients give a good qualitative assessment of each linearization method. The piecewise linear model with 24 interpolation points replicates the continuously interpolated model very accurately. In fact, it has fewer numerical issues (such as convergence to the wrong solution due to discontinuous slopes in the performance maps) than the continuously interpolated model. Therefore, the piecewise linear model with 24 interpolation points is used as the baseline traditional piecewise linear model for the comparison study. If the nonlinear simulation does not exhibit convergence error, the increasing number of interpolation points for the piecewise linear model will result in a more accurate capture of the truth model. The fidelity of the model decreases as the number of interpolation point decreases. The linear coefficients of the piecewise linear model with six interpolation points deviate far away from the linear coefficients of the truth model, especially when rapid changes occur in the trajectory.

The conventional piecewise linear model is more accurate than the analytical real time linear model during the steady-state operation as shown by overlapping linear coefficients of the truth model and the piecewise linear model near the end of the trajectory. This is expected since the truth model and the piecewise linear model are derived at the same operating conditions using the same numerical perturbation method during steady-state operation. Nonetheless, the analytical real time linear model captures the truth model more closely than the piecewise linear model during large transient operation. The difference between the piecewise linear model and analytical linear model is elaborated during the rapid change in engine dynamics due to the sudden change in fuel flow rate as a result of snap acceleration that occurs at 8 seconds. Under these conditions, the analytical linear approach shows a significant improvement over the piecewise linear scheduled coefficient. Also, note that the improvement of using the analytical linear model over the piecewise linear model is more distinctive in $\mathbf{B_2}$ than $\mathbf{B_1}$ as the piecewise linear model is scheduled with N_1 and captures N_1 dynamics more accurately.

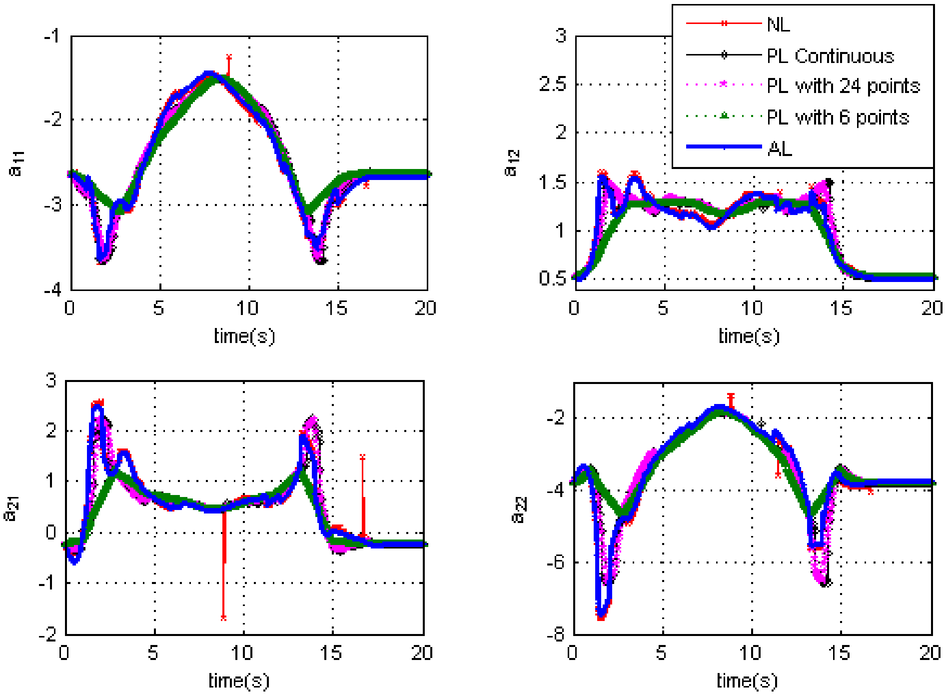

Figure 5.13 Evolution of elements of A matrix during *Bodie* manuever at sea-level static

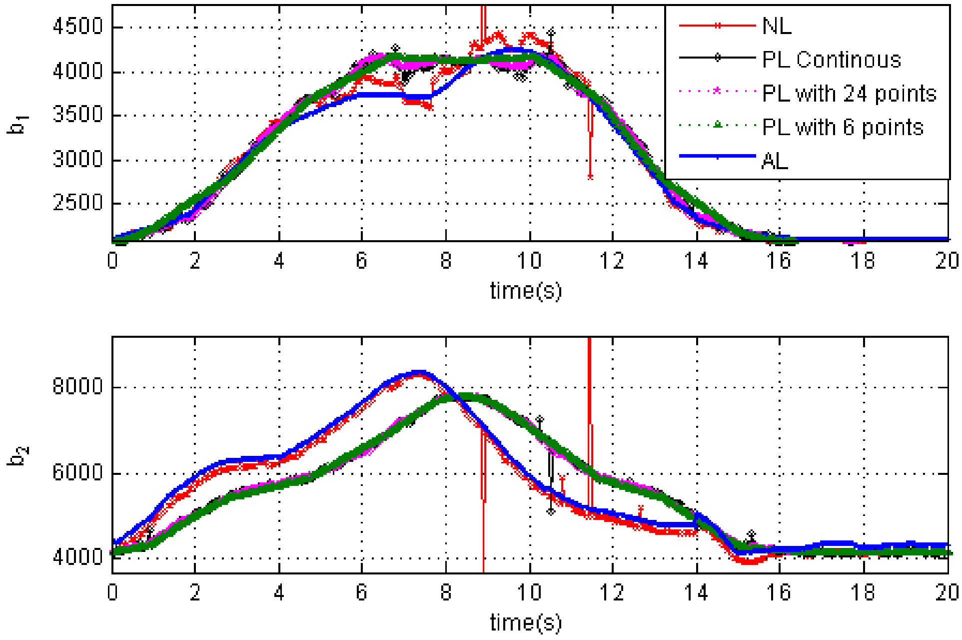

Figure 5.14 Evolution of element of B matrix during *Bodie* manuever at sea-level static

The model error in the time domain is quantified using NRMSE. Figure 5.15 shows the comparison of NRMSE for selected outputs using different linearization schemes along the *Bodie* maneuver at the sea-level static condition. The *y* axis on the plot represents the NRMSE and the *x*-axis represents the different outputs. Each bar is the NRMSE during the *Bodie* trajectory for a given output. The solid bar is the NRMSE for the analytical real time linearization, the horizontally lined bar is NRMSE for the piecewise linear model with 24 interpolation data points, and the vertically lined bar is NRMSE for the piecewise linear model with 6 interpolation points. The NRMSE for the analytical linear model for different outputs ranges from 0.010 to 0.022. The variation among the different outputs is unnoticeable since it is within the same order of magnitude. Much larger variation is observed in the NRMSE of different outputs of the piecewise linear model. The NRMSE of the scheduling parameter is much less than that of other parameters for the piecewise linear model. For example, the smallest NRMSE is 0.0038 for N_1 while the largest NRMSE is 0.06 for N_2. This is more than an order of magnitude difference whereas the variation using the analytical linear model was around a factor of two. It is concluded that the current state of art using piecewise linear model is fairly accurate for the state that it is scheduled along with; however, the error would be much larger if non-scheduling states are used for controller design as the trajectory moves away from the steady-state positions. As expected, the piecewise linear model with 24 interpolation points is much better than the piecewise linear model scheduled with 6 interpolation points.

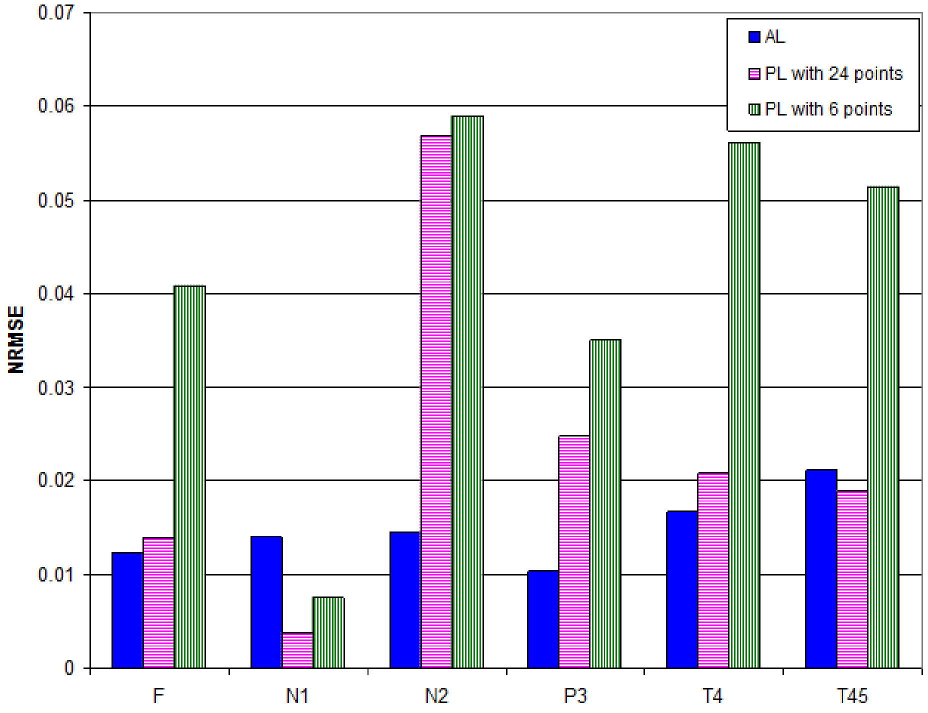

Figure 5.15 Comparison of normalized RMSE for selected outputs at sea-level static

5.2.3 Normalized Additive Uncertainty

Figure 5.16 and Figure 5.17 show the normalized additive uncertainty for different linearization schemes for the systems with outputs of N_1 and N_2, respectively. The advantage of using the off-equilibrium analytical linear model is illustrated by these plots. The normalized additive uncertainty is plotted against the corrected N_1 speed for the *Bodie* trajectory. The normalized additive uncertainty for analytical linear model is kept below 0.07 for both N_1 and N_2. The normalized additive uncertainty for the piecewise linear model with 24 points shoots up as high as 0.18, which is more than twice of that of the analytical linear model. The normalized additive uncertainty for the piecewise linear model with 6 points is much higher than that of the piecewise linear model with 24 points as expected. The normalized additive uncertainty of the piecewise linear model approaches zero near full shaft speed as it reaches the steady-state condition; however, it grows large during rapid transient operation. While the fidelity of the analytical linear model stays almost constant, the fidelity of the piecewise linear model changes drastically during transient operation.

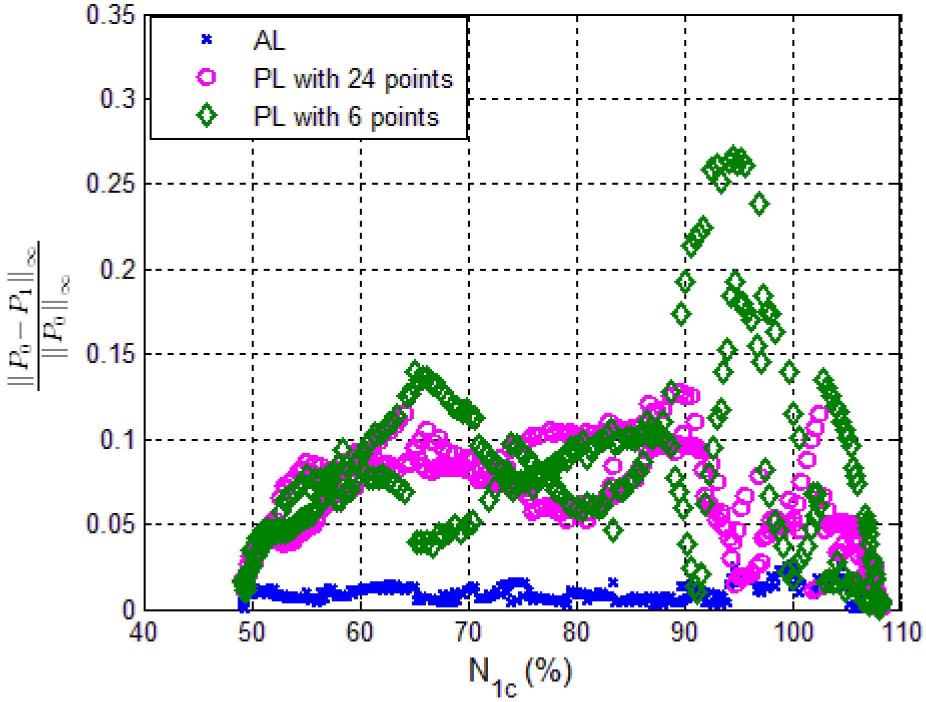

Figure 5.16 Comparison of additive uncertainty of system output of N_1 using different linearization schemes at sea-level static

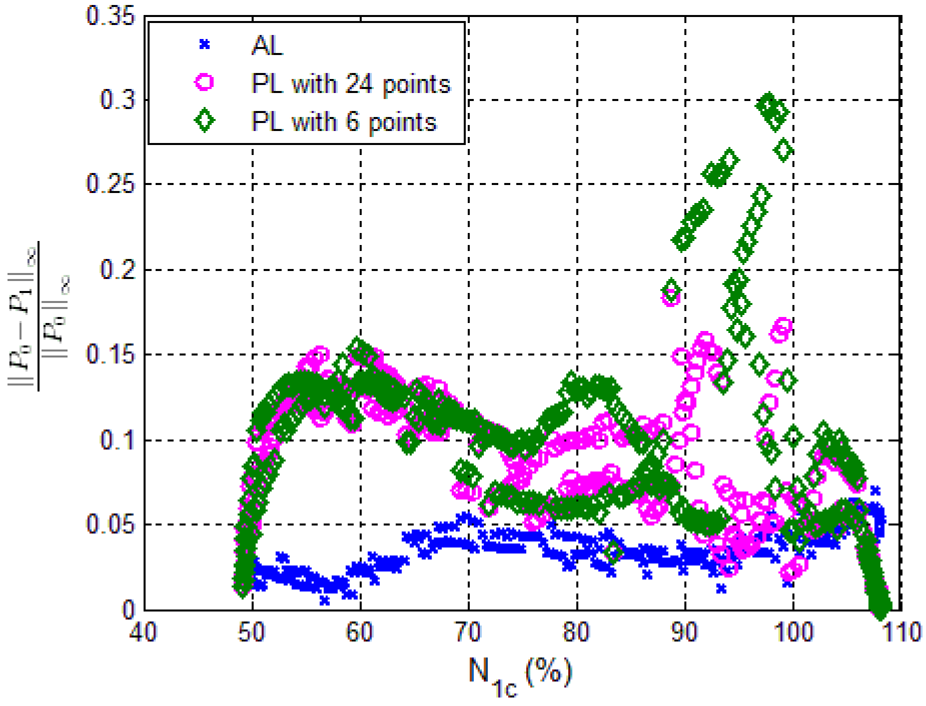

Figure 5.17 Comparison of additive uncertainty of system output of N_2 using different linearization schemes at sea-level static

5.2.4 The [nu]-Gap Metric

Figure 5.18 and Figure 5.19 show the ν-gap metric for the outputs of N_1 and N_2, respectively, for different linearization schemes. For the closed loop validation, the comparison between different linearization schemes for N_1 and N_2 are very different. For the system with output of N_1, the piecewise linear model works almost as well as the analytical linear model except at very low power, where the error of piecewise linear model is about twice that of the analytical linear model. This means that the reduction in the general stability margin $b_{p,c}$ due to the uncertainty in the real-time analytical model is less than 0.03 whereas it may decrease as much as 0.06 for the piecewise linear model.

The difference in the ν-gap metric is magnified for the system with output of N_2. The reduction in the general stability margin using piecewise linear model would be more than quadruple the analytical real time linear model as shown in Figure 5.19. The larger difference is due to the fact that the piecewise linear model is scheduled with N_1, causing larger discrepancy between the transient trajectory and the steady-state line for N_2 than N_1. As the example engine model in NPSS used for these comparisons does not fully include all the nonlinearities, it is expected that the error values seen by the piecewise linear model to be much larger if one were to include all the nonlinearities typical of a nonlinear engine model.

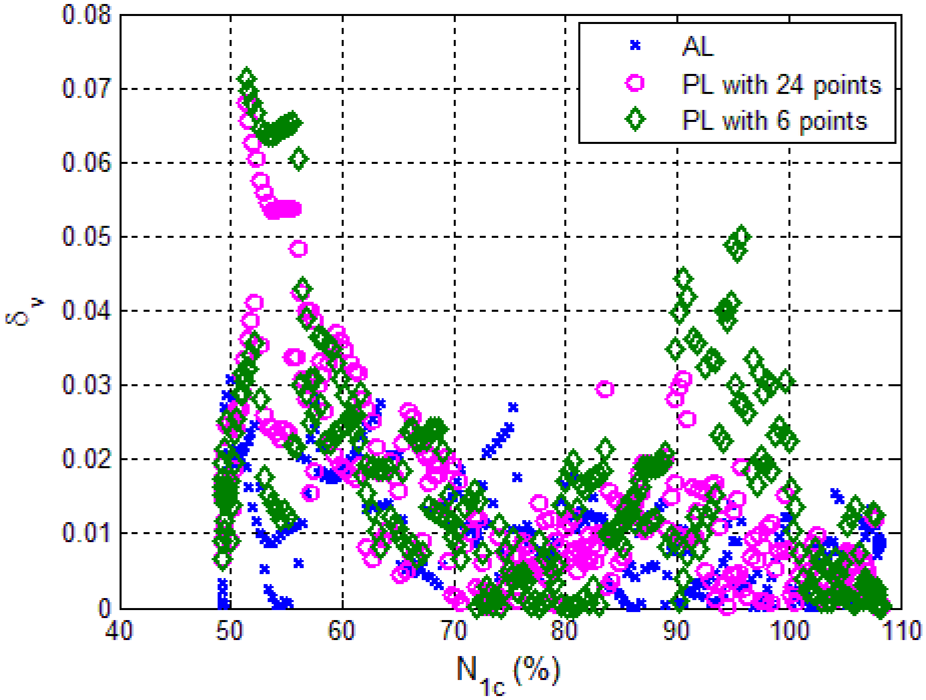

Figure 5.18 Comparison of the ν-gap metric of system output of N_1 using different linearization schemes at sea-level static

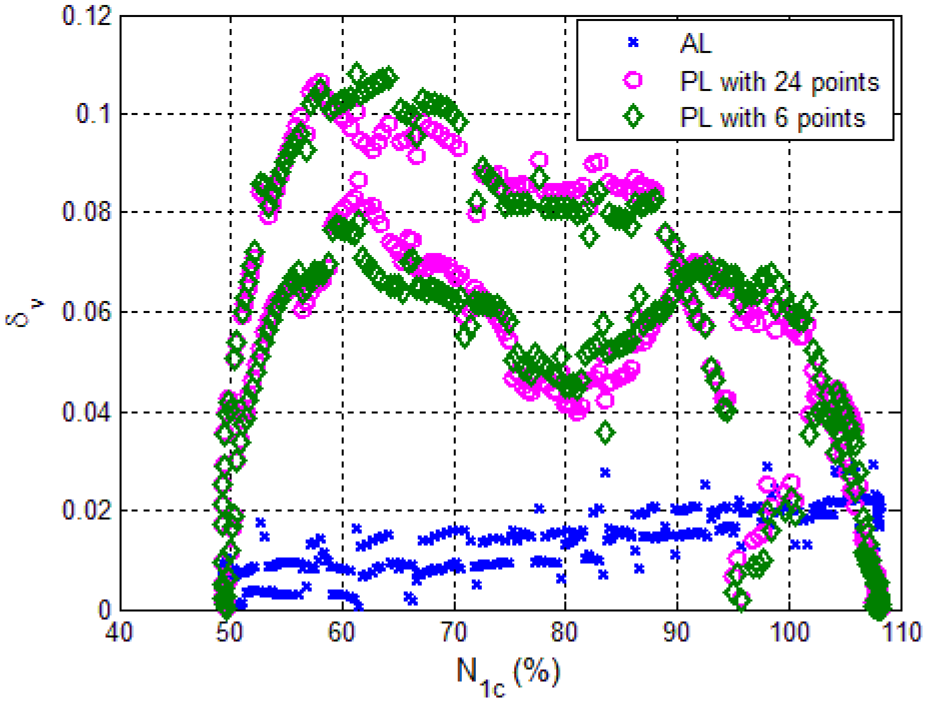

Figure 5.19 Comparison of the ν-gap metric of system output of N_2 using different linearization schemes at sea-level static

Figure 5.20 to Figure 5.26 present results during the *Bodie* maneuver at different operating conditions. The operation is performed at an altitude of 25000ft, Mach number of 0.5 and +20°R deviation from the standard day temperature. The piecewise linear model is developed at this ambient condition; therefore, there is no modeling error due to scheduling along the ambient condition for the piecewise linear model (equivalent to scheduling continuously along the operating condition). There is very little variation during the transient operation in the NRMSE, the additive uncertainty and the ν-gap metric of the analytical linear model due to change in ambient conditions. The range of these values is similar to that of the sea-level static condition. This suggests that the fidelity of the analytical linear model is independent of ambient conditions. On the other hand, the results of the piecewise linear model differ from the sea-level static condition. All NRMSE, additive uncertainty, and the ν-gap metric for the system with output of N_1 and N_2 are much higher than operation at sea-level static condition. This is due to the more drastic and frequent changes of direction in linear sensitivities than the sea-level static case as shown in Figure 5.20 and Figure 5.21 and the inability of the piecewise linear model to capture such dynamic behavior as they are developed along the steady-state line. It is concluded that the fidelity of the piecewise linear model depends on the ambient condition. This adds an additional advantage to the analytical real time linear model.

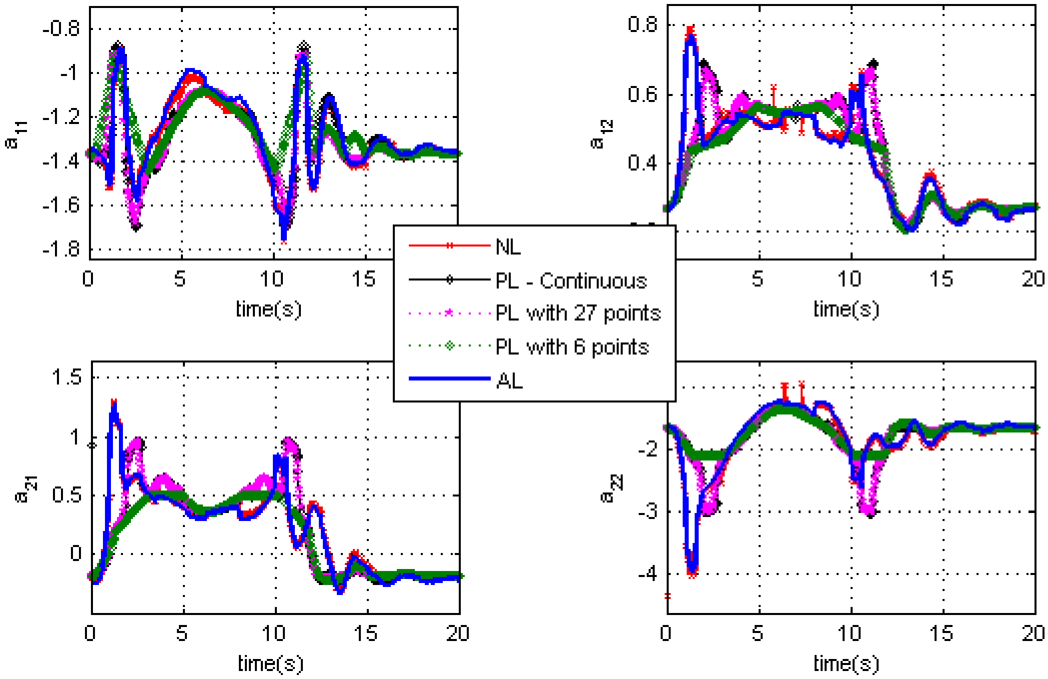

Figure 5.20 Evolution of elements of A matrix during *Bodie* manuever at alt=25000ft, dTs=20°R, M=0.5

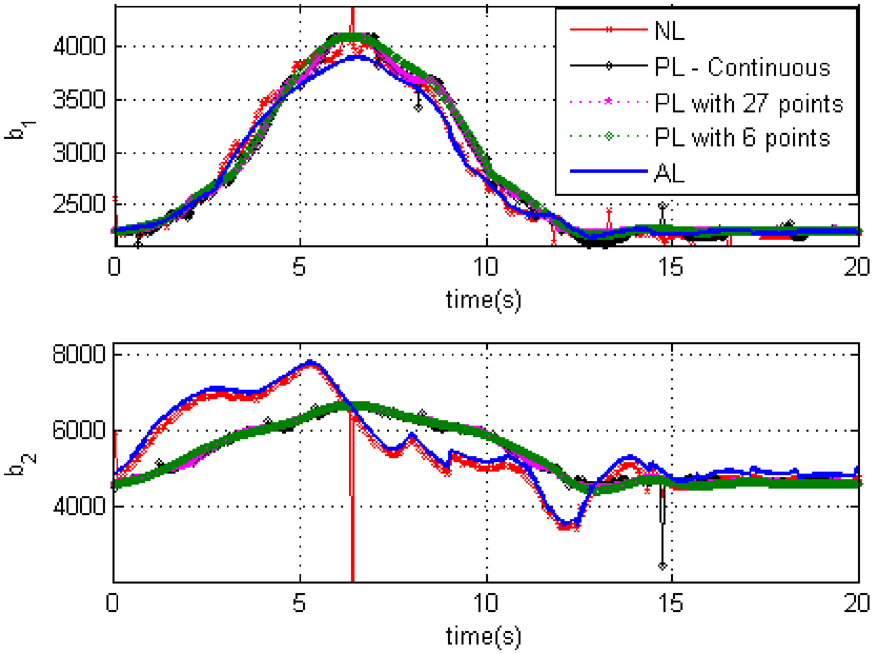

Figure 5.21 Evolution of elements of B matrix during *Bodie* manuever at alt=25000ft, dTs=20°R, M=0.5

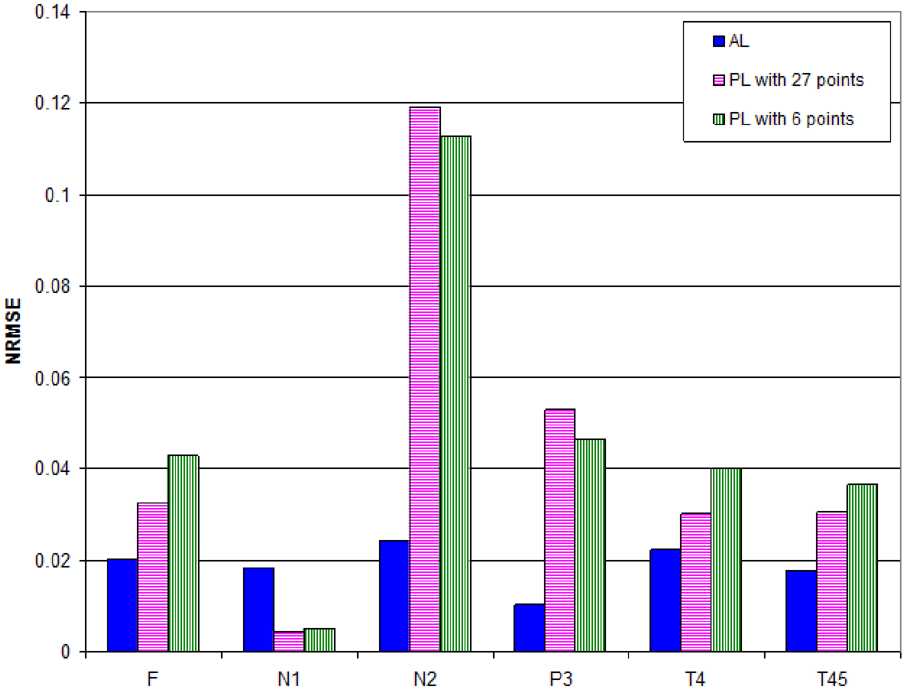

Figure 5.22 Comparison of RMSE for selected outputs using different linearization schemes at alt=25000ft, dTs=20°R, M=0.5

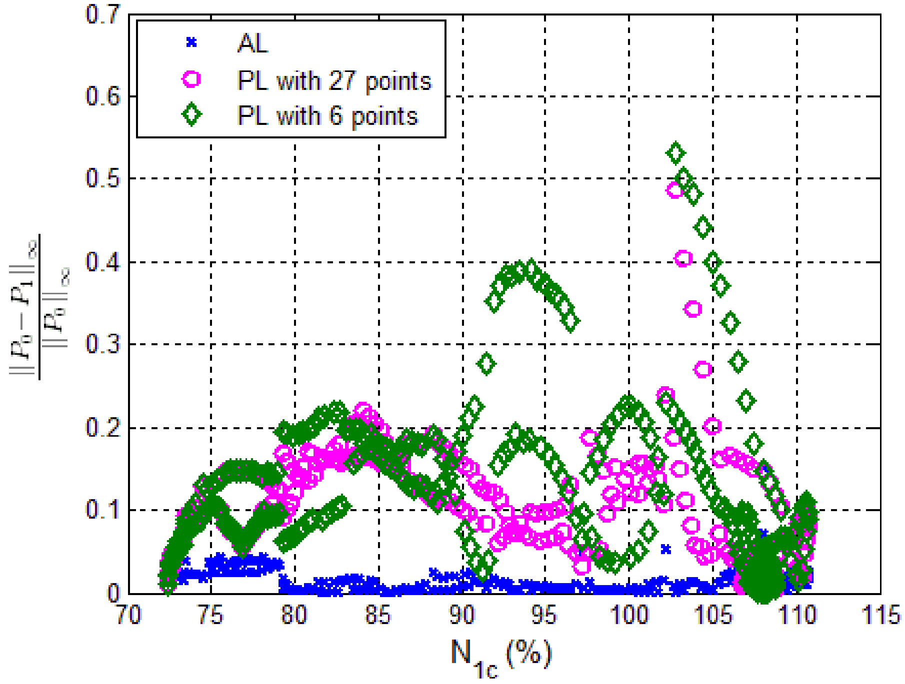

Figure 5.23 Comparison of additive uncertainty of system output of N_1 using different linearization schemes at alt=25000ft, dTs=20°R, M=0.5

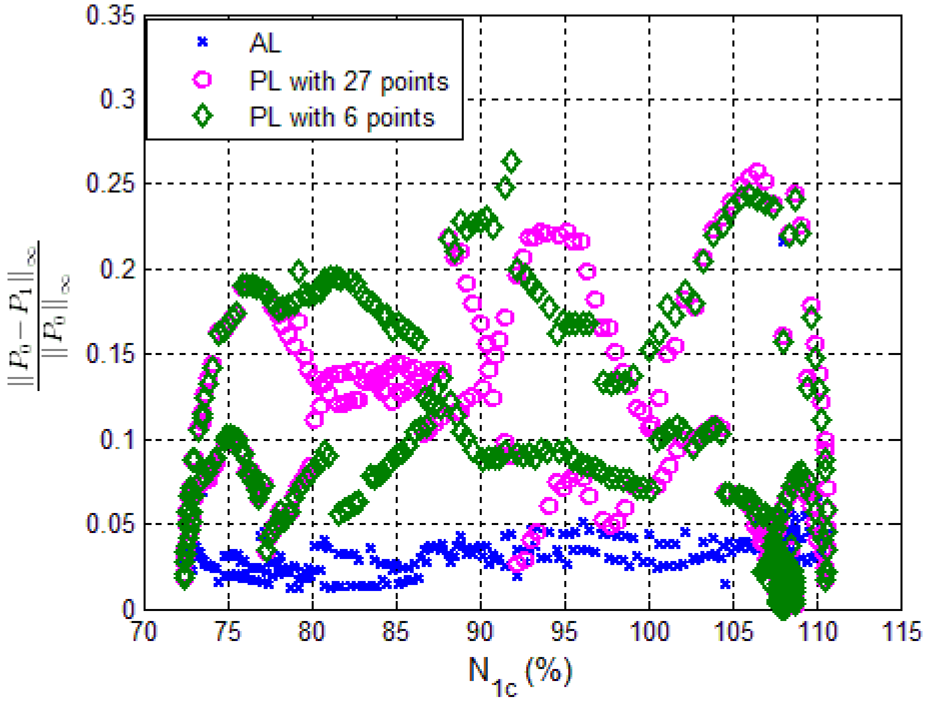

Figure 5.24 Comparison of additive uncertainty of system output of N_2 using different linearization schemes alt=25000ft, dTs=20°R, M=0.5

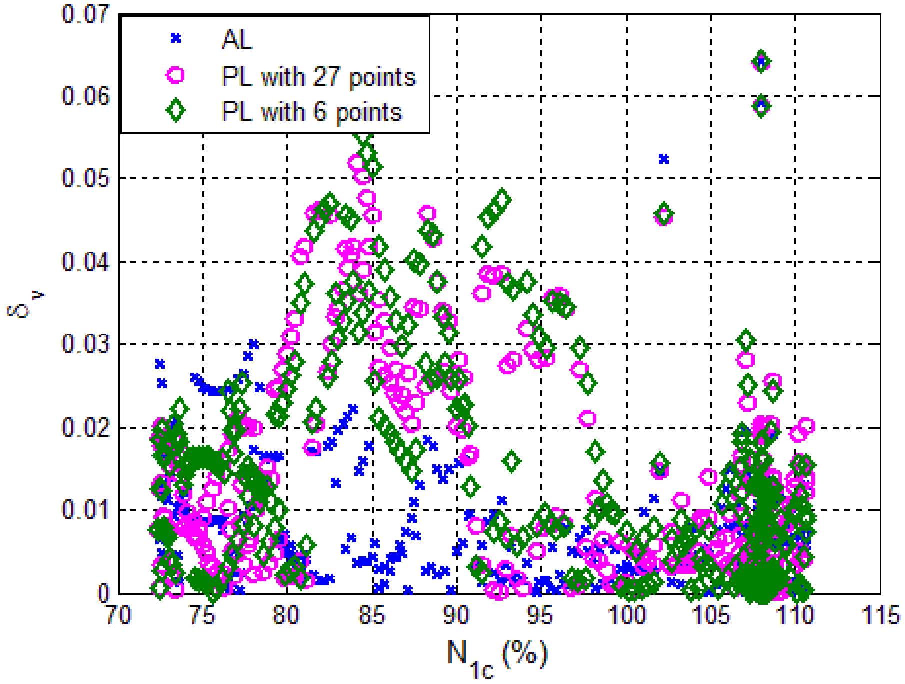

Figure 5.25 Comparison of ν-gap metric of system output of N_1 using different linearization schemes at alt=25000ft, dTs=20°R, M=0.5

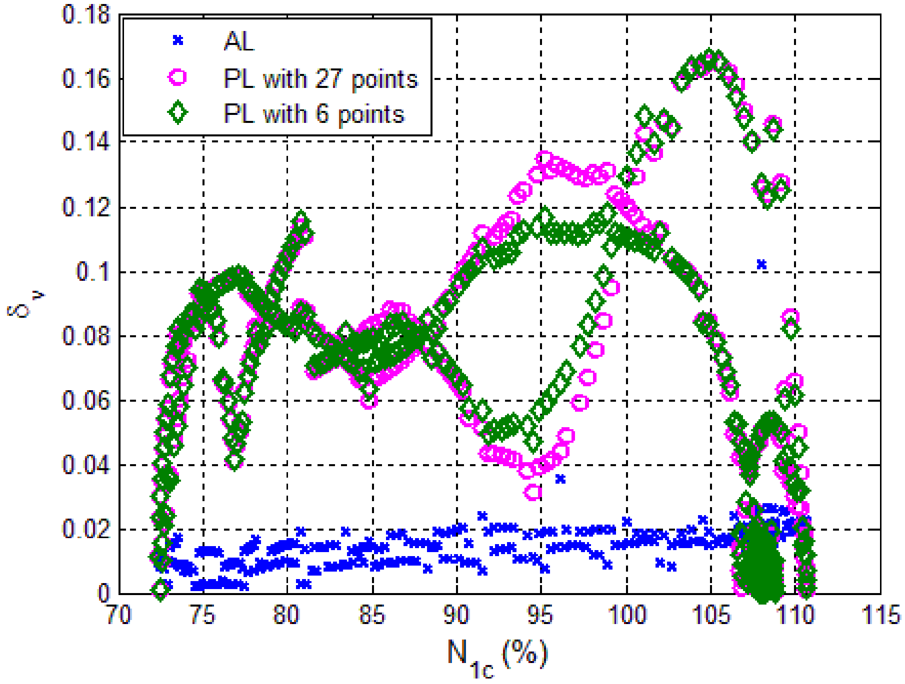

Figure 5.26 Comparison of ν-gap metric of system output of N_2 using different linearization schemes at alt=25000ft, dTs=20°R, M=0.5

5.2.5 *Effect of Flow Solver Tolerance*

The effect of flow solver tolerance on the fidelity of the analytical linearization scheme is examined in this section. The truth model is generated using a solver tolerance of 10^{-7}. The analytical linear model is derived using a solver tolerance between 10^{-7} and 10^{-3}. The normalized additive uncertainty and the ν-gap metric for the analytical linear model of different tolerance levels are shown in Figure 5.27-Figure 5.30. The effect of solver tolerance on evaluation of algebraic expression is minimal. Therefore, any difference in these plots of different solver tolerance levels can be explained by the nonlinear simulation converging to different values. Since only a minor difference is observed in these figures, it is concluded that the analytical linearization is robust to the level of flow solver tolerance.

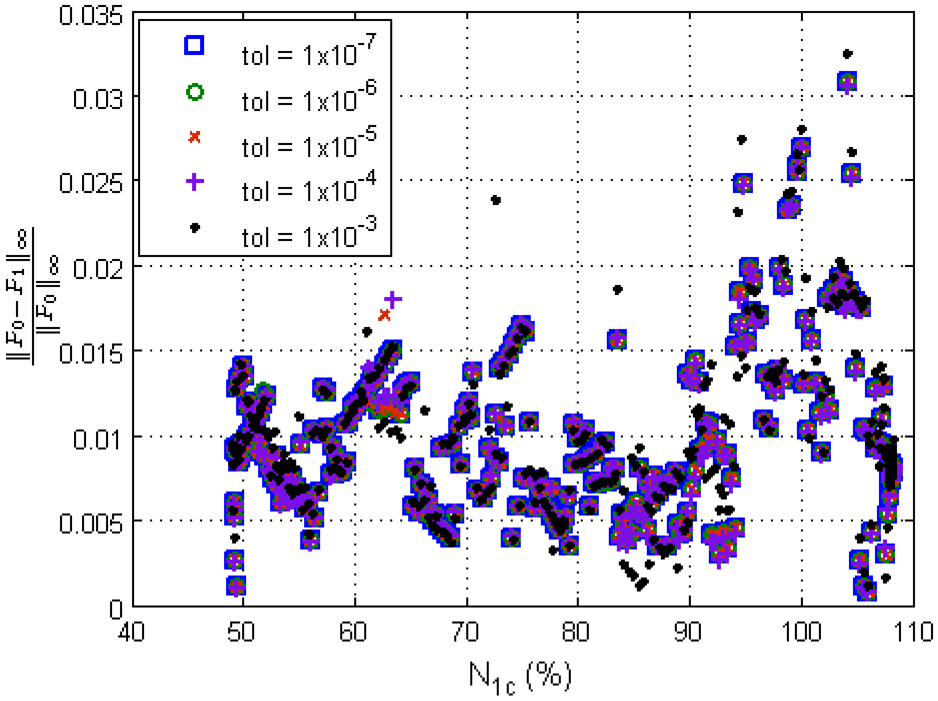

Figure 5.27 Normalized additive uncertainty of system output N_1 using different tolerance

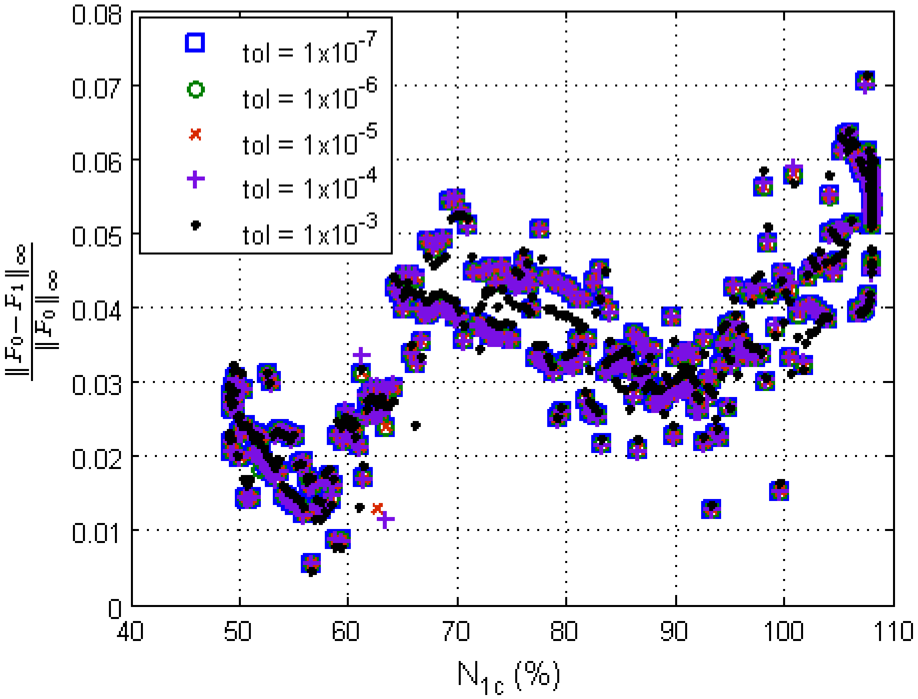

Figure 5.28 Normalized additive uncertainty of system output of N_2 using different tolerance

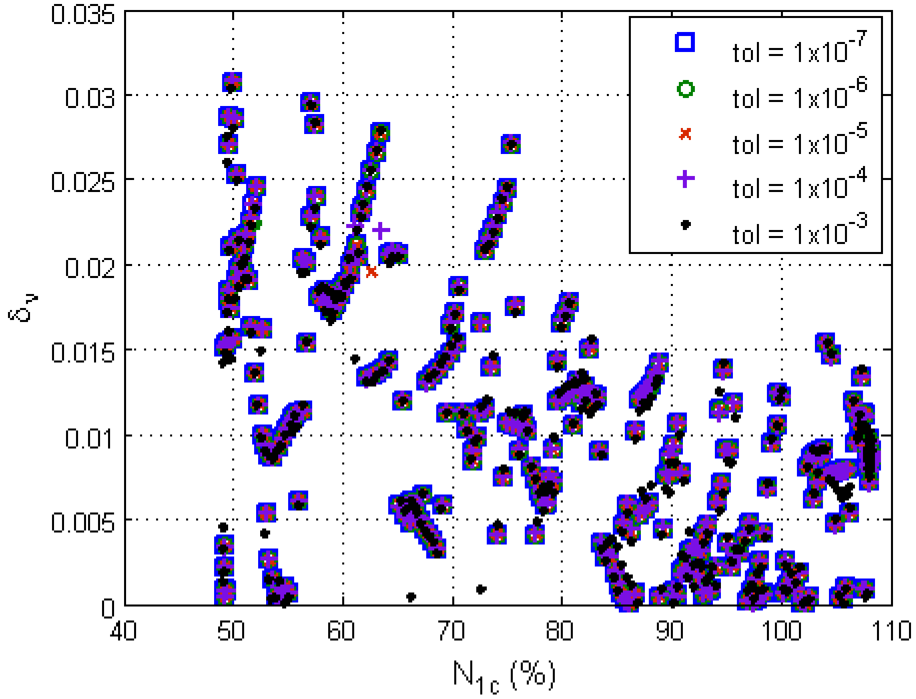

Figure 5.29 ν-gap metric for system output N_1 using different tolerance

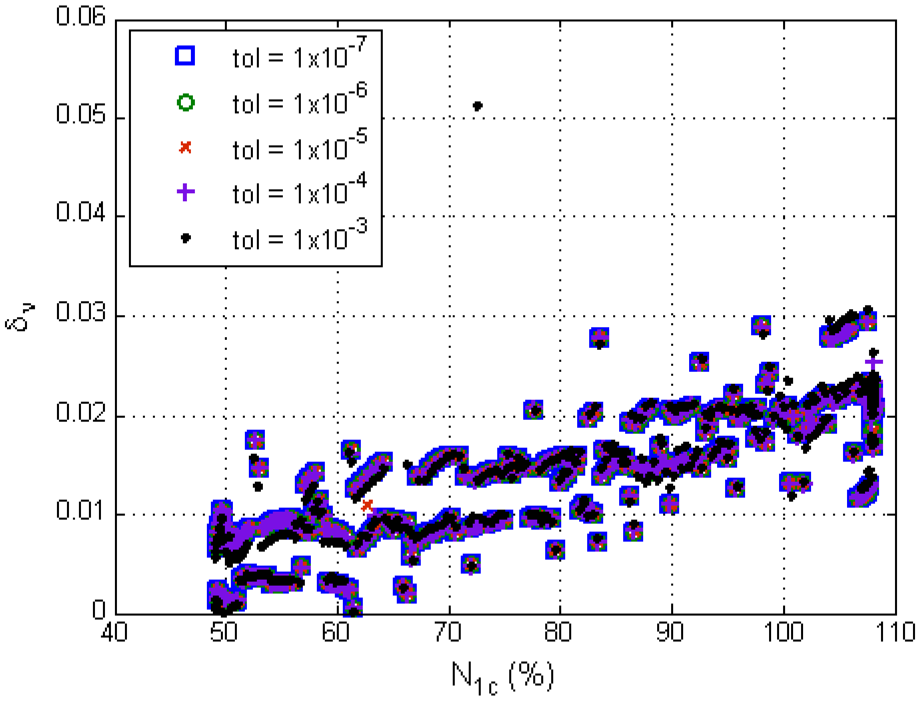

Figure 5.30 ν-gap metric of system output N_2 using different tolerance

5.2.6 Scaling

Figure 5.31 shows the ν-gap metric of the unscaled system for selected outputs. The ν-gap metric is plotted against the corrected N_1. The *y-axis* is in logarithmic scale to incorporate a large range of the ν-gap metric, which is primarily due to different units of outputs. Usually scaling is used for simpler controller design and analysis in practical applications. To eliminate the effect of different units, all system transfer functions are scaled to the magnitude of 1 using a DC gain, as explained in Chapter 4. Using the equivalent normalized system, the ν-gap metric computation is repeated. The scaled ν-gap metric is shown in Figure 5.32. The ν-gap metric for the scaled system for different outputs results in a similar range and exhibits similar behavior for the most of outputs.

Therefore, any of these outputs can be used for the controller synthesis. The turbine temperature exhibits the highest ν-gap metric presumably due to the bleed assumption. Scaling is more important in the MIMO system as different outputs possess different units. Two outputs, N_1 and N_2, that are examined in detail in this thesis use the same unit, so the magnitude of the DC gain of both SISO systems are in a similar range. Scaling and selection of weight should be carefully considered for a controller synthesis problem. Since the controller synthesis is out of the scope of the thesis, the rest of analysis in this thesis is done using the unscaled system for computing the ν-gap metric.

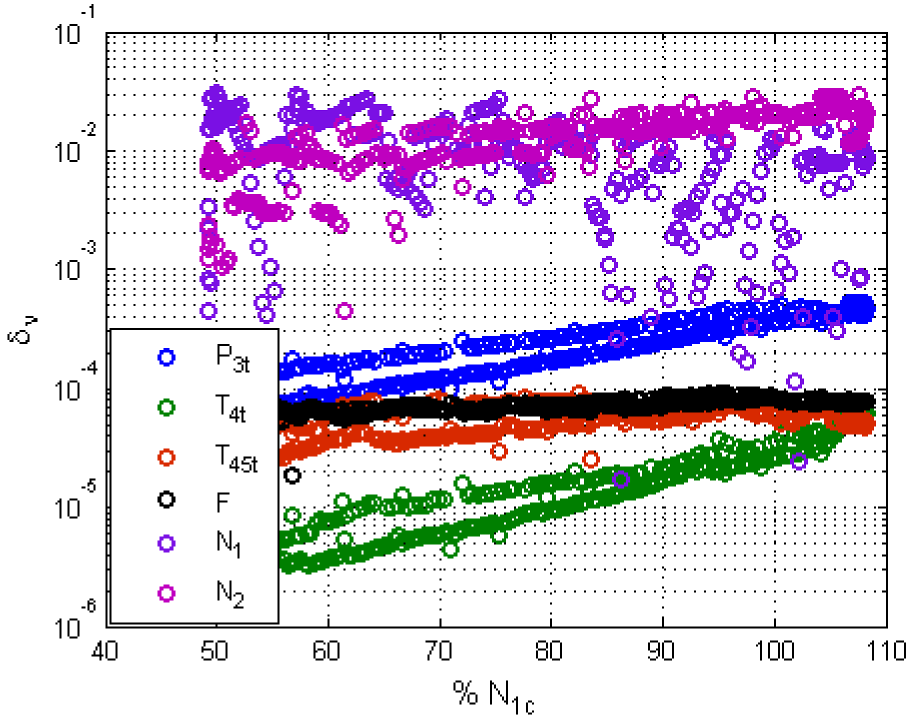

Figure 5.31 Unscaled ν-gap metric for selected outputs

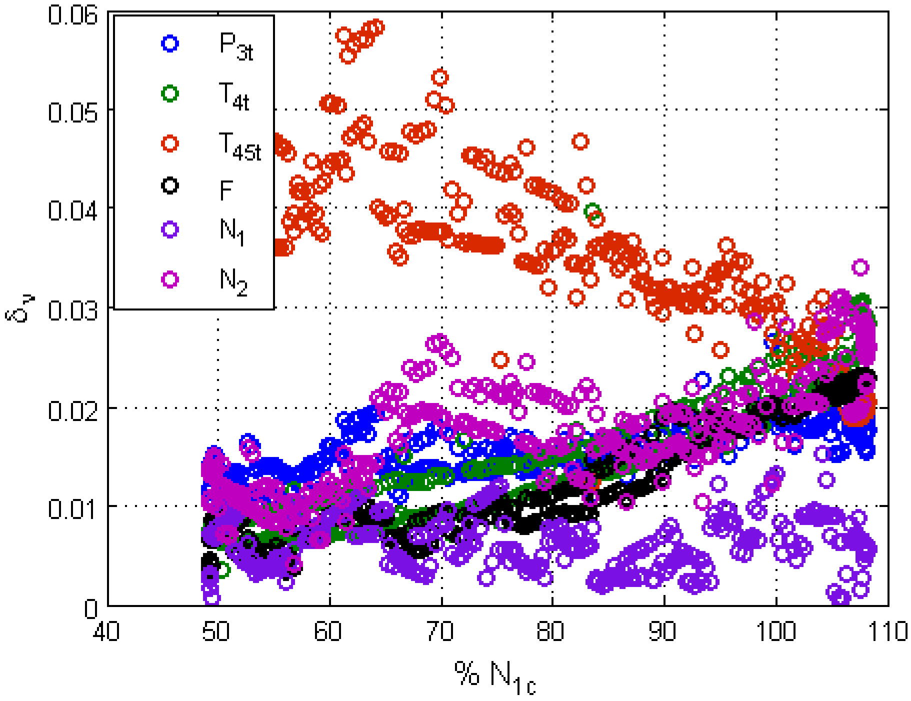

Figure 5.32 Scaled ν-gap metric for selected outputs

5.3 Summary

The off-equilibrium analytical linearization method has been applied to the example model in NPSS. The resulting linear model was validated against the truth model using the NRMSE, the normalized additive uncertainty and the ν-gap metric. Also, the conventional linearization approach was implemented on the same engine model to demonstrate the advantage of the proposed linearization method over the conventional piecewise linear model. The benefit of using off-equilibrium analytical linearization is more apparent in cases such as designing a controller for non-scheduling parameters. Improvements may not be as significant in certain cases such as a designing controller for scheduling parameters. Thus, the design requirement should be carefully considered before choosing the linearization scheme. For example, the conventional piecewise linear models proved to be adequate when designing a controller for the scheduling parameter. Also, the conventional piecewise linear models produced very small error for both scheduling and non-scheduling states near the steady-state conditions as expected. However, the results showed noticeable improvement in the fidelity of the linear model using an analytical off-equilibrium approach over that of the conventional linear models during a large transient operation especially for the non-scheduling parameters. The improvement is expected to be larger for an engine with more nonlinearity during transient operation.

CHAPTER 6

ANALYSIS OF SIMPLIFYING ASSUMPTIONS

In this chapter, the simplifying assumptions used for analytical linearization are analyzed in detail. The effect of each assumption on the fidelity of the model is discussed. Assumptions from chapter 3 are restated here for convenience.

1. Assume gas is ideal, where the following relationship holds.

$$PV = nRT \tag{6.1}$$

Moreover, the enthalpy of the thermally perfect gas is function of temperature only (not of pressure). Using this assumption, the following relationship for enthalpy is established.

$$dh = c_p(T)dT \tag{6.2}$$

2. Gas path thermodynamic properties, c_p and γ are assumed to be independent of temperature and, thus, constant (calorically perfect) within one component during one time step; however, variation in the properties due temperature differences among different components is considered. Using this assumption, the specific heat becomes constant and enthalpy can be further simplified as follows:

$$h = c_p T \tag{6.3}$$

This also causes γ to be constant.

Certain levels of simplifying assumptions are essential to put a nonlinear model into the analytically linearizable form. These assumptions may be relaxed slightly by using more complex representations of gas properties, such as a polynomial representation for c_p. The benefits of including more complex gas property representation are expected to be insignificant in comparison to the complexity that is added to the analytical linearization. Also, results may actually become worse due to inconsistency between equations. The effect of above stated assumptions on model fidelity is analyzed in detail to determine if the model error is within acceptable bounds in this chapter.

Before necessary simplifying assumptions are analyzed, two extra assumptions with respect to bleed are considered here. These extra assumptions are not absolutely necessary for analytical linearization, but would reduce the computational complexity. These assumptions are stated as follows.

1. Enthalpy change due to the turbine cooling air inside the turbine is assumed to be negligible. Assuming the bleed is expanded at the same efficiency as the primary flow (this is the assumption used in the detailed engine model), enthalpy at the outlet of the turbine is written as follows.

$$h_{45t} = \frac{1}{w_{45}}\left[h_{40t}w_{40} + h_{30t}w_{bleed} - \eta\{(h_{40t} - h_{45ti})w_4 + h_{bleedi}w_{bleed}\}\right] \tag{6.4}$$

The enthalpy change due to bleed fraction is assumed to be negligible. Then equation (6.4) is simplified as follows:

$$\begin{gathered} h_{45t} = \frac{1}{w_{45}}\left[h_{40t}w_{40} - \eta\{(h_{40t} - h_{45ti})w_{40}\}\right] \\ \eta = \frac{h_{40t}w_{40} - h_{45t}w_{45}}{(h_{40t} - h_{45ti})w_{40}} \end{gathered} \tag{6.5}$$

The expression for the stagnation temperature at the turbine outlet is obtained as equation (6.6) when c_p is also assumed to be constant (i.e. $c_{po} = c_{pi=}\ c_{pavg}$)

$$\eta = \frac{\frac{w_{40}}{w_{45}} - \frac{T_{45t}}{T_{40t}}}{\frac{w_{40}}{w_{45}}\left(1 - \left(\frac{P_{45t}}{P_{40t}}\right)^{\frac{\gamma-1}{\gamma}}\right)}$$

$$T_{45t} = T_{4t}\frac{w_{40}}{w_{45}}\left\{1 - \eta_t\left(1 - \left(\frac{P_{45t}}{P_{40t}}\right)^{\frac{\gamma-1}{\gamma}}\right)\right\} \tag{6.6}$$

2. The torque produced by turbine cooling air is assumed to be negligible.

$$\begin{aligned} \tau_{45} &= \left[\frac{c_p(T_{40t} - T_{45t})w_4}{N_2} + \frac{c_p(T_{30t} - T_{45t})w_{bld}}{N_2}\right]\left(\frac{60}{2\pi}\right) \\ &\approx \frac{c_p(T_{40t} - T_{45t})w_{40}}{N_2}\left(\frac{60}{2\pi}\right) \end{aligned} \tag{6.7}$$

The effect of these assumptions is analyzed in detail for the refinement of the model.

6.1 Analysis of Perfect Gas Assumption

The assumption of thermally perfect gas is necessary to use conventional analytical equations. It is shown in [16] and [10] that c_p and γ are both very weak functions of pressure below 3600 °R (2000K). In the range of temperatures of interest for a gas turbine, the effects of pressure on the values of c_p and γ are order of 0.1% and assumed negligible for the required precision [10]. Therefore, the thermally perfect gas assumptions is justified (that pressure dependence of these gas property is minor compared to the temperature dependence) and no further investigation is made with regard to the thermally perfect gas assumptions.

6.2 Analysis of Bleed Assumption

The bleed assumptions with respect to temperature and torque are treated together as they are closely coupled. Two levels of approximations are considered in this section.

The first set of assumptions is the original bleed assumptions stated in the previous section. The second set of assumptions is a relaxed version that accounts for the temperature change and torque produced by the bleed portion of the mass flow rate added at the inlet of the turbine as, shown in equations (6.9) and (6.10).

$$h_{45t} = \frac{1}{w_{45}}\left[h_{40t}w_{40} + h_{bleed}w_{bleed} - \eta\left\{(h_{40t} - h_{45ti})w_{40} + (h_{bleed} - h_{bleedi})w_{bleed}\right\}\right] \tag{6.8}$$

$$\begin{aligned} T_{45t} &= \frac{w_{40}}{w_{45}}T_{40t}\left[1-\eta_t\left(1-\left(\frac{P_{45t}}{P_{40t}}\right)^{\frac{\gamma-1}{\gamma}}\right)\right] + \frac{w_{bld}}{w_{45}}T_{30t}\left[1-\eta_t\left(1-\left(\frac{P_{45t}}{P_{30t}}\right)^{\frac{\gamma-1}{\gamma}}\right)\right] \\ &\approx kT_{40t}\left[1-\eta_t\left(1-\left(\frac{P_{45t}}{P_{40t}}\right)^{\frac{\gamma-1}{\gamma}}\right)\right] + (1-k)T_{30t}\left[1-\eta_t\left(1-\left(\frac{P_{45t}}{P_{30t}}\right)^{\frac{\gamma-1}{\gamma}}\right)\right] \end{aligned} \tag{6.9}$$

$$\tau_{45} = \left[\frac{c_p(T_{40t} - T_{45t})w_4}{N} + \frac{c_p(T_{30t} - T_{45t})w_{bld}}{N}\right]\left(\frac{60}{2\pi}\right) \tag{6.10}$$

Equation (6.9) and (6.10) assume constant c_p and γ at all flow levels. (Inflow from the combustor, inflow from the compressor, and outflow from the turbine; use the average between the inflow from the combustor and the outflow from the turbine).

The normalized additive uncertainty and the ν-gap metric for the system with outputs of N_1 and N_2 for different levels of approximations are presented in Figure 6.1-Figure 6.4.

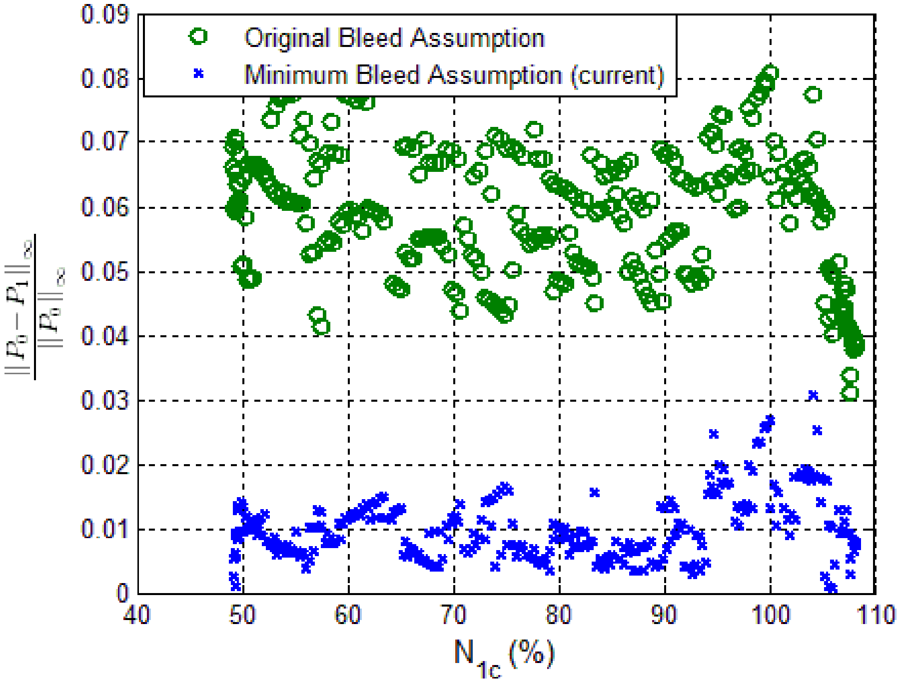

Figure 6.1 Additive uncertainty of system output of N_1 at sea-level static using different bleed assumptions

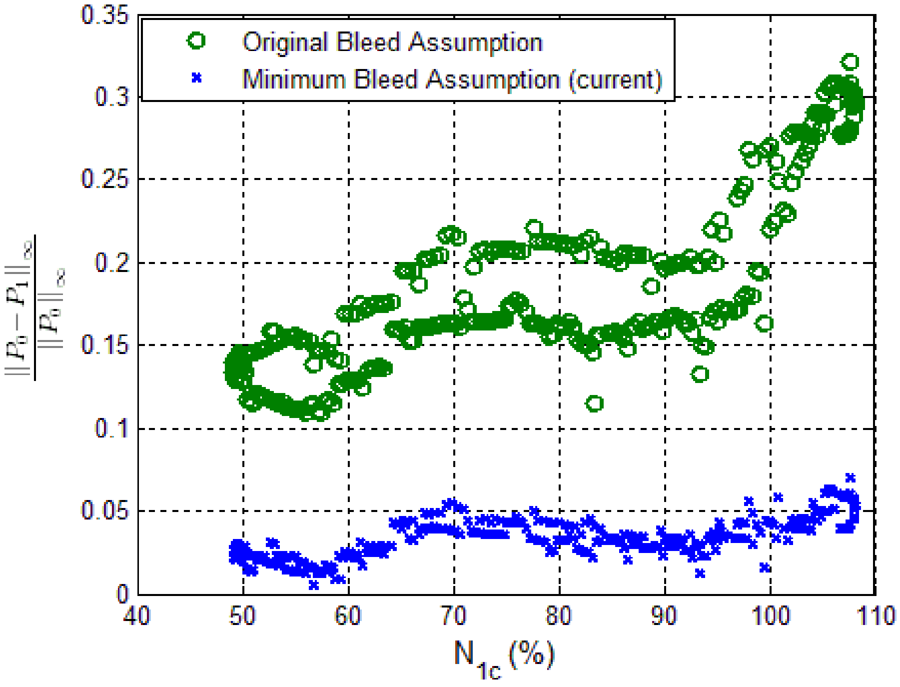

Figure 6.2 Additive uncertainty of system output of N_2 at sea-level static using different bleed assumptions

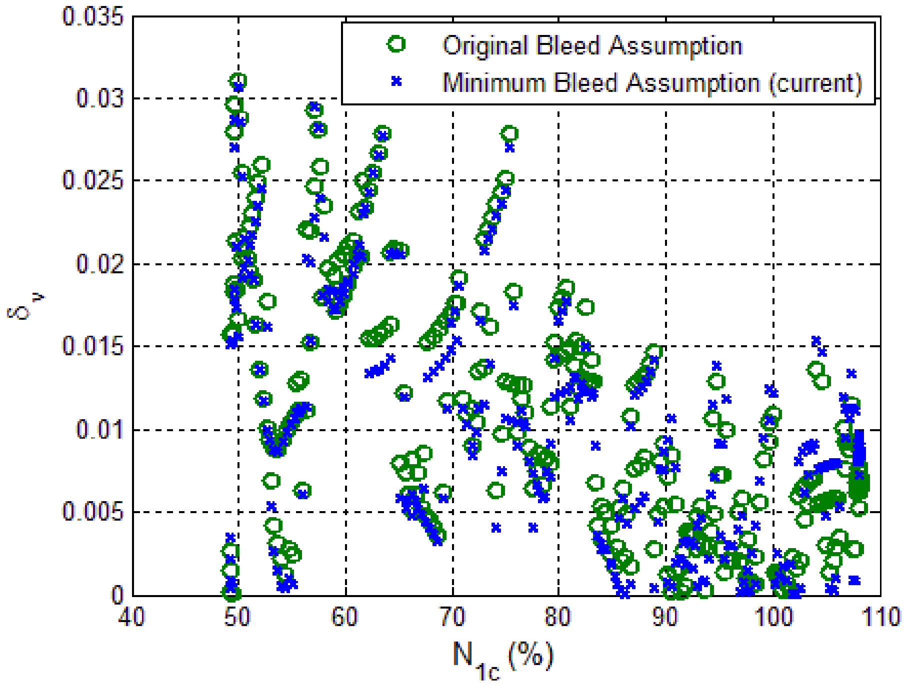

Figure 6.3 ν-gap metric of system output of N_1 at sea-level static using different bleed assumptions

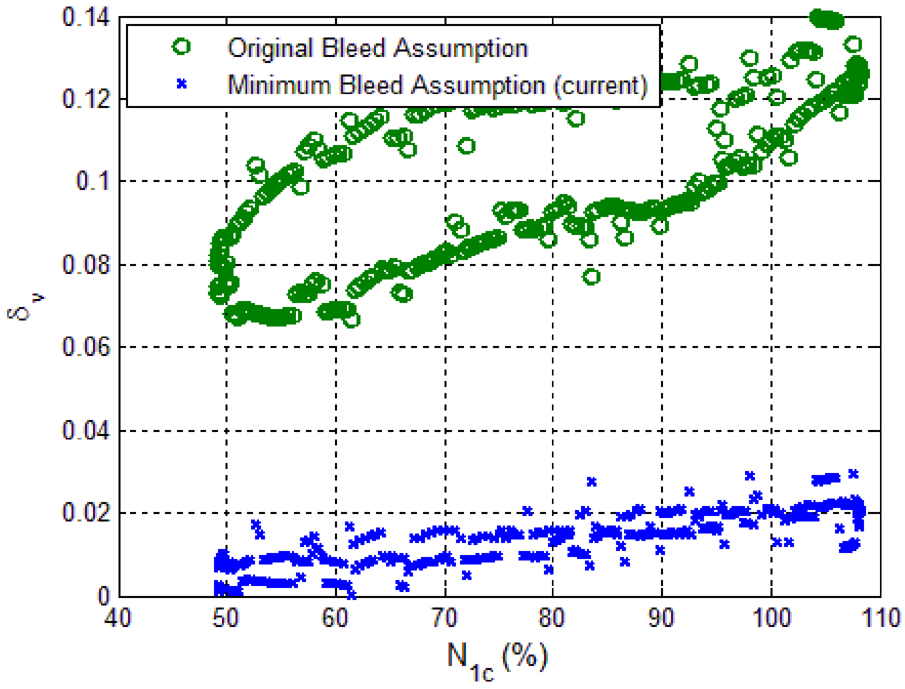

Figure 6.4 ν-gap metric of system output of N_2 at sea-level static using different bleed assumptions

The bleed assumptions have only minor effects on the system with an output of N_1. On the other hand, the large difference between models with different level of approximations for the system with an output of N_2 clearly indicates that the bleed flow has huge effects on the high spool shaft speed. Both normalized additive uncertainty and the ν-gap metric are an order of magnitude larger for the system with the original set of assumptions. Consequently, the bleed is accounted for using minimal assumptions to increase the accuracy in the final refined model. The variation in the additive uncertainty and the ν-gap metric due to the increase in bleed fraction is minimal in the refined model using minimal bleed assumptions, as shown in Figure 6.5 and Figure 6.6.

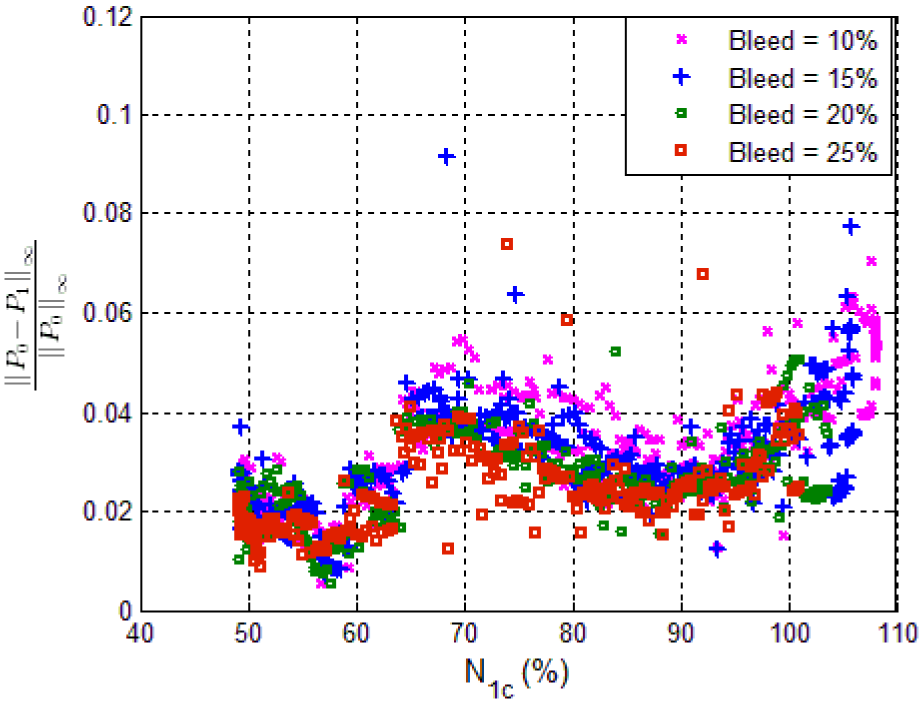

Figure 6.5 Additive uncertainty of system output of N_2 using different bleed fractions

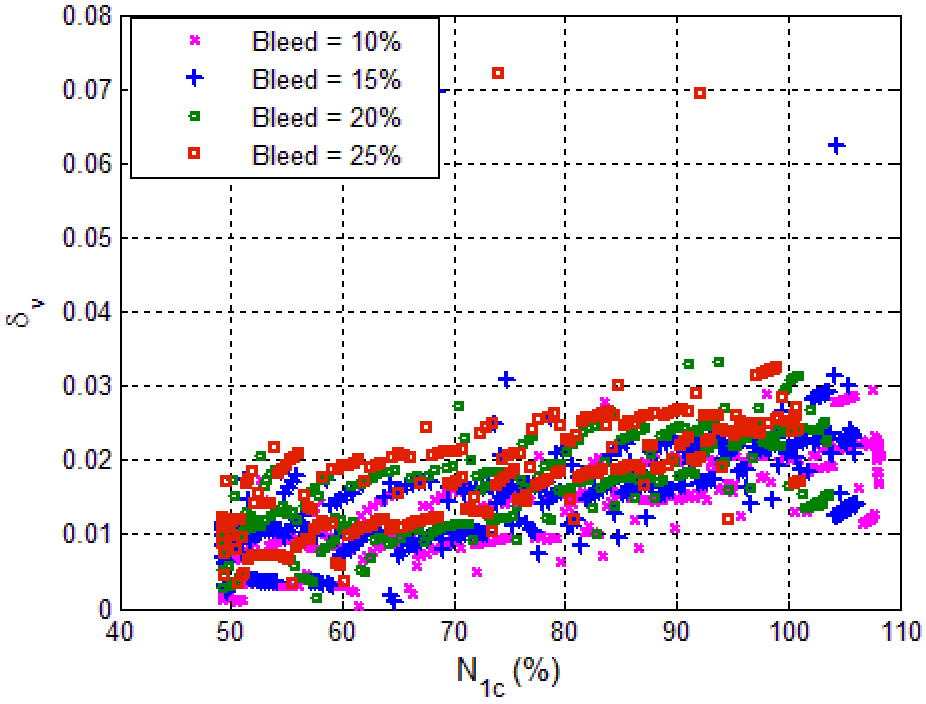

Figure 6.6 ν-gap metric of system output of N_2 using different bleed fractions

6.3 Analysis of Simplifying Assumption for the Combustor

In this section, gas property assumptions of the combustor are analyzed in detail. The enthalpy balance in equation (6.11) requires the assumption with respect to the gas properties.

$$F = \left(w_{30} + w_f\right)h_{40t} - w_{30}h_{30t} - w_f h_{PR}\eta_b = 0 \tag{6.11}$$

The equation (6.11) is linearized into a generic form as

$$\frac{\partial F}{\partial w_{30}}\delta w_{30} + \frac{\partial F}{\partial w_f}\delta w_f + \frac{\partial F}{\partial T_{30t}}\delta T_{30t} + \frac{\partial F}{\partial T_{40t}}\delta T_{40t} = 0 \tag{6.12}$$

Different levels of approximations can be applied to four different linear coefficients as shown in Table 6.1.

Table 6.1 Different level of assumption of the burner

Partial Derivative	**Case 1** c_p **=*f(T)***	**Case 2** c_p **=constant, but different at inlet and outlet**	**Case 3** c_p**=constant, average of inlet and outlet**
$\frac{\partial F}{\partial w_{30}}$	$h_{40t} - h_{30t}$	$c_{p40}T_{40t} - c_{p30}T_{30t}$	$c_{pavg}(T_{40t} - T_{30t})$
$\frac{\partial F}{\partial w_f}$	$h_{out} - h_{PR}\eta_b$	$c_{p40}T_{40t} - h_{PR}\eta_b$	$c_{pavg}T_{40t} - h_{PR}\eta_b$
$\frac{\partial F}{\partial T_{30t}}$	$-c_{p30}w_{30}$	$-c_{p30}w_{30}$	$-c_{pavg}w_{30}$
$\frac{\partial F}{\partial T_{40t}}$	$c_{p40}w_{40}$	$c_{p40}w_{40}$	$c_{pavg}w_{40}$

The Case 1 corresponds to the truth model. The Case 2 in the middle column assumes the constant c_p, but different at inlet and outlet of the burner while the Case 3 in the third column uses the average value of c_p, at inlet and outlet. Two of the linear sensitivities of second column, $\frac{\partial F}{\partial T_{30t}}$ and $\frac{\partial F}{\partial T_{40t}}$, match the truth value of the first column exactly. The *Bodie* trajectory is used to quantify the fidelity of the model with different approximations. The following tasks were applied to the engine model before an investigation of the burner approximations to minimize effects of other assumptions.

1. Remove the bleed from the model (both turbine cooling air and customer bleed are set to zero)
2. Other component level assumptions are minimized using numerical sensitivities where applicable.

First, the effect of simplifying assumption is analyzed in the component level. The change in the outlet temperature using each approximation is shown in Figure 6.7.

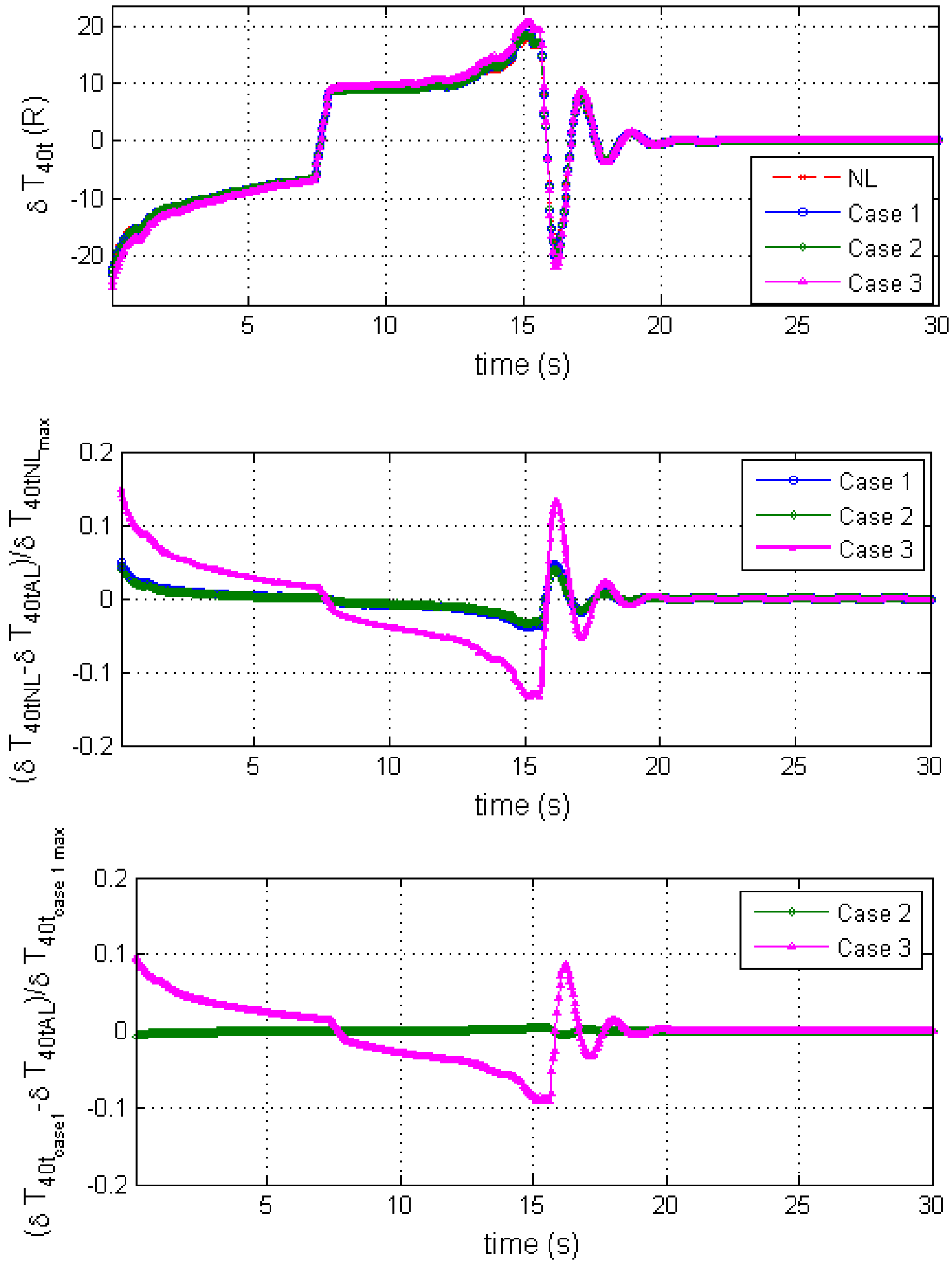

Figure 6.7 Comparison of temperature of burner using different assumptions

The top plot presents the change in temperature resulting from three different cases of linear models in addition to results from the nonlinear model. The middle plot shows the normalized error with respect to the results from nonlinear model. The error in Case 1 is caused by higher order terms (i.e. nonlinearity). The bottom plot exhibits the error of Case 2 and 3 when Case 1 is considered as the truth model. The purpose of this plot is to isolate the origin of the error to the simplifying assumptions of gas property inside the combustor. Results from Case 2 are very close to the results from the truth model given by Case 1 whereas Case 3 produces a much larger error.

The effects of simplifying assumptions are also analyzed using system level integrated results. The normalized additive uncertainty and the ν-gap metric of Cases 2 and 3 calculated with respect to Case 1 as the truth model are shown in Figure 6.8 and Figure 6.9. The normalized additive uncertainty and the ν-gap metric for both N_1 and N_2 of Case 2 are much smaller than those for Case 3. It is concluded that the effect of original assumption of the combustor is minimal and can safely be used for analytical linearization. Therefore, the constant gas property, different at the inlet and outlet, is selected for the combustor component in the final refined model.

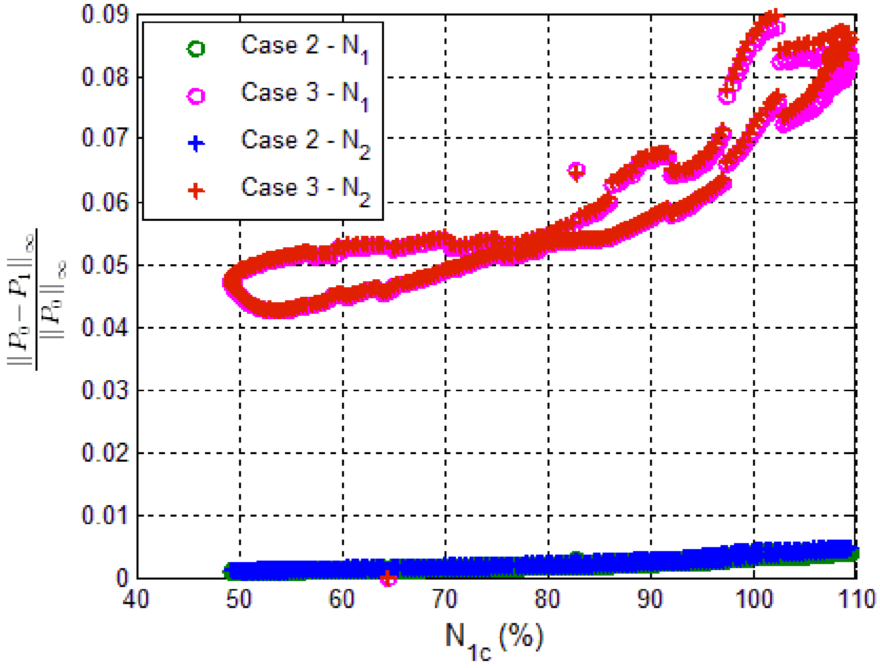

Figure 6.8 Additive uncertainty of system outputs of N_1 and N_2 vs. N_{1c} using different burner assumptions

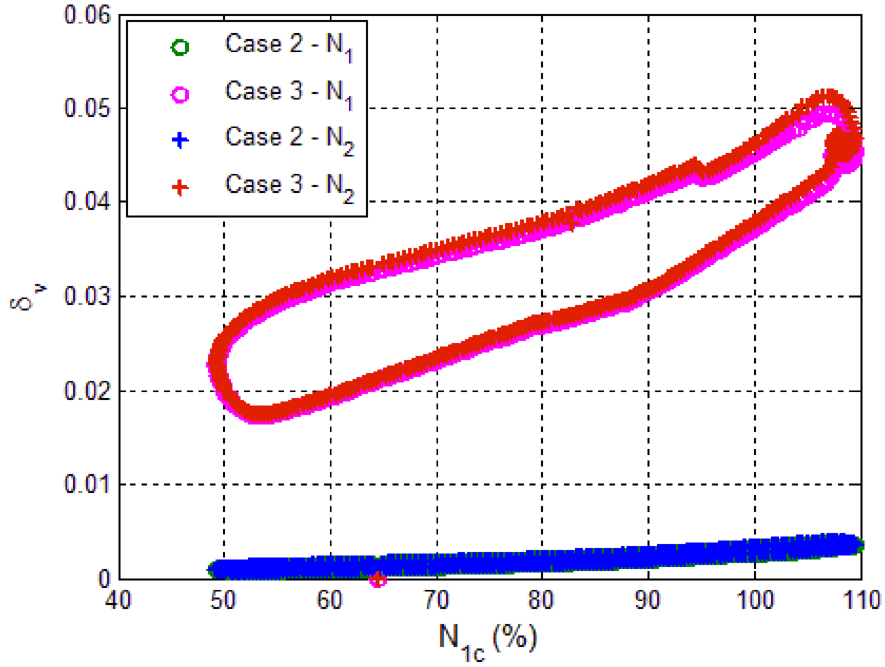

Figure 6.9 ν-gap metric of system outputs of N_1 and N_2 vs. N_{1c} using different burner assumptions

6.4 Gas Property Assumptions for Compressor and Turbine

In this section, assumption 2 (calorically perfect gas assumption) is analyzed for the compressor and turbine components. Case 1 utilizes numerical perturbation for temperature, and enthalpy (not temperature and specific heat) for the torque at the component level. Case 2 is defined as the model using original assumptions. The truth values of linear coefficients for the temperature are obtained by using numerical perturbation as shown in equations (6.13) and (6.14) for the compressor and turbine, respectively. The truth value of the torque is obtained using an analytical expression based on enthalpy as shown in Equation (6.15).

Case 1

Compressor

$$\delta T_{tout} = \frac{\partial f}{\partial T_{tin}} \delta T_{tin} + \frac{\partial f}{\partial P_{tin}} \delta P_{tin} + \frac{\partial f}{\partial Rline} \delta Rline + \frac{\partial f}{\partial N} \delta N \tag{6.13}$$

Turbine

$$\delta T_{tout} = \frac{\partial f}{\partial T_{tin}} \delta T_{tin} + \frac{\partial f}{\partial P_{tin}} \delta P_{tin} + \frac{\partial f}{\partial PR} \delta PR + \frac{\partial f}{\partial N} \delta N \tag{6.14}$$

$$\begin{aligned} \delta\tau &= \left[\frac{(h_{in} - h_{out})}{N} \delta w - \frac{w(h_{in} - h_{out})}{N_2} \delta N + \frac{w}{N} \delta h_{in} - \frac{w}{N} \delta h_{out} \right] \left(\frac{60}{2\pi} \right) \\ &= \left[\frac{(h_{in} - h_{out})}{N} \delta w - \frac{w(h_{in} - h_{out})}{N_2} \delta N + \frac{w}{N} c_{pin} \delta T_{tin} - \frac{w}{N} c_{pout} \delta T_{tout} \right] \left(\frac{60}{2\pi} \right) \end{aligned} \tag{6.15}$$

Equations (6.13) and (6.14) still assume that the change in gas properties are incorporated in direct changes in four parameters, T_{tin}, P_{tin}, $Rline$(or PR) and N. Then it is automatically assumed that the change in c_p and γ are included in the perturbation of T_{tin}, P_{tin}, $Rline$(or PR) and N. The equations for Case 2 are from chapter 3 and restated here for convenience. Only the nonlinear forms of the temperature equations are stated here, the linear form were described in the chapter 3. The efficiency is defined in terms of enthalpy in an example model. Equations (6.16) and (6.17) would have smaller error if the actual efficiency on the component map of the nonlinear model were defined using temperature instead of enthalpy.

Case 2:

Compressor

$$T_{tout} - T_{tin}\left[\frac{1}{\eta_c}\left(\left(\frac{P_{tout}}{P_{tin}}\right)^{\frac{\gamma-1}{\gamma}} - 1\right) + 1\right] = 0 \tag{6.16}$$

Turbine

$$-T_{tout} + T_{tin}\left[1 - \eta_t\left(1 - \left(\frac{P_{tout}}{P_{tin}}\right)^{\frac{\gamma-1}{\gamma}}\right)\right] = 0 \tag{6.17}$$

$$\delta\tau = \left[\frac{c_p(T_{tin} - T_{tout})}{N}\delta w - \frac{wc_p(T_{tin} - T_{tout})}{N}\delta N + \frac{w}{N}c_p\delta T_{tin} - \frac{w}{N}c_p\delta T_{tout}\right]\left(\frac{60}{2\pi}\right) \tag{6.18}$$

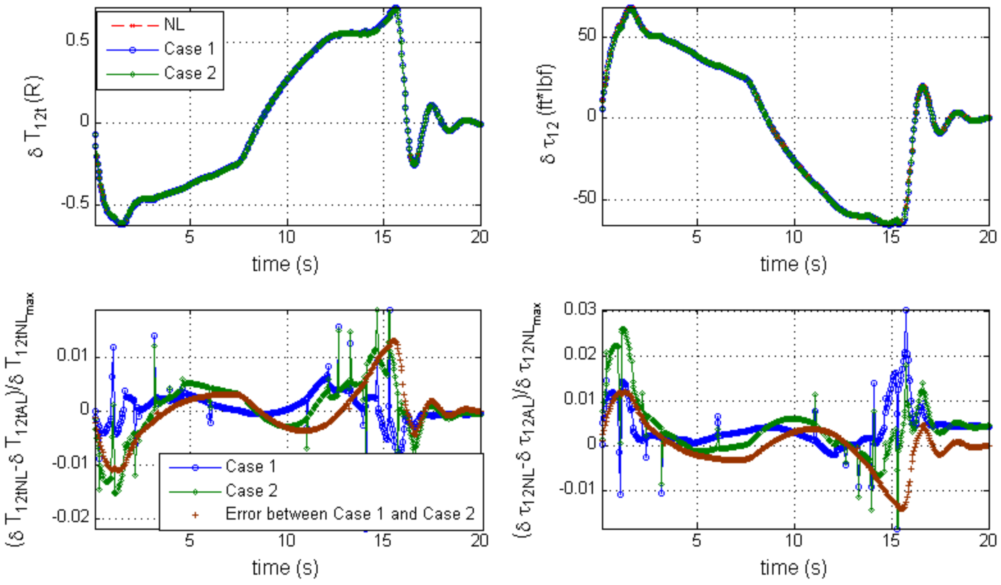

Figure 6.10 Fan simplifying assumption validation

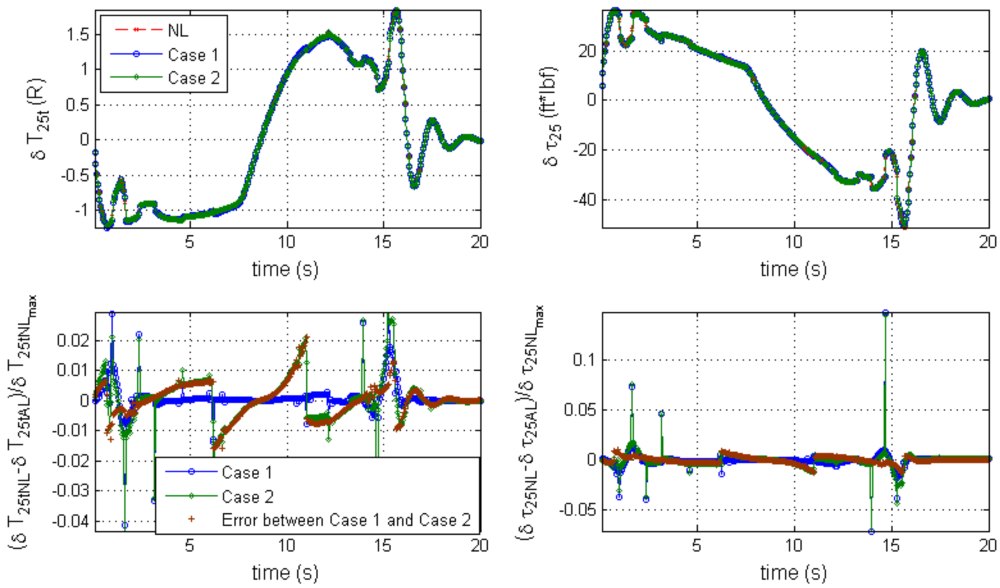

Figure 6.11 LPC simplifying assumption validation

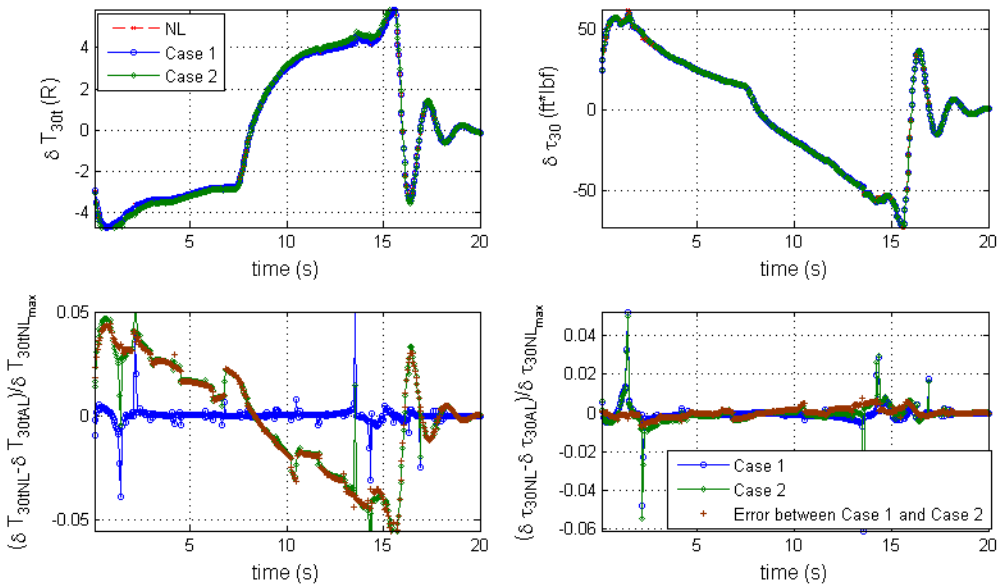

Figure 6.12 HPC simplifying assumption validation

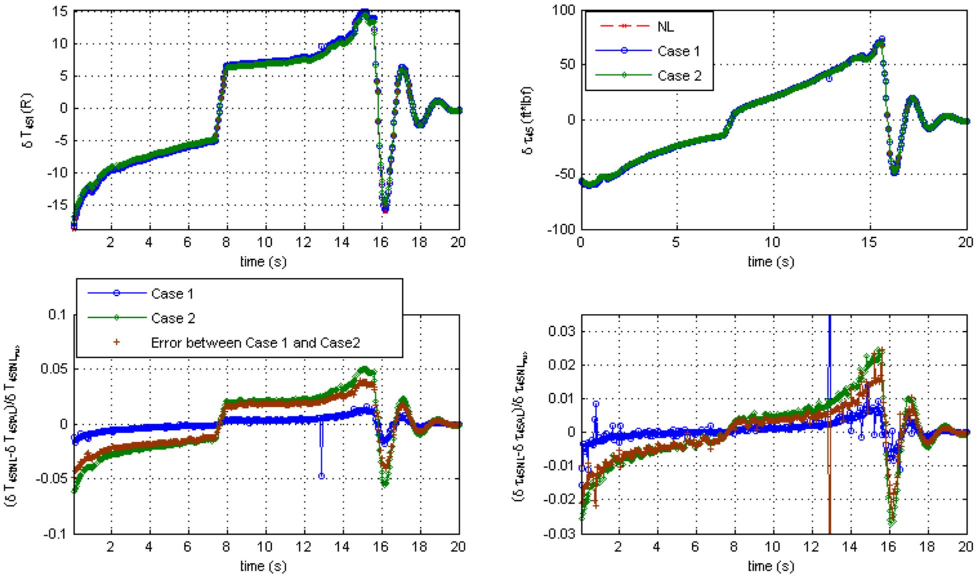

Figure 6.13 HPT simplifying assumption validation

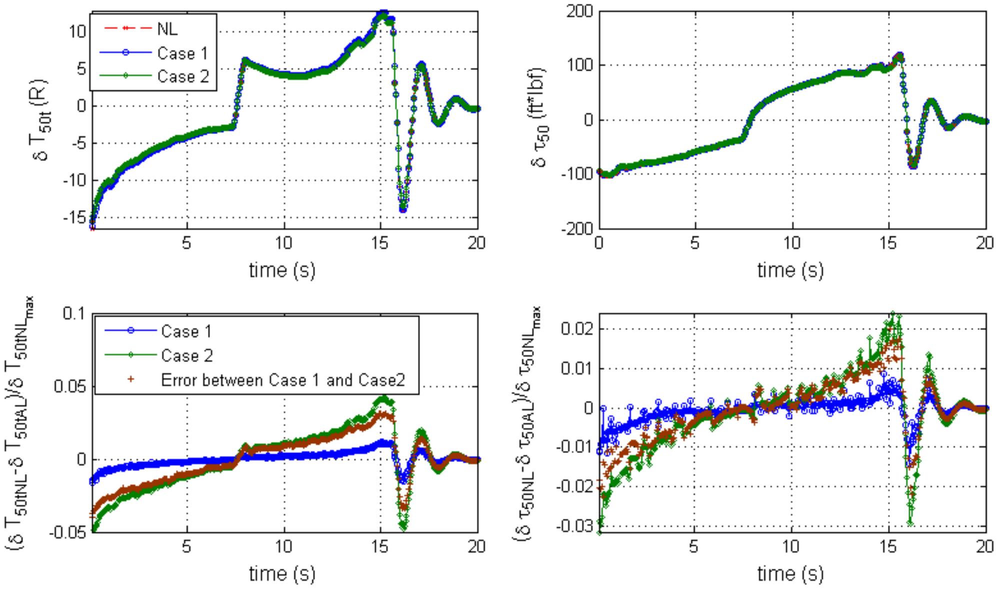

Figure 6.14 LPT simplifying assumption validation

The effect of simplifying assumptions is analyzed in each component using the *Bodie* maneuver and are shown in Figure 6.10-Figure 6.14. The results from the nonlinear truth model are plotted using the dashed lines. The solid lines with circular markers represent the results from Case 1, which is based on component level numerical linearization. The error in numerical linearization is caused by neglecting higher order terms and neglecting effects of other parameters. The error due to neglecting higher order terms is very small. The solid lines with diamond markers represent results using the original assumption of average gas properties. The errors include both the nonlinear effects and effects of simplifying assumptions. The error between Case 1 and Case 2, which is computed assuming that Case 1 is the truth model, is given by the brown cross marker. All errors between Case 1 and Case 2 are bounded by 5%. Errors are much smaller in the fan and LPC than other components because the variation in temperature is much smaller in these components and the effect of temperature variation on the gas property in these elements is negligible.

Caution should be exercised due to coupling between the assumptions for torque and temperature. The truth value of torque without using the truth value of temperature may result in larger error due to mismatching and vice versa.

Table 6.2 Case description for the analysis of gas property

Case 1	Everything using original assumption
Case 2	Fan using original assumption, everything else using minimum assumptions
Case 3	LPC using original assumption, everything else using minimum assumptions
Case 4	HPC using original assumption, everything else using minimum assumptions
Case 5	HPT using original assumption, everything else using minimum assumptions
Case 6	LPT using original assumption, everything else using minimum assumptions

The effect of simplifying assumptions is also analyzed in the integrated system level model. The truth system is derived using the linear model with fewer assumptions (numerically derived temperature coefficient and more accurate torque representation). This model is different from the truth model described in Chapter 4. In fact, this model is still derived using the analytical linearization method, but each linear coefficient of fast dynamic states are derived numerically or using fewer simplifications, resulting in reduced error. The normalized additive uncertainty and the ν-gap metric with respect to the truth system are computed for different cases described in Table 6.2. The results from these cases are shown in Figure 6.15 and Figure 6.18.

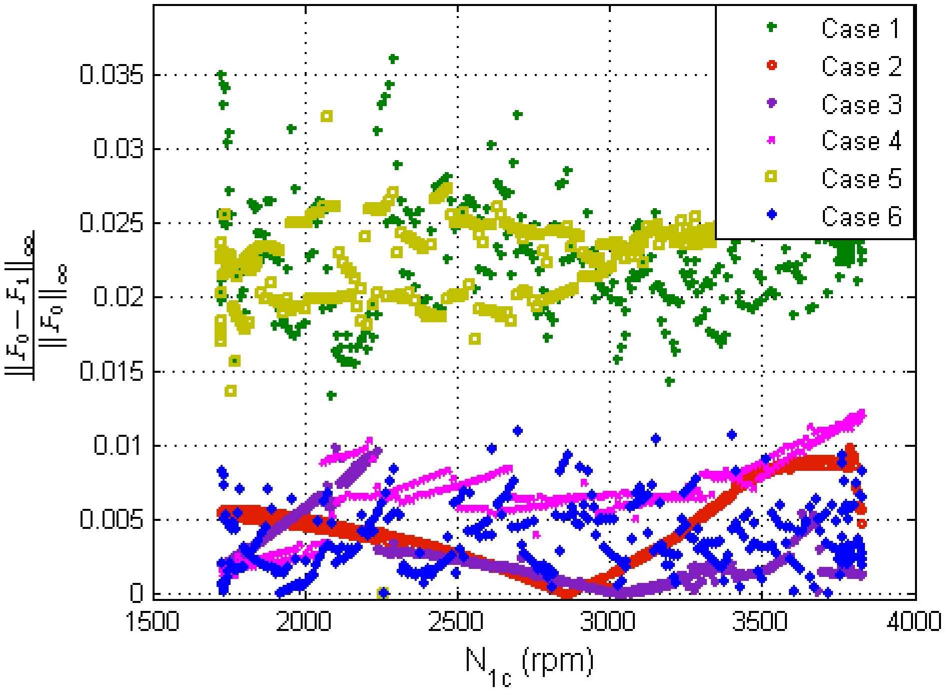

Figure 6.15 Normalized additive uncertainty of system output of N_1 vs. N_{1c} using different assumptions

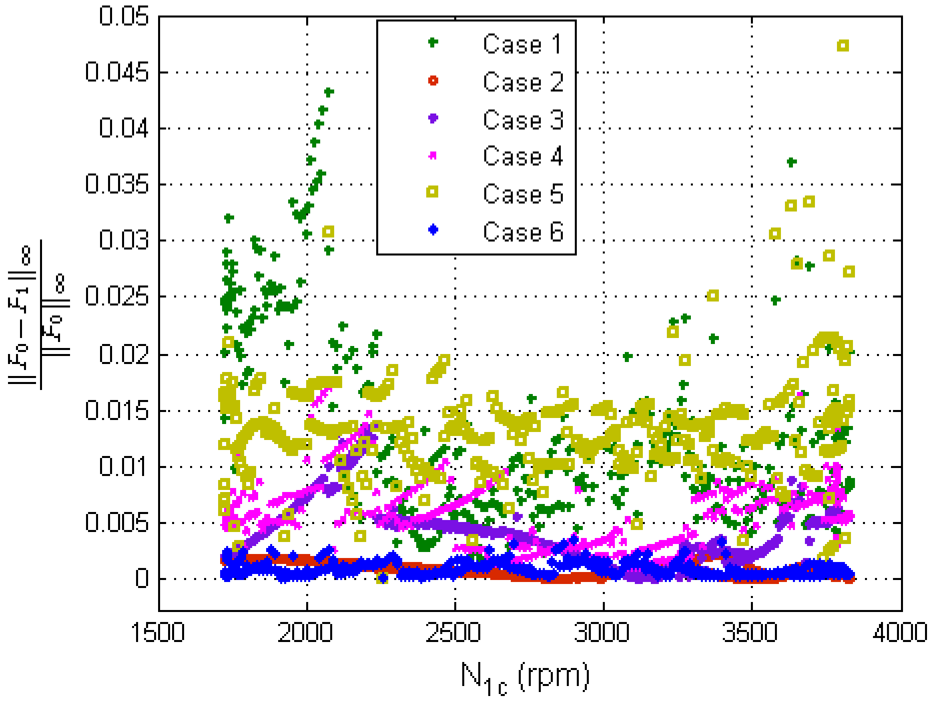

Figure 6.16 Normalized additive uncertainty of system output of N_2 vs. N_{1c} using different assumptions

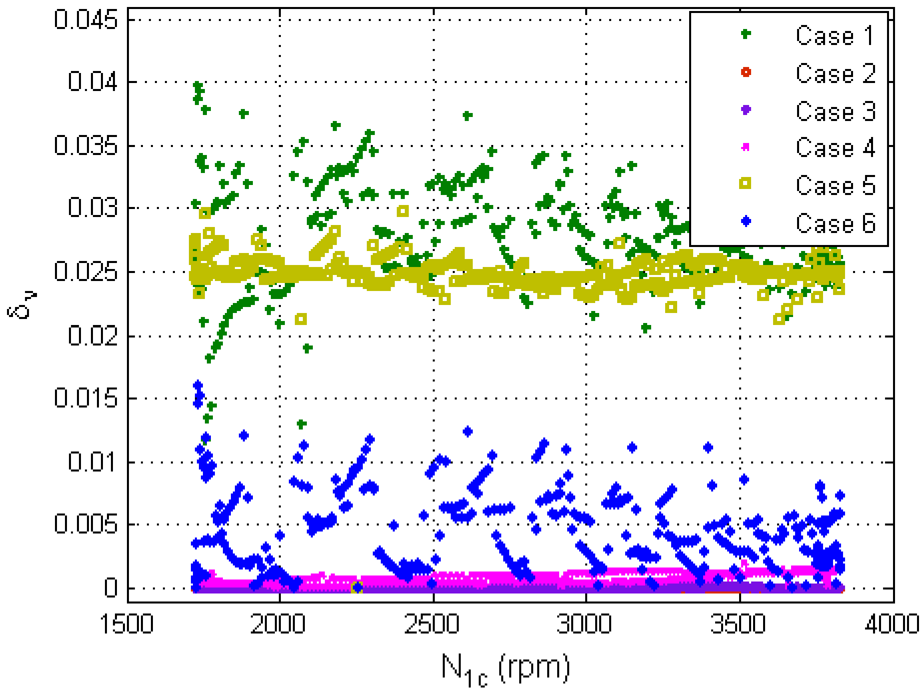

Figure 6.17 ν-gap metric of system output of N_1 vs. N_{1c} using different assumptions

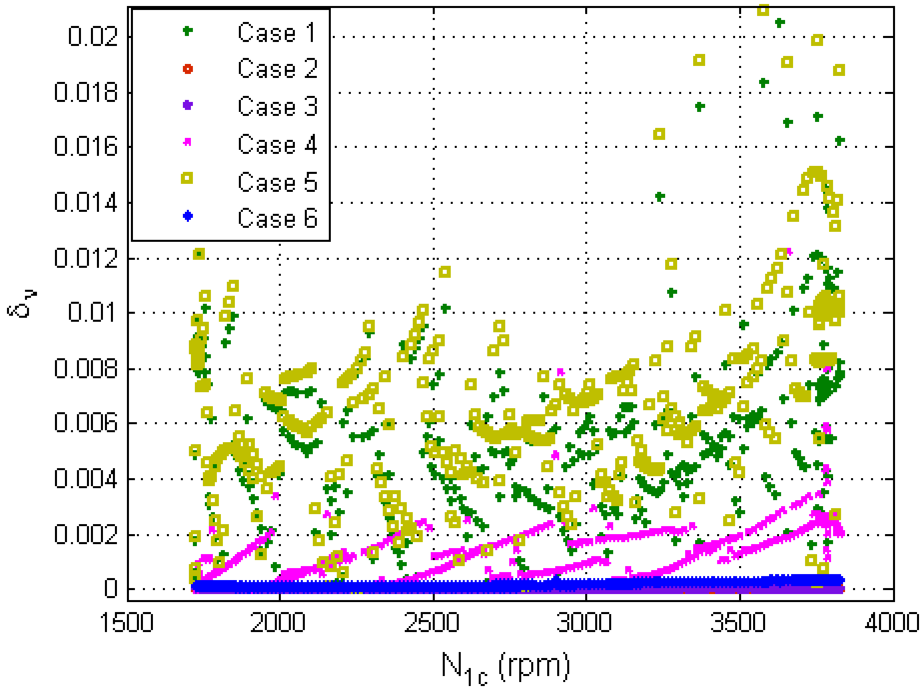

Figure 6.18 ν-gap metric of system output of N_2 vs. N_{1c} using different assumptions

The model errors caused by gas property assumptions are bounded by small values for both closed loop and open loop. This bound is a reasonable cost for achieving the analytical linear model. Note that the biggest contributor the error is from the high pressure turbine element. It is suspected that this is due to greater temperature variation in high pressure turbine compared to other elements.

The modeling error caused by the gas property assumptions in the compressor and turbine will disappear completely if the efficiency is obtained using the relationship between the temperatures instead of using enthalpy measure.

6.5 Summary

The effects of simplifying assumptions used in the analytical linearization on the fidelity of the linearized analytical model were analyzed in detail. Then the model was refined to achieve the desired level of fidelity while satisfying computational requirements. The assumptions on the bleed were relaxed because the original assumption caused large discrepancies from the truth model and the resulting linear model showed unsatisfactory level of fidelity. The refined model still requires some level of assumptions with respect to the gas property of the bleed flow; but the model with the relaxed assumption is able to achieve the required fidelity. The assumptions with respect to gas properties of the combustor, compressor and turbine were also analyzed in detail. The effect of the assumptions on model fidelity is within acceptable range. The benefits of making these assumptions far exceeded the cost of the small reduction on model fidelity.

CHAPTER 7

MODEL APPLICATIONS

This chapter performs case studies to investigate potential problems of the proposed linearization method and to introduce a useful control application.

7.1 Case Study

The presented linearization method is based on the assumption that the nonlinear values from the current operating condition are available. In this section, a study is performed to investigate the case when nonlinear simulation fails to generate a converged solution. Two possible solutions are investigated. The first method involves simply holding the previous linear sensitivities whenever the nonlinear simulation fails to converge in time. The second method is to use the previously developed linear coefficients to estimate the current nonlinear values to be used for the evaluation of the analytical expressions.

7.1.1 Solution 1: Use of Previously Converged Nonlinear Values

The solution of using previously converged nonlinear values is equivalent to placing a zero-order-hold (ZOH) in between evolving linear coefficients. The linear coefficients are held constant for a certain amount of time during the *Bodie* trajectory and compared with the truth model, which is updated every time step, using additive uncertainty and the ν–gap metric as shown in Figure 7.1. This ZOH results in the quantized linear coefficients as shown in Figure 7.2. The ZOH should not have too much effect on a slowly varying system; however, it would cause large errors in a rapidly varying system. Since the *Bodie* trajectory results in rapid changes in engine states, error due to ZOH is well illustrated.

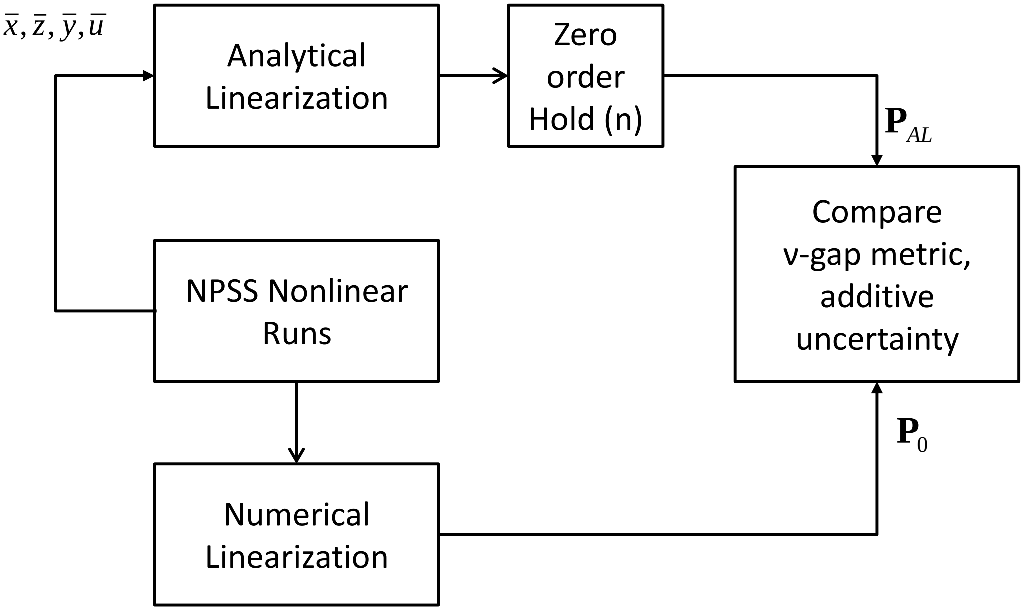

Figure 7.1 Structure of analytical linearization with ZOH

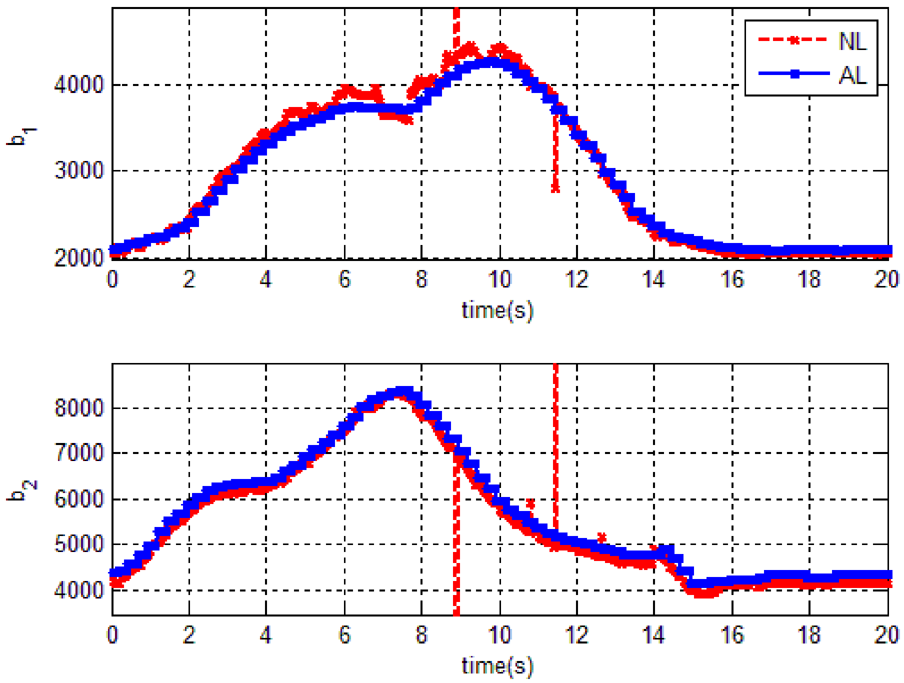

Figure 7.2 B matrix during *Bodie* trajectory with ZOH=5

Figure 7.3 and Figure 7.4 show the normalized additive uncertainty for the system with an output of N_1 and N_2, respectively, for different ZOHs. Figure 7.5 and Figure 7.6 show the ν-gap metric for the system with an output of N_1 and N_2, respectively, for different ZOHs. Each value is plotted against the corrected fan speed. The baseline case (AL) uses continuously updated nonlinear values for calculating linear coefficients with a sampling time of 0.05 seconds.

When the nonlinear values are held constant for two consecutive sampling periods, results do not deviate much from the case with the continuous update of linear coefficients for all additive uncertainty and ν-gap metric. The system with a ZOH of 3 starts to drift away from the baseline case. However, most of the time it still generates much smaller error than the piecewise linear model for both open loop and closed loop. The open loop system error grows as large as that for the piecewise linear model when the linear sensitivities are held constant for 5 sampling periods. However, the closed loop system uncertainty of the analytical linear model with a ZOH of 5 is still much smaller than that of the piecewise linear model, especially for the system with output of N_2. The additive uncertainty of the analytical linear model with a ZOH of 7 exceeds the additive uncertainty of the piecewise linear model in multiple places; but ν-gap metric for N_2 is still much smaller than the piecewise linear model and the ν-gap metric for N_1 is about the same as that of the piecewise linear model.

It is concluded that missing nonlinear values for a couple of time steps is not a serious issue and the real-time analytical linear model along the transient trajectory is still preferred over the piecewise linear model developed along the steady-state lines. With the robust controller design, the failure to achieve the nonlinear solution for multiple sampling times will not result in any catastrophic effects as conventional linear models already include large deviations during large transient. In fact, the reduction of the frequency of linear coefficients update can be considered if the computational aspect bears more weight than accuracy.

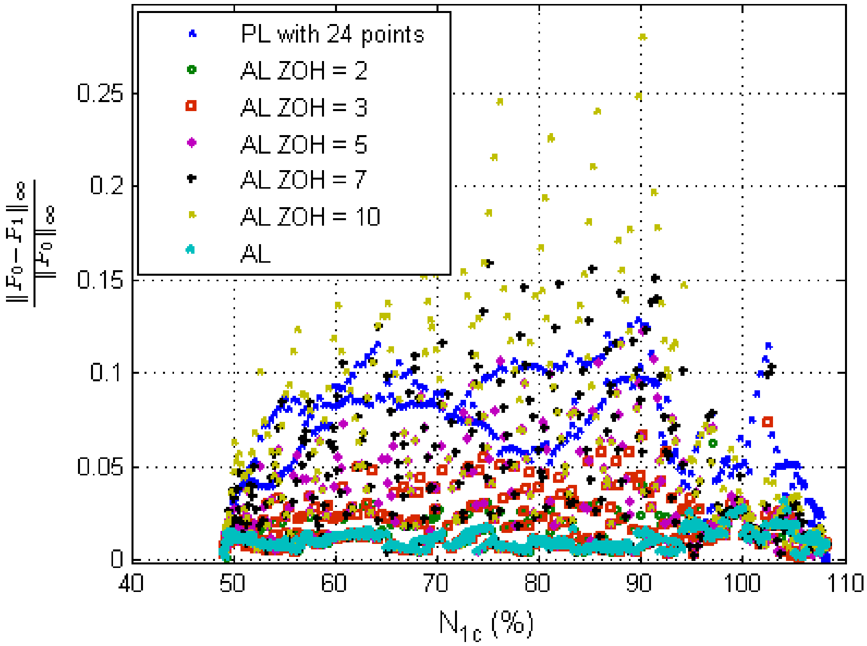

Figure 7.3 Additive uncertainty of system output of N_1 for different zero order hold time

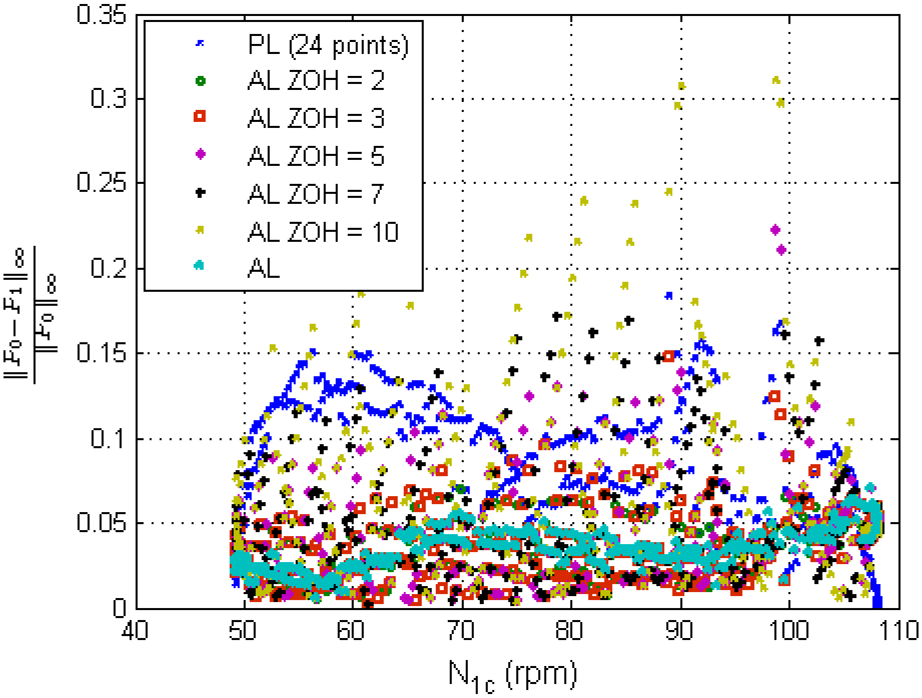

Figure 7.4 Additive uncertainty of system output of N_2 for different zero order hold time

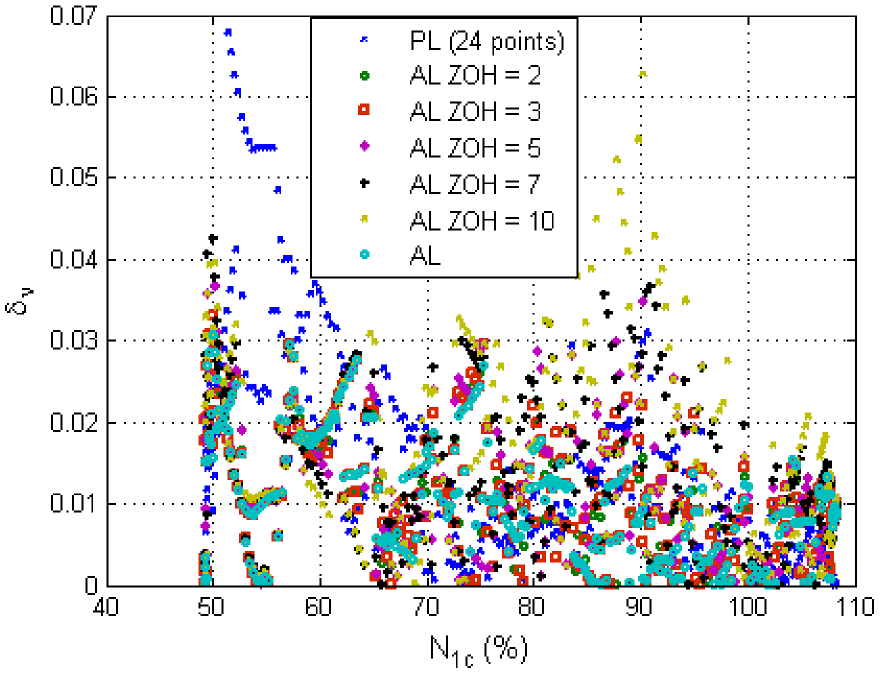

Figure 7.5 **ν-gap metric of system output of** N_2 **for different zero order hold time**

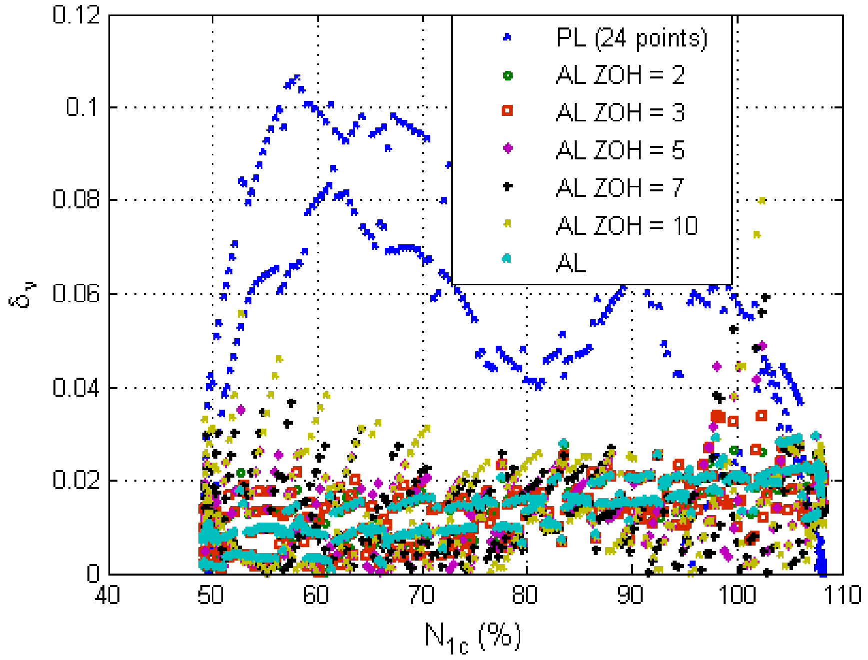

Figure 7.6 **ν-gap metric of system output of** N_2 **for different zero order hold time**

7.1.2 Solution 2: Use of Linear Model Estimation

The alternative solution is to use the linear model to estimate current values that can be used for calculating linear coefficients. This can be repeated as necessary for predicting an engine transient trajectory as shown in Figure 7.7. Gas properties are obtained from the table lookups from the NPSS gas table using the estimated value from the linear model. Also the map sensitivities are obtained using the estimated values from the linear model. This method is more complex than the first method described as it requires estimating the nonlinear values. On the other hand, this is more powerful as the linear model can replace the nonlinear model in the future if it can be enhanced with a Kalman filter using actual measurements. Such an enhanced model may also be used for improving solver convergence. The estimated values from the linear model can be used for the solver initial guess to speed up the solver convergence and to prevent solver instability. In the present work, such an estimation model is only briefly discussed to demonstrate the possibility for the potential future work as an extensive analysis is outside the scope of this thesis.

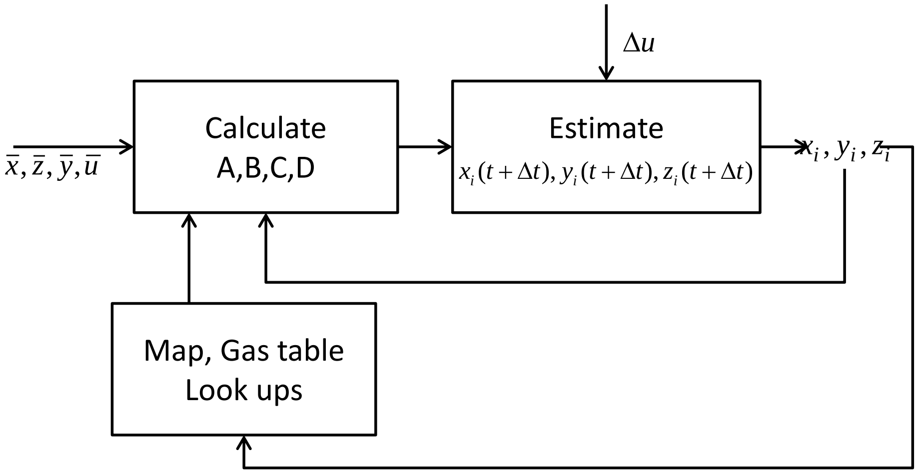

Figure 7.7 Estimation model

Since the setup does not include correction such as a Kalman filter, the estimated values slowly drift away from the actual trajectory with increasing time due to accumulated error. Also any hard nonlinearity, such as a discontinuous slope in the map, contributes to rapid accumulation of the error. Therefore, a carefully selected, modified, shorter, transient trajectory is used in this section for demonstration purposes. This is still snap deceleration followed by snap acceleration and there is rapid change in the states.

Figure 7.9 to Figure 7.11 present the linear estimates of selected shaft dynamics, temperature and pressure for the state and input trajectory shown in Figure 7.8. The linear estimates using analytical linearization is compared with the actual difference from the nonlinear simulation. The linear estimates capture the actual values well even though the linear coefficients are calculated using estimated nonlinear values from the linear model. The linear estimates start to drift away from the actual response at around 7 seconds. The linear coefficients are plotted against time in Figure 7.12 and Figure 7.13. Again, results are compared with the piecewise linear model. Even though the modeling error is larger than when the nonlinear simulation results are used for computing the linear coefficients, the benefit of using the analytical real time linear model over using the piecewise linear model is well demonstrated in coefficient $\mathbf{B_2}$, which is non-scheduling parameter.

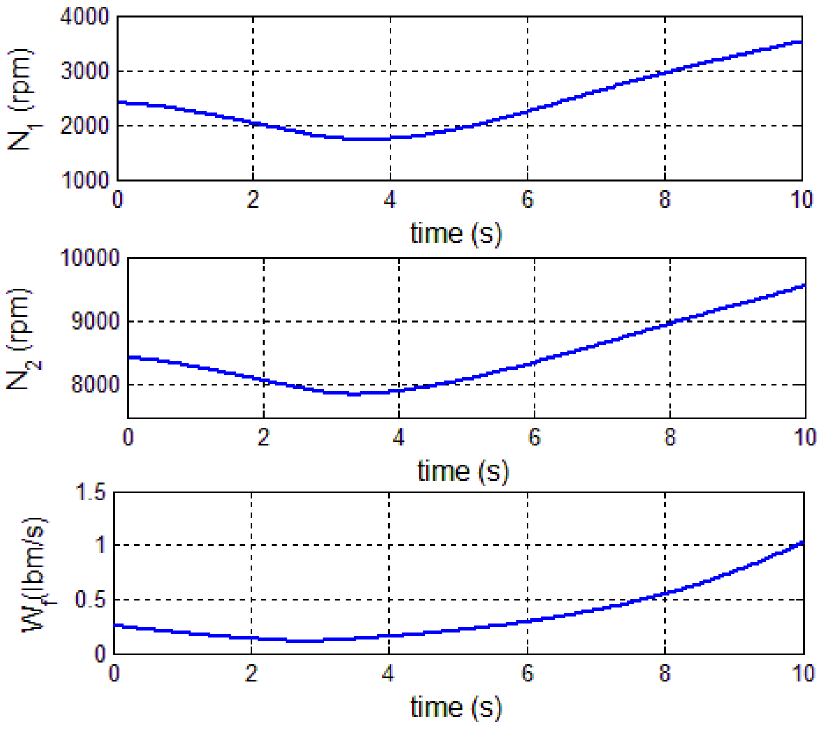

Figure 7.8 States and input during modified trajectory

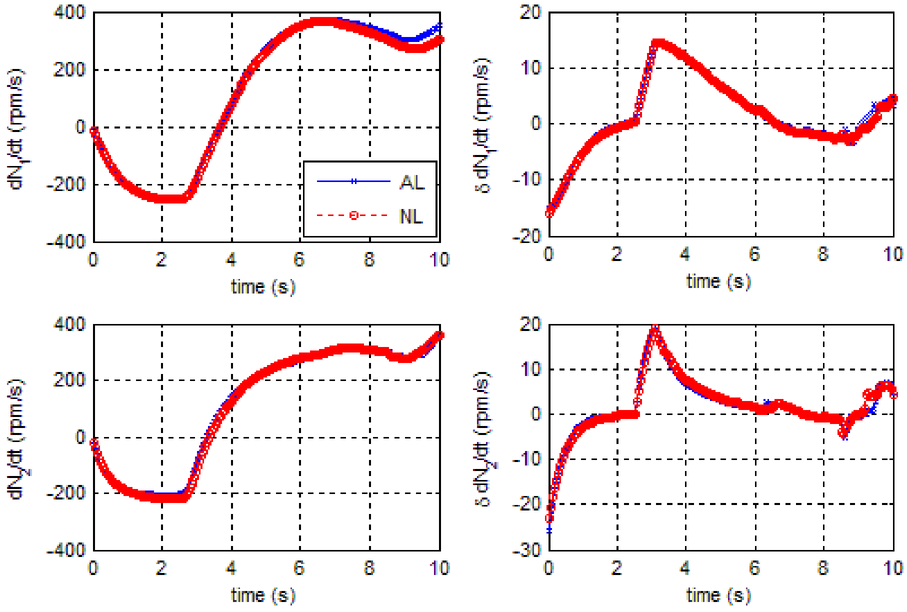

Figure 7.9 Shaft dynamics comparison between off-equilibrium analytical linear model using estimation, and nonlinear values

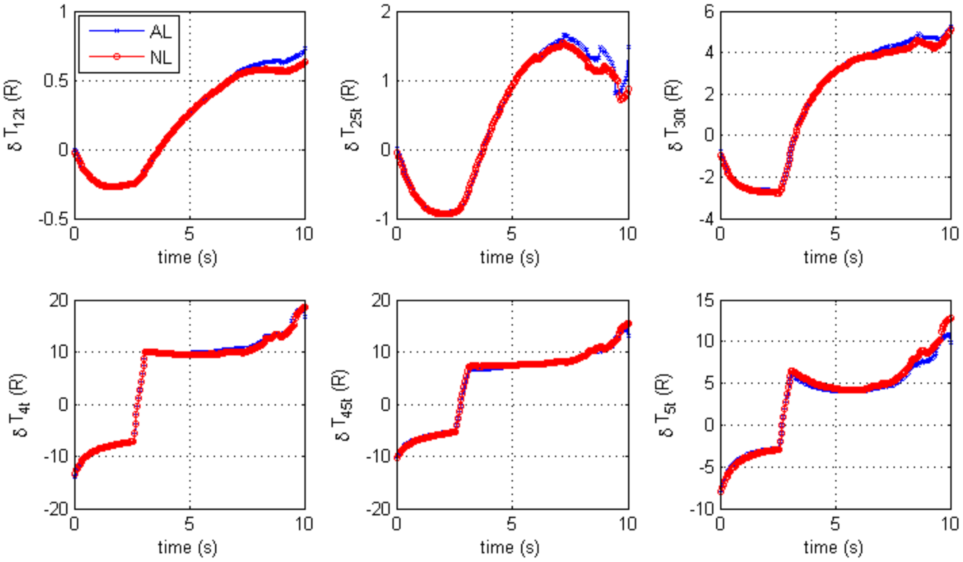

Figure 7.10 Temperature at different stations comparison between off-equilibrium analytical linear model using estimation, and nonlinear values

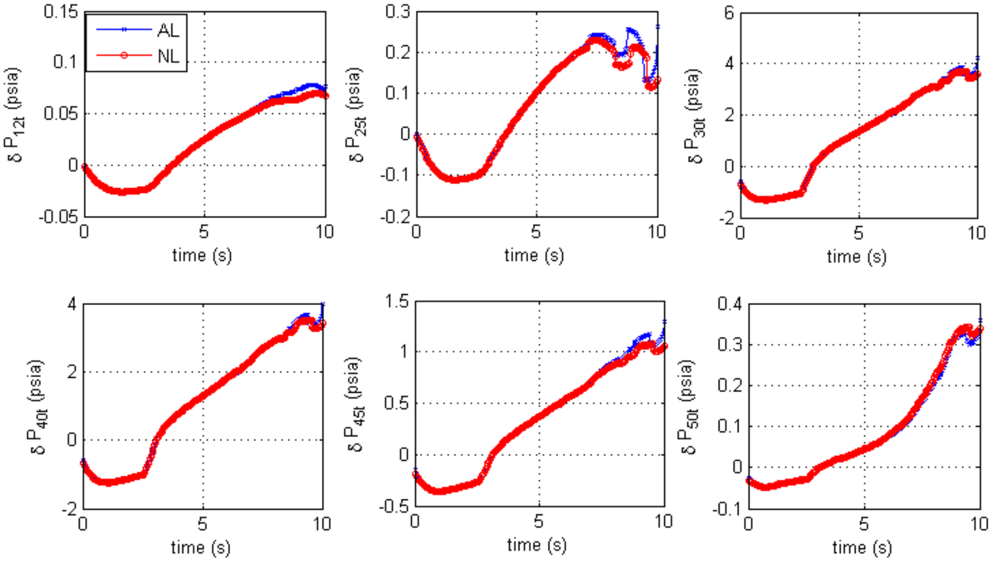

Figure 7.11 Pressure at different stations comparison between off-equilibrium analytical linear model using estimation, and nonlinear values

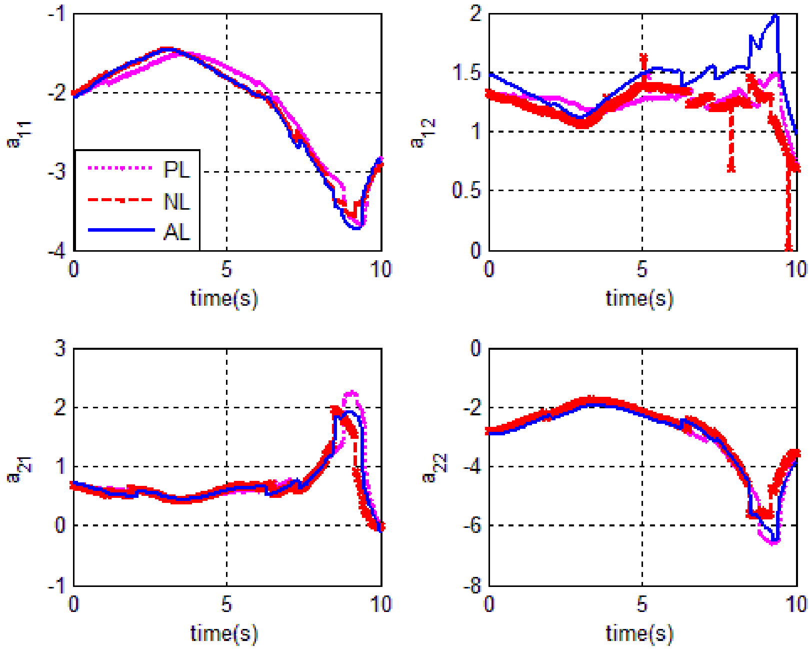

Figure 7.12 Evolution of elements of A matrix during transient operation using three different linearization methods

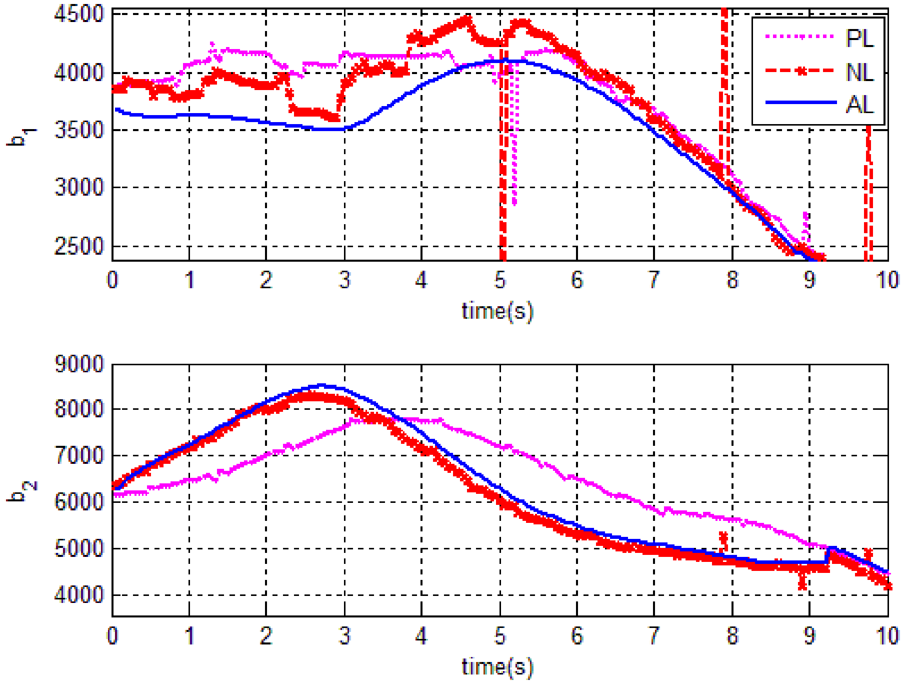

Figure 7.13 Evolution of elements of B matrix during transient operation using three different linearization methods

The quantitative model errors using additive uncertainty and ν-gap metric for different outputs is presented in Figure 7.14-Figure 7.17. The advantage of using off-equilibrium linearization is well demonstrated in all four parameters. The modeling errors using an estimated value for the computation of linear coefficients stay within reasonable bounds for designing a controller. In fact, the errors stay below the errors of the piecewise linear model for this particular trajectory most of time. The estimation model fares much better than the piecewise linear model during severe transient operation. The results are promising for potential future development of a linear estimation model for a nonlinear engine system.

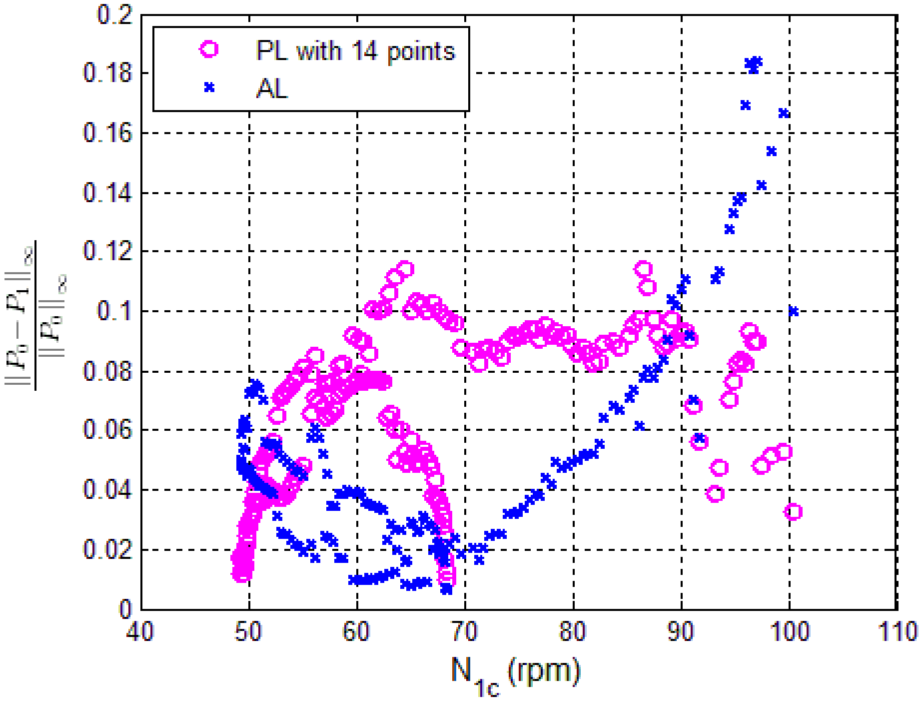

Figure 7.14 Normalized additive uncertainty of system outputof N_1

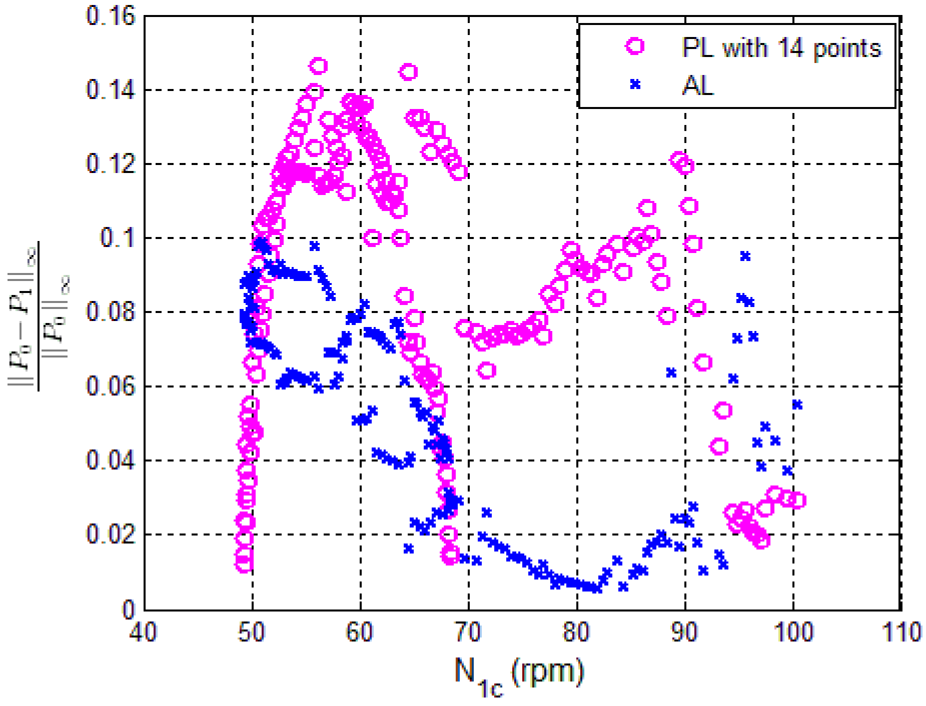

Figure 7.15 Normalized additive uncertainty of system output of N_2

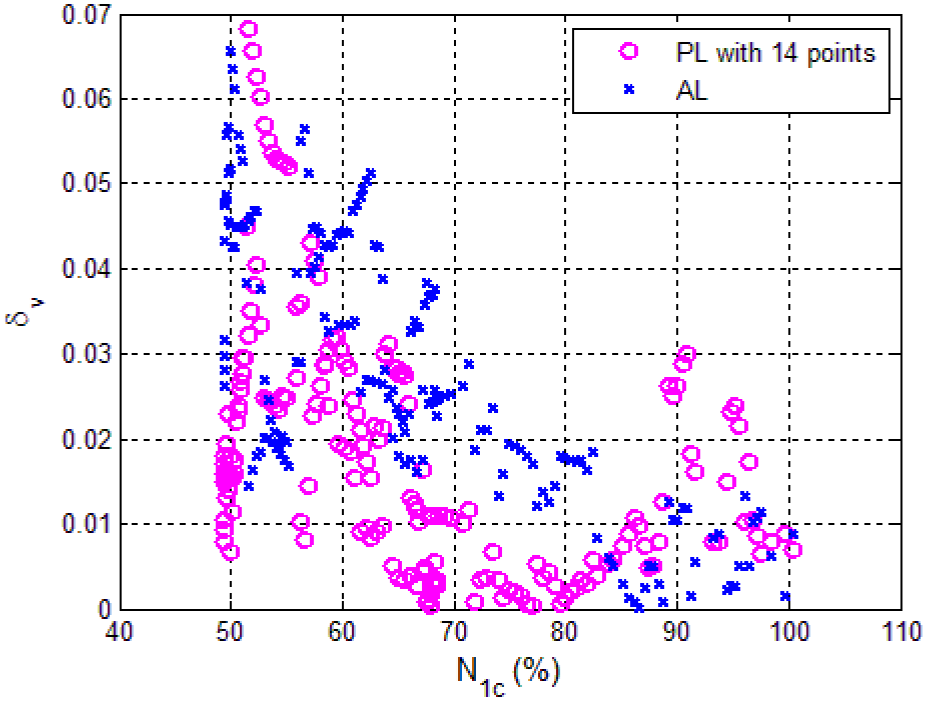

Figure 7.16 ν-gap metric of system output of N_1

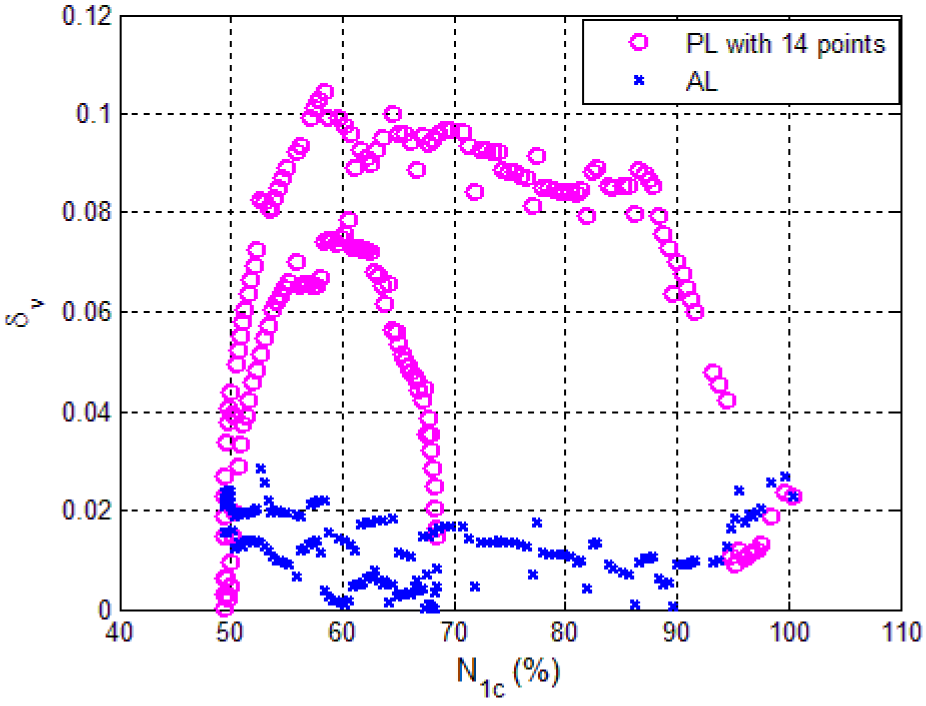

Figure 7.17 ν-gap metric of system output of N_2

The limitation of the model for a standalone estimation application is observed in a more aggressive trajectory. Although the trend of linear sensitivities are still well captured during the *Bodie* trajectory as shown in Figure 7.18 and Figure 7.19, model error accumulates much quicker than the previous example and the model loses accuracy, as shown by the quantified error in Figure 7.20 through Figure 7.23. The rate at which error accumulates depends on the trajectory as some trajectories are affected more severely by the simplifying assumptions. Also, fast accumulation of error occurs when the transient trajectory goes through areas where map sensitivities change rapidly (e.g. discontinuous map slope). This observation leads to the conclusion that the model by itself cannot replace the nonlinear model for estimation application and the addition of a correction filter such as a Kalman filter is required to improve accuracy.

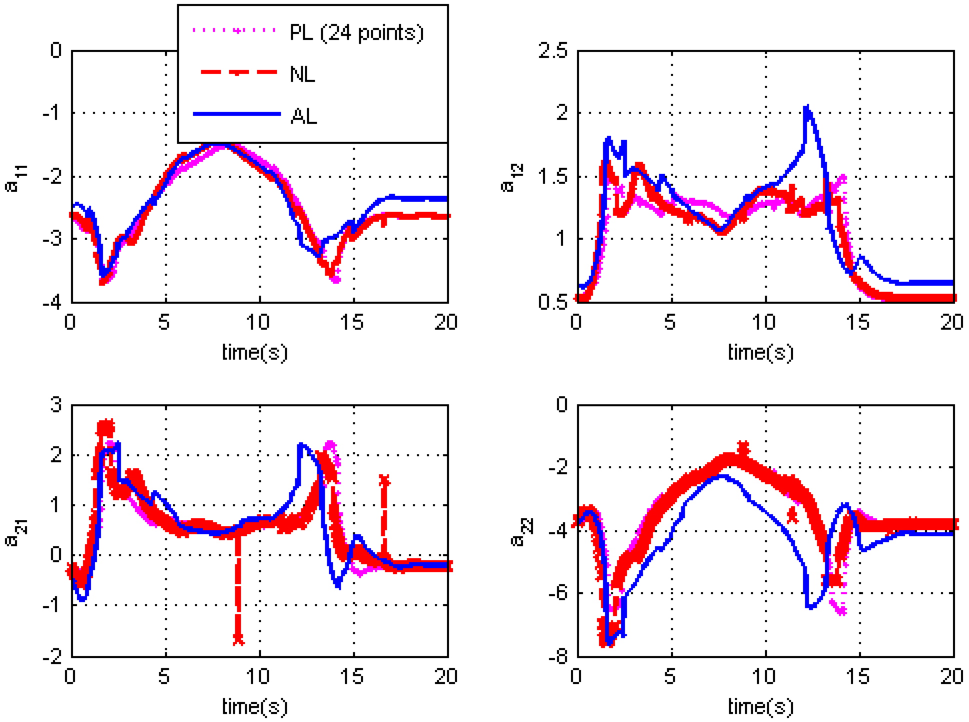

Figure 7.18 Evolution of elements of A matrix during *Bodie* manuever using three different linearization methods

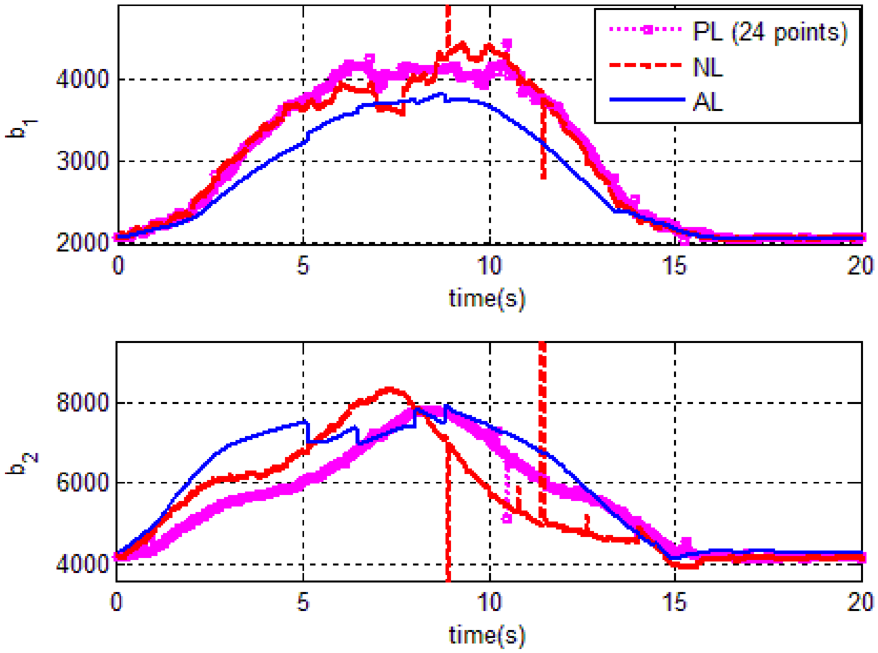

Figure 7.19 Evolution of elements of B matrix during *Bodie* manuever using three different linearization methods

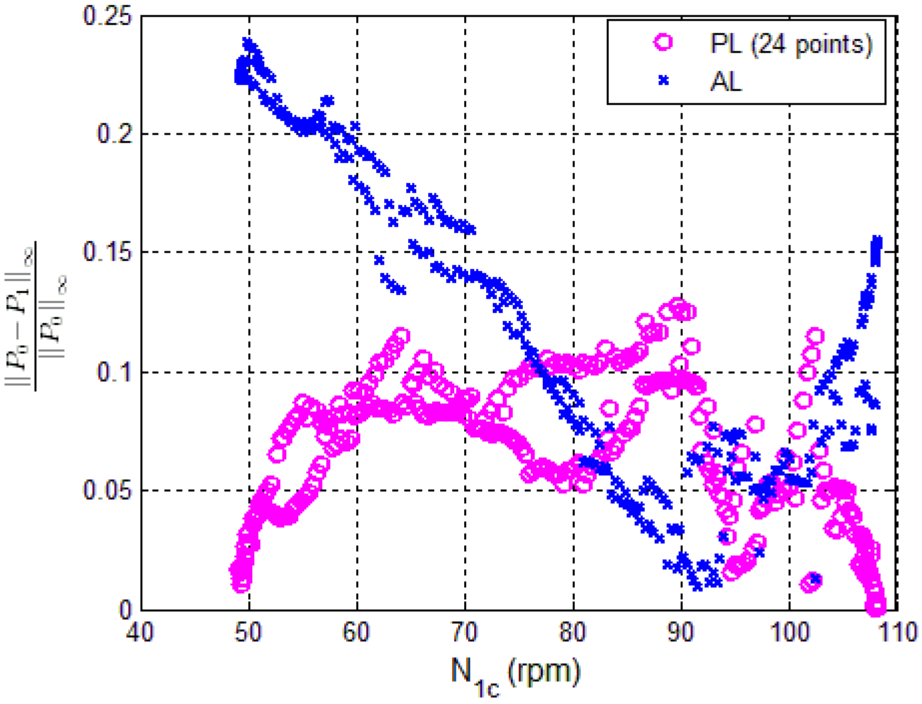

Figure 7.20 Normalized additive uncertainty of system output of N_1

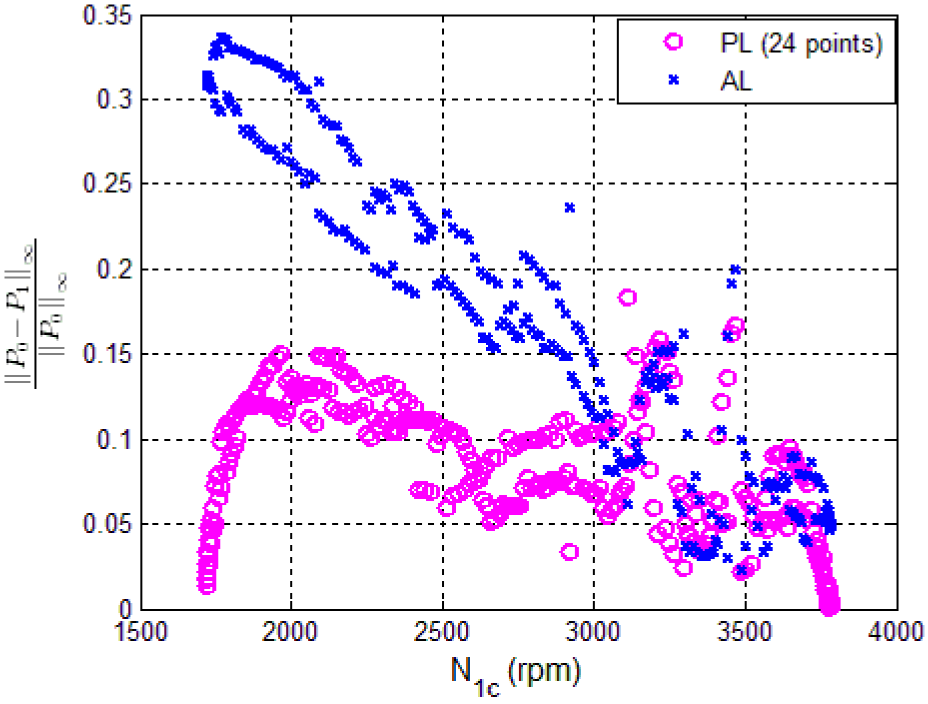

Figure 7.21 Normalized additive uncertainty of system output of N_2

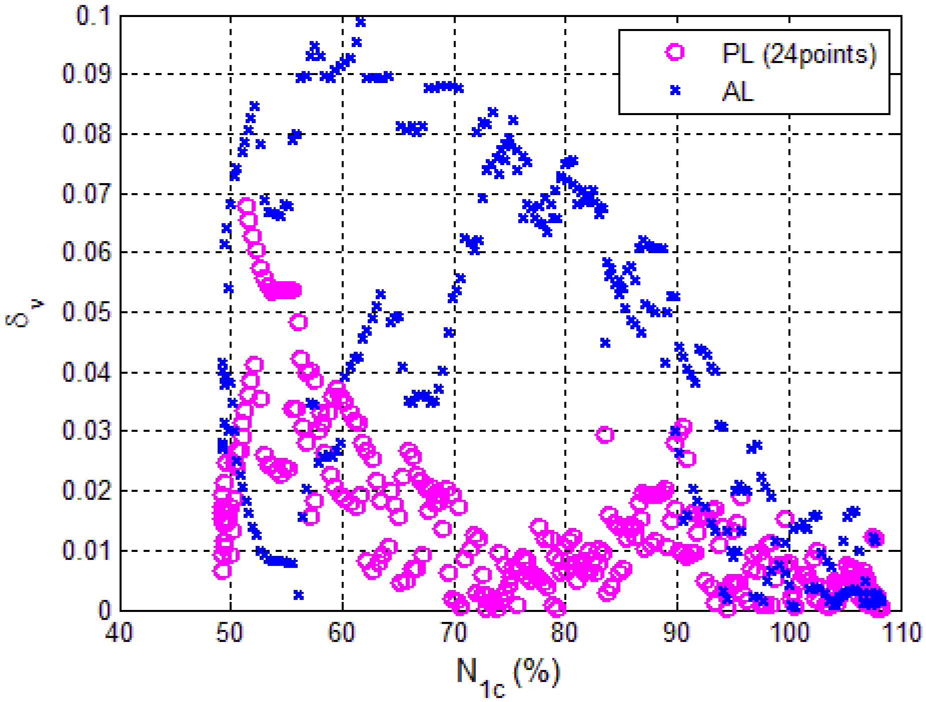

Figure 7.22 ν-gap metric of system output of N_1

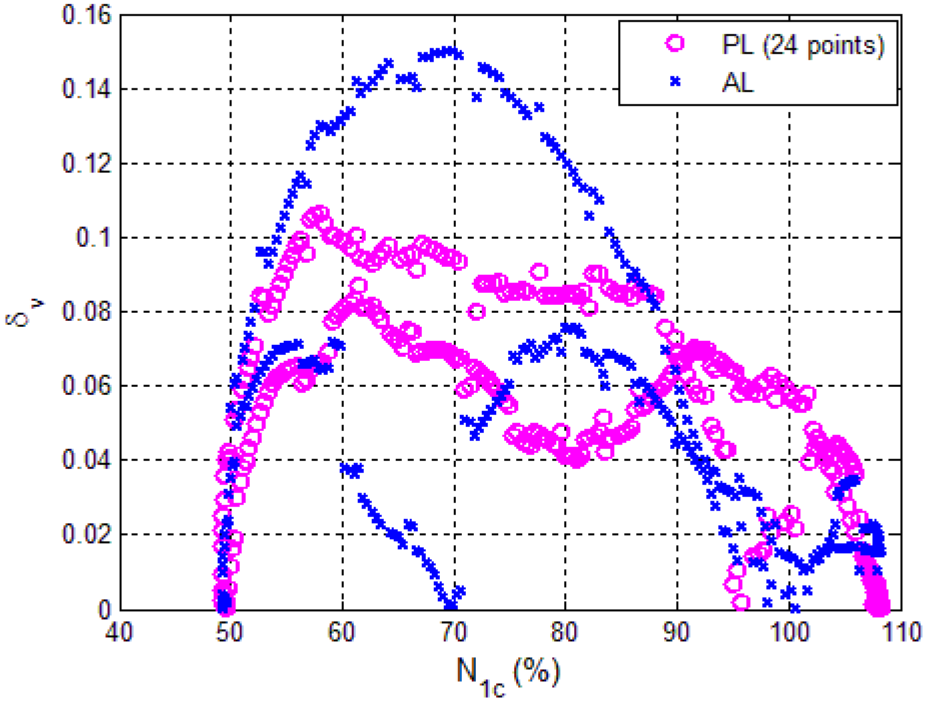

Figure 7.23 ν-gap metric of system output of N_2

7.2 Model Inversion Controller Example

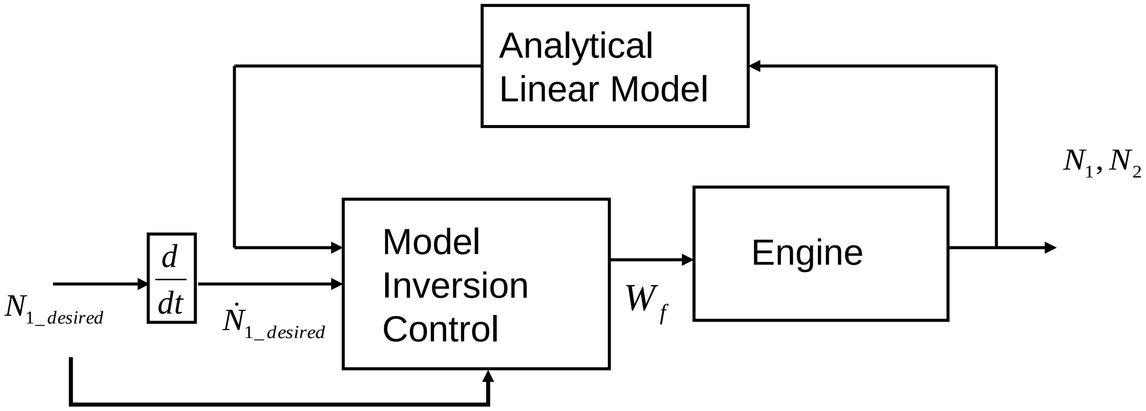

Figure 7.24 Model inversion control block diagram

A simple model inversion controller tracking the desired fan speed is implemented to demonstrate the benefits of using the proposed analytical real-time linear modeling approach. The model inversion controller using analytical real-time linearization is compared with the model inversion controller using a two-point piecewise linear model scheduled with N_1. The accuracy of a model based controller for the traditional piecewise linear model depends on the number of interpolation points and how the scheduling is achieved. For simplicity, two point piecewise linear model over approximately 10% speed increment is selected here. The reference trajectory of fan speed is given by equation (7.1). The derivative of y is taken until the control input explicitly appears in the expression.

$$y_r = \overline{N}_1 + \Delta N_1\left(1 - e^{-\frac{t}{\tau}}\right), \qquad \dot{y}_r = \frac{\Delta N_1}{\tau} e^{-\frac{t}{\tau}} \tag{7.1}$$

$$\begin{aligned} y &= Cx + \overline{y} \\ \dot{y} &= C\dot{x} = Cf(\overline{x}, \overline{u}) + CA\delta x + CB\delta u \end{aligned}$$

Let $\dot{y} = \nu$ (pseudo control), such that

$$\delta u = (\mathbf{CB})^{-1}(\nu - \mathbf{C}f(\bar{x},\bar{u}) - \mathbf{CA}x)$$

$$\nu = \dot{y}_r + K_p(y_r - y) + \int_0^t K_i(y_r - y)dt$$

Then the closed loop system becomes

$$\dot{y} = \dot{y}_r + K_p(y_r - y) + \int_0^t K_i(y_r - y)dt \tag{7.2}$$

The model inversion control input for the analytical linear model is given by equation (7.3) where δ is defined from an arbitrary condition. The model inversion control law for the traditional linear model is derived similarly and given by equation (7.4). Here, Δ is defined from the equilibrium operating condition.

$$\delta u = (\mathbf{CB})^{-1}\left[\dot{y}_r + K_p(y_r - y) + \int_0^t K_i(y_r - y)dt - \mathbf{C}f\left(\bar{x},\bar{u}\right) - \mathbf{CA}\delta x\right] \tag{7.3}$$

$$\Delta u = (\mathbf{CB})^{-1}\left[\dot{y}_r + K_p(y_r - y) + \int_0^t K_i(y_r - y)dt - \mathbf{CA}\Delta x\right] \tag{7.4}$$

Let $e = y - y_r$, then equation (7.2) can be rewritten as

$$\dot{e} + K_p e + \int_0^t K_i e dt = 0 \tag{7.5}$$

Substituting $e = {}^{dq}\!/_{dt}$,

$$\ddot{q} + K_p\dot{q} + K_i q = 0$$
$$\begin{bmatrix} \dot{q} \\ \ddot{q} \end{bmatrix} = \begin{bmatrix} 0 & 1 \\ -K_i & -K_p \end{bmatrix} \begin{bmatrix} q \\ \dot{q} \end{bmatrix} = \mathbf{A}_e \mathbf{q} \tag{7.6}$$

Error dynamics (7.5) is asymptotically stable for all $\mathbf{A_e} \in \Re^{2x2}, K_p > 0, K_i > 0$. Therefore, $e \to 0$ as $t \to \infty$.

The results for the two different model inversion controllers for tracking N_1 are presented in Figure 7.25. The model inversion controller using the analytical real-time linear model tracks the desired trajectory much better than the model inversion controller using the piecewise linear model. Results for similar model inversion controllers for tracking N_2 speed are shown in Figure 7.26. The benefits seen with the use of the proposed real time linear model for model based control are expected be greater compared to the use of piecewise linear models when the desired trajectory is more aggressive and distanced from the steady-state operating condition.

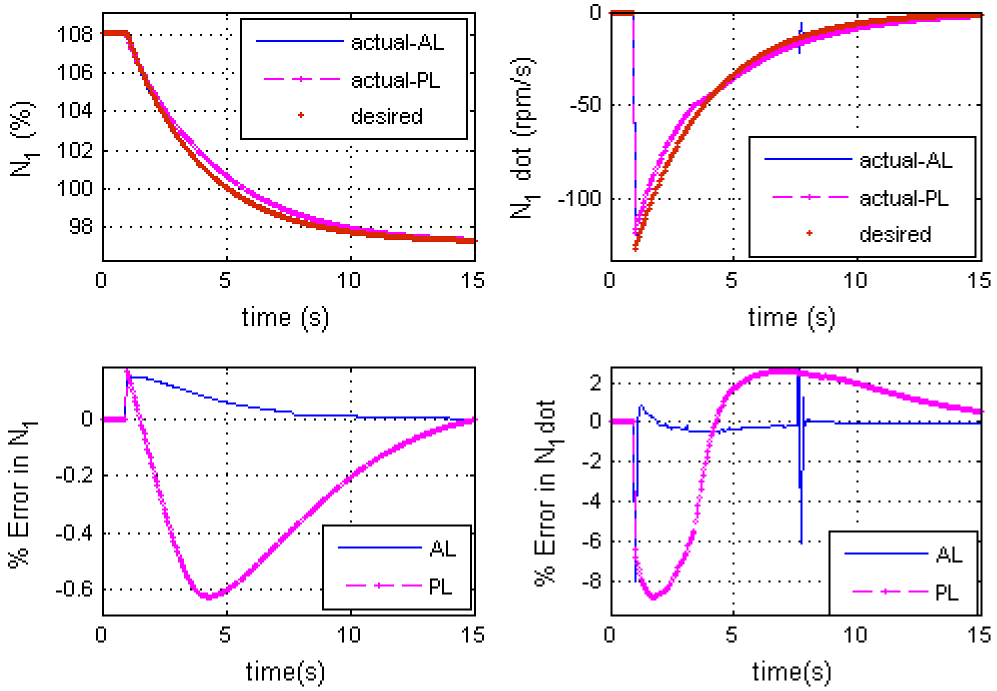

Figure 7.25 Model inversion controller for tracking N_1

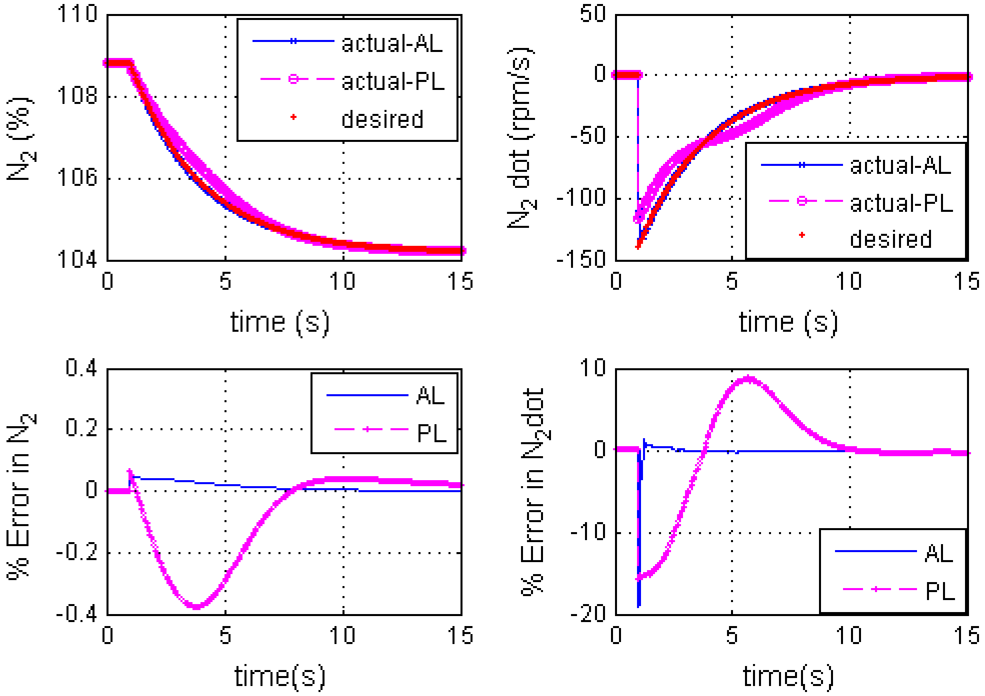

Figure 7.26 Model inversion controller for tracking N_2

7.3 Summary

In this chapter, two potential model applications were discussed. The first application was developed from the examination of the potential problem of failure to achieve the nonlinear values in time for the calculation of the linear coefficients. Holding the linear coefficients for multiple time steps is a quick and easy solution and it was shown that the analytical linear model was able to achieve the desired level of fidelity when the nonlinear convergence issue lasts for a short amount of time. The second solution provided potential benefits of using the analytical linear model as an estimation model. The estimated model without having nonlinear model could accurately estimate the nonlinear model behavior for a long period of time. With the help of a filter, this estimation model will be beneficial for many purposes. First, the model can be used for model predictive control. Secondly, the model may be used for possible improvement of the nonlinear solver. Moreover, the model can be used for estimating parameters for health diagnostics. The second application of a simple model inversion control example demonstrated the advantage of using the real time linear model over a piecewise linear model.

CHAPTER 8

CONCLUSIONS

8.1 Summary and Contribution

Recently, tremendous efforts have been made to improve engine performance while ensuring its operational and mechanical limits are met by applying more advanced engine control technology. These advanced control techniques are mostly based on model based control. While improvement of the control synthesis technique itself can be appealing, an alternative path to the enhancement of the engine control system can be taken by establishing a more accurate engine model that is the basis for the model based control synthesis. The current state of art for engine control system design is based on piecewise linear models. Piecewise linear models provide the required accuracy near steady-state operation, but model outputs drift away from the true value during large transient operation. Moreover, the scheduling of linear models is not a trivial task, especially with growth in the complexity of an engine.

In this thesis, an off-equilibrium linearization methodology was adapted to a jet engine model to enhance the performance by providing more accurate transient representation of the engine model. The use of off-equilibrium linearization approach improved the model accuracy significantly during large transient operation.

In order to reduce computational effort, analytical linearization was applied, enabling linearization in real time. In addition to reduction of computational effort, the analytical linearization method provides simpler analysis of the model due to its utilization of analytical algebraic expressions. Moreover, the analytical linearization approach provides physical insights to the model, enabling various analyses. This benefit alone encourages the use of the analytical linearization method and the analytical linearization approach can be used in combination either with off-equilibrium real time linearization approach or piecewise linearization approach.

The framework for validation of gas turbine linear models was established using existing control oriented metrics. The fidelity of the model was measured from different perspectives using a number of validation metrics. The validation of the model was conducted in both time and frequency domains while covering both open and closed loop contexts.

Some simplifying assumptions were unavoidable to enable analytical partial differentiation. In-depth investigations showed that the effect of applying simplifying assumptions with regard to gas properties on the fidelity of the model is minimal in comparison to the enhancement it offers. Potential model applications were demonstrated using a simple model inversion control and an estimation model.

Further analysis with more complex engine models would be necessary; but analysis has proved that the off-equilibrium analytical linear models are an effective way to accurately capture engine dynamics. Some control application may not require the improvement in engine dynamics while other applications may benefit tremendously. The control designer needs to make a full assessment of the problem and complexity before selecting the linearization method.

The contribution of this thesis can be summarized as following.

1. Adaptation of off-equilibrium linearization into jet engine for more accurate capture of engine dynamics during large transient operation
2. Development and analysis of methodology of analytical linearization to improve physical understanding and provide computationally simple

linearization method. This model also provides a platform for various analyses.

3. Adaptation of existing metrics for the validation of the engine linear models from the control system perspective (framework of the validation of linear models by adapting existing metrics)
4. Demonstration of potential applications of proposed model using simple control and estimation example

8.2 Conclusions

The following conclusions are drawn from the analysis performed on the off-equilibrium analytical linearization approach.

- The analytical linearization method causes a minor degradation of fidelity in comparison to the numerical perturbation method during steady-state operation due to simplifying assumptions. The degradation is bounded by 0.063 for the normalized additive uncertainty and 0.027 for the ν-gap metric.

- Time domain responses show that the off-equilibrium linearization method tracks linear coefficients of non-scheduling parameters of the truth model much better than the piecewise linear model. This trend is quantified using the NRMSE. The NRMSE of a non-scheduling state of the off-equilibrium linear model is much lower than that of the piecewise linear model. On the other hand, the NRMSE of the scheduling state of the piecewise linear model is slightly better than the off-equilibrium linear model. Variation of the NRMSE among the different outputs is very small for the analytical off-equilibrium linear model, whereas significantly larger variation is observed in the NRMSE of different outputs of the piecewise linear model.

- The normalized additive uncertainty for the system with outputs of N_1 and N_2 is kept below 0.07 for the off-equilibrium linear model during the *Bodie* trajectory. The normalized additive uncertainty for the piecewise linear model can be as high as 0.18 during aggressive transient operation.

- Significantly larger variation is observed in both the normalized additive uncertainty and the ν-gap metric during the *Bodie* maneuver in the piecewise linear model than the analytical off-equilibrium linear model.

- The ν-gap metric for the system with an output of N_1 shows similarity between the piecewise linear model and the off-equilibrium linear model. The ν-gap metric of the piecewise linear model is about twice that of the off-equilibrium linear model at its highest. The ν-gap metric for the system with an output of N_2 shows significantly larger improvement using the analytical off-equilibrium linear models. The improvement using the off-equilibrium linearization is more than quadruple for the system with an output of N_2. It is concluded that the improvement of using off-equilibrium linear model is more significant for a non-scheduling output. The conventional piecewise linear model is adequate for the system with an output of scheduling parameter.

- The off-equilibrium analytical linear model exhibits similar magnitude of the ν-gap metric for different outputs when scaled using the DC gains. The system with an output of HPT outlet temperature has the highest ν-gap metric, suggesting that HPT outlet temperature may not be an appropriate design parameter when using the proposed analytical linearized models.

- The effect of the flow solver tolerance on the fidelity of the analytical linearization scheme is found to be negligible.

- Both additive uncertainty and the ν-gap metric for the system with an output of N_2 is an order of magnitude larger when the enthalpy change and torque change due to bleed portion is neglected. This proves that the bleed flow is an important contributor to linear coefficients and cannot be neglected entirely.
- The assumption of constant gas properties within one component during one time step has minor effects on model fidelity as shown by component model level and integrated model level validations. Effects of this assumption are larger for a component with higher temperature variation such as HPT, but still within 5% during the *Bodie* trajectory. This is the cost of achieving the proper analytical linearization. This cost may be decreased using a polynomial representation of gas properties at the expense of computational complexity.
- The combustor is better approximated using the constant c_p, which is different at inlet and outlet, than using an average c_p for calculating linear coefficients. The improvement using c_p, which is different at inlet and outlet, is an order of magnitude for both normalized additive uncertainty and the ν-gap metric.
- Holding off-equilibrium linear coefficients for a few time steps in case of a failure to achieve nonlinear model convergence does not result in a significant loss of the analytical linear model fidelity. The off-equilibrium analytical linear model exhibits higher model fidelity than the piecewise linear model up to loss of flow solver convergence for 5 successive time steps of 0.05s each.

8.3 Recommendations for Future Work

This thesis lays out a strong basis for potential development of many useful applications. Also, some modifications can be made to enhance the analytical linearization approach. The following selective applications of the model are suggested for future work.

1. Study of parametric uncertainty of selected variables

The analytical linear model is a powerful tool for analysis of the effect of parametric uncertainty in selected parameters on the system level linear model. Uncertainty can be represented in terms of a bounded fraction of actual value. For example, uncertainty in T_4 can be implemented by replacing T_4 with $(1+l_p)T4$ in all algebraic expressions for computing linear coefficients where l_p is a fraction of known upper bound of the uncertainty. Different ranges of upper bounds can be examined. The difference between the model with different levels of parametric uncertainties and the model without parametric uncertainty can be captured using validation tools described in this thesis. A parameter which has more weight on system level dynamic model uncertainty can be determined by using this uncertainty model. Furthermore, the effect of changing certain engine parameters on the linear coefficients can be studied using analytical expressions. The analysis can be done at the steady-state operation as well as during transient operation

2. Development of stand-alone linear model by applying filter

The estimation model that was briefly discussed in chapter 7 can be enhanced by applying periodic correction using actual measurements. This may enable the potential linear estimation model along the trajectory without running a nonlinear model onboard or with only minimum nonlinear model involvement. This would increase computational speed as well as eliminate flow solver convergence issues. In addition, approximating thermodynamic properties in terms of simple algebraic expression (replacing thermodynamic table with simple algebraic expressions) would speed up the estimation process. Furthermore, the analytical linear model can run parallel with the nonlinear model by providing initial solver guesses to help convergence of the nonlinear model.

3. Control synthesis problem for off-equilibrium linearization

This thesis only briefly described the control applications. Detailed study on the controller synthesis using the off-equilibrium linear model is desirable as it involves non-conventional definition of the states.

The following offers suggestions to improve the current linearization approach.

4. Enhancement of map representations

   The sensitivities with respect to the compressor and turbine maps were calculated using the numerical perturbation method in this thesis. Replacing the tabular form of map with a functional representation, such as a neural network or state vector machine, can enhance the model by providing computational flexibility and eliminating discontinuity caused by the maps.

5. Increasing complexity of nonlinear model

   An analytical off-equilibrium linearization method can be applied to a more complex engine model with more inputs and states. The advantage of this approach is that it can be applied to any type of gas turbine engine with minor modifications.

6. Development of model in corrected domain

   The analytical off-equilibrium linear engine model was developed for dynamic states of uncorrected shaft speeds. The linear model can be simplified using the corrected domain using ambient condition at the engine’s inlet[62].

APPENDIX A

EXAMPLE OF SYSTEM MATRIX

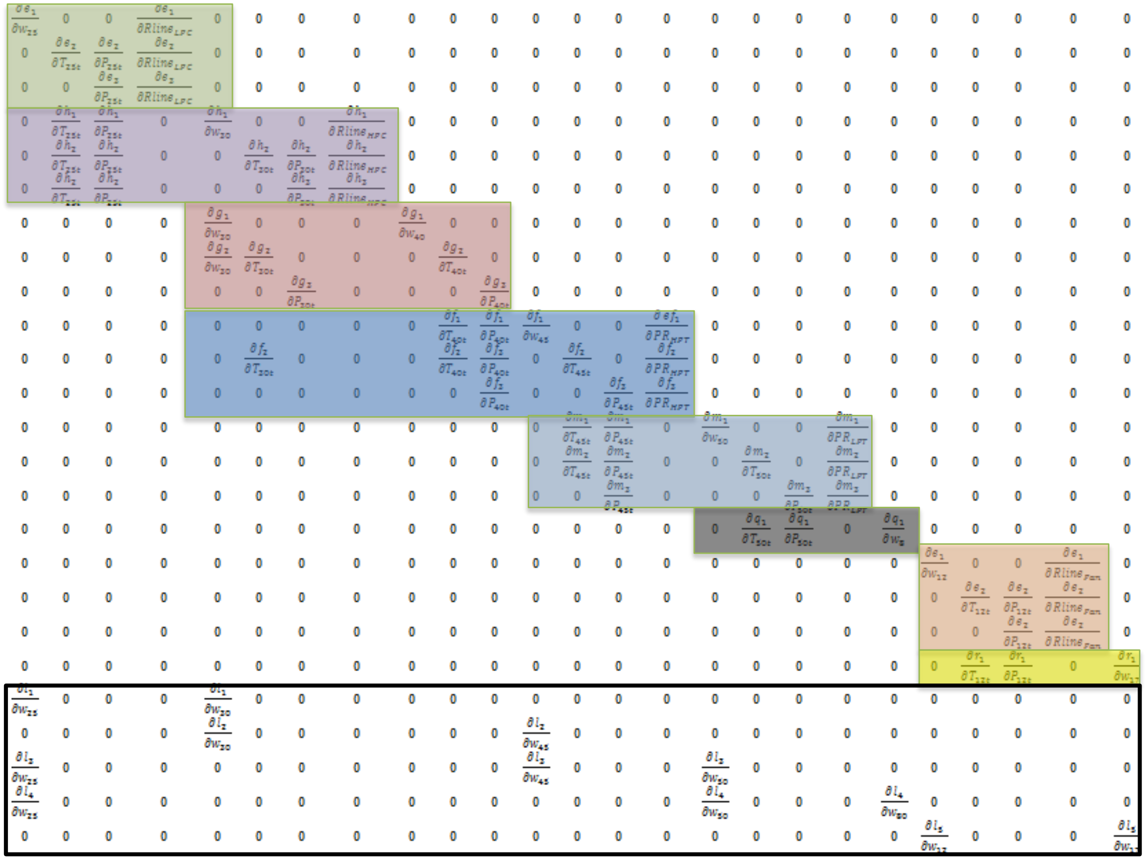

$$\left[\begin{array}{ccccccccccccccccccccccccc}
\frac{\partial e_1}{\partial w_{25}} & 0 & 0 & \frac{\partial e_1}{\partial Rline_{LPC}} & 0 & 0 & 0 & 0 & 0 & 0 & 0 & 0 & 0 & 0 & 0 & 0 & 0 & 0 & 0 & 0 & 0 & 0 & 0 & 0 & 0 \\
0 & \frac{\partial e_2}{\partial T_{25t}} & \frac{\partial e_2}{\partial P_{25t}} & \frac{\partial e_2}{\partial Rline_{LPC}} & 0 & 0 & 0 & 0 & 0 & 0 & 0 & 0 & 0 & 0 & 0 & 0 & 0 & 0 & 0 & 0 & 0 & 0 & 0 & 0 & 0 \\
0 & 0 & \frac{\partial e_3}{\partial P_{25t}} & \frac{\partial e_3}{\partial Rline_{LPC}} & 0 & 0 & 0 & 0 & 0 & 0 & 0 & 0 & 0 & 0 & 0 & 0 & 0 & 0 & 0 & 0 & 0 & 0 & 0 & 0 & 0 \\
0 & \frac{\partial h_1}{\partial T_{25t}} & \frac{\partial h_1}{\partial P_{25t}} & 0 & \frac{\partial h_1}{\partial w_{30}} & 0 & 0 & \frac{\partial h_1}{\partial Rline_{HPC}} & 0 & 0 & 0 & 0 & 0 & 0 & 0 & 0 & 0 & 0 & 0 & 0 & 0 & 0 & 0 & 0 & 0 \\
0 & \frac{\partial h_2}{\partial T_{25t}} & \frac{\partial h_2}{\partial P_{25t}} & 0 & 0 & \frac{\partial h_2}{\partial T_{30t}} & \frac{\partial h_2}{\partial P_{30t}} & \frac{\partial h_2}{\partial Rline_{HPC}} & 0 & 0 & 0 & 0 & 0 & 0 & 0 & 0 & 0 & 0 & 0 & 0 & 0 & 0 & 0 & 0 & 0 \\
0 & \frac{\partial h_3}{\partial T_{25t}} & \frac{\partial h_3}{\partial P_{25t}} & 0 & 0 & 0 & \frac{\partial h_3}{\partial P_{30t}} & \frac{\partial h_3}{\partial Rline_{HPC}} & 0 & 0 & 0 & 0 & 0 & 0 & 0 & 0 & 0 & 0 & 0 & 0 & 0 & 0 & 0 & 0 & 0 \\
0 & 0 & 0 & 0 & \frac{\partial g_1}{\partial w_{30}} & 0 & 0 & 0 & \frac{\partial g_1}{\partial w_{40}} & 0 & 0 & 0 & 0 & 0 & 0 & 0 & 0 & 0 & 0 & 0 & 0 & 0 & 0 & 0 & 0 \\
0 & 0 & 0 & 0 & \frac{\partial g_2}{\partial w_{30}} & \frac{\partial g_2}{\partial T_{30t}} & 0 & 0 & 0 & \frac{\partial g_2}{\partial T_{40t}} & 0 & 0 & 0 & 0 & 0 & 0 & 0 & 0 & 0 & 0 & 0 & 0 & 0 & 0 & 0 \\
0 & 0 & 0 & 0 & 0 & 0 & \frac{\partial g_3}{\partial P_{30t}} & 0 & 0 & 0 & \frac{\partial g_3}{\partial P_{40t}} & 0 & 0 & 0 & 0 & 0 & 0 & 0 & 0 & 0 & 0 & 0 & 0 & 0 & 0 \\
0 & 0 & 0 & 0 & 0 & 0 & 0 & 0 & 0 & \frac{\partial f_1}{\partial T_{40t}} & \frac{\partial f_1}{\partial P_{40t}} & \frac{\partial f_1}{\partial w_{45}} & 0 & 0 & \frac{\partial ef_1}{\partial PR_{HPT}} & 0 & 0 & 0 & 0 & 0 & 0 & 0 & 0 & 0 & 0 \\
0 & 0 & 0 & 0 & 0 & \frac{\partial f_2}{\partial T_{30t}} & 0 & 0 & 0 & \frac{\partial f_2}{\partial T_{40t}} & \frac{\partial f_2}{\partial P_{40t}} & 0 & \frac{\partial f_2}{\partial T_{45t}} & 0 & \frac{\partial f_2}{\partial PR_{HPT}} & 0 & 0 & 0 & 0 & 0 & 0 & 0 & 0 & 0 & 0 \\
0 & 0 & 0 & 0 & 0 & 0 & 0 & 0 & 0 & 0 & \frac{\partial f_3}{\partial P_{40t}} & 0 & 0 & \frac{\partial f_3}{\partial P_{45t}} & \frac{\partial f_3}{\partial PR_{HPT}} & 0 & 0 & 0 & 0 & 0 & 0 & 0 & 0 & 0 & 0 \\
0 & 0 & 0 & 0 & 0 & 0 & 0 & 0 & 0 & 0 & 0 & 0 & \frac{\partial m_1}{\partial T_{45t}} & \frac{\partial m_1}{\partial P_{45t}} & 0 & \frac{\partial m_1}{\partial w_{50}} & 0 & 0 & \frac{\partial m_1}{\partial PR_{LPT}} & 0 & 0 & 0 & 0 & 0 & 0 \\
0 & 0 & 0 & 0 & 0 & 0 & 0 & 0 & 0 & 0 & 0 & 0 & \frac{\partial m_2}{\partial T_{45t}} & \frac{\partial m_2}{\partial P_{45t}} & 0 & 0 & \frac{\partial m_2}{\partial T_{50t}} & 0 & \frac{\partial m_2}{\partial PR_{LPT}} & 0 & 0 & 0 & 0 & 0 & 0 \\
0 & 0 & 0 & 0 & 0 & 0 & 0 & 0 & 0 & 0 & 0 & 0 & 0 & \frac{\partial m_3}{\partial P_{45t}} & 0 & 0 & 0 & \frac{\partial m_3}{\partial P_{50t}} & \frac{\partial m_3}{\partial PR_{LPT}} & 0 & 0 & 0 & 0 & 0 & 0 \\
0 & 0 & 0 & 0 & 0 & 0 & 0 & 0 & 0 & 0 & 0 & 0 & 0 & 0 & 0 & 0 & \frac{\partial q_1}{\partial T_{50t}} & \frac{\partial q_1}{\partial P_{50t}} & 0 & \frac{\partial q_1}{\partial w_8} & 0 & 0 & 0 & 0 & 0 \\
0 & 0 & 0 & 0 & 0 & 0 & 0 & 0 & 0 & 0 & 0 & 0 & 0 & 0 & 0 & 0 & 0 & 0 & 0 & 0 & \frac{\partial e_1}{\partial w_{13}} & 0 & 0 & \frac{\partial e_1}{\partial Rline_{Fan}} & 0 \\
0 & 0 & 0 & 0 & 0 & 0 & 0 & 0 & 0 & 0 & 0 & 0 & 0 & 0 & 0 & 0 & 0 & 0 & 0 & 0 & 0 & \frac{\partial e_2}{\partial T_{13t}} & \frac{\partial e_2}{\partial P_{13t}} & \frac{\partial e_2}{\partial Rline_{Fan}} & 0 \\
0 & 0 & 0 & 0 & 0 & 0 & 0 & 0 & 0 & 0 & 0 & 0 & 0 & 0 & 0 & 0 & 0 & 0 & 0 & 0 & 0 & 0 & \frac{\partial e_3}{\partial P_{13t}} & \frac{\partial e_3}{\partial Rline_{Fan}} & 0 \\
0 & 0 & 0 & 0 & 0 & 0 & 0 & 0 & 0 & 0 & 0 & 0 & 0 & 0 & 0 & 0 & 0 & 0 & 0 & 0 & 0 & \frac{\partial r_1}{\partial T_{13t}} & \frac{\partial r_1}{\partial P_{13t}} & 0 & \frac{\partial r_1}{\partial w_{17}} \\
\frac{\partial l_1}{\partial w_{25}} & 0 & 0 & 0 & \frac{\partial l_1}{\partial w_{30}} & 0 & 0 & 0 & 0 & 0 & 0 & 0 & 0 & 0 & 0 & 0 & 0 & 0 & 0 & 0 & 0 & 0 & 0 & 0 & 0 \\
0 & 0 & 0 & 0 & \frac{\partial l_2}{\partial w_{30}} & 0 & 0 & 0 & 0 & 0 & 0 & \frac{\partial l_2}{\partial w_{45}} & 0 & 0 & 0 & 0 & 0 & 0 & 0 & 0 & 0 & 0 & 0 & 0 & 0 \\
\frac{\partial l_3}{\partial w_{25}} & 0 & 0 & 0 & 0 & 0 & 0 & 0 & 0 & 0 & 0 & \frac{\partial l_3}{\partial w_{45}} & 0 & 0 & 0 & \frac{\partial l_3}{\partial w_{50}} & 0 & 0 & 0 & 0 & 0 & 0 & 0 & 0 & 0 \\
\frac{\partial l_4}{\partial w_{25}} & 0 & 0 & 0 & 0 & 0 & 0 & 0 & 0 & 0 & 0 & 0 & 0 & 0 & 0 & \frac{\partial l_4}{\partial w_{50}} & 0 & 0 & 0 & \frac{\partial l_4}{\partial w_{80}} & 0 & 0 & 0 & 0 & 0 \\
0 & 0 & 0 & 0 & 0 & 0 & 0 & 0 & 0 & 0 & 0 & 0 & 0 & 0 & 0 & 0 & 0 & 0 & 0 & 0 & \frac{\partial l_5}{\partial w_{13}} & 0 & 0 & 0 & \frac{\partial l_5}{\partial w_{17}}
\end{array}\right]$$

Figure A 1 Example of matrix K for twin-spool turbofan

$$\mathbf{E} = \left[\begin{array}{cccc|cccc|ccc|cccc|cccc|c|cccc|c}
\frac{\partial k_2}{\partial w_{25}} & \frac{\partial k_2}{\partial T_{25t}} & 0 & 0 & 0 & 0 & 0 & 0 & 0 & 0 & 0 & 0 & 0 & 0 & 0 & 0 & 0 & 0 & 0 & 0 & 0 & 0 & 0 & 0 & 0 \\
\frac{\partial k_3}{\partial w_{25}} & \frac{\partial k_3}{\partial T_{25t}} & 0 & 0 & 0 & \frac{\partial k_3}{\partial T_{30t}} & 0 & 0 & 0 & 0 & 0 & 0 & 0 & 0 & 0 & 0 & 0 & 0 & 0 & 0 & 0 & 0 & 0 & 0 & 0 \\
0 & 0 & 0 & 0 & \frac{\partial k_4}{\partial w_{30}} & 0 & 0 & 0 & 0 & 0 & 0 & 0 & 0 & 0 & 0 & 0 & 0 & 0 & 0 & 0 & 0 & 0 & 0 & 0 & 0 \\
0 & 0 & 0 & 0 & 0 & \frac{\partial k_5}{\partial T_{30t}} & 0 & 0 & \frac{\partial k_5}{\partial w_{40}} & \frac{\partial k_5}{\partial T_{40t}} & 0 & \frac{\partial k_5}{\partial w_{45}} & \frac{\partial k_5}{\partial T_{45t}} & 0 & 0 & 0 & 0 & 0 & 0 & 0 & 0 & 0 & 0 & 0 & 0 \\
0 & 0 & 0 & 0 & 0 & 0 & 0 & 0 & 0 & 0 & 0 & 0 & \frac{\partial k_6}{\partial T_{45t}} & 0 & 0 & \frac{\partial k_6}{\partial w_{50}} & \frac{\partial k_6}{\partial T_{50t}} & 0 & 0 & 0 & 0 & 0 & 0 & 0 & 0 \\
0 & 0 & 0 & 0 & 0 & 0 & 0 & 0 & 0 & 0 & 0 & 0 & 0 & 0 & 0 & 0 & \frac{\partial k_7}{\partial T_{50t}} & \frac{\partial k_7}{\partial P_{50t}} & 0 & 0 & 0 & 0 & 0 & 0 & 0 \\
0 & 0 & 0 & 0 & 0 & 0 & 0 & 0 & 0 & 0 & 0 & 0 & 0 & 0 & 0 & 0 & \frac{\partial k_8}{\partial T_{50t}} & \frac{\partial k_8}{\partial P_{50t}} & 0 & 0 & 0 & 0 & 0 & 0 & 0 \\
0 & 0 & 0 & 0 & 0 & 0 & 0 & 0 & 0 & 0 & 0 & 0 & 0 & 0 & 0 & 0 & 0 & 0 & 0 & 0 & \frac{\partial k_1}{\partial w_{12}} & \frac{\partial k_1}{\partial T_{12t}} & 0 & 0 & 0 \\
0 & 0 & 0 & 0 & 0 & 0 & 0 & 0 & 0 & 0 & 0 & 0 & 0 & 0 & 0 & 0 & 0 & 0 & 0 & 0 & 0 & \frac{\partial k_9}{\partial T_{12t}} & \frac{\partial k_9}{\partial P_{12t}} & 0 & 0 \\
0 & 0 & 0 & 0 & 0 & 0 & 0 & 0 & 0 & 0 & 0 & 0 & 0 & 0 & 0 & 0 & 0 & 0 & 0 & 0 & 0 & \frac{\partial k_{10}}{\partial T_{12t}} & \frac{\partial k_{10}}{\partial P_{12t}} & 0 & 0
\end{array}\right]$$

$$
\mathbf{M}=\left[\begin{array}{c:c}
\frac{\partial e_1}{\partial N_1} & 0 \\
\frac{\partial e_2}{\partial N_1} & 0 \\
\frac{\partial e_3}{\partial N_1} & 0 \\ \hdashline
0 & \frac{\partial h_1}{\partial N_2} \\
0 & \frac{\partial h_2}{\partial N_2} \\
0 & \frac{\partial h_3}{\partial N_2} \\ \hdashline
0 & 0 \\
0 & 0 \\
0 & 0 \\ \hdashline
0 & \frac{\partial f_1}{\partial N_2} \\
0 & \frac{\partial f_2}{\partial N_2} \\
0 & \frac{\partial f_3}{\partial N_2} \\ \hdashline
\frac{\partial m_1}{\partial N_1} & 0 \\
\frac{\partial m_2}{\partial N_1} & 0 \\
\frac{\partial m_3}{\partial N_1} & 0 \\ \hdashline
0 & 0 \\ \hdashline
\frac{\partial a_1}{\partial N_1} & 0 \\
\frac{\partial a_2}{\partial N_1} & 0 \\
\frac{\partial a_3}{\partial N_1} & 0 \\ \hdashline
0 & 0 \\ \hdashline
0 & 0 \\
0 & 0 \\
0 & 0 \\
0 & 0 \\
0 & 0
\end{array}\right],
\mathbf{L}=\left[\begin{array}{c}
0 \\ 0 \\ 0 \\ \hdashline
0 \\ 0 \\ 0 \\ \hdashline
\frac{\partial g_1}{\partial w_f} \\ \frac{\partial g_2}{\partial w_f} \\ 0 \\ \hdashline
0 \\ 0 \\ 0 \\ \hdashline
0 \\ 0 \\ 0 \\ \hdashline
0 \\ \hdashline
0 \\ 0 \\ 0 \\ \hdashline
0 \\ \hdashline
0 \\ 0 \\ 0 \\ 0 \\ 0
\end{array}\right],
\mathbf{R}=\left[\begin{array}{c:c}
\frac{\partial e_1}{\partial T_{20t}} & \frac{\partial e_1}{\partial P_{20t}} \\
\frac{\partial e_2}{\partial T_{20t}} & \frac{\partial e_2}{\partial P_{20t}} \\
\frac{\partial e_3}{\partial T_{20t}} & \frac{\partial e_3}{\partial P_{20t}} \\ \hdashline
0 & 0 \\
0 & 0 \\
0 & 0 \\ \hdashline
0 & 0 \\
0 & 0 \\
0 & 0 \\ \hdashline
0 & 0 \\
0 & 0 \\
0 & 0 \\ \hdashline
0 & 0 \\
0 & 0 \\
0 & 0 \\ \hdashline
0 & 0 \\ \hdashline
\frac{\partial a_1}{\partial T_{20t}} & \frac{\partial a_1}{\partial P_{20t}} \\
\frac{\partial a_2}{\partial T_{20t}} & \frac{\partial a_2}{\partial P_{20t}} \\
\frac{\partial a_3}{\partial T_{20t}} & \frac{\partial a_3}{\partial P_{20t}} \\ \hdashline
0 & 0 \\ \hdashline
0 & 0 \\
0 & 0 \\
0 & 0 \\
0 & 0 \\
0 & 0
\end{array}\right],
\mathbf{F}=\begin{bmatrix}
0 \\ 0 \\ \frac{\partial k_4}{\partial w_f} \\ 0 \\ 0 \\ 0 \\ 0 \\ 0 \\ 0 \\ 0
\end{bmatrix},
\mathbf{G}=\left[\begin{array}{c:c}
\frac{\partial k_2}{\partial N_1} & 0 \\
0 & \frac{\partial k_3}{\partial N_2} \\
0 & 0 \\
0 & \frac{\partial k_5}{\partial N_2} \\
\frac{\partial k_6}{\partial N_1} & 0 \\
0 & 0 \\
0 & 0 \\
\frac{\partial k_1}{\partial N_1} & 0 \\
0 & 0 \\
0 & 0
\end{array}\right]
$$

$$
\mathbf{P}=\begin{bmatrix}
1 & 0 & 0 & 0 & 1 & 0 & 0 & 1 & 0 & 0 \\
0 & 1 & 0 & 1 & 0 & 0 & 0 & 0 & 0 & 0
\end{bmatrix}
$$

REFERENCES

[1] Ananthkrishnan, N., 2004, “Small-Perturbation Analysis of Airplane Flight Dynamics – A Reappraisal. I: Longitudinal Modes,” AIAA Atmospheric Flight Mechanics Conference 2004, AIAA, Providence, RI, pp. 643–659.

[2] Aström, K. J., and Murray, R. M., 2008, *Feedback Systems: An Introduction for Scientists and Engineers,* Princeton University Press.

[3] Ballin, M. G., 1988, “A High Fidelity Real-time Simulation of a Small Turboshaft Engine,”, NASA TM-100991, NASA.

[4] Brunell, B. J., Viassolo, D. E., and Prasanth, R., 2004, “Model Adaptation and Nonlinear Model Predictive Control of an Aircraft Engine,” Proceedings of the ASME Turbo Expo 2004, ASME, Atlanta, pp.673.

[5] Camporeale, S. M., Fortunato, B., and Mastrovito, M., 2006, “A modular code for real time dynamic simulation of gas turbines in simulink,” Journal of Engineering for Gas Turbines and Power, **128**(3), pp. 506–517.

[6] Chung, G.-Y., Dhingra, M., Prasad, J. V. R., Meisner, R., and Sirica, S., 2011, “An Analytical Approach to Gas Turbine Engine Model Linearization,” Proceedings of the ASME Turbo Expo 2011, AMSE, Vancouver, Canada, pp. 105–115.

[7] Chung, G.-Y., Prasad, J. V. R., Dhingra, M., and Meisner, Richard, “Real time analytical linearization of turbofan engine model,” Proceedings of the ASME Turbo Expo 2013, ASME, San Antonio, TX.

[8] Csank, J., May, R. D., Litt, J. S., and Guo, T.-H., 2010, “Control Design for a Generic Commercial Aircraft Engine,” 46th AIAA/ASME/SAE/ASEE Joint Propulsion Conference & Exhibit, AIAA, Nashville.

[9] Culley, D et al, 2009, “More Intelligent Gas Turbine Engines (Des turbomoteurs plus intelligents),”,TR-AVT-128, RTO Technical report.

[10] Cumpsty, N., 2003, *Jet Propulsion: A Simple Guide to the Aerodynamic and Thermodynamic Design and Performance of Jet Engines,* Cambridge University Press.

[11] Curry, T., and Behbahani, A., 2004, “Propulsion Directorate/Control and Engine Health Management(CEHM): Real-Time Turbofan Engine Simulation,” 2004 IEEE Aerospace Conference Proceedings, IEEE, Piscataway, NJ, USA, pp. 3414–23.

[12] DeCastro, J. A., 2007, “Rate-Based Model Predictive Control of Turbofan Engine Clearance,” Journal of Propulsion and Power, **23**(4), pp. 804–813.

[13] DeCastro, J. A., Litt, J. S., and Frederick, D. K., 2008, “A modular aero-propulsion system simulation of a large commercial aircraft engine,” 44th AIAA/ASME/SAE/ASEE Joint Propulsion Conference and Exhibit, July 21, 2008 - July 23, 2008, American Institute of Aeronautics and Astronautics Inc., Hartford, CT, United states.

[14] Edmunds, D. B., 1977, “Multivariable Control for a Variable Area Turbine Engine,” ASD-TR-77-59, Air Force.

[15] El-Sakkary, A., 1985, “The gap metric: Robustness of stabilization of feedback systems,” IEEE Transactions on Automatic Control, **30**(3), pp. 240– 247.

[16] Flack, R. D., 2010, *Fundamentals of Jet Propulsion with Applications*, Cambridge University Press.

[17] Frederick, D. K., DeCastro, J. A., and Litt, J. S., 2007, “User’s Guide for the Commercial Modular Aero-Propulsion System Simulation (C-MAPSS),” NASA/TM-2007-215026, NASA.

[18] Ghorbanian, K., and Gholamrezaei, M., 2009, “An artificial neural network approach to compressor performance prediction,” Applied Energy, **86**(7-8), pp. 1210–21.

[19] James, M. R., Smith, M. C., and Vinnicombe, G., 2005, “Gap Metrics, Representations, and Nonlinear Robust Stability,” SIAM Journal on Control and Optimization, **43**(5), p. 1535.

[20] Jaw, L. C., 2009, *Aircraft engine controls : design, system analysis, and health monitoring*, AIAA, Reston.

[21] Jaw, L. C., and Garg S., 2005, “Propulsion Control Technology Development in the United States A Historical Perspective,” NASA/TM-2005-213978, NASA.

[22] Johansen, T. A., Hunt, K. J., Gawthrop, P. J., and Fritz, H., 1998, “Off-equilibrium linearisation and design of gain-scheduled control with application to vehicle speed control,” Control Engineering Practice, **6**(2), pp. 167–80.

[23] Jones, Scott M., “An Introduction to Thermodynamic Performance Analysis of Aircraft Gas Turbine Engine Cycles Using the Numerical Propulsion System Simulation Code,” NASA/TM-2007-214690, NASA.

[24] Kim, S., Ellis, S., and Challener, M., 2006, "Real-Time Engine Modelling of a Three Shafts Turbofan Engine: From Sub-Idle To Max Power Rate," Proceedings of the ASME Turbo Expo 2006, ASME, Barcelona, Spain, pp. 699–705.

[25] Kulikov, G. G., and Thompson, H. A., 2004, *Dynamic modelling of gas turbines: identification, simulation, condition monitoring, and optimal control*, Springer, London.G.G.

[26] Kumar, A., and Viassolo, D., 2008, "Model-Based Fault Tolerant Control," NASA/CR-2008-215273, NASA.

[27] Leith, D. J., and Leithead, W. E., 1998, "Gain-scheduled and nonlinear systems: Dynamic analysis by velocity-based linearization families," International Journal of Control, **70**(2), pp. 289–317.

[28] Lichtsinder, M., and Levy, Y., 2006, "Jet engine model for control and real-time simulations," Journal of Engineering for Gas Turbines and Power, **128**(4), pp. 745–753.

[29] Lietzau, K., and Kreiner, A., 2004, "The Use of Onboard Real-Time Models for Jet Engine Control," MTU Aero Engine, Germany.

[30] Litt, J. S., Simon, D. L., Garg, S., Guo, T.-H., Mercer, C., Millar, R., Behbahani, A., Bajwa, A., and Jensen, D. T., 2004, "A survey of intelligent control and health management technologies for aircraft propulsion systems," Journal of Aerospace Computing, Information and Communication, (DEC.), pp. 543–563.

[31] Lytle, J. K., "Numerical Propulsion System Simulation: An Overview," CAS 2000 Workshop/The Ames Research Center, February, **15**, p. 2000.

[32] Maciejowski, J., 2000, *Predictive Control with Constraints*, Prentice Hall.

[33] Maciejowski, J. M., 1989, *Multivariable feedback design*, Addison-Wesley.

[34] Mahmood, S., Griffin, I. A., Fleming, P. J., and Shutler, A. J., 2005, "Inverse Model Control of a Three Spool Gas Turbine Engine," Proceedings of the ASME Turbo Expo 2005, ASME, Reno-Tahoe, NV, pp. 731–736.

[35] Martin, S., Wallace, I., and Bates, D. G., 2008, "Development and validation of a civil aircraft engine simulation model for advanced controller design," Journal of Engineering for Gas Turbines and Power, **130**(5).

[36] Mattingly, J. D., 1996, *Elements of gas turbine propulsion*, McGraw-Hill.

[37] Mattingly, J. D., Heiser, W. H., and Pratt, D. T., 2002, *Aircraft Engine Design*, Second Edition, AIAA, Reston.

[38] McFarlane, D., and Glover, K., 1992, "A loop-shaping design procedure using H∞ synthesis," IEEE Transactions on Automatic Control, **37**(6), pp. 759–769.

[39] Merrill, W., Lehtinen, B., and Zeller, J., 1984, "The role of modern control theory in the design of controls for aircraft turbine engines," Journal of Guidance, Control, and Dynamics, **7**(6), pp. 652–61.

[40] Murray-smith, R., Johansen, T. A., and Shorten, R., 1999, "On Transient Dynamics, Off-Equilibrium Behaviour and Identification in Blended Multiple Model Structures," In European Control Conference, p. 14.

[41] NATO RESEARCH AND TECHNOLOGY ORGANIZATION NEUILLY-SUR-SEINE (FRANCE), "Performance Prediction and Simulation of Gas Turbine Engine Operation for Aircraft, Marine, Vehicular, and Power Generation," 2007.

[42] Pakmehr, M., Fitzgerald, N., Feron, E., Shamma, J., and Behbahani, A., "Gain Scheduling Control of Gas Turbine Engines: Absolute Stability by Computing a Single Lyapunov Function," in: ASME Conference Proceedings, San Antonio, TX, USA, 2013.

[43] Qi, O. F., Gawthrop, P. J., and Maccallum, N. R. L., 1992, "Model-Based Observer: A Gas Turbine Engine Case Study," First IEEE Conference on, New York, pp. 877–82.

[44] Rahman, N. U., and Whidborne, J. F., 2009, "Real-time transient three spool turbofan engine simulation: A hybrid approach," Journal of Engineering for Gas Turbines and Power, **131**(5), pp. 1–8.

[45] Rezvani, R., Ozcan, M., Kestner, B., Tai, J, Marvis, D.N, Meisner, R., and Sirica, S., 2011, "A Gas Turbine Engine Model of Transient Operation Across the Flight Envelope," Proceedings of ASME Turbo Expo 2011, ASME, Vancouver, Canada.

[46] Richter, H., Singaraju, A., and Litt, J. S., 2008, "Multiplexed predictive control of a large commercial turbofan engine," Journal of Guidance, Control, and Dynamics, **31**(2), pp. 273–81.

[47] Sanghi, V., Lakshmanan, B. K., and Rajasekaran, R., 2001, "Aerothermal model for real-time digital simulation of a mixed-flow turbofan engine," Journal of Propulsion and Power, **17**(3), pp. 629–635.

[48] Seldner, K., Cwynar, D. S.,1978, "Procedures for generation and reduction of linear models of a turbofan engine," NASA Technical Report 1261, NASA, Washington.

[49] Sellers, J. F., and Daniele, C. J., 1975, “DYNGEN - A Program for Calculating Steady-State and Transient Performance of Turbojet and Turbofan Engines,” SNAS TN D-7901, NASA.

[50] Shankar, P., and Yedavalli, R. K., 2009, “Neural-network-based observer for turbine engine parameter estimation,” Proceedings of the Institution of Mechanical Engineers, Part I: Journal of Systems and Control Engineering, **223**(6), pp. 821–832.

[51] Spang, III A., and Brown, H., 1999, “Control of jet engines,” Control Engineering Practice, **7**(9), pp. 1043–1059.

[52] Steele, J., and Vinnicombe, G., “The ν-Gap Metric and the Generalised Stability Margin,” Advanced Techniques for Clearance of Flight Control Laws, C. Fielding, A. Varga, S. Bennani, and M. Selier, eds., Springer Berlin Heidelberg, Berlin, Heidelberg, pp. 57–75.

[53] Sugiyama, N., 1994, “Derivation of system matrices from nonlinear dynamic simulation of jet engines,” Journal of Guidance, Control, and Dynamics, **17**(6), pp. 1320–1326.

[54] Tagashira, T., Mizuno, T., Koh, M., and Sugiyama, N., 2009, “ATF Test Evaluation Of Model Based Control For a Single Spool Turbojet Engine,” Proceedings of the ASME Turbo Expo 2009, ASME, Orlando, FL, United states, pp. 673–685.

[55] Turevskiy, A., Meisner, R., Luppold, R. H., Kern, R. A., and Fuller, J. W., 2002, “A Model-Based Controller for Commercial Aero Gas Turbines,” Proceedings of the ASME Turbo Expo 2002, ASME, Amsterdam, The Netherlands, pp. 189–195.

[56] van Essen, H. A., 1998, “Modelling and model based control of turbomachinery,” Technische Universiteit Eindhoven, Eindhoven.

[57] van Essen, H. A., and De Lange, H. C., 2001, “Nonlinear Model Predictive Control Experiments on a Laboratory Gas Turbine Installation,” J. Eng. Gas Turbines Power, **123**(2), pp. 347–352.

[58] Venturini, M., 2006, “Simulation of compressor transient behavior through recurrent neural network models,” Journal of Turbomachinery, **128**(3), pp. 444–454.

[59] Vinnicombe, G., 1992, “Measuring robustness of feedback systems”, University of Cambridge.

[60] Vinnicombe, G., 2001, *Uncertainty and Feedback: H [infinity] Loop-shaping and the [nu]-gap Metric*, World Scientific.

[61] Volponi, A., 2008, “Enhanced Self Tuning On-Board Real-Time Model (eSTORM) For Aircraft Engine Performance Health Tracking,” NASA/CR-2008-215272, NASA.

[62] Volponi, A. J., 1999, “Gas Turbine Parameter Corrections,” J. Eng. Gas Turbines Power, **121**(4), pp. 613–621.

[63] Walsh, P. P., and Fletcher, P., 2004, *Gas Turbine Performance*, Second Edition, John Wiley & Sons.

[64] Zhou, K., and Doyle, J. C., 1997, *Essentials of Robust Control*, Prentice Hall.

[65] Zhou, K., Doyle, J. C., and Glover, K., 1995, *Robust and Optimal Control,* Prentice Hall.

[66] 2006, “NPSS User Guide,” NPSS-User, NASA.